Tabulated chemistry for turbulent combustion modeling and simulation

Ronan Vicquelin

Ecole Centrale Paris

THESE

présentée par

Ronan VICQUELIN

pour l'obtention du

GRADE de DOCTEUR

Formation doctorale : Energétique

Laboratoire d'accueil : Laboratoire d'Énergétique Moléculaire et Macroscopique, Combustion (EM2C) du CNRS et de l'ECP

Tabulation de la cinétique chimique pour la modélisation et la simulation de la combustion turbulente.

Soutenue le 17 Juin 2010

Jury :	MM.	Christophe	Bailly	Président
		Michel	Champion	Rapporteur
		Thierry	Poinsot	Rapporteur
		Stéphane	Carpentier	Examinateur
		Heinz	Pitsch	Examinateur
		Benoît	Fiorina	Co-encadrant
		Olivier	Gicquel	Directeur de thèse

Ecole Centrale des Arts et Manufactures
Grand Établissement sous tutelle
du Ministère de l'Éducation Nationale
Grande Voie des Vignes
92295 Châtenay-Malabry Cedex
Tél : 33 (1) 41 13 10 00
Télex : 634 991 F EC PARIS

Laboratoire d'Énergétique Moléculaire et Macroscopique, Combustion (E.M2.C.)
UPR 288, CNRS et Ecole Centrale Paris
Tél : 33 (1) 41 13 10 31
Fax : 33 (1) 47 02 80 35

2010ECAP0015

Remerciements

Cette thèse a été réalisée au laboratoire EM2C de l'Ecole Centrale Paris et au centre de recherche CRIGEN de GDF SUEZ qui a financé avec l'Agence Nationale de la Recherche ces travaux.

Je tiens, tout d'abord, à remercier très chaleureusement Benoît Fiorina et Olivier Gicquel pour leur excellent encadrement. Ils m'ont fait profiter de leur grande expérience en combustion et ont su me guider efficacement tout au long de cette thèse. Ils ont été très impliqués dans ces travaux de recherche, ce qui a donné lieu à plusieurs moments de profusion d'idées. Ces instants où la passion pour leur métier se lisaient dans leurs regards ont marqué mon esprit. Sur un plan personnel, j'ai énormément apprécié leur dynamisme, leur sympathie et leur optimisme à toute épreuve. Enfin, merci à Olivier de m'avoir converti au Mac, je ne reviendrai plus en arrière !

Je remercie tout le personnel du pôle CHENE pour leur excellent accueil. Je remercie particulièrement Stéphane Carpentier pour avoir suivi mon travail et avoir accepté de participer au jury. Je remercie aussi Ghislain Lartigue qui m'a encadré chez GDF SUEZ depuis mon stage de Master et pendant le début de la thèse. Il a fait preuve d'une grande gentillesse et a toujours su se rendre disponible à chaque fois que j'avais une question. Je remercie aussi Sandra Payet qui m'a encadré par la suite. Sa bonne humeur m'a permis de passer les caps difficiles sans encombre. J'ai aussi une pensée pour Guillaume Daill et Erwin George du pôle INDUSTRIE qui m'ont appris les mystères de la programmation dans CFX.

Je remercie sincèrement Christophe Bailly pour avoir assuré la présidence de mon jury de thèse, Michel Champion et Thierry Poinsot pour avoir relu avec minutie mon manuscrit en tant que rapporteurs, et Heinz Pitsch pour avoir accepté de participer au jury en tant qu'examinateur.

J'adresse mes remerciements à tout le personnel du laboratoire EM2C, doctorants et permanents. Ils m'ont offert un environnement et une ambiance de travail exceptionnels. J'ai une pensée particulière pour Antoine Mazas qui a partagé mon bureau et a manié des flammes laminaires (en vrai !),

pour Paul Palies qui a envoyé/envoit/enverra toujours du "fat", pour Pierre Auzillon pour sa sympathie et à qui j'ai laissé TTC et F-TACLES en toute confiance. Je pense aussi à Jean Lamouroux qui poursuit la voie vers un modèle pour la combustion sans flamme.
Je suis aussi très reconnaissant envers les chercheurs du laboratoire toujours disponibles pour répondre à mes questions. Je pense notamment à Nasser Darabiha et à Denis Veynante que j'ai accompagnés pendant un mois à l'université de Stanford, séjour durant lequel j'ai beaucoup apprécié leur compagnie (sans oublier Benoît qui connaissait toujours une bonne adresse où manger un burger). Je remercie aussi très sincèrement Thierry Schuller qui m'a offert l'opportunité d'enseigner la mécanique des fluides en classe de TD aux élèves de Centrale. Ce fut une expérience que j'ai beaucoup aimée.

Merci à Yoann Méry (ami/co-étage/co-bureau/témoin/et maintenant collègue docteur), qui (comme moi) est entré au laboratoire EM2C après ses études à l'Ecole Centrale, pour tous ces bons moments de rire (et fou-rire), d'aventures (cf. Californie) mais aussi de science !

Ce travail n'aurait pas été le même sans mon stage de Master que j'ai effectué au CERFACS. Sous la direction de Thierry Poinsot, j'y ai appris l'art et la manière de faire des calculs LES. Quand, pendant ma thèse, il a fallu mettre les mains dans AVBP, j'ai toujours trouvé une personne au CERFACS pour répondre à mes questions. Je remercie en particulier Gabriel Staffelbach et Olivier Vermorel qui savaient éclairer ma lanterne lorsque je parcourais AVBP. J'ai aussi une pensée pour Guilhem Lacaze et Thomas Schmitt qui m'ont fait part de leur expérience sur la LES des jets ronds. Un grand merci aussi à Matthieu Boileau qui met son expérience au service de tous depuis son arrivée au laboratoire EM2C.

Merci à ma famille (père, mère, frères, grand-mére, oncles, tantes, cousin(e)s, ..) et à mes amis (de Bayeux et de Centrale) pour leur attention lorsque je leur parlais de combustion sans flamme sans qu'ils ne me prennent pour un ahuri. Je les remercie pour leur soutien et leurs encouragements.

Un très grand merci à Juliette, mon épouse, qui m'a accompagné et soutenu tout au long de ces travaux et lors de la période de rédaction.

Résumé

Cette thèse se situe dans le cadre de la simulation numérique de la combustion turbulente à l'aide de méthodes de tabulation de la cinétique chimique. En approximant la structure fine des flammes turbulentes, ces méthodes prennent en compte des effets fins de cinétique chimique pour un faible coup dans les calculs numériques. Ceci permet de prédire les champs de température et d'espèces chimiques incluant les polluants. Le champ d'application de la chimie tabulée a d'abord été réservé à la simulation des écoulements moyens (RANS) dans une hypothèse de faible nombre de Mach pour une combustion dite "conventionnelle". Cependant, le développement actuel de nouvelles technologies de combustion ainsi que celui de modèles numériques plus avancés que les approches RANS nécessite d'étendre ce champ d'application. Les travaux de cette thèse ont mené au développement de nouveaux modèles de chimie tabulée afin de répondre à ces nouvelles exigences.
L'émergence de nouvelles technologies comme la combustion sans flamme nécessite le développement de modèles dédiés. Ce mode de combustion présente en effet des structures de flamme mixtes. C'est pourquoi un modèle de tabulation de la cinétique chimique nommé UTaC (Unsteady flamelets Tabulated Chemistry) est proposé pour prédire la combustion diluée à haute température qui caractérise la combustion sans flamme. Le modèle est basé sur la tabulation de solutions instationnaires de flammelettes non-prémelangées qui s'auto-allument. Les pertes thermiques et la dilution variable des gaz brûlés sont négligés dans le cadre de cette thèse par soucis de simplification et de clarté de la validation du modèle. Le modèle est appliqué au cas d'un jet de combustible dilué dans un environnement de gaz vicié qui favorise l'auto-allumage comme moyen de stabilisation d'une flamme liftée. Plusieurs simulations RANS sont réalisées en faisant varier le combustible utilisé. Enfin, une simulation aux grandes échelles (LES) est aussi conduite pour le mélange méthane/air.
Plusieurs codes numériques dédiés à la LES sont basés sur une formulation compressible des équations de Navier-Stokes. Cependant les méthodes de tabulation ne permettent pas directement de prendre en compte les effets acoustiques. Un modèle appelé TTC (Tabulated Thermo-chemistry for Compressible flows) a été créé afin d'introduire les méthodes de chimie tabulée dans les codes numériques compressibles. Pour cela, le calcul de la

température est reformulé ainsi que le traitement des conditions aux limites à l'aide d'ondes caractéristiques.
Enfin, l'application de modèle RANS de tabulation de la cinétique chimique à la LES est souvent faite sans tenir compte des spécificités de la simulation aux grandes échelles. Ainsi, les fonctions de densité de probabilités de type β qui traduisent l'interaction de la combustion avec la turbulence en RANS sont utilisées telles quelles en LES. Nous montrerons que cette hypothèse est mauvaise car elle ne conserve pas l'intégrale du terme source dans une flamme prémélangée. Un nouveau modèle de chimie tabulée nommé F-TACLES (Filtered Tabulated Chemistry for Large Eddy Simulation) est alors développé spécifiquement pour la simulation aux grandes échelles de la combustion parfaitement prémélangée. Le modèle est basé sur le filtrage de flammes laminaires de prémélange mono-dimensionelles.

Abstract

The thesis subject is located in the domain of numerical simulation of turbulent combustion through tabulated chemistry methods. These methods allow to include detailed chemistry effects at low cost in numerical simulation by approximating the fine scales structure of turbulent flames. Prediction of temperature and chemical species including pollutants becomes then possible. Tabulated chemistry models were first dedicated to low Mach-number RANS approaches for "conventional" combustion applications. However, the current uprising of new combustion configurations and of more precise numerical modeling than RANS approach requires to widen these range of applications. For that purpose, this thesis led to the development of new tabulated chemistry models.
Flameless combustion is one of these new combustion technology that requires dedicated models. Indeed, complex flame structures are encountered in this combustion mode. That is why a tabulated chemistry model called UTaC (Unsteady flamelets Tabulated Chemistry) is derived to simulate high temperature diluted combustion which characterizes flameless combustion. The model lies on the tabulation of laminar unsteady non-premixed flamelets that auto-ignite. Heat losses and variation of dilution with burnt gases are neglected in the topic of this thesis for brevity and simplification of the model validation. The investigated configuration is a fuel jet diluted in a vitiated coflow. The hot coflow promotes auto-ignition in the lifted flame stabilization mechanism. Several RANS computations are performed by changing the fuel composition. Finally, a Large Eddy Simulation (LES) is also realized using a methane/air mixture as the impinging fuel stream.
Several numerical codes for LES use a fully compressible formulation of Navier-Stokes equations. However, tabulated chemistry techniques do not take into account acoustic perturbations. A model called TTC (Tabulated Thermo-chemistry for Compressible flows) formalism is therefore developed in order to include tabulated chemistry in compressible CFD codes. TTC formalism consists in reformulating both temperature computation inside the numerical code and the characteristic boundary treatment.
Finally, application of tabulated chemistry model to LES is usually done by a straightforward derivation from its RANS version without taking into account LES requirements. Indeed, β-probability density functions which

accounts for turbulence-chemistry interaction in RANS are used in LES although this technique does not conserve the source terms integral in premixed flames. A new model, F-TACLES (Filtered Tabulated Chemistry for Large Eddy Simulation), is then derived specifically for LES of perfectly premixed combustion. This model is based on filtering of 1D laminar premixed flamelets.

Contents

Introduction

Cette thèse est le fruit d'une collaboration entre le laboratoire CNRS EM2C de l'École Centrale Paris et GDF SUEZ au travers d'une convention CIFRE financée par l'ANRT (Agence Nationale de la Recherche et de la Technologie). La thèse fait aussi partie du programme Pan-H financé par l'Agence National de la Recherche (ANR).

Challenges of combustion science

The demand for energy has never been so high. Figure 1(a) shows that the Total Primary Energy Supply (TPES) has more than doubled since 1971. This demand will increase even more in the following decades with the emergence of China and India. Indeed, according to the International Energy Agency (IEA), both countries will account for 45% of the increase in global primary energy demand by 2030. Hence, the global energy supply will have to follow the corresponding demand. However, the majority of energy resources comes from fossil fuels (oil, coal and gas) which are to disappear in the future. The combination of increase in energetic demand and of the shortcoming of fossil resources is one of the biggest challenge in the 21st Century. Beyond the development of non-fossil energies, this will require the improvement of combustion-based technologies in order to reduce fuel consumption. Indeed, combustion is responsible for more than 90% of energy conversion as depicted in Fig. 1(b). Combustion will then remain ineluctable for a certain time but leads to several environmental issues that need to be addressed.

During combustion of hydrocarbons with air, burnt gases are not only composed of carbon dioxide and water vapor. In fact, several pollutants can also be produced. The emission of such chemical species is hazardous for human health. This concerns for instance the carbon monoxide CO, Unburnt HydroCarbons (UHC), Volatile Organic Compounds (VOC) and particulate matter (PM). Besides causing breathing problems, sulfur oxides (SO_x) are also responsible for acid rain. Acid rain is also induced by nitrogen oxides (NO_x) emission. These are major pollutants that produce urban smog and harmful ozone at ground level. All these pollutants emissions are restricted

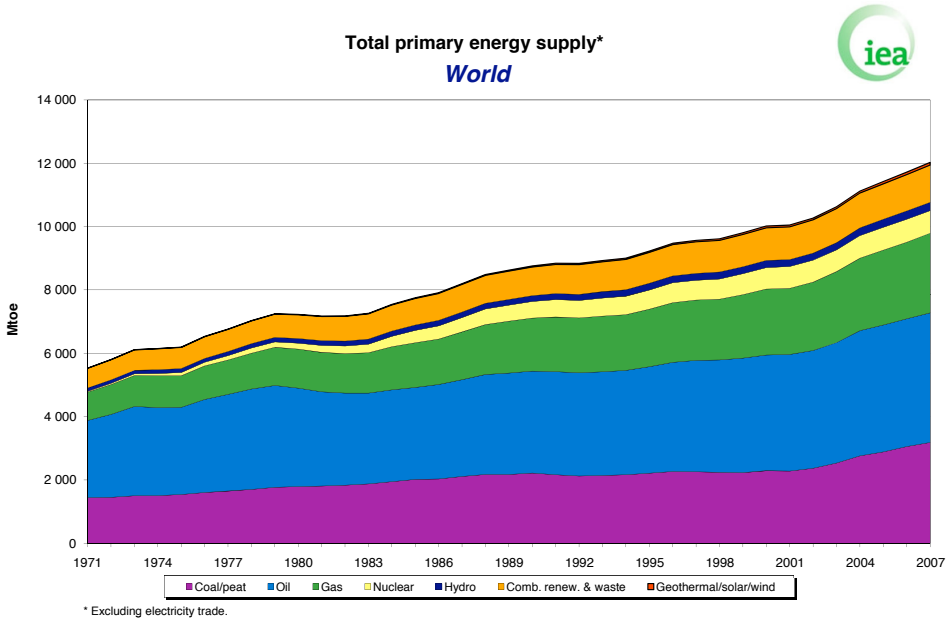

(a)

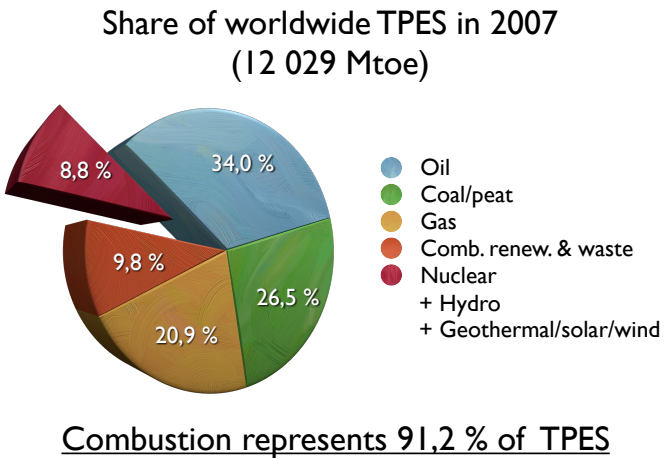

(b)

Figure 1: *Total Primary Energy Supply (TPES) in the world shared between different resources: coal/peat, oil, gas, nuclear energy, hydraulic power, combustible renewables and waste, and geothermal/solar/wind energy. TPES is expressed in Million tons of oil equivalent (Mtoe). (a) Evolution of global TPES from 1971 to 2007. (b) Share of global TPES in 2007. Data are available on the IEA website (International Energy Agency, 2010).*

by different standards. These standards can exist at several levels (national, european, international) and apply to all industrial sectors where combustion is used: cars, planes, industrial plants, gas turbines, domestic boilers, ... The elaboration of more and more severe standards on pollutants emissions leads engineers and researchers to develop cleaner and cleaner combustion devices.
Besides restriction of pollutants emission whose noxiousness is direct, additional environmental considerations are nowadays directed to global warming. This phenomenon is due to the human production of greenhouse gases. The major human impact is carbon dioxide (CO_2) emission. Methane and indirectly NO_x are also greenhouse gases. Human CO_2 emission is due to the combustion of fossil fuel which releases large quantity of carbon trapped inside the ground in the earth atmosphere. The Kyoto protocol adopted on 11 December 1997 marks the realization of the need to regulate carbon dioxide emission, and in spite of the recent failure of the Copenhagen climate conference in 2009, this awareness need has never stopped growing since.
To respond to these global challenges of the 21^{st} Century, GDF SUEZ has made sustainable development the heart of its strategy. By helping to prevent climate warming, preserving fossil fuels and natural resources and promoting environmentally friendly energy, GDF SUEZ is working to control the impact of its own activities and those of its customers on the environment. This is done in a changing economical context: the liberalization of the EU energy sector led the industrial market in 2004 and then the household market in 2007 to open up to competition. In this context, for GDF SUEZ, respect for the environment is not a constraint, it is a development opportunity. That is why the development and study of clean energetic solutions such as flameless combustion for instance is seen as a competitive asset.

Hot temperature diluted combustion

In order to respond to environmental problematics, new technical solutions are developed. For that purpose, two main objectives are considered. The first one demands to reduce the fuel consumption by improving thermal efficiency and the other one to decrease pollutants emission. Unfortunately, these two objectives are usually contradictory. Indeed, fuel consumption reduction can, for instance, be enhanced by preheating the air, which increases the thermal efficiency of the process. However, NO_x emission grows exponentially with temperature. The development of clean and efficient combustion process is therefore difficult but breakthrough solutions such as flameless combustion exist.
Applied in industrial furnaces, flameless combustion (shown in Fig. 2) allows to reduce significantly fuel consumption while keeping very low NO_x

(a) (b)

Figure 2: *Photographs of a laboratory scale furnace (Rottier, 2010). Transition from a conventional flame (a) to the flameless combustion mode (b) as the furnace power and temperature increase. The nominal power is* 18.6 *kW.*

emission. This process is based on the large dilution of fresh gases with hot burnt gases. The hot temperature allows to sustain combustion while dilution erases high temperature peaks responsible for NO_x emission. However, in order to develop hot temperature diluted combustion, a deeper understanding of the combustion mode is necessary. Experimental study and numerical simulation are both complementary ways to achieve characterization of flameless combustion. Thanks to the progress in computing resources and in combustion modeling, the use of numerical simulation in the industrial sector is widely spread during the last decades.

Numerical simulation using tabulated chemistry

Numerical simulation of combustion belongs to the wider area of Computational Fluid Dynamics (CFD). The fluid motion is described in terms of mathematical equations that are discretized in order to be solved by a numerical solver. The different terms in the equations represent several physical phenomena. An exact formulation of each phenomenon is not feasible in practice. Consequently, insignificant effects are neglected and models are used to take into account the dominant physical features. For instance, combustion is composed of a multitude of elementary reaction whose production rates is expressed from empirical laws. Such a description remains too expensive to simulate practical applications. Simplifications such as tabulated chemistry models are used instead.

Tabulated chemistry models allow to include detailed chemistry effects at low cost inside numerical simulations. Indeed, combustion is described by a reduced set of parameters that are representative of the flame structure at small scales. As the flame structure depends on the combustion mode, tabulated chemistry models are dedicated to specific configurations. Current

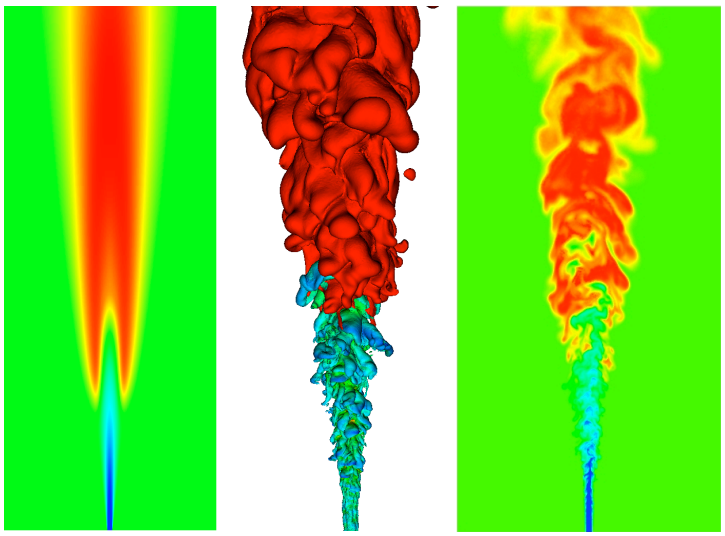

(a) (b) (c)

Figure 3: *Numerical simulation of the Cabra flame (Cabra et al., 2005) with RANS (a) and LES (b,c) approaches. (a,c) Plane colored by temperature. (b) Isosurfaces of temperature (colored in red) and mixture fraction (colored by axial velocity).*

developments attempt to extend the application range of tabulated chemistry to more and more complex situations.
As most industrial applications involve turbulent flows, these techniques are often combined with turbulence modeling. Two main approaches exist to simulate turbulence. The first one is the RANS (Reynolds Averaged Navier Stokes) approach where equations are solved for averaged quantity. The second one called Large Eddy Simulation (LES) resolves large vortices present in turbulence while smaller ones are modeled. Solutions of the same configuration with both methods are shown in Fig. 3. The RANS solution is steady and smooth while the LES solution is unsteady and captures large turbulent eddies in space. Despite the predictive power of LES is larger, its application in industries is limited because it requires high computing resources. That is why RANS approach is widely used in industries. However punctual use of LES grows. Tabulated chemistry models were first applied in RANS approaches with low-Mach number approximation. Nowadays, the natural evolution of tabulated chemistry models is directed towards LES in order to have a great description of both turbulence and chemistry.

The contribution of this thesis

New problematics have raised from the evolution of tabulated chemistry models. This evolution follows two ways:

- Development of new models in order to widen the range of applications of tabulated chemistry to more complex combustion mode.
- Application of tabulated chemistry models to Large Eddy Simulation (LES).

The different points developed in the thesis explore both these features and lead us to the following main contributions of our work.

- Several numerical codes dedicated to large eddy simulation are based on fully compressible Navier-Stokes equations. However, tabulated chemistry models have first been dedicated to low-Mach number flow and do not take into account compressible effects. Consequently, in order to perform LES with compressible codes, a new tabulated chemistry formalism called TTC (Tabulated Thermo-chemistry for Compressible flows) has been derived. In this formulation, the temperature computation and the characteristic boundary treatment are reformulated to account for compressible effects.
- The TTC formalism has been validated and applied to a three-dimensional non-reactive LES, a mono-dimensional premixed flame and finally to a 3D LES of a lifted flame.
- In order to describe diluted combustion with hot temperature gases, a new tabulated chemistry model called UTaC (Unsteady flamelets Tabulated Chemistry) has been developed. The model is based on the tabulation of auto-igniting non-premixed flamelet solutions. The behavior of such solutions has been studied and a corrective source term has been introduced to retrieve auto-ignition time delays.
- The UTaC model was applied in RANS computations of a round jet in a vitiated co-flow for two fuel compositions: hydrogen/nitrogen and methane/air. Results are compared to experimental profiles and the flame lift-off height sensitivity to the co-flow temperature is studied.
- The UTaC model was applied in LES with the TTC formalism to the round jet in vitiated co-flow configuration using the methane/air mixture as fuel. Results were found better than obtained in RANS and it was shown that the independence assumption made in RANS between mixture fraction and progress variable is false.
- Derivation of tabulated chemistry models for LES is usually done by a direct transplantation of the RANS model. With such an approach, tabulated chemistry models are not able to tackle specific characteristics of large-eddy simulations. For instance, PCM-FPI methods can not predict the correct flame speed of perfectly premixed turbulent flames when flame wrinkling is negligible at the subgrid scales and the

filter size is still large in comparison the the flame thickness. This is corrected by a new modeling strategy called F-TACLES (Filtered Tabulated Chemistry for Large Eddy Simulation). The filtered flame structure is mapped using 1-D filtered laminar premixed flames and the model is applied in a LES of a 3-D turbulent premixed flame.

Publications related to the thesis

Several results obtained during this thesis have led to the following international publications:

- Vicquelin, R., Fiorina, B., Payet, S., Darabiha, N., and Gicquel, O. (2010). Coupling tabulated chemistry with compressible cfd solvers. Accepted in *Proceedings of the Combustion Institute*.
- Vicquelin, R., Fiorina, B., Darabiha, N., Gicquel, O., and Veynante, D. (2009). Coupling tabulated chemistry with large eddy simulation of turbulent reactive flows. *Comptes Rendus Mecanique*, 337(6-7):329–339.
- Auzillon, P., Fiorina, B., Vicquelin, R., Darabiha, N., Gicquel, O., and Veynante, D. (2010). Modeling chemical flame structure and combustion dynamics in LES. Accepted in *Proceedings of the Combustion Institute*.
- Fiorina, B., Vicquelin, R., Auzillon, P., Darabiha, N., Gicquel, O., and Veynante, D. (2010). A filtered tabulated chemistry model for LES of premixed combustion. *Combustion and Flame*, 157(3):465–475.

Further published material include several AIAA papers (Esnault et al., 2010; Auzillon et al., 2010b) and contributions to conference proceedings: ICDERS (Vicquelin et al., 2007), SIAM (Vicquelin et al., 2008b), ECM (Esnault et al., 2009). Participation to the CTR Summer Program in Stanford University, USA, during July, 2008 led to publication in the CTR Proceedings (Vicquelin et al., 2008a).

Structure of the manuscript

- **Part I** deals with the general aspect of tabulated chemistry models and their coupling with Navier-Stokes equations. This is described though the three following chapters:

  Chapter 1 Notions of mixture composition and thermo-chemistry are first introduced before presenting the governing equations of reactive flows.

Chapter 2 Different reduction methods to include detailed chemistry at low cost are reviewed. Among them, manifold generation techniques allow to decrease significantly the dimensionality of detailed kinetics. Three categories of manifolds are identified depending on their approach: chemical, mathematical and physical. The latter approximates chemical trajectories in state space with flamelet solutions. This tabulated chemistry model is a good compromise between computational cost and accuracy.

Chapter 3 Coupling between tabulated chemistry models and Navier-Stokes equation is studied. It appears that coupling with low-Mach number codes is straightforward although it is not the case when dealing with fully compressible CFD codes. That is why a new formalism called TTC (Tabulated Thermo-chemistry for Compressible flows) is developed for compressible codes to be consistent with tabulated chemistry framework. In this new model, temperature computation and characteristic boundary conditions are reformulated. This is first validated on one-dimensional tests. A three-dimensional non-reactive case is then computed by performing a large eddy simulation of a turbulent round jet. Finally, a one-dimensional laminar flame simulation assesses the method performances.

- **Part II** focuses on the derivation and application of tabulated chemistry models for hot temperature diluted combustion.

Chapter 4 Properties of flameless combustion are reviewed. The need of simpler configurations than those met in flameless combustion furnaces is outlined. This allows a better understanding of the reaction zone structure and a better confidence in the numerical models validation.

Chapter 5 A general modeled configuration corresponding to a simplification to flameless combustion furnaces is presented. Auto-igniting one-dimensional flamelets are chosen to represent self-igniting non-premixed flames. The behavior of flamelets solutions is illustrated by examples. The impact of differential diffusion is discussed. Then, a chemical database is built from the non-premixed flamelet solutions in order to include detailed chemistry effects at low CPU cost in numerical simulations. The resulting tabulated chemistry model is named UTaC (Unsteady flamelets Tabulated Chemistry).

Chapter 6 The tabulated chemistry model UTaC is applied to the experimental configuration of a jet in vitiated coflow with Reynolds

Averaged Navier-Stokes (RANS) computations. Experimental results on the CH_4/air case are first summed up. RANS equations are then presented and a turbulent combustion model for UTaC is derived using presumed Probability Density Functions (PDFs). Finally, RANS simulations are performed on CH_4/air and H_2/N_2 cases.

Chapter 7 A large eddy simulation (LES) of the methane/air Cabra flame is performed. The model UTaC is coupled with the compressible solver AVBP following the TTC formalism. First, the equations for compressible LES are given before specifying how the UTaC model is implemented in AVBP. Numerical parameters of the simulation are then given and the solution is compared with experimental and the RANS simulation data.

- In **Part III**, a new tabulated chemistry model for perfectly premixed combustion in LES is presented.

Chapter 8 A new modeling strategy called F-TACLES (Filtered Tabulated Chemistry for Large Eddy Simulation) is developed to introduce tabulated chemistry methods in Large Eddy Simulation (LES) of turbulent premixed combustion. The objective is to recover the correct laminar flame propagation speed of the filtered flame front when subgrid scale turbulence vanishes as LES should tend toward Direct Numerical Simulation (DNS). The filtered flame structure is mapped using 1-D filtered laminar premixed flames. Closure of the filtered progress variable and the energy balance equations are carefully addressed in a fully compressible formulation. The methodology is first applied to 1-D filtered laminar flames, showing the ability of the model to recover the laminar flame speed and the correct chemical structure when the flame wrinkling is completely resolved. The model is then extended to turbulent combustion regimes by including subgrid scale wrinkling effects in the flame front propagation. Finally, preliminary tests of LES in a 3-D turbulent premixed flame are performed.

Part I

Including detailed chemistry with tabulated chemistry

Chapter 1

Equations for reactive flows

In this section, governing balance equations of reactive flows are presented. In order to describe reactive systems, species transport equations are added to Navier-Stokes balance equations. Only the case of ideal gaseous flows is considered.

1.1 Introduction

Reactive flows are described by several balance equations for the following controlling variables: the mass density, ρ, the velocity components, u_i, the total energy, e_t and the species mass fractions Y_k.

1.2 Mixture composition description

The mass m of a fluid contained in a homogeneous control volume V is given by the mass density defined as:

$$\rho = \frac{m}{V} \tag{1.1}$$

The ratio of m and the number of moles n is the mixture molar weight W:

$$W = \frac{m}{n} \tag{1.2}$$

The fluid composition is defined by the number N of species and by their proportion. Mole fraction X_k and mass fraction Y_k of the k^{th} species are defined as:

$$X_k = \frac{n_k}{n} \tag{1.3}$$

$$Y_k = \frac{m_k}{m} \tag{1.4}$$

where n_k is the number of mole and m_k is the mass of the species in the volume. Summing over the total number of species N, molar and mass fractions verify:

$$\sum_{k=1}^{N} X_k = 1 \quad \text{and} \quad \sum_{k=1}^{N} Y_k = 1 \tag{1.5}$$

Conversion from mole fractions to mass fractions is done as:

$$Y_k = \frac{W_k}{W} X_k \tag{1.6}$$

The mixture molar weight of the mixture W can be written from W_k and the molar mass of each species:

$$W = \sum_{k=1}^{N} X_k W_k \tag{1.7}$$

or, with mass fractions,

$$\frac{1}{W} = \sum_{k=1}^{N} \frac{Y_k}{W_k} \tag{1.8}$$

Other variables such as mole concentrations, $[X_k]$ can also describe the mixture composition. They are given by the following relations:

$$[X_k] \quad = \quad \rho \frac{W}{W_k} Y_k \tag{1.9}$$

1.3 Thermo-chemistry

1.3.1 Equation of state

The description of reactive flows can be written for a general equation of state, nonetheless, for the sake of simplicity, the gas is assumed ideal. In that case, the pressure P is linked to mass density and temperature T through the ideal gas law:

$$P = \rho r T \quad \text{with} \quad r = \frac{R}{W} \tag{1.10}$$

where $R = 8.314$ J.K^{-1}.mol^{-1} is the ideal gas constant.

1.3.2 Species internal energy and enthalpy

Species energy and enthalpy are defined in reference to a given temperature T_0. For instance, species enthalpy h_k is the sum of a reference enthalpy at $T = T_0$ and a sensible enthalpy h_{sk}:

$$h_k = h_{sk} + \Delta h^0_{f,k} \tag{1.11}$$

where $\Delta h^0_{f,k}$ are the species standard enthalpies of formation at the reference temperature T_0. The specific heat capacity at constant pressure, $C_{pk} = (\frac{\partial h_k}{\partial T})_P$ is introduced to compute h_{sk}:

$$h_{sk} = \int_{T_0}^{T} C_{pk}(T')dT' \tag{1.12}$$

The internal energy of the k^{th} species, $e_k = h_k - \frac{RT}{W_k}$, can also be split into a sensible and a chemical contribution (Poinsot and Veynante, 2005):

$$e_k = e_{sk} + \Delta h^0_{f,k} = \left(\int_{T_0}^{T} C_{vk}(T')dT' - \frac{RT_0}{W_k} \right) + \Delta h^0_{f,k} \tag{1.13}$$

where $C_{vk} = (\frac{\partial e_k}{\partial T})_V$ is the specific heat capacity at constant volume. For an ideal gas, the following relation between C_{vk} and C_{pk} was used:

$$C_{pk} = C_{vk} + \frac{R}{W_k} \tag{1.14}$$

1.3.3 Mixture internal energy and enthalpy

Specific heat capacities at constant pressure, C_p, and at constant volume, C_v, of a mixture composed of N species are:

$$C_p = \sum_{k=1}^{N} C_{pk} Y_k \tag{1.15}$$

$$C_v = \sum_{k=1}^{N} C_{vk} Y_k \tag{1.16}$$

Their ratio is denoted as γ:

$$\gamma = \frac{C_p}{C_v} \tag{1.17}$$

Mixture specific enthalpy h and energy e are given by:

$$h = \sum_{k=1}^{N} h_k Y_k \tag{1.18}$$

$$e = \sum_{k=1}^{N} e_k Y_k \tag{1.19}$$

Similarly to the species enthalpy and energy, mixture enthalpy and energy can also be split into two parts:

$$h = \sum_{k=1}^{N} \left(\int_{T_0}^{T} C_{pk} dT' + \Delta h^0_{f,k} \right) Y_k \tag{1.20}$$

$$h = \int_{T_0}^{T} C_p dT' + \sum_{k=1}^{N} \Delta h^0_{f,k} Y_k \tag{1.21}$$

Form	Energy	Enthalpy
Sensible	$e_s = \int_{T_0}^{T} C_v dT - \frac{RT_0}{W}$	$h_s = \int_{T_0}^{T} C_p dT$
Sensible Chemical	$e = e_s + \sum_{k=1}^{N} \Delta h^0_{f,k} Y_k$	$h = h_s + \sum_{k=1}^{N} \Delta h^0_{f,k} Y_k$
Total Chemical	$e_t = e + \frac{1}{2} u_i^2$	$h_t = h + \frac{1}{2} u_i^2$
Total non Chemical	$E = e_s + \frac{1}{2} u_i^2$	$H = h_s + \frac{1}{2} u_i^2$

Table 1.1: *Different energy and enthalpy definitions.*

$$e = \sum_{k=1}^{N} \left(\int_{T_0}^{T} C_{vk} dT' - \frac{RT_0}{W_k} + \Delta h^0_{f,k} \right) Y_k \tag{1.22}$$

$$e = \left(\int_{T_0}^{T} C_v dT' - \frac{RT_0}{W} \right) + \sum_{k=1}^{N} \Delta h^0_{f,k} Y_k \tag{1.23}$$

Finally, the introduction of the kinetic energy into energy and enthalpy allows four new definitions. It is synthesized in Tab. 1.1.

1.4 Chemical kinetics

Combustion process can be modeled by a global reaction where a budget between reactants and major products is written. For example, the global reaction of methane oxidation is:

$$CH_4 + 2O_2 \rightarrow CO_2 + 2H_2O \tag{1.24}$$

Such global reaction does not describe elementary reactions that effectively occur and lead to final products. Combustion of reactants is in fact a set of reactions involving major and minor species. If N_R reactions are considered between N species, reactions can be written as:

$$\sum_{k=1}^{N} \nu'_{rk} \mathscr{S}_k \leftrightarrow \sum_{k=1}^{N} \nu''_{rk} \mathscr{S}_k \quad , \quad r = 1, N_R \tag{1.25}$$

where $\mathscr{S}_k$ are the species symbols, ν'_{rk} and ν''_{rk} are the species stoichiometric coefficients in reaction r. A net stoichiometric coefficient $\nu_{rk} = \nu''_{rk} - \nu'_{rk}$ is introduced. The rate of progress of reaction r, $\dot{\Omega}_r$, is written as:

$$\dot{\Omega}_r = k_{fr} \prod_{k=1}^{N} [X_k]^{\nu'_{rk}} - k_{br} \prod_{k=1}^{N} [X_k]^{\nu''_{rk}} \tag{1.26}$$

k_{fr} and k_{br} are the forward and backward reaction rates*. The chemical reaction rate of each species, $\dot{\omega}'_k$ in kg.m^{-3}.s^{-1}, is computed from the sum of all reactions contributions, $\dot{\omega}'_{kr}$:

$$\dot{\omega}'_k = \sum_{r=1}^{N_R} \dot{\omega}'_{kr} \tag{1.27}$$

where $\dot{\omega}'_{kr}$ is proportional to the reaction rate of progress:

$$\dot{\omega}'_{kr} = W_k \nu_{rk} \dot{\Omega}_r \tag{1.28}$$

Chemical source terms $\dot{\omega}_k$, in s^{-1}, are defined by:

$$\dot{\omega}_k = \frac{\dot{\omega}'_k}{\rho} \tag{1.29}$$

1.5 Governing balance equations

Using transport theorems, local partial differential equations in space x_i and time t are derived for the conservative variables ρ, ρu_i, ρe_t and ρY_k.

1.5.1 Mass balance

The transport equation for mass density is:

$$\frac{\partial \rho}{\partial t} + \frac{\partial}{\partial x_j}(\rho u_j) = 0 \tag{1.30}$$

1.5.2 Momentum balance

Neglecting body forces in the fluid, conservation of the momentum ρu_j is written as:

$$\frac{\partial \rho u_i}{\partial t} + \frac{\partial}{\partial x_j}(\rho u_i u_j) = \frac{\partial \sigma_{ij}}{\partial x_j} \tag{1.31}$$

where σ_{ij} is the stress tensor composed of a pressure isotropic part and the viscous stress tensor τ_{ij}:

$$\sigma_{ij} = -P\delta_{ij} + \tau_{ij} \tag{1.32}$$

δ_{ij} is the Kronecker operator: $\delta_{ij} = \begin{cases} 1 & \text{if } i = \text{j} \\ 0 & \text{unless} \end{cases}$. For a newtonian fluid, if bulk viscosity effects are neglected, τ_{ij} is given by:

$$\tau_{ij} = \mu\left(\frac{\partial u_i}{\partial x_j} + \frac{\partial u_j}{\partial x_i}\right) - \frac{2}{3}\mu\frac{\partial u_k}{\partial x_k}\delta_{ij} \tag{1.33}$$

*k_{fr} is usually modeled with an Arrhenius law while k_{br} is written as the ratio between k_{fr} and the reaction equilibrium constant.

where μ is the dynamic viscosity. The kinematic viscosity ν is defined as:

$$\nu = \frac{\mu}{\rho} \tag{1.34}$$

1.5.3 Species balance

Species balance equations include convective and diffusive transport and chemical terms:

$$\frac{\partial \rho Y_k}{\partial t} + \frac{\partial}{\partial x_j}\left(\rho u_j Y_k\right) = -\frac{\partial}{\partial x_j}\left(\rho V_{k,j} Y_k\right) + \rho \dot{\omega}_k \tag{1.35}$$

where $V_{k,j}$ is the diffusion velocity of the k^{th} species and $\dot{\omega}_k$ is the species net chemical production rate in s^{-1} defined in section 1.4. The sum of Eq. 1.35 over the N species leads to the mass balance equation (Eq. 1.30). This equality is consequence of the following conditions on species diffusion velocities and reaction rates:

$$\sum_{k=1}^{N} V_{k,j} Y_k = 0 \quad \text{and} \quad \sum_{k=1}^{N} \dot{\omega}_k = 0 \tag{1.36}$$

1.5.4 Species diffusion velocities

$V_{k,j}$ are given by the multicomponent diffusion equation[†] (Williams, 1985):

$$\boldsymbol{\nabla} X_k = \sum_{j=1}^{N} \left(\frac{X_k X_j}{D_{kj}}\right)\left(\boldsymbol{V_j} - \boldsymbol{V_k}\right) + \left(Y_k - X_k\right)\left(\frac{\boldsymbol{\nabla P}}{P}\right) \tag{1.37}$$

where D_{kj} are the binary diffusion coefficients for species k and j. Without simplification, Eq. 1.37 couples all species and must be solved in each point in each direction. This is highly expensive and approximations are used instead, as done by Curtiss and Hirschfelder (1949):

$$V_{k,j} X_k = -D_k \frac{\partial X_k}{\partial x_j} \tag{1.38}$$

where $D_k = (1 - X_k)/\sum_{j \neq k}(X_j/D_{kj})$ is the species diffusion coefficient in the mixture. This approximation does not verify Eq. 1.36 if D_k is not the same for all species and if W cannot be assumed as constant:

$$\sum_{k=1}^{N} V_{k,j} Y_k = -\sum_{k=1}^{N} D_k \frac{W_k}{W} \frac{\partial X_k}{\partial x_j} = -\sum_{k=1}^{N} \frac{D_k}{W} \frac{\partial}{\partial x_j}(W Y_k) \neq 0 \tag{1.39}$$

[†]Body forces and Soret effect are neglected.

This difficulty is overcome by adding a corrective diffusive velocity $V_{c,j}$:

$$V_{k,j}Y_k = -D_k \frac{W_k}{W} \frac{\partial X_k}{\partial x_j} + V_{c,j}Y_k \tag{1.40}$$

with

$$V_{c,j} = \sum_{k=1}^{N} D_k \frac{W_k}{W} \frac{\partial X_k}{\partial x_j} \tag{1.41}$$

Species balance equation becomes then:

$$\frac{\partial \rho Y_k}{\partial t} + \frac{\partial}{\partial x_j}\left(\rho(u_j + V_{c,j})Y_k\right) = \frac{\partial}{\partial x_j}\left(\rho D_k \frac{W_k}{W} \frac{\partial X_k}{\partial x_j}\right) + \rho\dot{\omega}_k \tag{1.42}$$

In the specific case where $D_k = D$ is assumed identical for all species and where gradients of W are neglected (hence $\frac{\partial Y_k}{\partial x_i} = \frac{W_k}{W}\frac{\partial X_k}{\partial x_i}$), species diffusion velocities are given by:

$$V_{k,j}Y_k = -D \frac{\partial Y_k}{\partial x_j} \tag{1.43}$$

Therefore, Eq. 1.42 reads:

$$\frac{\partial \rho Y_k}{\partial t} + \frac{\partial}{\partial x_j}\left(\rho u_j Y_k\right) = \frac{\partial}{\partial x_j}\left(\rho D \frac{\partial Y_k}{\partial x_j}\right) + \rho\dot{\omega}_k \tag{1.44}$$

Eq. 1.44 is sometimes used with $D = D_k$, which violates Eq. 1.36 because $\sum_{k=1}^{N} \rho D_k \frac{\partial Y_k}{\partial x_j} \neq 0$. Results are however good in several applications where the introduced error is small.

1.5.5 Dimensionless numbers of transport properties

Several diffusion coefficients are introduced in balance equations: species diffusion coefficients D_k, the dynamic viscosity μ and the thermal conductivity λ. These quantities can be arranged to form the following dimensionless numbers:

- Lewis number

$$\mathrm{Le}_k = \frac{\lambda}{\rho C_p D_k} \approx \frac{\text{Heat Diffusion}}{\text{Species Diffusion}} \tag{1.45}$$

- Schmidt number

$$\mathrm{S}_{c_k} = \frac{\mu}{\rho D_k} = \frac{\nu}{D_k} \approx \frac{\text{Momentum Diffusion}}{\text{Species Diffusion}} \tag{1.46}$$

- Prandtl number

$$\mathrm{Pr} = \frac{\mu C_p}{\lambda} \approx \frac{\text{Momentum Diffusion}}{\text{Heat Diffusion}} \tag{1.47}$$

1.5.6 Energy balance

Conservation of the total energy is written from the first law of thermodynamics:

$$\frac{\partial \rho e_t}{\partial t} + \frac{\partial}{\partial x_j}\left(\rho u_j e_t\right) = -\frac{\partial q_j}{\partial x_j} + \frac{\partial}{\partial x_j}(\sigma_{ij} u_i) + \dot{Q} - \frac{\partial q_j^r}{\partial x_j} \tag{1.48}$$

where $\dot{Q}$ is a heat source or sink term and q^r is the radiative flux. Using Fourier's law, the heat diffusion flux q_i is expressed as[‡]:

$$q_j = -\lambda \frac{\partial T}{\partial x_j} + \rho \sum_{k=1}^{N} h_k V_{k,j} Y_k \tag{1.49}$$

where λ is the thermal conductivity. Note that the balance equation for the total non-chemical energy is:

$$\begin{aligned} \frac{\partial \rho E}{\partial t} + \frac{\partial}{\partial x_j}\left(\rho u_j E\right) &= \frac{\partial}{\partial x_j}\left(\lambda \frac{\partial T}{\partial x_j}\right) - \frac{\partial}{\partial x_j}\left(\rho \sum_{k=1}^{N} h_{sk} V_{k,j} Y_k\right) \\ &\quad + \frac{\partial}{\partial x_j}(\sigma_{ij} u_i) + \rho \dot{\omega}_T + \dot{Q} - \frac{\partial q_j^r}{\partial x_j} \end{aligned} \tag{1.50}$$

where the heat release rate is introduced:

$$\dot{\omega}_T = -\sum_{k=1}^{N} \Delta h_{f,k}^0 \dot{\omega}_k \tag{1.51}$$

Balance equations for energy and enthalpy forms listed previously in Tab. 1.1 are given in Poinsot and Veynante (2005).
If Eq. 1.43 is used to compute species diffusion velocities and if unity species Lewis numbers are considered i.e. $D_k = D = \lambda/(\rho C_p)$, heat diffusion flux q_i is expressed as:

$$\begin{aligned} -q_j &= \lambda \frac{\partial T}{\partial x_j} + \sum_{k=1}^{N} \rho h_k D \frac{\partial Y_k}{\partial x_j} \\ &= \lambda \frac{\partial T}{\partial x_j} + \frac{\lambda}{C_p} \sum_{k=1}^{N} h_k \frac{\partial Y_k}{\partial x_j} \end{aligned} \tag{1.52}$$

[‡]Dufour effects are neglected.

On the other side:

$$\begin{aligned}
\frac{\lambda}{C_p}\frac{\partial h}{\partial x_j} &= \frac{\lambda}{C_p}\frac{\partial}{\partial x_j}\sum_{k=1}^{N} h_k Y_k \\
&= \frac{\lambda}{C_p}\sum_{k=1}^{N}\left(\frac{\partial h_k}{\partial x_j}Y_k + h_k\frac{\partial Y_k}{\partial x_j}\right) \\
&= \frac{\lambda}{C_p}(\sum_{k=1}^{N} C_{pk}Y_k)\frac{\partial T}{\partial x_j} + \frac{\lambda}{C_p}\sum_{k=1}^{N} h_k\frac{\partial Y_k}{\partial x_j} \\
&= \lambda\frac{\partial T}{\partial x_j} + \frac{\lambda}{C_p}\sum_{k=1}^{N} h_k\frac{\partial Y_k}{\partial x_j} \qquad (1.53)
\end{aligned}$$

Consequently, as Eq. 1.52 and 1.53 are identical, heat flux can be written without including species derivatives:

$$q_j = -\frac{\lambda}{C_p}\frac{\partial h}{\partial x_j} \qquad (1.54)$$

Using Eq. 1.54, total energy balance equation (Eq. 1.48) reads:

$$\frac{\partial \rho e_t}{\partial t} + \frac{\partial}{\partial x_j}\left(\rho u_j e_t\right) = \frac{\partial}{\partial x_j}\left(\frac{\lambda}{C_p}\frac{\partial h}{\partial x_j}\right) + \frac{\partial}{\partial x_j}(\sigma_{ij}u_i) + \dot{Q} - \frac{\partial q_r}{\partial x_j} \qquad (1.55)$$

Eq. 1.50 is also rewritten:

$$\begin{aligned}
\frac{\partial \rho E}{\partial t} + \frac{\partial}{\partial x_j}\left(\rho u_j E\right) &= \frac{\partial}{\partial x_j}\left(\frac{\lambda}{C_p}\frac{\partial h_s}{\partial x_j}\right) + \frac{\partial}{\partial x_j}(\sigma_{ij}u_i) \qquad (1.56) \\
&\quad + \rho\dot{\omega}_T + \dot{Q} - \frac{\partial q_r}{\partial x_j}
\end{aligned}$$

1.6 Conclusion

Reactive flows are described by balance equations that stand for the conservation of mass, momentum and energy. These equations have been detailed in this chapter. Several physical phenomena have been encountered such as thermodynamics, transport, radiation, chemical kinetics. Different models for each feature exist. They depend on the required level of precision in the studied configuration.

For example in thermodynamics, a first guess of adiabatic temperature can be found by assuming constant heat capacities. But polynomial fits or tabulation can be used to provide higher precision.

Complex transport description is not necessary in most industrial application. In practice, dynamic viscosity is computed from an empirical law and other diffusion coefficients are given from dimensionless numbers. The level

of accuracy is dominant at scales where the flow is laminar. However, large scale property can depend on small scales description. For example, simple transport assumption such as unity species Lewis numbers leads to underestimate by 30% the laminar flame speed S_l in a stoichiometric methane/air mixture. It is even worse when the fuel is hydrogen, which is highly diffusive. This error can be reported on the overall flame consumption rate where S_l is an input parameter of the simulation.
Chemical source terms are computed thanks to a chemical mechanism. The simplest mechanism is a global reaction. Several asymptotic studies were derived from one-step chemistry and have been able to predict many flame behaviors. Detailed mechanisms introduce a vast range of chemical time scales. This level of description is necessary in many cases: predicting laminar premixed flame speed, autoignition, quenching, pollutant emission. Because full description of chemistry is only feasible for simple configuration and/or simple fuels, chemistry reduction methods have been developed to reduce computation cost and keep good level of accuracy. The state of the art of these methods is addressed in the next chapter.

Chapter 2

Detailed chemistry reduction

In order to decrease computational cost of detailed chemistry, different reduction methods have been developed and some of them are reviewed in this chapter. The different methods have been derived by considering the chemical reduction problem with different points of view. A first category of methods studies links between species through the elementary reactions. This chemical point of view allows to identify unnecessary species in a detailed mechanism. A second category with a mathematical approach analyses the reduction of a system of ordinary differential equations. Finally, a last family of models can be defined where chemistry reduction is achieved by practical and physical considerations. Indeed, using flamelets in tabulated chemistry appears as a good compromise between computational cost and accuracy.

2.1 Introduction

Depending on the fuel complexity, detailed chemistry may deal with a large number of species. For instance, about ten species are present in hydrogen/air combustion mechanism, whereas several dozens of species has to be considered for methane/air chemistry. Several hundreds of species may participate to heavy hydrocarbons combustion mechanism. Chemical species participate to the global mechanism through elementary reactions. For heavy hydrocarbons combustion, more than one thousand of elementary reactions occur.

Nowadays, performing Computational Fluid Dynamics (CFD) simulations with many species and reactions remains out of reach in most practical applications. The cost is due both to the solving of species transport equations (Eq. 1.35) and to chemical reaction rates computation (Eq. 1.27). Direct Numerical Simulation (DNS) of hydrogen flames with complex chemistry becomes affordable only in simple jet configurations (Mizobushi et al., 2002;

Yoo et al., 2009). Numerical simulations of realistic configurations with complex fuel is not feasible in the near future. That is why, several methods have been developed to decrease the computational cost induced by detailed chemistry.

The reactive mixture is described as a high-dimensional system. Any thermochemical state of a multicomponent system is identified by the mixture composition and two state variables. Hence, the system has $N+2$ degrees of freedom where N is the number of species. If pressure and enthalpy are chosen as state variables, the state vector is $(P, h, Y_1, Y_2, ..., Y_N)^\top$. The space of dimensions $N+2$ where the thermochemical system evolves is called the state space. Reduction methods consist in reducing the state space dimension.

In an adiabatic and isobaric chemical reaction, several quantities are conserved: mass, pressure, enthalpy and the chemical elements assembled in species. Consequently, P, h and element mass fractions constitute $N_e + 2$ independent and conserved quantities built from combination of the state vector coordinates, where N_e is the number of elements. The state space reduces therefore to $(N+2)-(N_e+2) = N-N_e$ dimensions once the conserved quantities are given. In practice, the state space is restricted to a realizable subspace where mass fractions of each species is bounded: $0 \leq Y_k \leq 1$. This properties allow to reduce the number of governing equations. If only chemical kinetics is considered, the evolution of the system in the state space is given by:

$$(S) \quad \begin{cases} h = h_0 \\ P = P_0 \\ z_i = z_{i0} \qquad \text{for } i = 1, N_e \\ \frac{d\boldsymbol{\psi}}{dt} = \dot{\boldsymbol{\Omega}}(\boldsymbol{\psi}) \end{cases} \quad \begin{array}{l} \text{with } \boldsymbol{\psi} = (Y_1, Y_2, ..., Y_N)^\top \\ \text{and } \dot{\boldsymbol{\Omega}}(\boldsymbol{\psi}) = (\dot{\omega}_1, \dot{\omega}_2, ..., \dot{\omega}_N)^\top \end{array} \tag{2.1}$$

where h_0 and P_0 are respectively the constant enthalpy and pressure. Temperature is computed from pressure and enthalpy for a given composition by reversing Eq. 1.20. z_i, the mass fraction of element i, is defined by:

$$z_i = \sum_{k=1}^{N} a_{ki} Y_k \tag{2.2}$$

where a_{ki} is the number of elements i is species k. Because of element conservation, z_i remains constant: $z_i = z_{i0}$. This relation in addition to boundedness of species mass fractions defines the realizability conditions that constraint $\boldsymbol{\psi}$.

$\boldsymbol{\psi}(t)$ will reach a steady state which corresponds to equilibrium conditions $\boldsymbol{\psi}^{eq}(h_0, P_0, z_{i0})$. For a given enthalpy, pressure and element composition, chemical state space trajectories end at this singular point for $t = +\infty$.

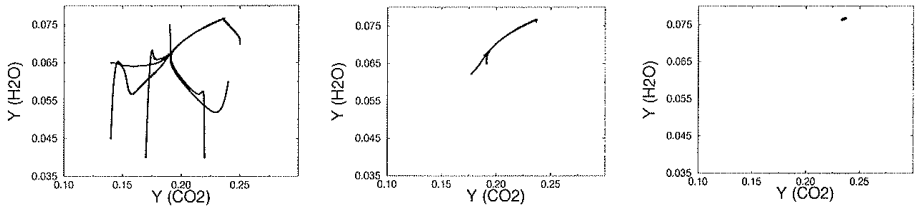

(a) Full trajectories (b) Trajectories after $50\mu s$ (c) Trajectories after $50ms$

Figure 2.1: *Evolution of composition projected in the (Y_{CO_2},Y_{H_2O}) plane for eight different initial mixtures (Gicquel et al., 1999)*

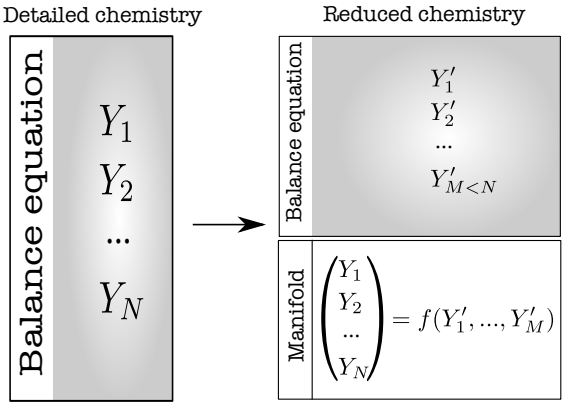

Figure 2.2: *Scheme of reduction by manifold generation of a detailed mechanism of N species to a system involving only $M < N$ parameters. The whole system is constraint to a manifold of dimension M.*

Only a small portion of the realizable subspace is covered by practical combustion system. For instance, figure 2.1 shows several trajectories in state space, where different initial mixtures are chosen with identical h, P, z_i. Therefore, all paths reach the same equilibrium point (Fig. 2.1(c)). Although initial mixtures were dispersed in the (Y_{CO_2},Y_{H_2O}) plane, composition trajectories quickly converge to a one-dimensional manifold. Afterwards, evolution towards equilibrium is slower. This example emphasizes that detailed chemistry introduces a large range of chemical time scales. If fast time scales species are filtered out of the chemical mechanism, dimension reduction can be realized by only considering limiting slow species. Moreover, the whole composition can be approximated from knowledge of slow species. This leads to the identification of a lower-dimensional manifold as represented in Fig. 2.2.

Reduction methods by identification of lower-dimensional manifold must be distinguished from reduction achieved by direct elimination of species and reactions (Fig. 2.3). In the latter, this skeletal reduction is conducted so that information (species, reactions) considered unnecessary is erased. Therefore,

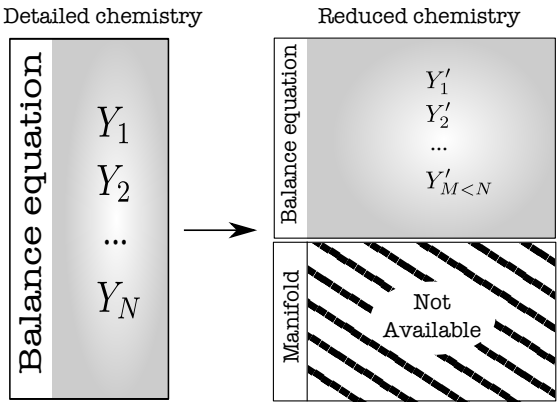

Figure 2.3: *Scheme of skeletal reduction of a detailed mechanism of N species to a system involving only $M < N$ parameters. Information estimated as unnecessary is lost during the reduction step.*

a manifold that gives all species from the new parameters cannot be found. In practice, both methods are used when reduction of very large detailed mechanism (several hundreds off species) is searched: a skeletal reduction is first realized for the manifold reduction method to perform efficiently. In the next section, skeletal reduction and criteria to identify which species/reactions can be neglected are presented. Reductions involving manifolds are then described following the approach point of view: chemical, mathematical and physical.

2.2 Skeletal reduction by elimination of species and reactions

In a large detailed mechanism, three kinds of species are identified:

- **Important species** are crucial to represent the reaction process. These are the major reactants and products of the reaction.

- **Necessary species** are not important species but must be considered to know important species profiles or global properties such as ignition delays or flame propagation speed.

- **Redundant species** can be eliminated from the detailed mechanism without noticeable impact on the mechanism performances.

A first step toward chemistry mechanism reduction is to identify the redundant species. Then, like for species, redundant reactions can be defined and are eliminated in order to obtain a semi-detailed mechanism.

2.2.1 Decreasing the number of species

A systematic reaction rate analysis can be performed (Turanyi, 1990) to find redundant species. First, a sample of physical properties to be reproduced by the reduced mechanism is chosen. It can be major species profiles or global properties. Then, one species is suppressed: all reactions where the particular species is involved are deleted from the detailed mechanism. It forms a reduced mechanism. Ability of the new mechanism to predict the target physical properties is evaluated. If these properties are not affected, the tested species is not necessary. The major drawback is that this method becomes quickly expensive when several species are tested.
Another approach consist in jacobian analysis (Tomlin et al., 1997). It is less expensive than systematic evaluation of reduced mechanisms. The dependance of a specific species k to another species i is quantified by the jacobian matrix $\boldsymbol{J}$:

$$J_{ki} = \frac{\partial \dot{\omega}_k}{\partial [X_i]} \tag{2.3}$$

It gives source terms absolute dependance to the different species concentrations. Relative dependance is computed in the matrix $\boldsymbol{J}^*$:

$$J^*_{ki} = \frac{[X_i]}{\dot{\omega}_k} \frac{\partial \dot{\omega}_k}{\partial [X_i]} = \frac{\partial \ln \dot{\omega}_k}{\partial \ln [X_i]} \tag{2.4}$$

To investigate if a species i is redundant, a global sensitivity parameter B_i is evaluated. A group of N_{test} important and necessary species is chosen to measure the impact of species i. B_i is given by:

$$B_i = \sum_{k=1}^{N_{test}} J^{*^2}_{ki} \tag{2.5}$$

where identical weight is given to each species. If B_i is below a given tolerance, the species i is neglected. The efficiency of the method is correlated with the definition of B_i and the tolerance factor.
Other methods exist such as the direct relation graph method (Lu and Law, 2005) for example. Figure 2.4 shows how the new skeletal mechanism size can depend on the tolerance factor. Initializing the reduced mechanism with the detailed one, redundant species are found only if the tolerance factor is high enough. Then, the species number decreases by steps because several groups of species are highly coupled. Reduction is conducted until good compromise between accuracy and computational cost is found. Further simplification of the mechanism is realized by removing unnecessary reactions.

2.2.2 Decreasing the number of reactions

The identification of redundant reactions has been highly investigated by sensitivity analysis (Warnatz et al., 2006). Absolute and relative sensitivities

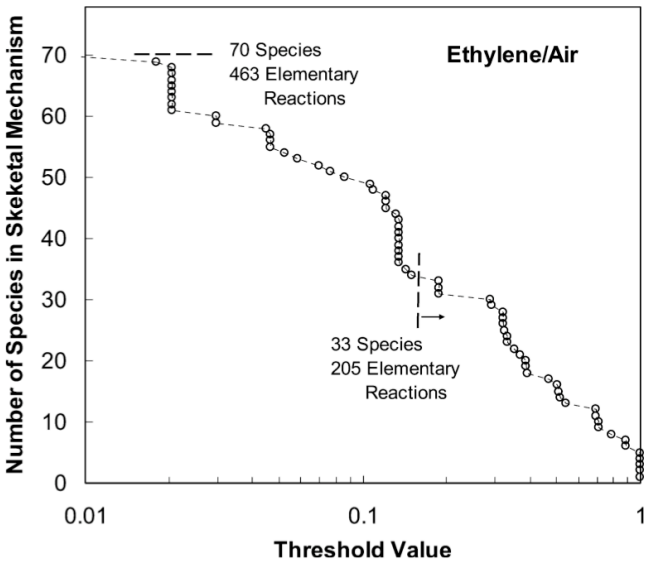

Figure 2.4: *Dependance of the species number of the reduced mechanism on the threshold tolerance parameter during a direct relation graph analysis (Lu and Law, 2005). The starting detailed mechanism for ethylene/air combustion is composed of* 70 *species and* 463 *elementary reactions.*

are defined as:

$$S_{kr} = \frac{\partial[X_k]}{\partial k_r} \tag{2.6}$$

$$S^*_{kr} = \frac{\partial \ln[X_k]}{\partial \ln k_r} \tag{2.7}$$

These quantities are very interesting in mechanism reactions analysis since they compute the dependance of each species concentration $[X_k]$ on reaction rate coefficient k_r. Sensitivities are calculated at several point in the flame, providing only local information. Figure 2.5 shows maximal relative sensitivities of OH in an igniting mixture. Reactions with small sensitivities can be removed. However, if sensitivity of OH to a specific reaction is low, it might not be the case for another species. To consider the influence of parameter k_r on a group of N_{test} species, an overall sensitivity is defined (Vajda et al., 1985):

$$B'_r = \sum_{k=1}^{N_{test}} \left(\frac{\partial \ln[X_k]}{\partial \ln k_r} \right)^2 \tag{2.8}$$

However, B'_r shows the effect of only one parameter whereas in most applications several parameters change at the same time. The impact of simultaneous variations of parameters can be studied by principal component

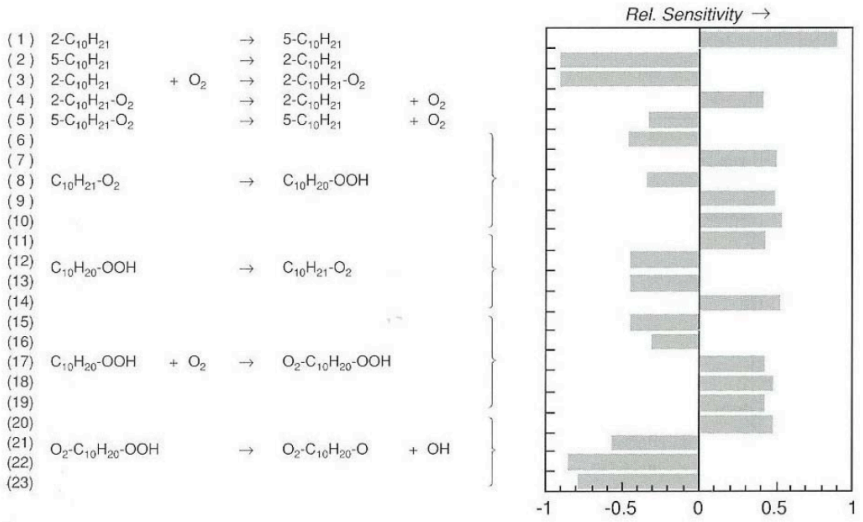

Figure 2.5: *Sensitivity analysis for the OH concentration in an igniting stoichiometric $C_{10}H_{22}$-air mixture at a 13 bar pressure and an initial temperature of 800 K. Maximal relative sensitivity is given for different reactions (Warnatz et al., 2006).*

analysis (Vajda et al., 1985). It summarizes information contained in sensitivity coefficients but also brings new insights since reaction parameters are not regarded as independent.
In addition to sensitivity analysis, reaction flow analysis provides a better understanding of the reaction path in the chemical mechanism (Warnatz et al., 2006). This analysis is conducted on two steps. During the first step, relative contributions of each reactions for each species is computed and synthesized in a table (Fig. 2.6). The contribution is the reaction rate due to one reaction compared to the total species reaction rate. Hence, sum of all percentages in each column is 100%. The reaction rates are evaluated in one of these two ways:

- **Local reaction flow analysis**: reaction rates are computed at a specific point
- **Integral reaction flow analysis**: reaction rates are integrated over the all reaction process

In the last step, the table is transformed into a reaction flow diagram. An example of integral reaction flow diagram is shown in figure 2.7. The arrows size is proportional to the reaction contribution and allows to identify the main reaction path in the mechanism. With this method, groups of minor reactions can be found and eliminated. This must be carefully addressed since the reaction flow analysis is sensitive to equivalence ratio and the initial temperature.

Reaction ⇓	Species ⇒ 1	2	3	.....	S-1	S
1	20%	3%	0	.....	0	0
2	0	0	0	.....	0	0
3	2%	5%	0	.....	100%	90%
.	.	.	.		.	.
.	.	.	.		.	.
.	.	.	.		.	.
R-1	78%	90%	100%	.....	0	5%
R	0	2%	0	.....	0	0

Figure 2.6: *Illustration of the output of a reaction flow analysis (Warnatz et al., 2006).*

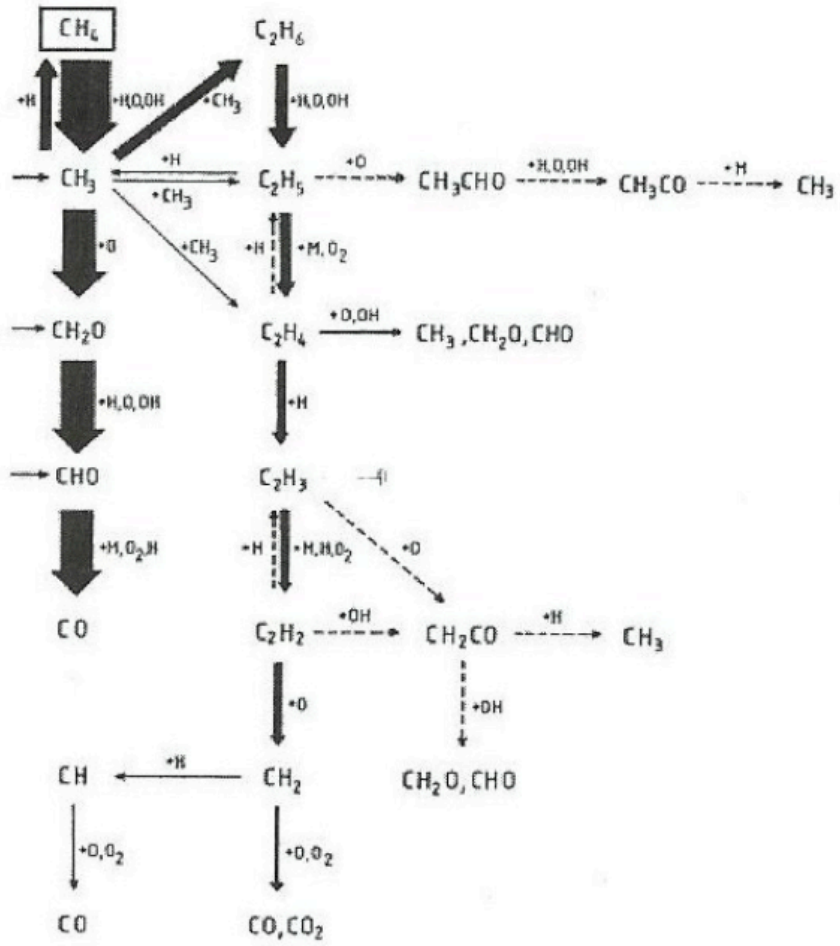

Figure 2.7: *Integral reaction flow analysis in a premixed stoichiometric CH_4-air flame with atmospheric pressure and a fresh gases temperature of $298K$ (Warnatz et al., 2006).*

In this section, the presented methods removed unnecessary species and reactions to build a skeletal mechanism. Further reduction is not possible by simply eliminating one of the remaining species since skeletal reduction keeps only necessary species. However, necessary species can be expressed in function of others to build manifolds, which is the subject of the following section.

2.3 Reduction by manifold generation

Several manifold reduction methods identify "fast" species which can be expressed in function of limiting species involved in slow chemical reactions. Other techniques adopt a different point of view on the reduction problem instead of looking for fast time scales. In order to study the panel of manifold reduction methods, the different manifolds are classified following the approach point of view: chemical, mathematical and physical through flamelet computations.

2.3.1 Manifold generation: chemical perspective

Previous methods have reduced the number of degrees of freedom of the chemical system by eliminating redundant species and reactions. This dimension reduction was achieved by keeping necessary species and reactions but time scale analysis was not considered. Fig 2.1 has shown that reaction trajectories quickly merge on a one-dimensional subspace before reaching the thermodynamical equilibrium. This points out the existence of fast time scales which can lead to further reduction of the chemistry.
In fact, a wide range of chemical time scales is covered by combustion (Fig 2.8). Fast processes can change quickly to adapt themselves so that they are limited by slow reactions. The difference of magnitude orders introduces a decoupling of fast time scales with other scales. Therefore, a highly reactive species which is essentially governed by fast reactions is close to quasi-steady-state (Peters, 1985). This Quasi-Steady-State Assumption (QSSA) is a classical way to decrease the number of dimensions.
For instance, in the case of the following sequential reactions:

$$A \xrightarrow{k_1} B \xrightarrow{k_2} C \tag{2.9}$$

Species time variation of A, B and C are expressed as:

$$\frac{d[A]}{dt} = -k_1[A] \tag{2.10}$$

$$\frac{d[B]}{dt} = k_1[A] - k_2[B] \tag{2.11}$$

$$\frac{d[C]}{dt} = k_2[B] \tag{2.12}$$

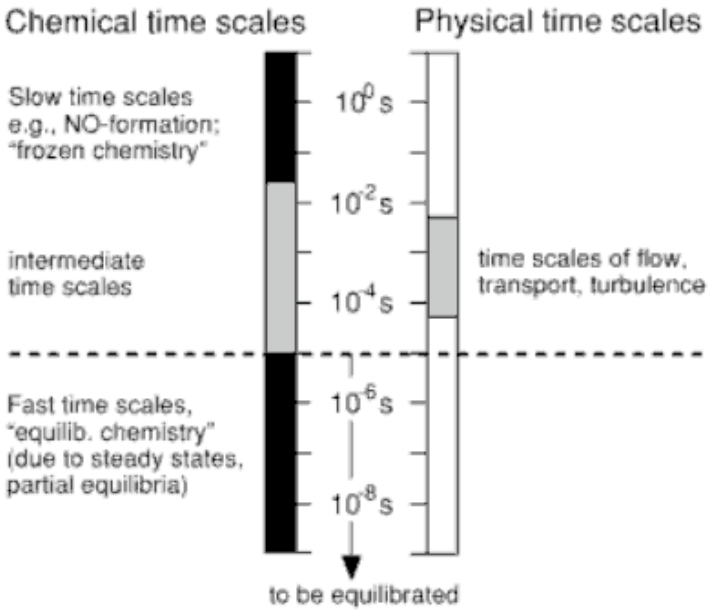

Figure 2.8: *Range of chemical times scales (Warnatz et al., 2006).*

If B is a highly reactive species intermediate, it will be consumed as soon as it is produced:

$$k_2 \gg k_1 \tag{2.13}$$

B can then be assumed in its steady state ($\frac{d[B]}{dt} \approx 0$), and the system of Ordinary Differential Equations (ODEs) composed of Eq. 2.10, 2.11 and 2.12 becomes:

$$\frac{d[A]}{dt} = -k_1[A] \tag{2.14}$$

$$[B]_{st} \approx \frac{k_1}{k_2}[A] \tag{2.15}$$

$$\frac{d[C]}{dt} = k_2[B]_{st} \approx k_1[A] \tag{2.16}$$

From a mathematical point of view, the problem is simplified because Eq. 2.10 has been replaced by an algebraic equation (Eq. 2.15). If a system of N species is considered, time scales analysis of the different species allows to determine N_f fast time scales. The N_f "fast" species are assumed in quasi-steady state. The vector $\boldsymbol{\psi}$ defined in Eq. 2.1 is split into two parts:

$$\boldsymbol{\psi} = \begin{pmatrix} \boldsymbol{\psi_s} \\ \boldsymbol{\psi_f} \end{pmatrix} \tag{2.17}$$

where $\boldsymbol{\psi_f}$ is composed of N_f species in quasi-steady state and $\boldsymbol{\psi_s}$ are the $N_s = N - N_f$ remaining species. The same decomposition is applied to the source term vector:

$$\dot{\boldsymbol{\Omega}}(\boldsymbol{\psi_s}, \boldsymbol{\psi_f}) = \begin{pmatrix} \boldsymbol{\Omega}_s(\boldsymbol{\psi_s}, \boldsymbol{\psi_f}) \\ \boldsymbol{\Omega}_f(\boldsymbol{\psi_s}, \boldsymbol{\psi_f}) \end{pmatrix} \tag{2.18}$$

As $\boldsymbol{\psi_f}$ are assumed in steady state, their reaction rates are null:

$$\boldsymbol{\Omega}_f(\boldsymbol{\psi_s}, \boldsymbol{\psi_f}) = \mathbf{0} \tag{2.19}$$

Eq. 2.19 defines N_f algebraic relations to compute species in quasi-steady state $\boldsymbol{\psi_f}$ knowing other species. If the manifold defined by Eq. 2.19 is not folded, then $\boldsymbol{\psi_f}$ can be computed by:

$$\boldsymbol{\psi_f} = f(\boldsymbol{\psi_s}) \tag{2.20}$$

The system (S) in Eq 2.1 is then simplified as:

$$(S') \quad \begin{cases} h = h_0 \\ P = P_0 \\ z_i = z_{i0} & \text{for } i = 1, N_e \\ \boldsymbol{\psi_f} = f(\boldsymbol{\psi_s}) \\ \frac{d\boldsymbol{\psi_s}}{dt} = \dot{\boldsymbol{\Omega}}_s(\boldsymbol{\psi_s}, f(\boldsymbol{\psi_s})) \end{cases} \tag{2.21}$$

Hence, the system, which previously evolved in $N - N_e$ dimensions, is now constrained to a manifold of $N_s - N_e$ dimensions. Indeed, N_f dimensions associated to fast time scales have been removed. This reduction allows to know the whole system from $N_s - N_e$ reduced parameters, which is different from simply eliminating redundant species.
In practice, QSSA difficulties arise from the identification of species associated to fast time scales and from solving algebraic relations (Eq. 2.19). The algebraic equations can be significantly simplified by using partial-equilibrium assumption (Peters, 1985). Concerning species identification, quasi-steady state is assumed when the destruction rate is much higher than the production rate. However, one species can participate in several reactions characterized by different time scales. Hence, the QSSA might be valid for only one part of the mechanism. In the following section, a more rigorous mathematical derivation of the problem enables to better introduce the notion of time scales.

2.3.2 Manifold generation: mathematical perspective

An eigenvalues analysis is conducted on the system (S) described in Eq. 2.1. The system is first linearized at a reference point $\boldsymbol{\psi_0}$:

$$\frac{d\boldsymbol{\psi}}{dt} = \dot{\boldsymbol{\Omega}}(\boldsymbol{\psi_0}) + \dot{\boldsymbol{\Omega}}_\psi(\boldsymbol{\psi} - \boldsymbol{\psi_0}) \tag{2.22}$$

The $N \times N$ matrix Jacobian $\dot{\boldsymbol{\Omega}}_{\psi_{ij}} = \frac{\partial \dot{\omega}_i}{\partial Y_j}$ is diagonalized:

$$\dot{\boldsymbol{\Omega}}_{\psi} = \boldsymbol{P}\boldsymbol{\Lambda}\boldsymbol{P}^{-1} \tag{2.23}$$

$\boldsymbol{\Lambda}$ is a diagonal matrix composed of the eigenvalues λ_i and $\boldsymbol{P}$ is the transformation matrix composed of the right eigenvectors $\boldsymbol{V_i}$:

$$\boldsymbol{P} = (\boldsymbol{V_1}\boldsymbol{V_2}...\boldsymbol{V_N}) \tag{2.24}$$

Time scales analysis is obtained after writing Eq. 2.22 in eigenvector basis for $\hat{\boldsymbol{\psi}} = \boldsymbol{P}^{-1}\boldsymbol{\psi}$. Each component $\hat{\psi}_i$ evolves as:

$$\frac{d\hat{\psi}_i}{dt} = \hat{\dot{\Omega}}_{0i} + \lambda_i(\hat{\psi}_i - \hat{\psi}_{0i}) \tag{2.25}$$

where $\hat{\dot{\boldsymbol{\Omega}}}_0 = \boldsymbol{P}^{-1}\dot{\boldsymbol{\Omega}}(\boldsymbol{\psi}_0)$. In Eq. 2.25, each component $\hat{\psi}_i$ is independent from each other and is given by:

$$\hat{\psi}_i = \hat{\psi}_{0i} + \frac{\hat{\dot{\Omega}}_{0i}}{\lambda_i}(\exp(\lambda_i t) - 1) \tag{2.26}$$

Time scales can now be estimated from Eq. 2.26:

- if $|\lambda_i| \ll 1$, Eq. 2.26 reduces to $\hat{\psi}_i = \hat{\psi}_{0i} + \hat{\dot{\Omega}}_{0i}t$. The corresponding time scale is:

$$\tau_i = \frac{1}{|\hat{\dot{\Omega}}_{0i}|} \tag{2.27}$$

- if $|\lambda_i| \gg 1$, the corresponding time scale is:

$$\tau_i = |\lambda_i|^{-1} \tag{2.28}$$

- if $|\lambda_i| = 0$, $\hat{\psi}_i$ is constant and it can be shown it is a combination of conserved variables such as element mass fractions (Eggels, 1996).

On the one hand, for large positive values of λ_i, $\hat{\psi}_i$ will grow exponentially. On the other hand, large negative eigenvalues make $\hat{\psi}_i$ reach the steady state very fast. If eigenvalues are ordered properly, N_s slow and N_f fast modes can be defined and transformation matrices can be written as:

$$\boldsymbol{P} = (P_s \; P_f) \text{ and } \boldsymbol{P}^{-1} = \begin{pmatrix} p_s \\ p_f \end{pmatrix} \tag{2.29}$$

P_s is a $N \times N_s$ matrix including the slow right eigenvectors. Fast right eigenvectors are in the $N \times N_f$ matrix P_f. Same case for left eigenvectors in

the $N_s \times N$ matrix p_s and the $N_f \times N$ matrix p_f. Any vector $\hat{\boldsymbol{\psi}}$ in eigenvector basis is also decomposed in slow and fast components:

$$\hat{\boldsymbol{\psi}} = \begin{pmatrix} \hat{\boldsymbol{\psi}}_{\boldsymbol{s}} \\ \hat{\boldsymbol{\psi}}_{\boldsymbol{f}} \end{pmatrix} \tag{2.30}$$

In terms of $\boldsymbol{\psi}$, vector in the original basis, $\hat{\boldsymbol{\psi}}_{\boldsymbol{s}}$ and $\hat{\boldsymbol{\psi}}_{\boldsymbol{f}}$ are given as:

$$\hat{\boldsymbol{\psi}}_{\boldsymbol{s}} = p_s \boldsymbol{\psi} \text{ and } \hat{\boldsymbol{\psi}}_{\boldsymbol{f}} = p_f \boldsymbol{\psi} \tag{2.31}$$

An Intrinsec-Low-Dimensional Manifold (ILDM) is built by assuming steady states for N_f fast eigenvectors with negative λ_i of large magnitude (Maas and Pope, 1992; Gicquel et al., 1999; Ren and Pope, 2006):

$$\frac{d\hat{\psi}_f}{dt} = \frac{d}{dt}(p_f \psi) = 0 \tag{2.32}$$

Using Eq. 2.1, the ILDM is defined by the N_f algebraic relations:

$$p_f \dot{\boldsymbol{\Omega}}(\boldsymbol{\psi}) = \mathbf{0} \tag{2.33}$$

Like for the QSSA manifold, these relations along with information from slow modes enable to define a reduced manifold of $N_s - N_e$ dimensions. The manifold is different from the one obtained by QSSA where algebraic relations were identified with null source terms of specific species and not eigenvectors. However, if a specific species is always a combination of fast eigenvectors only, then the species source term is null and the QSSA is retrieved.

The construction of the ILDM starts with the choice of N_s species to represent slow processes. Their mass fractions are noted Y_{sj} for $j = 1, N_s$. A reference point $\boldsymbol{\psi}_0$ that belongs to the manifold must also be found to perform the eigenvalues analysis. The equilibrium point defined by conserved quantities is such a point. Then, the eigenvalues analysis provides the transformation matrix p_s to build the manifold. The subspace is extended in slow eigenvectors directions step by step. Finally, the resulted manifold verifies in each point:

$$\begin{cases} h = h_0 & \\ P = P_0 & \\ z_i = z_{i0} & \text{for } i = 1, N_e \\ p_f \dot{\boldsymbol{\Omega}}(\boldsymbol{\psi}) = \mathbf{0} & \\ Y_{sj} = c_j & \text{for } j = 1, N_s \end{cases} \tag{2.34}$$

where c_j are points coordinates to map the slow species space. Example of one-dimensional ILDM is given in Fig. 2.9. The manifold acts as an

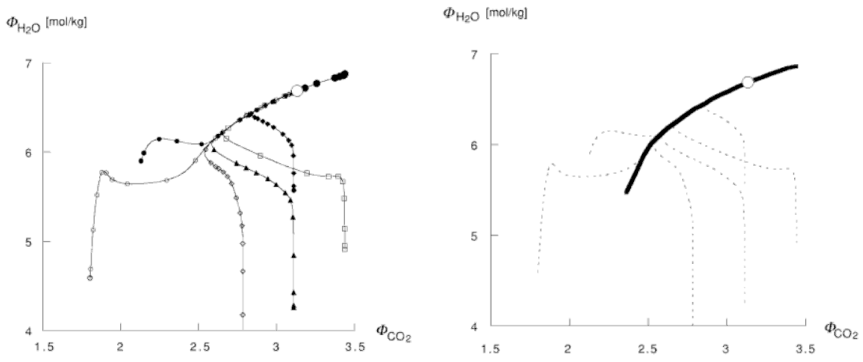

(a) (b)

Figure 2.9: *Trajectories of chemical reactions (a) and one-dimensional manifold (b) projected in the (CO_2, H_2O) plane. (a) Line with different symbols represents chemical paths from different initial point. (b) Line: 1D-ILDM ; dashed lines: trajectories. The plane coordinates are expressed in weighted mass fractions $\phi_i = Y_i/W_i$. ◯ represents the equilibrium point. (Warnatz et al., 2006).*

attractor of reaction trajectories. Any point around quickly tends to the one-dimensional curve by fast time scales reaction.
ILDM was found to be very effective at high temperature but suffers from several limitations. The first one occurs at low temperature. The number of slow time scales increases and the initial choice of slow species is not relevant anymore, leading to no solution of algebraic relations. Another limitation is the influence of transport which can modify the composition faster than slow chemical time scales (Fig. 2.8). In this case, species trajectories in state space step aside from the ILDM without converging to the manifold. Finally, the intrinsic low-dimensional manifold is not invariant i.e., starting from a point of the manifold, the unconstrained system will step away from the manifold. Other methods to construct reduced dimension manifold have been developed and allow to solve the cited limitations.
The Invariant Constrained Equilibrium-PreImage Curve (ICE-PIC) method builds a manifold from reaction trajectories (Ren et al., 2006). By using reaction paths, the ICE-PIC manifold is de facto invariant. Moreover, the manifold always exist, even at low-temperature in opposite to ILDM. However, like ILDM, ICE-PIC method was first devoted to chemical manifold in homogeneous flows and effects of non-homogeneities through species transport are often not negligible. For instance, premixed and no-premixed flames are balanced by diffusion and reaction. In such situations, physical time scales are within the wide range of chemical time scales and perturb the purely chemical manifold. That is why, Ren and Pope (2006) studied the origins of departure from the manifold and showed existence of a new manifold which can be computed with a close-parallel assumption (Ren et al., 2007). Trans-

port effects were also introduced by Bykov and Maas (2007) to extend ILDM in a REaction-DIffusion Manifold (REDIM).

2.3.3 Manifold generation: flamelets

Aforementioned manifold have been derived by mathematical considerations. However, taking into account general properties of a flame such as transport-chemistry coupling demands additional development. Flamelets are a more direct and pragmatic approach. From a physical point of view, the combustion is looked as a family of small flame elements called flamelets. These elements chosen to be representative of combustion are computed with detailed chemistry. Then, a couple of controlling parameters are identified to build a flamelet manifold. Obviously, depending on the mode of combustion, different types of flamelets must be considered.
In the following, different examples of combustion element are listed. Then, a detailed description of the Flamelet Prolongation of ILDM (FPI) model is developed. Finally, database storage difficulties are discussed.

2.3.3.1 Flamelets to describe combustion

In many models, the same controlling parameters are used to describe combustion like:

- **Mixture fraction** z
  In most applications, mixing occurs between only two composition: the first one being the fuel and the other the oxidizer. The mixture fraction is a passive scalar i.e. it has no reaction source term and its balance equation is:

$$\frac{\partial \rho z}{\partial t} + \frac{\partial}{\partial x_j}\left(\rho u_j z\right) = \frac{\partial}{\partial x_j}\left(\rho D \frac{\partial z}{\partial x_j}\right) \tag{2.35}$$

  By definition, it equals one in fuel and zero in oxidizer. For a single step chemistry, a passive scalar is formed from fuel and oxidizer mass fractions, respectively Y_f and Y_{ox}, as $(sY_f - Y_{ox})$ (Poinsot and Veynante, 2005), where s is the mass stoichiometric ratio. The factor $(sY_f - Y_{ox})$ is then normalized by its values in oxidizer and fuel to compute the mixture fraction.

  For detailed chemistry, $(sY_f - Y_{ox})$ is not a passive scalar anymore. That is why element mass fractions z_i which are passive scalars, are used instead to define z. If there is no differential diffusion, each element mass fraction can be normalized and defines the same mixture fraction. However, in the general case where differential diffusion is not neglected, several mixture fractions, one for each element, must be considered. Nonetheless, a mixture fraction is sometimes defined as a

combination of different element mass fractions (Bilger et al., 1990), although it does not follow a simple passive scalar balance equation anymore.

- **Progress variable** c
  In comparison to mixture fraction, used to distinguish fuel from oxidizer mixtures, a progress variables is defined to differentiate burnt gases from fresh ones. The progress variable c is defined as a reactive scalar that is null in fresh gases and unity in burnt gases. Hence, balance equation for c is written as:

$$\frac{\partial \rho c}{\partial t} + \frac{\partial}{\partial x_j}\left(\rho u_j c\right) = \frac{\partial}{\partial x_j}\left(\rho D \frac{\partial c}{\partial x_j}\right) + \rho \dot{\omega}_c \tag{2.36}$$

Depending on the tabulated chemistry model, incoming parameters of the manifold, such as z and c, differ:

- **Flamelet Prolongation of ILDM** (FPI) assembles one-dimensional laminar premixed flames in a database (Gicquel, 1999; Gicquel et al., 2000). The main parameter is the progress variable. Mixture fraction is added by computing flamelets at different equivalence ratio. Fiorina et al. (2003) also developed a non-adiabatic version including enthalpy as a new dimension of the database.

- **Homogeneous autoignition** simulations follow a different path than premixed flamelets in state space. That is why they have been used to build chemical database (Embouazza, 2005; Galpin et al., 2008a) to tackle configurations with such phenomena. The different input parameters can be c, z, the initial temperature, the pressure.

- **Perfectly Stirred Reactor** (PSR) were also used to map autoignition (Fichet, 2008). A new parameter, the residence time, is added.

- **Steady non-premixed flamelets** can be computed and stored in function of mixture fraction (Peters, 2000). This method has been extensively applied to diffusion flames. Each flamelet is generated for a given strain rate, a or a specified stoichiometric scalar dissipation rate χ_{st}.

- In order to tackle quenching and reignition phenomena, a **flamelet/progress variable approach** was used to tabulate diffusion flamelets from quenched to fully burning state (Pierce and Moin, 2004; Ihme et al., 2005; Ihme and Pitsch, 2008b). Input parameters of the table are mixture fraction and a redefined progress variable.

- **Unsteady non-premixed flamelets** were chosen to include autoignition effects (Zhang et al., 1995; Chang et al., 1996) or enthalpy variation (Ihme and Pitsch, 2008a).

Most of these chemical databases are parametrized by the couple of variables (z, c) but have different trajectories in the whole composition state space. These deviations are due to:

- **Different reaction development history**. In this case, chemistry follows a different path because of the external conditions imposed in the configuration as in, for instance, homogeneous autoignition and PSR, and also in isobar and isochoric transformations.

- **Species diffusion between fresh and burnt gases at fixed equivalence ratio**. This is diffusion in c-direction. Diffusion of heat and species change reaction trajectories. Premixed flamelets include such effect in contrary to homogeneous reactors.

- **Species diffusion between fuel and oxidizer mixtures** or diffusion in z-direction. Computing individual and independent premixed flamelets neglects diffusion whereas they are close to each other in reality (Fiorina et al., 2005a).

Despite *a priori* intrinsic incompatibility between models, connections exist. Fiorina et al. (2005a) investigated the ability of FPI to reproduce diffusion flames. In an other study, premixed flamelets database is used to build an autoignition table (Domingo et al., 2008).
Compared with mathematical or chemical derived manifold, flamelets tabulation requires a lower computational cost and provides manifolds with few dimensions. A part of the flamelet database coordinates is sometimes similar to other tabulation methods. These are the global parameters which control the chemical system as described in Eq. 2.1: pressure, enthalpy and element mass fractions dimensions are retrieved in flamelets generation in terms of pressure, initial temperature and mixture fraction. Hence, if variations of these quantities must be considered in the studied configuration, the number of dimensions increases the same way for both flamelet manifolds and other techniques. In fact, the ability of flamelets to provide low-dimensional manifold lies in the reaction description: flamelets consider only one progress variable (when there is one) whereas other manifolds use N_s dimensions*. This makes flamelets databases much simpler to build.
Generally, no further comparisons between flamelets and other manifolds is possible in terms of the reaction description. However, it is not the case concerning the FPI method: being a flamelet library, it turns out to be an extension of ILDM in low-temperature range. This model is detailed in the following.

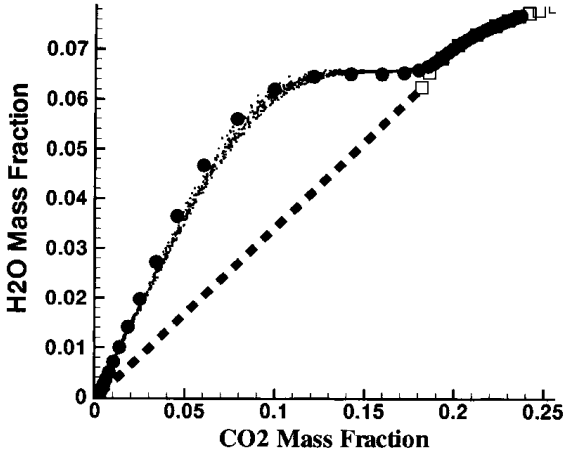

Figure 2.10: *Comparison of FPI (filled circles) and one-dimensional ILDM (hollow squares) manifolds with a premixed turbulent $CO/H_2/air$ flame (black dots) in the (Y_{CO_2},Y_{H_2O}) plane (Gicquel et al., 2000).*

2.3.3.2 Flamelet Prolongation of ILDM

In order to overcome ILDM discrepancies, the Flamelet Prolongation of ILDM (FPI) (Gicquel, 1999; Gicquel et al., 2000) uses a laminar premixed flamelet to build a one-dimensional manifold in the N dimensions state space. The flamelet solution identifies a specific path in state space from fresh gas to burnt gas composition. This choice is interesting since it estimates premixed turbulent combustion data quite accurately (Fig. 2.10). Indeed, all chemical time scales of the trajectory as well as the impact of transport are included by definition of this one-dimensional manifold. Moreover, at high temperature, the slow manifold ILDM is retrieved because chemical time scales become smaller than physical ones. A similar model called Flamelet Generated Manifold was proposed by van Oijen and de Goey (2000).
In practice, for a given pressure, enthalpy and composition of elements, all species profiles $Y_k(x)$ are extracted from the laminar premixed flamelet solution and expressed in function of a progress variable c to be defined. This progress variable is reconstructed from a non-normalized progress variable Y_c, easier to define. Indeed, Y_c is chosen as one specific species or a combination of different species. Next, the profile $Y_c(x)$ is extracted and the relations between x and Y_c are reversed to map all species in a database. For that purpose, a couple of conditions needs to be fulfilled (Naudin, 2008):

- Y_c must follow the reaction progress: if Y_c does not vary properly while combustion occurs, some chemical time scales are missed.

*Flamelets manifold with several progress variables can be built (van Oijen, 2002) but are rarely used.

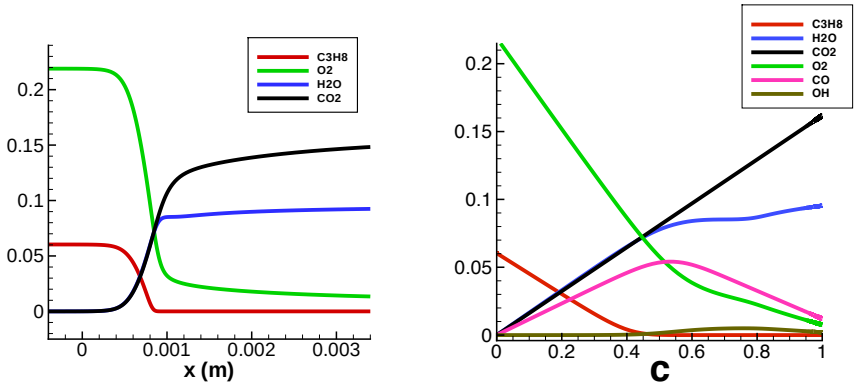

(a) Physical space (b) State space

Figure 2.11: *Projection of a stoichiometric laminar premixed propane/air flame from physical space to state space. (a) Species profiles from a one-dimensional laminar flame solution. (b) Species are remapped in c-space.* $Y_c = Y_{CO_2}$ *in this example.*

- There must be one-point correspondence between the physical space dimension x and Y_c. If it is not the case, the manifold is folded (several solution for the same Y_c value). Therefore, Y_c is chosen as a monotonic function of x.

The definition of Y_c depends on the fuel considered. For instance, Y_c can be equal to Y_{H_2O} for hydrogen combustion or Y_{CO_2} for methane. In rich mixture of methane/air, Y_{CO_2} is not monotonic because carbon dioxide is transformed back into carbon monoxide. Fiorina et al. (2003) have then retained $Y_c = Y_{CO} + Y_{CO_2}$ as a preferable definition. Once Y_c is defined, the normalized progress variable c is given by (Fiorina et al., 2003):

$$c = \frac{Y_c - Y_{c_f}}{Y_{c_{eq}} - Y_{c_f}} \tag{2.37}$$

Y_{c_f} and $Y_{c_{eq}}$ are the values of Y_c in fresh gases and in burnt gases at equilibrium composition. Hence, definition requirement for c are met since c is respectively equal to zero in fresh gases and one in burnt gases. This allows to remap a reference solution with detailed chemistry in state space in terms of c (Fig. 2.11). The FPI manifold is built by discretizing the progress variable direction and by tabulating all relevant variables φ.
A thermochemical table $\varphi^{tab}(c)$ is obtained for a specific element composition and a specific enthalpy and pressure. To describe partially premixed flows, premixed flamelets can be computed for different fresh gas composition i.e. mixture fraction, z. For different mixture fraction within flammability limits, a two-dimensional table $\varphi^{tab}(z, c)$ is built. Non-flammable regions are filled by interpolation. Fiorina et al. (2003) also developed a table for non-adiabatic configuration by adding enthalpy as a new parameter: $\varphi^{tab}(z, c, h)$.

2.3.3.3 Storage of the database

In every manifold construction, combustion description is better when a large number of dimensions is considered. However, the computation cost to build the whole manifold becomes important and the storage of the table may be an issue. Such cost could be avoided since only a small portion of the database is accessed in practical simulations.
That is why In Situ Adaptive Tabulation (ISAT) was proposed by Pope (1997): the database and the CFD simulation are computed simultaneously. Given a control error parameter, required information on the manifold are either interpolated from previous points in the table, either created if the estimated interpolation error is too high. This method is not yet been applied to flamelets because they are non-local: in order to know one point in the flamelet database, one needs to compute the whole flamelet solution.
For flamelets database, other techniques to reduce the memory space usage have been developed. Ihme et al. (2009) saved considerable memory using artificial neural network and compared numerical simulation with classic interpolation reading in database. Table reduction was also investigated by identifying intrinsic properties of flamelets such as self-similarity in both laminar (Ribert, 2005; Ribert et al., 2006) and turbulent flames (Veynante et al., 2008; Fiorina et al., 2009).

2.4 Conclusion

Different approaches to reduce complex chemistry cost have been presented. Skeletal reduction can be used to create a semi-detailed mechanism from a very large one but cannot obtain large reduction. Additional time scale information allows to define manifolds of reduced dimensions. The fast time scales are filtered using chemical or mathematical considerations. However, these manifolds suffer from limitations that vanish when flamelets are used. In these methods, flamelets solution are stored in a library to build a tabulated chemistry model with few controlling parameters (for instance: mixture fraction, progress variable, enthalpy, ...). The method has been applied to many cases in conventional combustion.
The main limitations of flamelets models come from its inherent definition: a flamelet model is adapted to a dedicated combustion regime. This restriction to a specific case allows large dimension reduction. However, recent technologies use configurations where flame can present more complex modes of combustion. One-dimensional elements cannot describe accurately these configurations where the reaction zone is multidimensional and diffusion is not necessary oriented only between fresh and burnt gas, or between fuel and oxidizer. Recent works have investigated the generation of multidimensional flamelets: for partially premixed flames (Nguyen et al., 2010) or for multiple fuels injection (Hasse and Peters, 2005). These models take into account

more complex physical features but introduce additional dimensions to the table.
In order to compute a numerical simulation using tabulated chemistry, the first step consists in choosing and generating the appropriate database for the given configuration. The numerical simulation is conducted in a next step where the chemical database reading is coupled with the balance equations solver. This steps is detailed in the next chapter.

Chapter 3

Coupling tabulated chemistry with Navier-Stokes equations

This chapter focuses on the coupling between tabulated chemistry techniques with compressible solvers in a new formalism called TTC (Tabulated Thermo-chemistry for Compressible flows). In low Mach-number CFD solvers, thermo-chemical quantities are directly read in a thermo-chemical database. However, because of perturbations introduced by acoustics, the coupling with fully compressible Navier-Stokes equations is not straightforward. In order to be consistent with tabulated chemistry framework, a new strategy to predict temperature field from the transported energy is developed. Boundary conditions are reformulated following Navier-Stokes Characteristic Boundary Conditions (NSCBC) formalism. The method is implemented in a compressible CFD code and validated by comparison with multi-component simulations. Temperature computation and characteristic boundary conditions reformulations are first validated on one-dimensional tests. A three-dimensional non-reactive case is then computed by performing a large eddy simulation of a turbulent round jet. Finally, a one-dimensional laminar flame simulation assesses the method performances in a reactive case.

3.1 Introduction

Large Eddy Simulation (LES) has become an affordable tool. This major evolution is due to the important improvement of the available computational power during the last decade. Using parallel computational resources, Boileau *et al.* (Boileau et al., 2008) were able to simulate the ignition of a full combustion chamber. Similar simulations of realistic systems were also performed by Raman and Pitsch (2005) and Undapalli et al. (2009). All these works are of great interest to study turbulent flame dynamics, com-

bustion instabilities or mixing characterization but they are limited in terms of chemistry description.
Indeed, because of large number of species, detailed chemistry simulations remain too expensive in terms of CPU time to be achieved in such configurations. Some direct numerical simulations were performed using detailed chemistry mechanisms for hydrogen-air flames (Mizobuchi et al., 2002) or methane-air flames (Hawkes and Chen, 2004) but they are limited to very small configurations that are far from industrial needs.
A classical approach used to take into account detailed chemistry effects in realistic LES for a low CPU cost is to use tabulated chemistry. Tabulated chemistry methods assume that chemical evolutions in the composition space can be parameterized and tabulated by a reduced set of variables $(\psi_1, ..., \psi_n)$ where n is the number of chemical database coordinates. In general, ψ_l are combinations of species mass fractions:

$$\psi_l = \sum_{k=1}^{N} \alpha_{lk} Y_k \tag{3.1}$$

where α_{lk} are constant numbers. Knowing the variables ψ_l in a simulation, all thermo-chemical variables φ can then be estimated by using the chemical database $\varphi^{tab}(\psi_1, ..., \psi_n)$. Among these tabulation techniques one can mention ILDM (Maas and Pope, 1992), FPI (Gicquel et al., 2000), FGM van Oijen and de Goey (2000), REDIM Bykov and Maas (2007) or ICE-PIC (Ren et al., 2006) methods which were presented in chapter 2. In these methods, instead of solving one balance equation for each chemical species involved in the detailed elementary reactions, only few equations for the reduced set of variables are solved. The balance equation for ψ_l is deduced from species balance equations (Eq. 1.35):

$$\frac{\partial \rho \psi_l}{\partial t} + \frac{\partial}{\partial x_j}\left(\rho u_j \psi_l\right) = \frac{\partial}{\partial x_j}\left(\rho D \frac{\partial \psi_l}{\partial x_j}\right) + \rho \dot{\omega}_{\psi_l} \tag{3.2}$$

Fick law for each species and unity Lewis numbers were assumed to derive Eq. 3.2. If complex transport is necessary, additional terms appear in Eq. 3.2. Another way is not to retain Eq. 3.1 and to choose Eq. 3.2 as a phenomenological equation that defines ψ_l. This choice was retained by (Pitsch and Peters, 1998) to redefine mixture fraction to compute steady non-premixed flamelets with differential diffusion.
A compressible formulation of balance equations is used in several LES solvers (DesJardin and Frankel, 1998; Huang et al., 2003; Selle et al., 2004; El-Asrag and Menon, 2009). The main problem when coupling tabulated chemistry with compressible Navier-Stokes equations is that perturbations due to compressibility effects are not considered during the database generation. This limitation is not a problem if the CFD solver is based on a low Mach-number assumption where the introduction of tabulated chemistry is

straightforward (Kempf et al., 2000; Fiorina et al., 2003, 2005b). But introducing tabulated chemistry in a compressible CFD solver is more challenging. In this case, temperature can not be directly read in the database because the tabulated temperature does not take into account acoustic perturbations. A second problem in compressible codes is the interaction between acoustics and boundaries (Poinsot and Lele, 1992; Baum et al., 1995). When using tabulated chemistry, boundary conditions for the reduced set of variables should therefore take into account perturbations due to acoustics.
This chapter is organized as follows: coupling between tabulated chemistry and low Mach-number solvers is first presented before considering fully compressible flows. Some existing methods to compute temperature in this specific case are detailed. Nonetheless, these methods use large memory space and numerical artifacts. That is why a new technique called TTC (Tabulated Thermo-chemistry for Compressible flows) formalism is developed to introduce tabulated chemistry strategies in compressible solvers. This approach only requires to solve additional balance equations for the database coordinates. A method is proposed to take into account temperature deviation due to acoustics. Then characteristic boundary condition treatment is detailed for tabulated chemistry. Finally, validation tests are presented. Reformulations of temperature computation and boundary treatment are validated with 1-D tests by comparison with multi-component simulations. Further validations are conducted by performing a non-reactive 3-D large eddy simulation of a round jet and a reactive case where the FPI tabulation method is chosen to reproduce a 1-D laminar flame.

3.2 Low Mach-Number code

In several industrial configurations, compressibility effects can be neglected. In such circumstances, solving acoustic waves becomes unnecessary and the effect of pressure fluctuations on density (and also temperature) are neglected. This assumption is valid in low Mach-number flows. The Mach number, M, is defined as:

$$\mathrm{M} = \frac{u}{a} \tag{3.3}$$

where u is a characteristic velocity magnitude in the studied configuration and a is the speed of sound:

$$a^2 = \left(\frac{\partial P}{\partial \rho}\right)_s \tag{3.4}$$

For an ideal gas, it is given by:

$$a = \sqrt{\gamma r T} \tag{3.5}$$

For low Mach-Number flow (M $\ll 1$), several simplifications are introduced in the Navier-Stokes equations. First, a PDE on pressure is often used instead of mass density (Patankar, 1980). Taking the divergence of the momentum equation (Eq. 1.31) and using continuity equation (Eq. 1.30), a Poisson equation is derived for pressure:

$$\frac{\partial^2 P}{\partial x_j \partial x_j} = \frac{\partial^2 \rho}{\partial t^2} - \frac{\partial^2}{\partial x_i \partial x_j}\left(\rho u_i u_j\right) + \frac{\partial^2 \tau_{ij}}{\partial x_i \partial x_j} \tag{3.6}$$

As acoustic waves are not resolved, Eq. 3.6 is solved at each iteration so that local pressure perturbations are propagated instantaneously to the entire pressure field. Once the pressure is known, mass density is computed by the equation of state (Eq. 1.10). Finally, low Mach-Number assumption introduces simplifications in the energy equation: viscous dissipation and spatial derivatives of pressure can be neglected. For instance, balance equation for the total non-chemical energy E (Eq. 1.50) becomes:

$$\begin{aligned} \frac{\partial \rho E}{\partial t} + \frac{\partial}{\partial x_i}\left(\rho u_i E\right) &= \frac{\partial}{\partial x_i}\left(\frac{\partial T}{\partial x_i}\right) - \frac{\partial}{\partial x_i}\left(\rho \sum_{k=1}^{N} h_{sk} V_{k,i} Y_k\right) \\ &\quad + \dot{Q} + \rho \dot{\omega}_T \end{aligned} \tag{3.7}$$

If detailed chemistry is used, balance equations for each species are solved. When using tabulated chemistry instead, computational cost is saved by replacing species transport equations by Eq. 3.2. Moreover, the low Mach-number assumption is used while generating the chemical database. Hence, the tabulated chemistry is coherent with low Mach-number flows solvers. Therefore, in addition to composition, mass density and temperature can be read directly from the table:

$$\rho = \rho^{tab}(\psi_1, \psi_2, ..., \psi_n) \tag{3.8}$$

$$T = T^{tab}(\psi_1, \psi_2, ..., \psi_n) \tag{3.9}$$

Any terms required to solve the system of equation such as transport, thermodynamic coefficients or reaction rates are also stored in the table:

$$\begin{aligned} \mu &= \mu^{tab}(\psi_1, \psi_2, ..., \psi_n) \\ \lambda &= \lambda^{tab}(\psi_1, \psi_2, ..., \psi_n) \\ c_p &= c_p^{tab}(\psi_1, \psi_2, ..., \psi_n) \\ \dot{\omega}_{\psi_l} &= \dot{\omega}_{\psi_l}^{tab}(\psi_1, \psi_2, ..., \psi_n) \\ &... \end{aligned} \tag{3.10}$$

3.3 Compressible formulation

3.3.1 Difficulties

In compressible solver with detailed chemistry, balance equations are solved for mass, momentum, energy and species mass fractions. These equations written in chapter 1 are reminded here:

- **Mass density** (Eq. 1.30)

$$\frac{\partial \rho}{\partial t} + \frac{\partial}{\partial x_j}\left(\rho u_j\right) = 0$$

- **Momentum** (Eq. 1.31)

$$\frac{\partial \rho u_i}{\partial t} + \frac{\partial}{\partial x_j}\left(\rho u_i u_j\right) = -\frac{\partial P}{\partial x_i} + \frac{\partial \tau_{ij}}{\partial x_j}$$

- **Total non-chemical energy** (Eq. 1.50)

$$\begin{aligned}\frac{\partial \rho E}{\partial t} + \frac{\partial}{\partial x_j}\left(\rho u_j E\right) &= \frac{\partial}{\partial x_j}\left(\lambda \frac{\partial T}{\partial x_j}\right) - \frac{\partial}{\partial x_j}\left(\rho \sum_{k=1}^{N} h_{sk} V_{k,j} Y_k\right) \\ &\quad + \frac{\partial}{\partial x_j}(\sigma_{ij} u_i) + \dot{Q} + \rho \dot{\omega}_T\end{aligned}$$

- **Species mass fractions** (Eq. 1.35)

$$\frac{\partial \rho Y_k}{\partial t} + \frac{\partial}{\partial x_j}\left(\rho u_j Y_k\right) = -\frac{\partial}{\partial x_j}\left(\rho V_{k,j} Y_k\right) + \rho \dot{\omega}_k$$

Pressure is given by the equation of state (Eq. 1.10) and temperature is usually computed from the energy definition* and the local composition:

$$e = \sum_{k=1}^{N} \int_{T_0}^{T} C_{vk}(T') Y_k dT' - \frac{R T_0}{W} + \sum_{k=1}^{N} \Delta h^0_{f,k} Y_k \tag{3.11}$$

Here, the energy definition of e (Eq. 1.22) is used, it is computed from the transported total non-chemical energy E.
Using tabulated chemistry, generation of the database does not include compressibility effects. This is incompatible with compressible flow solver in opposition to low Mach-number codes. Usually, the chemical table is generated at constant pressure and the energy fluctuations due to acoustic pressure perturbations are not tackled by tabulated chemistry. Consequently, for a

*The energy definition is used here for brevity but temperature can be found similarly from sensible energy or enthalpy and other energy defined in chapter 1.

fully compressible code, mass density, temperature and energy cannot be read from the table as previously:

$$\begin{aligned} \rho &\neq \rho^{tab}(\psi_1, \psi_2, ..., \psi_n) \\ T &\neq T^{tab}(\psi_1, \psi_2, ..., \psi_n) \\ e &\neq e^{tab}(\psi_1, \psi_2, ..., \psi_n) \end{aligned} \tag{3.12}$$

Instead, as in multi-component compressible computations, balance equation are solved for mass density, momentum and energy. Hence, ρ and e are correctly computed and not read in the database. Then, species transport equations are replaced by PDEs on ψ_i, leaving the temperature as the last unknown. Reversing Eq. 3.11 requires to know species formation enthalpies and C_{vk} as function of temperature. It is possible for a multi-component solver for simple configurations with many species considered or for more complex cases with only a limiting number of species. However, to be consistent with the database, Y_k, $h^0_{f,k}$ and $C_{vk}(T)$ should then be tabulated for all species of the detailed mechanism. This is not feasible in practice and other solutions have been developed.

3.3.2 Existing solutions and limitations

Introducing an additional database coordinate

The storage of all species with their heat capacities temperature functions is not possible in practice. A possible solution could be to compute Eq. 3.11 for all points in the database and for different temperature in order to build a new chemical database:

$$e^{tab}(\psi_1, ..., \psi_n, T) = \sum_{k=1}^{N} \int_{T_0}^{T} C_{vk}(T') Y_k^{tab} dT' - \frac{RT_0}{W^{tab}} + \sum_{k=1}^{N} \Delta h^0_{f,k} Y_k^{tab}$$

This new table contains a supplemental temperature coordinate allowing to take into account compressibility effects. However, the cost of the additional dimension on the database size is significant. That is why other methods are used.

Computing temperature without all tabulated species

Another method consists in approximating the thermo-chemistry description with a subset of $N_{tab} < N$ tabulated species. Equation 3.11 is then written as:

$$e \approx \sum_{k=1}^{N_{tab}} \int_{T_0}^{T} C_{vk}(T') Y_k^{tab} dT' - \frac{RT_0}{W^{tab}} + \sum_{k=1}^{N_{tab}} \Delta h^0_{f,k} Y_k^{tab}$$

Temperature is then computed from the N_{tab} tabulated species. This method was mentioned by Galpin et al. (2008b) and applied in the compressible LES structured code used by Domingo et al. (2005, 2008).

Special care is addressed to the choice of the tabulated species. Even with a reduced number of tabulated species, the solution generates databases whose size can be too large for massive parallel computers that do not have enough RAM. This can be avoided by approximating each term $\int_{T_0}^{T} C_{vk}(T')dT'$ as a polynomial and by storing only the polynomial coefficients as explained by Godel (2010, Annexe A).
Finally if transport equation for total non-chemical energy (Eq. 1.50) is used, two different heat release rates are available:

$$\dot{\omega}_T^{tab}(\psi_1, \psi_2, ..., \psi_n) \neq -\sum_{k=1}^{N_{tab}} \Delta h_{f,k}^0 \dot{\omega}_k^{tab}(\psi_1, \psi_2, ..., \psi_n)$$

The first one is the "true" heat release rate where all species have been accounted for. The second term computes the heat release with only the N_{tab} tabulated species. Depending on which formulation is used, inconsistency with temperature retrieval might raise and lead to divergence between temperature and T^{tab}. Indeed, the bigger the departure from the table is, the larger the error becomes since a wrong source term is imposed at the wrong temperature.

Transport of selected species

Another strategy was adopted in other works (Galpin et al., 2008b,a). N_{tab} species are chosen to be transported in addition to the n balance equation for ψ_l and ρ is computed as $\sum_{k=1}^{N_{tab}}(\rho Y_k)$. The choice of the transported species is critical. Besides, species chemical reaction rates cannot be read from the table since it does not conserve mass:

$$\sum_{k=1}^{N_{tab}<N} \dot{\omega}_k^{tab}(\psi_1, \psi_2, ..., \psi_n) \neq 0 \tag{3.13}$$

Different technical corrections have then been developed to make coherent transport of N_{tab} species with a chemical table built from a N-species detailed mechanism. To ensure elements conservation, two groups of transported species are formed:

- The first one is composed of species where $\dot{\omega}_k$ can be arbitrary fixed (to $\dot{\omega}_k^{tab}$ for example).
- The second group of species is responsible for elements conservation. $\dot{\omega}_k$ is written as a combination of other transported species source terms.

In spite of the mass conservation correction, departure of Y_k from the database value Y_k^{tab} is not prevented. This effect is minimized by replacing $\dot{\omega}_k^{tab}$ by

relaxation expressions:

$$\dot{\omega}_k = \frac{Y_k^{tab}(z, c + \delta c) - Y_k}{\tau} \tag{3.14}$$

where mixture fraction z and progress variable c are used for tabulation. τ is an ad hoc parameter and δc is the progress variable variation between two iterations of the simulation. With such source terms, Y_k tend to their tabulated values, estimated at the next step of the simulation. The time response τ fixes how fast mass fractions are brought back on the database manifold. However, for multi-dimensional case and turbulent combustion model, approximation given by Eq. 3.14 introduces mismatch between transported species and tabulated data. Indeed, only the variation of the progress variable coordinate is considered and this variation δc is approximated by considering chemistry only. In fact, this set of corrections has been validated for one-dimensional flame (Galpin, 2007; Galpin et al., 2008b).
Advantages of tabulated chemistry methods are to solve balance equations for database input parameters, which introduces CPU saving. Unfortunately, in the previously described implementation (Galpin et al., 2008b), balance equations for species mass fractions are solved in addition to the database coordinates. To properly describe methane/air combustion, nine species are necessary Galpin et al. (2008b). For hydrogen/air combustion, nine species are also transported in addition to the database coordinates (Galpin et al., 2008a). Finally, as Eq. 3.14 requires $Y_k^{tab}(\psi_1, .., \psi_n)$ for each transported species, the size of the thermochemical database can be problematic on massively parallel architecture where memory space is limited.
These limitations are intrinsic to the method which was designed for multi-component based solver. It can however be notified that transport equation for one species only ($Y_k = 1$) gives the mass density equation. Then, by modifying the coded thermodynamical description to take into account tabulated chemistry, which can be a heavy task, it is possible to change a multi-component based solver into the problem described in 3.3.1. In this case, as stressed previously, a new way to compute temperature to account for compressible effects is required.

3.4 TTC formalism: temperature computation for tabulated chemistry

ρ, ρu_i, $\rho\psi_l$ and $\rho e_t = \rho(e + u_i u_i/2)$ are solved from their respective balance equations. One remaining difficulty is the computation of temperature as stressed in 3.3.1. Indeed, the transported values e and T are different from those that are tabulated: e^{tab} and T^{tab}. The difference $\Delta e =$

$e - e^{tab}(\psi_1, ..., \psi_n)$ between transported and tabulated energies is given by:

$$\begin{aligned}\Delta e &= \left(\int_{T_0}^{T} C_v(T')\mathrm{d}T' - \frac{RT_0}{W} + \sum_{k=1}^{N} \Delta h^0_{f,k} Y_k\right) \\ &\quad - \left(\int_{T_0}^{T^{tab}} C_v(T')\mathrm{d}T' - \frac{RT_0}{W^{tab}} + \sum_{k=1}^{N} \Delta h^0_{f,k} Y^{tab}_k\right) \end{aligned} \tag{3.15}$$

Assuming that composition is given by the chemical database:

$$\begin{aligned} Y_k &= Y_k^{tab}(\psi_1, \psi_2, ..., \psi_n) \\ C_v(T^{tab}) &= C_v^{tab}(\psi_1, \psi_2, ..., \psi_n) \\ W &= W^{tab}(\psi_1, \psi_2, ..., \psi_n) \end{aligned}$$

the energy difference is

$$\begin{aligned}\Delta e &\approx \int_{T^{tab}(\psi_1,...,\psi_n)}^{T} C_v(T')\mathrm{d}T' \\ &= \int_{T^{tab}(\psi_1,...,\psi_n)}^{T} \left(C_v(T^{tab}) + \frac{\partial C_v}{\partial T}(T^{tab})(T' - T^{tab}) + \cdots\right)\mathrm{d}T'\end{aligned}$$

The function $C_v(T')$ is approximated by a Taylor series. Assuming that C_v is constant within the temperature range $[T^{tab}, T]$[†], only the first term is kept and energy difference is written as:

$$e - e^{tab}(\psi_1, ..., \psi_n) \approx C_v^{tab}(\psi_1, ..., \psi_n)\left(T - T^{tab}(\psi_1, ..., \psi_n)\right) \tag{3.16}$$

The "compressible" temperature T can therefore be approximated from the tabulated energy and temperature e^{tab} and T^{tab}, respectively and the transported energy $e = e_t - u_i u_i/2$:

$$T = T^{tab}(\psi_1, ..., \psi_n) + \frac{e - e^{tab}(\psi_1, ..., \psi_n)}{C_v^{tab}(\psi_1, ..., \psi_n)} \tag{3.17}$$

Note that this assumption is valid in the case of small acoustic perturbations but is not realistic for highly compressible flow, where higher order approximation should be retained.

3.5 TTC formalism: characteristic boundary conditions for tabulated chemistry

In compressible CFD solvers, boundary conditions are provided using characteristic wave considerations where boundary conditions are specified for

[†]In practice the temperature deviation due to acoustic waves is limited to a small range where thermodynamical quantities such as heat capacities remain constant

characteristic waves then expressed for Navier-Stokes conservative variables. Navier-Stokes Characteristic Boundary Conditions (NSCBC) have been first derived for single-component flows (Poinsot and Lele, 1992), and later for multi-component flows (Baum et al., 1995; Okong'o and Bellan, 2002). In tabulated chemistry framework, as N species transport equations have been replaced by $n < N$ equations for variables ψ_l, characteristic wave decomposition must be expressed in terms of n characteristic waves corresponding to ψ_l and not N species waves anymore.
A similar procedure to derive NSCBC for multi-component flows (Baum et al., 1995) is applied for compressible flows to be described by tabulated chemistry:

- Balance equations are written in vectorial form for non-conservative variable.
- Eigenvalues analysis enables to introduce characteristic waves amplitudes.
- Characteristic wave amplitudes are given by the boundary conditions.
- Balance equations for conservative variables are expressed by introducing the known characteristic waves amplitudes.

Additional definitions are first presented.

3.5.1 Additional definitions

Balance equations for conservative variables are solved for: mass density, ρ, momentum, ρu, ρv, ρw, total energy ρe_t and the n database coordinates $\rho\psi_l$. (u, v, w) are the velocity components and total energy is composed of two contributions: $e_t = e + e_c$, where e is the internal energy and $e_c = \frac{1}{2}(u^2+v^2+w^2)$ is the kinetic energy. Mixture composition is parametrized by the n variables ψ_l which account for N real species. The previously defined parameter r is:

$$r = \sum_{k=1}^{N} \frac{R}{W_k} Y_k \tag{3.18}$$

Mixture heat capacities, C_v and C_p, difference and ratio are:

$$r = C_p - C_v \quad \text{and} \quad \gamma = \frac{C_p}{C_v} \tag{3.19}$$

As the factor $\gamma - 1$ will often appear, a new mixture property β is defined:

$$\beta = \gamma - 1 \tag{3.20}$$

C_v and C_p are then given by:

$$C_v = \frac{r}{\beta} \quad \text{and} \quad C_p = \frac{(\beta+1)r}{\beta} \tag{3.21}$$

An additional mixture quantity Π is introduced:

$$\Pi = \sum_{k=1}^{N} \left(\frac{RT}{W_k} - \beta e_k \right) Y_k = rT - \beta e \tag{3.22}$$

Characteristic wave decomposition will introduce new quantities specific to tabulated chemistry such as:

$$\vartheta_{\psi_l} = \sum_{k=1}^{N} \left(\frac{RT}{W_k} - \beta e_k \right) \frac{\partial Y_k}{\partial \psi_l} \tag{3.23}$$

3.5.2 Transport equation for non-conservative variables

Conservative variables are gathered in the vector $\boldsymbol{U}$ defined as:

$$\boldsymbol{U} = (\rho, \rho u, \rho v, \rho w, \rho e_t, \rho\psi_1, ..., \rho\psi_n)^\top$$

When using tabulated chemistry, governing equations for adiabatic reactive flows can be written as:

$$\frac{\partial \boldsymbol{U}}{\partial t} + \frac{\partial \boldsymbol{F}^j}{\partial x_j} + \frac{\partial \boldsymbol{F}_d^j}{\partial x_j} = \boldsymbol{S} \tag{3.24}$$

where $\boldsymbol{F}^j$ is the Eulerian flux in direction j:

$$\boldsymbol{F}^1 = \begin{pmatrix} \rho u \\ \rho uu + P \\ \rho uv \\ \rho uw \\ \rho u e_t + uP \\ \rho u\psi_1 \\ \vdots \\ \rho u\psi_n \end{pmatrix} \quad \boldsymbol{F}^2 = \begin{pmatrix} \rho v \\ \rho uv \\ \rho vv + P \\ \rho vw \\ \rho v e_t + vP \\ \rho v\psi_1 \\ \vdots \\ \rho v\psi_n \end{pmatrix} \quad \boldsymbol{F}^3 = \begin{pmatrix} \rho w \\ \rho uw \\ \rho vw \\ \rho ww + P \\ \rho w e_t + wP \\ \rho w\psi_1 \\ \vdots \\ \rho w\psi_n \end{pmatrix}$$

$\boldsymbol{F}_d^j$ are the diffusive fluxes:

$$\boldsymbol{F}_d^1 = \begin{pmatrix} 0 \\ -\tau_{11} \\ -\tau_{21} \\ -\tau_{31} \\ -u_i\tau_{i1} + q_1 \\ -\rho D \frac{\partial \psi_1}{\partial x_1} \\ \vdots \\ -\rho D \frac{\partial \psi_n}{\partial x_1} \end{pmatrix} \quad \boldsymbol{F}_d^2 = \begin{pmatrix} 0 \\ -\tau_{12} \\ -\tau_{22} \\ -\tau_{32} \\ -u_i\tau_{i2} + q_2 \\ -\rho D \frac{\partial \psi_l}{\partial x_2} \\ \vdots \\ -\rho D \frac{\partial \psi_n}{\partial x_2} \end{pmatrix} \quad \boldsymbol{F}_d^3 = \begin{pmatrix} 0 \\ -\tau_{13} \\ -\tau_{23} \\ -\tau_{33} \\ -u_i\tau_{i3} + q_3 \\ -\rho D \frac{\partial \psi_l}{\partial x_3} \\ \vdots \\ -\rho D \frac{\partial \psi_n}{\partial x_3} \end{pmatrix}$$

$\boldsymbol{S} = (0, 0, 0, 0, 0, \rho\dot{\omega}_{\psi_1}, ..., \rho\dot{\omega}_{\psi_n})^\top$ gathers the source terms. Using jacobian matrices of Eulerian flux, $\boldsymbol{J}^j = \frac{\partial \boldsymbol{F}^j}{\partial \boldsymbol{U}}$, Eq. 3.24 reads:

$$\frac{\partial \boldsymbol{U}}{\partial t} + \boldsymbol{J}^j \frac{\partial \boldsymbol{U}}{\partial x_j} + \frac{\partial \boldsymbol{F}_d^j}{\partial x_j} = \boldsymbol{S} \tag{3.25}$$

The vector of non-conservative variable $\boldsymbol{V} = (\rho, u, v, w, P, \psi_1, ..., \psi_n)^\top$ is now considered. Using the jacobian matrix between conservative and non-conservative variables $\boldsymbol{M} = \frac{\partial \boldsymbol{U}}{\partial \boldsymbol{V}}$, Eq. 3.25 reads

$$\boldsymbol{M}\frac{\partial \boldsymbol{V}}{\partial t} + \boldsymbol{J}^j \boldsymbol{M} \frac{\partial \boldsymbol{V}}{\partial x_j} + \frac{\partial \boldsymbol{F}_d^j}{\partial x_j} = \boldsymbol{S} \tag{3.26}$$

The evolution of non-conservative variables is given by multiplying Eq. 3.26 by $\boldsymbol{M}^{-1}$:

$$\frac{\partial \boldsymbol{V}}{\partial t} + \boldsymbol{M}^{-1}\boldsymbol{J}^j \boldsymbol{M} \frac{\partial \boldsymbol{V}}{\partial x_j} = \boldsymbol{M}^{-1}\boldsymbol{S} - \boldsymbol{M}^{-1}\frac{\partial \boldsymbol{F}_d^j}{\partial x_j} \tag{3.27}$$

or

$$\frac{\partial \boldsymbol{V}}{\partial t} + \boldsymbol{A}^j \frac{\partial \boldsymbol{V}}{\partial x_j} = \text{RHS}_1 \tag{3.28}$$

where $\boldsymbol{A}^j = \boldsymbol{M}^{-1}\boldsymbol{J}^j\boldsymbol{M}$ and $\text{RHS}_1 = \boldsymbol{M}^{-1}\boldsymbol{S} - \boldsymbol{M}^{-1}\frac{\partial \boldsymbol{F}_d^j}{\partial x_j}$ is composed of diffusive and source terms. In order to compute $\boldsymbol{A}^j$, the matrices $\boldsymbol{M}$ and $\boldsymbol{M}^{-1}$ are first written, then flux jacobian matrices $\boldsymbol{J}^j$ are given.

3.5.3 Conservative/non-conservative variables transformation (Matrix $\boldsymbol{M}$)

$\boldsymbol{M}$ is determined from these relations:

$$\begin{aligned}
\partial(\rho u) &= \rho\partial u + u\partial\rho && (3.29)\\
\partial(\rho v) &= \rho\partial v + v\partial\rho && (3.30)\\
\partial(\rho w) &= \rho\partial w + w\partial\rho && (3.31)\\
\partial(\rho e_t) &= \rho\partial e_t + e_t\partial\rho && (3.32)\\
\partial(\rho\psi_l) &= \psi_l\partial\rho + \rho\partial\psi_l && (3.33)
\end{aligned}$$

Eq. 3.32 requires further development to be expressed in terms of $\boldsymbol{V}$ components variations only. e_t is split into kinetic and internal energy:

$$\partial(\rho e_t) = \rho\partial e_c + \rho\partial e + (e_c + e)\partial\rho \tag{3.34}$$

Kinetic and internal energies variation are:

$$\begin{aligned}
\partial e_c &= \partial\left(\frac{1}{2}(u^2 + v^2 + w^2)\right)\\
&= u\partial u + v\partial v + w\partial w && (3.35)
\end{aligned}$$

and

$$\begin{aligned}\partial e &= \sum_k \partial(e_k Y_k) \\ &= \sum_k Y_k \partial e_k + \sum_k e_k \partial Y_k \\ &= \sum_k C_{vk} Y_k \partial T + \sum_k e_k \partial Y_k \\ &= C_v \partial T + \sum_k e_k \partial Y_k \end{aligned} \tag{3.36}$$

Variation of temperature is expressed in term of pressure variation through the equation of state (Eq. 1.10):

$$\partial P = \partial(\rho r T) \tag{3.37}$$
$$= \rho r \partial T + r T \partial \rho + \rho T \partial r \tag{3.38}$$
$$= \rho r \partial T + r T \partial \rho + \rho T \sum_k \frac{R}{W_k} \partial Y_k \tag{3.39}$$

Hence,

$$\partial T = \frac{1}{\rho r}\partial P - \frac{T}{\rho}\partial \rho - T \sum_k \frac{R}{r W_k} \partial Y_k \tag{3.40}$$

Eq. 3.40 is introduced in Eq. 3.36:

$$\partial e = \frac{C_v}{\rho r}\partial P - C_v \frac{T}{\rho}\partial \rho + \sum_k \left(e_k - \frac{C_v}{r}\frac{RT}{W_k} \right) \partial Y_k \tag{3.41}$$

With $C_v = \frac{r}{\beta}$, Eq. 3.41 is written:

$$\partial e = \frac{1}{\rho\beta}\partial P - \frac{rT}{\rho\beta}\partial \rho - \frac{1}{\beta}\sum_k \left(\frac{RT}{W_k} - \beta e_k \right) \partial Y_k \tag{3.42}$$

The variation ∂Y_k is expressed using $\partial \psi_l$:

$$\partial e = \frac{1}{\rho\beta}\partial P - \frac{rT}{\rho\beta}\partial \rho - \frac{1}{\beta}\sum_k \left(\frac{RT}{W_k} - \beta e_k \right) \sum_l \frac{\partial Y_k}{\partial \psi_l} \partial \psi_l \tag{3.43}$$
$$= \frac{1}{\rho\beta}\partial P - \frac{rT}{\rho\beta}\partial \rho - \sum_{k,l} \frac{1}{\beta}\left(\frac{RT}{W_k} - \beta e_k \right) \frac{\partial Y_k}{\partial \psi_l} \partial \psi_l \tag{3.44}$$
$$= \frac{1}{\rho\beta}\partial P - \frac{rT}{\rho\beta}\partial \rho - \sum_l \frac{\vartheta_{\psi_l}}{\beta} \partial \psi_l \text{‡} \tag{3.45}$$

‡This equality shows that $\vartheta_{\psi_l} = -\beta \left(\frac{\partial e}{\partial \psi_l} \right)_{P,\rho,\psi_1,\ldots,\psi_{p\neq l},\ldots\psi_n}$.

Finally, total energy equation (Eq. 3.34) becomes:

$$\begin{aligned}\partial(\rho e_t) &= \left(e_c + e - \frac{rT}{\beta}\right)\partial\rho \\ &\quad +\rho u\partial u + \rho v\partial v + \rho w\partial w + \frac{1}{\beta}\partial P \\ &\quad -\sum_l \frac{\rho}{\beta}\vartheta_{\psi_l}\partial\psi_l \end{aligned} \tag{3.46}$$

or

$$\begin{aligned}\partial(\rho e_t) &= \left(e_c - \frac{\Pi}{\beta}\right)\partial\rho \\ &\quad +\rho u\partial u + \rho v\partial v + \rho w\partial w + \frac{1}{\beta}\partial P \\ &\quad -\sum_l \frac{\rho}{\beta}\vartheta_{\psi_l}\partial\psi_l \end{aligned} \tag{3.47}$$

Finally, the transformation matrix $\boldsymbol{M}$ is:

$$\boldsymbol{M} = \begin{pmatrix} 1 & 0 & 0 & 0 & 0 & 0 & \cdots & 0 \\ u & \rho & 0 & 0 & 0 & 0 & \cdots & 0 \\ v & 0 & \rho & 0 & 0 & 0 & \cdots & 0 \\ w & 0 & 0 & \rho & 0 & 0 & \cdots & 0 \\ e_c - \frac{\Pi}{\beta} & \rho u & \rho v & \rho w & \frac{1}{\beta} & -\frac{\rho}{\beta}\vartheta_{\psi_1} & \cdots & -\frac{\rho}{\beta}\vartheta_{\psi_n} \\ \psi_1 & 0 & 0 & 0 & 0 & \rho & \cdots & 0 \\ \vdots & \vdots & \vdots & \vdots & \vdots & \vdots & \ddots & \vdots \\ \psi_n & 0 & 0 & 0 & 0 & 0 & \cdots & \rho \end{pmatrix} \tag{3.48}$$

The inverse transformation matrix $\boldsymbol{M}^{-1}$ is found by reversing Eq. 3.29, 3.30, 3.31, 3.47, 3.33 in order to express non-conservative variables in function of conservative ones:

$$\partial u = -\frac{u}{\rho}\partial\rho + \frac{1}{\rho}\partial(\rho u) \tag{3.49}$$

$$\partial v = -\frac{v}{\rho}\partial\rho + \frac{1}{\rho}\partial(\rho v) \tag{3.50}$$

$$\partial w = -\frac{w}{\rho}\partial\rho + \frac{1}{\rho}\partial(\rho w) \tag{3.51}$$

$$\partial\psi_l = -\frac{\psi_l}{\rho}\partial\rho + \frac{1}{\rho}\partial(\rho\psi_l) \tag{3.52}$$

$$\begin{aligned}\partial P &= (-\beta e_c + \Pi)\,\partial\rho - \beta u(\rho\partial u) - \beta v(\rho\partial v) - \beta w(\rho\partial w) \\ &\quad +\beta\partial(\rho e_t) + \sum_l \vartheta_{\psi_l}(\rho\partial\psi_l)\end{aligned}$$

Replacing variations ∂u, ∂v, ∂w and $\partial\psi_l$ by conservative variables variations, pressure variation becomes:

$$\begin{aligned}
\partial P &= (-\beta e_c + \Pi)\,\partial\rho - \beta u\,(\partial(\rho u) - u\partial\rho) \\
&\quad -\beta v\,(\partial(\rho v) - v\partial\rho) - \beta w\,(\partial(\rho w) - w\partial\rho) \\
&\quad +\beta\partial(\rho e_t) + \sum_l \vartheta_{\psi_l}\,(\partial(\rho\psi_l) - \psi_l\partial\rho) \\
&= \left(\beta e_c + \Pi - \sum_l \vartheta_{\psi_l}\psi_l\right)\partial\rho \\
&\quad -\beta u\partial(\rho u) - \beta v\partial(\rho v) - \beta w\partial(\rho w) \\
&\quad +\beta\partial(\rho e_t) + \sum_l \vartheta_{\psi_l}\partial(\rho\psi_l)
\end{aligned} \tag{3.53}$$

The transformation matrix $\boldsymbol{M}^{-1}$ is:

$$\boldsymbol{M}^{-1} = \begin{pmatrix}
1 & 0 & 0 & 0 & 0 & 0 & \cdots & 0 \\
-\frac{u}{\rho} & \frac{1}{\rho} & 0 & 0 & 0 & 0 & \cdots & 0 \\
-\frac{v}{\rho} & 0 & \frac{1}{\rho} & 0 & 0 & 0 & \cdots & 0 \\
-\frac{w}{\rho} & 0 & 0 & \frac{1}{\rho} & 0 & 0 & \cdots & 0 \\
\beta e_c+\Pi-\sum_l \vartheta_{\psi_l}\psi_l & -\beta u & -\beta v & -\beta w & \beta & \vartheta_{\psi_1} & \cdots & \vartheta_{\psi_n} \\
-\frac{\psi_1}{\rho} & 0 & 0 & 0 & 0 & \frac{1}{\rho} & \cdots & 0 \\
\vdots & \vdots & \vdots & \vdots & \vdots & \vdots & \ddots & \vdots \\
-\frac{\psi_n}{\rho} & 0 & 0 & 0 & 0 & 0 & \cdots & \frac{1}{\rho}
\end{pmatrix} \tag{3.54}$$

3.5.4 Jacobian of Eulerian flux (Matrix $\boldsymbol{J}$)

A detailed computation of $\boldsymbol{J^1}$ is given. The infinitesimal variations $\partial(\rho u)$, $\partial(\rho uu + P)$, $\partial(\rho uv)$, $\partial(\rho uw)$, $\partial(\rho ue_t + uP)$ and $\partial(\rho u\psi_l)$ are expressed in

terms of conservative variables variations:

$$
\begin{aligned}
\partial(\rho u) &= \partial(\rho u) \\
\partial(\rho uu + P) &= \partial(\rho uu) + \partial P \\
&= u\partial(\rho u) + \rho u\partial u + \partial P \\
&= u\partial(\rho u) + u(\partial(\rho u) - u\partial\rho) + \partial P \\
&= -u^2\partial\rho + 2u\partial(\rho u) + \partial P \\
\partial(\rho uv) &= -uv\partial\rho + v\partial(\rho u) + u\partial(\rho v) \\
\partial(\rho uw) &= -uw\partial\rho + w\partial(\rho u) + u\partial(\rho w) \\
\partial(\rho ue_t + uP) &= -ue_t\partial\rho + e_t\partial(\rho u) + u\partial(\rho e_t) + P\partial u + u\partial P \\
&= (ue_t - u\frac{P}{\rho})\partial\rho + (e_t + \frac{P}{\rho})\partial(\rho u) \\
&\quad +u\partial(\rho e_t) + u\partial P \\
\partial(\rho u\psi_l) &= -u\psi_l\partial\rho + \psi_l\partial(\rho u) + u\partial(\rho\psi_l)
\end{aligned}
$$

The term ∂P is replaced by Eq. 3.53, hence

$$
\begin{aligned}
\partial(\rho uu + P) &= (\beta e_c - u^2 + \Pi - \sum_l \vartheta_{\psi_l}\psi_l)\partial\rho \\
&\quad +(2u - \beta u)\partial(\rho u) - \beta v\partial(\rho v) - \beta w\partial(\rho w) \\
&\quad +\beta\partial(\rho e_t) + \sum_l \vartheta_{\psi_l}\partial(\rho\psi_l) \\
\partial(\rho ue_t + uP) &= (-uh_t + u\beta e_c + u\Pi - u\sum_l \vartheta_{\psi_l}\psi_l)\partial\rho \\
&\quad +(h_t - \beta u^2)\partial(\rho u) - \beta uv\partial(\rho v) - \beta uw\partial(\rho w) \\
&\quad +(\beta + 1)u\partial(\rho e_t) + \sum_l u\vartheta_{\psi_l}\partial(\rho\psi_l)
\end{aligned}
$$

where the total non-chemical enthalpy $h_t = e_t + P/\rho$ has been introduced. Hence, the matrix $\boldsymbol{J}^1$ is given by:

$$\boldsymbol{J}^1 = \begin{pmatrix} 0 & 1 & 0 & 0 & 0 & 0 & \cdots & 0 \\ \beta e_c - u^2 + \Pi - \sum_l \vartheta_{\psi_l}\psi_l & 2u - \beta u & -\beta v & -\beta w & \beta & \vartheta_{\psi_1} & \cdots & \vartheta_{\psi_n} \\ -uv & v & u & 0 & 0 & 0 & \cdots & 0 \\ -uw & w & 0 & u & 0 & 0 & \cdots & 0 \\ -uh_t + u\beta e_c + u\Pi - u\sum_l \vartheta_{\psi_l}\psi_l & h_t - \beta u^2 & -\beta uv & -\beta uw & (\beta+1)u & u\vartheta_{\psi_1} & \cdots & u\vartheta_{\psi_n} \\ -u\psi_1 & \psi_1 & 0 & 0 & 0 & u & \cdots & 0 \\ \vdots & \vdots & \vdots & \vdots & \vdots & \vdots & \ddots & \vdots \\ -u\psi_n & \psi_n & 0 & 0 & 0 & 0 & \cdots & u \end{pmatrix}$$

Matrices $\boldsymbol{J}^2$ and $\boldsymbol{J}^3$ are computed the same way and read:

$$\boldsymbol{J}^2 = \begin{pmatrix} 0 & 0 & 1 & 0 & 0 & 0 & \cdots & 0 \\ -uv & v & u & 0 & 0 & 0 & \cdots & 0 \\ \beta e_c - v^2 + \Pi - \sum_l \vartheta_{\psi_l}\psi_l & -\beta u & 2v - \beta v & -\beta w & \beta & \vartheta_{\psi_1} & \cdots & \vartheta_{\psi_n} \\ -vw & 0 & w & v & 0 & 0 & \cdots & 0 \\ -vh_t + v\beta e_c + v\Pi - v\sum_l \vartheta_{\psi_l}\psi_l & -\beta uv & h_t - \beta v^2 & -\beta vw & (\beta+1)v & v\vartheta_{\psi_1} & \cdots & v\vartheta_{\psi_n} \\ -v\psi_1 & 0 & \psi_1 & 0 & 0 & v & \cdots & 0 \\ \vdots & \vdots & \vdots & \vdots & \vdots & \vdots & \ddots & \vdots \\ -v\psi_n & 0 & \psi_n & 0 & 0 & 0 & \cdots & v \end{pmatrix}$$

$$\boldsymbol{J}^3 = \begin{pmatrix} 0 & 0 & 0 & 1 & 0 & 0 & \cdots & 0 \\ -uw & w & 0 & u & 0 & 0 & \cdots & 0 \\ -vw & 0 & w & v & 0 & 0 & \cdots & 0 \\ \beta e_c - w^2 + \Pi - \sum_l \vartheta_{\psi_l}\psi_l & -\beta u & -\beta v & 2w - \beta w & \beta & \vartheta_{\psi_1} & \cdots & \vartheta_{\psi_n} \\ -wh_t + w\beta e_c + w\Pi - w\sum_l \vartheta_{\psi_l}\psi_l & -\beta uw & -\beta vw & h_t - \beta w^2 & (\beta+1)w & w\vartheta_{\psi_1} & \cdots & w\vartheta_{\psi_n} \\ -w\psi_1 & 0 & 0 & \psi_1 & 0 & w & \cdots & 0 \\ \vdots & \vdots & \vdots & \vdots & \vdots & \vdots & \ddots & \vdots \\ -w\psi_n & 0 & 0 & \psi_n & 0 & 0 & \cdots & w \end{pmatrix}$$

3.5.5 Computing $\boldsymbol{A}^j = \boldsymbol{M}^{-1}\boldsymbol{J}^j\boldsymbol{M}$

The matrix $\boldsymbol{A}^1$ is the product of $\boldsymbol{M}^{-1}$ and $\boldsymbol{J}^1\boldsymbol{M}$ where $\boldsymbol{J}^1\boldsymbol{M}$ is given by:

$$\boldsymbol{J}^1\boldsymbol{M} = \begin{pmatrix} u & \rho & 0 & 0 & 0 & 0 & \cdots & 0 \\ u^2 & 2\rho u & 0 & 0 & 1 & 0 & \cdots & 0 \\ uv & \rho v & \rho u & 0 & 0 & 0 & \cdots & 0 \\ uw & \rho w & 0 & \rho u & 0 & 0 & \cdots & 0 \\ ue_c - \frac{u}{\beta}\Pi & \rho h_t + \rho u^2 & \rho uv & \rho uw & \frac{\beta+1}{\beta}u & -\rho\frac{u}{\beta}\vartheta_{\psi_1} & \cdots & -\rho\frac{u}{\beta}\vartheta_{\psi_n} \\ u\psi_1 & \rho\psi_1 & 0 & 0 & 0 & \rho u & \cdots & 0 \\ \vdots & \vdots & \vdots & \vdots & \vdots & \vdots & \ddots & \vdots \\ u\psi_n & \rho\psi_n & 0 & 0 & 0 & 0 & \cdots & \rho u \end{pmatrix}$$

Finally, the matrix $\boldsymbol{A}^1$ is given by:

$$\boldsymbol{A}^1 = \boldsymbol{M}^{-1}(\boldsymbol{J}^1\boldsymbol{M}) = \begin{pmatrix} u & \rho & 0 & 0 & 0 & 0 & \cdots & 0 \\ 0 & u & 0 & 0 & \frac{1}{\rho} & 0 & \cdots & 0 \\ 0 & 0 & u & 0 & 0 & 0 & \cdots & 0 \\ 0 & 0 & 0 & u & 0 & 0 & \cdots & 0 \\ 0 & \rho a^2 & 0 & 0 & u & 0 & \cdots & 0 \\ 0 & 0 & 0 & 0 & 0 & u & \cdots & 0 \\ \vdots & \vdots & \vdots & \vdots & \vdots & \vdots & \ddots & \vdots \\ 0 & 0 & 0 & 0 & 0 & 0 & \cdots & u \end{pmatrix} \tag{3.55}$$

Matrices $\boldsymbol{A}^2$ and $\boldsymbol{A}^3$ are identically computed:

$$\boldsymbol{A}^2 = \boldsymbol{M}^{-1}\boldsymbol{J}^2\boldsymbol{M} = \begin{pmatrix} v & 0 & \rho & 0 & 0 & 0 & \cdots & 0 \\ 0 & v & 0 & 0 & 0 & 0 & \cdots & 0 \\ 0 & 0 & v & 0 & \frac{1}{\rho} & 0 & \cdots & 0 \\ 0 & 0 & 0 & v & 0 & 0 & \cdots & 0 \\ 0 & 0 & \rho a^2 & 0 & v & 0 & \cdots & 0 \\ 0 & 0 & 0 & 0 & 0 & v & \cdots & 0 \\ \vdots & \vdots & \vdots & \vdots & \vdots & \vdots & \ddots & \vdots \\ 0 & 0 & 0 & 0 & 0 & 0 & \cdots & v \end{pmatrix} \tag{3.56}$$

$$\boldsymbol{A}^3 = \boldsymbol{M}^{-1}\boldsymbol{J}^3\boldsymbol{M} = \begin{pmatrix} w & 0 & 0 & \rho & 0 & 0 & \cdots & 0 \\ 0 & w & 0 & 0 & 0 & 0 & \cdots & 0 \\ 0 & 0 & w & 0 & 0 & 0 & \cdots & 0 \\ 0 & 0 & 0 & w & \frac{1}{\rho} & 0 & \cdots & 0 \\ 0 & 0 & 0 & \rho a^2 & w & 0 & \cdots & 0 \\ 0 & 0 & 0 & 0 & 0 & w & \cdots & 0 \\ \vdots & \vdots & \vdots & \vdots & \vdots & \vdots & \ddots & \vdots \\ 0 & 0 & 0 & 0 & 0 & 0 & \cdots & w \end{pmatrix} \tag{3.57}$$

3.5.6 Projection of non-conservative variable in normal frame of the boundary

To impose boundary conditions at surfaces of the computational domain, Eq. 3.28 is written in the frame locally orthogonal to the boundary patch. This boundary patch referential is defined by three orthonormal vectors: one normal vector $\boldsymbol{n} = (n_x, n_y, n_z)^\top$ and two transverse vectors $\boldsymbol{t_1} = (t_{1x}, t_{1y}, t_{1z})^\top$, $\boldsymbol{t_2} = (t_{2x}, t_{2y}, t_{2z})^\top$. The change of referential is a rotation transformation. $\boldsymbol{V}$ is linked to the vector of non-conservative variables in boundary face referential $\boldsymbol{V_n} = (\rho, u_n, u_{t1}, u_{t2}, P, \psi_1, .., \psi_n)^\top$ as:

$$\mathbf{V} = \mathbf{\Omega_V}\mathbf{V_n} \tag{3.58}$$

where $\boldsymbol{\Omega_V}$ is an orthogonal matrix standing for the rotation transformation:

$$\boldsymbol{\Omega_V} = \begin{pmatrix} 1 & 0 & 0 & 0 & 0 & 0 & \cdots & 0 \\ 0 & n_x & t_{1x} & t_{2x} & 0 & 0 & \cdots & 0 \\ 0 & n_y & t_{1y} & t_{2y} & 0 & 0 & \cdots & 0 \\ 0 & n_z & t_{1z} & t_{2z} & 0 & 0 & \cdots & 0 \\ 0 & 0 & 0 & 0 & 1 & 0 & \cdots & 0 \\ 0 & 0 & 0 & 0 & 0 & 1 & \cdots & 0 \\ \vdots & \vdots & \vdots & \vdots & \vdots & \vdots & \ddots & \vdots \\ 0 & 0 & 0 & 0 & 0 & 0 & \cdots & 1 \end{pmatrix} \tag{3.59}$$

As $\boldsymbol{\Omega_V}$ is orthogonal, $\boldsymbol{\Omega_V^{-1}} = \boldsymbol{\Omega_V^{\top}}$:

$$\boldsymbol{\Omega_V^{-1}} = \begin{pmatrix} 1 & 0 & 0 & 0 & 0 & 0 & \cdots & 0 \\ 0 & n_x & n_y & n_z & 0 & 0 & \cdots & 0 \\ 0 & t_{1x} & t_{1y} & t_{1z} & 0 & 0 & \cdots & 0 \\ 0 & t_{2x} & t_{2y} & t_{2z} & 0 & 0 & \cdots & 0 \\ 0 & 0 & 0 & 0 & 1 & 0 & \cdots & 0 \\ 0 & 0 & 0 & 0 & 0 & 1 & \cdots & 0 \\ \vdots & \vdots & \vdots & \vdots & \vdots & \vdots & \ddots & \vdots \\ 0 & 0 & 0 & 0 & 0 & 0 & \cdots & 1 \end{pmatrix} \tag{3.60}$$

Introducing Eq. 3.58 in non-conservative variable PDE (Eq. 3.28) gives:

$$\boldsymbol{\Omega_V}\frac{\partial \boldsymbol{V_n}}{\partial t} + \boldsymbol{A}^j\boldsymbol{\Omega_V}\frac{\partial \boldsymbol{V_n}}{\partial x_j} = \mathrm{RHS}_1$$

which is written as:

$$\frac{\partial \boldsymbol{V_n}}{\partial t} + \boldsymbol{\Omega_V^{-1}}\boldsymbol{A}^j\boldsymbol{\Omega_V}\frac{\partial \boldsymbol{V_n}}{\partial x_j} = \mathrm{RHS}_2 \tag{3.61}$$

where $\mathrm{RHS}_2 = \boldsymbol{\Omega_V^{-1}}\mathrm{RHS}_1$. The coordinates referential (x, y, z) is replaced by coordinates (x_n, x_{t1}, x_{t2}) along the vectors $(\boldsymbol{n}, \boldsymbol{t_1}, \boldsymbol{t_2})$. Hence, coordinates partial derivatives are written as:

$$\begin{aligned} \frac{\partial}{\partial x} &= n_x\frac{\partial}{\partial x_n} + t_{1x}\frac{\partial}{\partial x_{t1}} + t_{2x}\frac{\partial}{\partial x_{t2}} \\ \frac{\partial}{\partial y} &= n_y\frac{\partial}{\partial x_n} + t_{1y}\frac{\partial}{\partial x_{t1}} + t_{2y}\frac{\partial}{\partial x_{t2}} \\ \frac{\partial}{\partial z} &= n_z\frac{\partial}{\partial x_n} + t_{1z}\frac{\partial}{\partial x_{t1}} + t_{2z}\frac{\partial}{\partial x_{t2}} \end{aligned}$$

Eq. 3.61 is therefore written as:

$$\begin{aligned} \frac{\partial \boldsymbol{V_n}}{\partial t} + \boldsymbol{\Omega_V^{-1}}\boldsymbol{A}_n\boldsymbol{\Omega_V}\frac{\partial \boldsymbol{V_n}}{\partial x_n} \quad & + \boldsymbol{\Omega_V^{-1}}\boldsymbol{A}_{t1}\boldsymbol{\Omega_V}\frac{\partial \boldsymbol{V_n}}{\partial x_{t1}} \\ & + \boldsymbol{\Omega_V^{-1}}\boldsymbol{A}_{t2}\boldsymbol{\Omega_V}\frac{\partial \boldsymbol{V_n}}{\partial x_{t2}} \quad = \mathrm{RHS}_2 \end{aligned} \tag{3.62}$$

where

$$\begin{aligned}\boldsymbol{A}_n &= n_x\boldsymbol{A}^1 + n_y\boldsymbol{A}^2 + n_z\boldsymbol{A}^3\\ \boldsymbol{A}_{t1} &= t_{1x}\boldsymbol{A}^1 + t_{1y}\boldsymbol{A}^2 + t_{1z}\boldsymbol{A}^3\\ \boldsymbol{A}_{t2} &= t_{2x}\boldsymbol{A}^1 + t_{2y}\boldsymbol{A}^2 + t_{2z}\boldsymbol{A}^3\end{aligned}$$

After computation using the relation $u_n = un_x + vn_y + wn_z$,

$$\boldsymbol{A}_n = \begin{pmatrix} u_n & \rho n_x & \rho n_y & \rho n_z & 0 & 0 & \cdots & 0\\ 0 & u_n & 0 & 0 & \frac{n_x}{\rho} & 0 & \cdots & 0\\ 0 & 0 & u_n & 0 & \frac{n_y}{\rho} & 0 & \cdots & 0\\ 0 & 0 & 0 & u_n & \frac{n_z}{\rho} & 0 & \cdots & 0\\ 0 & \rho a^2 n_x & \rho a^2 n_y & \rho a^2 n_z & u_n & 0 & \cdots & 0\\ 0 & 0 & 0 & 0 & 0 & u_n & \cdots & 0\\ \vdots & \vdots & \vdots & \vdots & \vdots & \vdots & \ddots & \vdots\\ 0 & 0 & 0 & 0 & 0 & 0 & \cdots & u_n \end{pmatrix} \tag{3.63}$$

Keeping only the normal contribution on the left hand side, Eq. 3.62 reads:

$$\frac{\partial \boldsymbol{V_n}}{\partial t} + \boldsymbol{N}\frac{\partial \boldsymbol{V_n}}{\partial x_n} = \mathrm{RHS}_3 \tag{3.64}$$

where $\boldsymbol{N} = \boldsymbol{\Omega_V^{-1}}\boldsymbol{A}_n\boldsymbol{\Omega_V}$ and $\mathrm{RHS}_3 = \mathrm{RHS}_2 - \boldsymbol{\Omega_V^{-1}}\boldsymbol{A}_{t1}\boldsymbol{\Omega_V}\frac{\partial \boldsymbol{V_n}}{\partial x_{t1}} - \boldsymbol{\Omega_V^{-1}}\boldsymbol{A}_{t2}\boldsymbol{\Omega_V}\frac{\partial \boldsymbol{V_n}}{\partial x_{t2}}$ gathers transverse, diffusive and source terms contributions. The matrix $\boldsymbol{N}$ is given as:

$$\boldsymbol{N} = \boldsymbol{\Omega_V^{-1}}(\boldsymbol{A}_n\boldsymbol{\Omega_V})$$

As the vectors $\boldsymbol{n}$, $\boldsymbol{t_1}$ and $\boldsymbol{t_2}$ are orthogonal, it comes:

$$\boldsymbol{N} = \boldsymbol{\Omega_V^{-1}} \begin{pmatrix} u_n & \rho & 0 & 0 & 0 & 0 & \cdots & 0\\ 0 & n_x u_n & t_{1x}u_n & t_{2x}u_n & \frac{n_x}{\rho} & 0 & \cdots & 0\\ 0 & n_y u_n & t_{1y}u_n & t_{2y}u_n & \frac{n_y}{\rho} & 0 & \cdots & 0\\ 0 & n_z u_n & t_{1z}u_n & t_{2z}u_n & \frac{n_z}{\rho} & 0 & \cdots & 0\\ 0 & \rho a^2 & 0 & 0 & u_n & 0 & \cdots & 0\\ 0 & 0 & 0 & 0 & 0 & u_n & \cdots & 0\\ \vdots & \vdots & \vdots & \vdots & \vdots & \vdots & \ddots & \vdots\\ 0 & 0 & 0 & 0 & 0 & 0 & \cdots & u_n \end{pmatrix}$$

$$\boldsymbol{N} = \begin{pmatrix} u_n & \rho & 0 & 0 & 0 & 0 & \cdots & 0\\ 0 & u_n & 0 & 0 & \frac{1}{\rho} & 0 & \cdots & 0\\ 0 & 0 & u_n & 0 & 0 & 0 & \cdots & 0\\ 0 & 0 & 0 & u_n & 0 & 0 & \cdots & 0\\ 0 & \rho a^2 & 0 & 0 & u_n & 0 & \cdots & 0\\ 0 & 0 & 0 & 0 & 0 & u_n & \cdots & 0\\ \vdots & \vdots & \vdots & \vdots & \vdots & \vdots & \ddots & \vdots\\ 0 & 0 & 0 & 0 & 0 & 0 & \cdots & u_n \end{pmatrix} \tag{3.65}$$

3.5.7 Characteristic wave decomposition

Matrix $\boldsymbol{N}$ has $5+n$ eigenvalues λ^m which are given with an example of right eigenvectors r_m:

$$\begin{aligned}
\lambda^1 = u_n \quad &, \quad r_1 = (1,0,0,0,0,0,...,0)^\top \\
\lambda^2 = u_n + a \quad &, \quad r_2 = (\frac{\rho}{2a}, \frac{1}{2}, 0, 0, \frac{\rho a}{2}, 0, ..., 0)^\top \\
\lambda^3 = u_n - a \quad &, \quad r_3 = (\frac{\rho}{2a}, -\frac{1}{2}, 0, 0, \frac{\rho a}{2}, 0, ..., 0)^\top \\
\lambda^4 = u_n \quad &, \quad r_4 = (0,0,1,0,0,0,...,0)^\top \\
\lambda^5 = u_n \quad &, \quad r_5 = (0,0,0,1,0,0,...,0)^\top \\
\lambda^6 = u_n \quad &, \quad r_6 = (0,0,0,0,0,1,...,0)^\top \\
&... \\
\lambda^{5+n} = u_n \quad &, \quad r_{5+n} = (0,0,0,0,0,0,...,1)^\top
\end{aligned}$$

Each right eigenvector r_m verifies

$$\boldsymbol{N} r_m = \lambda^m r_m \tag{3.66}$$

Right eigenvectors are gathers in the transformation matrix $\boldsymbol{R}$ in columns:

$$\boldsymbol{R} = \begin{pmatrix}
1 & \frac{\rho}{2a} & \frac{\rho}{2a} & 0 & 0 & 0 & \cdots & 0 \\
0 & \frac{1}{2} & -\frac{1}{2} & 0 & 0 & 0 & \cdots & 0 \\
0 & 0 & 0 & 1 & 0 & 0 & \cdots & 0 \\
0 & 0 & 0 & 0 & 1 & 0 & \cdots & 0 \\
0 & \frac{\rho a}{2} & \frac{\rho a}{2} & 0 & 0 & 0 & \cdots & 0 \\
0 & 0 & 0 & 0 & 0 & 1 & \cdots & 0 \\
\vdots & \vdots & \vdots & \vdots & \vdots & \vdots & \ddots & \vdots \\
0 & 0 & 0 & 0 & 0 & 0 & \cdots & 1
\end{pmatrix} \tag{3.67}$$

Inverting $\boldsymbol{R}$ gives the matrix $\boldsymbol{L}$ whose lines are the left eigenvectors l_m:

$$\boldsymbol{L} = \boldsymbol{R}^{-1} = \begin{pmatrix}
1 & 0 & 0 & 0 & -\frac{1}{a^2} & 0 & \cdots & 0 \\
0 & 1 & 0 & 0 & \frac{1}{\rho a} & 0 & \cdots & 0 \\
0 & -1 & 0 & 0 & \frac{1}{\rho a} & 0 & \cdots & 0 \\
0 & 0 & 1 & 0 & 0 & 0 & \cdots & 0 \\
0 & 0 & 0 & 1 & 0 & 0 & \cdots & 0 \\
0 & 0 & 0 & 0 & 0 & 1 & \cdots & 0 \\
\vdots & \vdots & \vdots & \vdots & \vdots & \vdots & \ddots & \vdots \\
0 & 0 & 0 & 0 & 0 & 0 & \cdots & 1
\end{pmatrix} \tag{3.68}$$

The left eigenvectors l_m are then:

$$\begin{aligned}
l_1 &= (1,0,0,0,-\frac{1}{a^2},0,\cdots,0)\\
l_2 &= (0,1,0,0,\frac{1}{\rho a},0,\cdots,0)\\
l_3 &= (0,-1,0,0,\frac{1}{\rho a},0,\cdots,0)\\
l_4 &= (0,0,1,0,0,0,\cdots,0)\\
l_5 &= (0,0,0,1,0,0,\cdots,0)\\
l_6 &= (0,0,0,0,0,1,\cdots,0)\\
&\ldots\\
l_{5+n} &= (0,0,0,0,0,0,\cdots,1)
\end{aligned}$$

The matrix $\boldsymbol{N}$ can be written as:

$$\boldsymbol{N} = \boldsymbol{R}\boldsymbol{\Lambda}\boldsymbol{L} \tag{3.69}$$

where $\boldsymbol{\Lambda}$ is the diagonal matrix composed of the eigenvalues λ^m:

$$\boldsymbol{\Lambda} = \begin{pmatrix}
u_n & & & & & & & \\
 & u_n + a & & & 0 & & & \\
 & & u_n - a & & & & & \\
 & & & u_n & & & & \\
 & & & & u_n & & & \\
 & & 0 & & & u_n & & \\
 & & & & & & \ddots & \\
 & & & & & & & u_n
\end{pmatrix} \tag{3.70}$$

Introducing the eigenvectors decomposition of $\boldsymbol{N}$, Eq. 3.64 is written as:

$$\frac{\partial \boldsymbol{V_n}}{\partial t} + \boldsymbol{R}\boldsymbol{\Lambda}\boldsymbol{L}\frac{\partial \boldsymbol{V_n}}{\partial x_n} = \mathrm{RHS}_3 \tag{3.71}$$

Variations of characteristic variables $\partial \boldsymbol{W}$ are defined as:

$$\partial \boldsymbol{W} = \boldsymbol{L}\partial \boldsymbol{V_n} \tag{3.72}$$

Hence, with $\boldsymbol{L} = \boldsymbol{R}^{-1}$, Eq. 3.71 is written for characteristic variables:

$$\frac{\partial \boldsymbol{W}}{\partial t} + \boldsymbol{\Lambda}\frac{\partial \boldsymbol{W}}{\partial x_n} = \mathrm{RHS}_4 \tag{3.73}$$

where $\mathrm{RHS}_4 = \boldsymbol{L}\mathrm{RHS}_3$. Amplitude time variations of characteristic waves are introduced in the vector $\mathscr{L}$ defined as (Thompson, 1987)

$$\mathscr{L} = \boldsymbol{\Lambda}\frac{\partial \boldsymbol{W}}{\partial x_n} = \boldsymbol{\Lambda}\boldsymbol{L}\frac{\partial \boldsymbol{V_n}}{\partial x_n} \tag{3.74}$$

and Eq. 3.73 is then written as:

$$\frac{\partial \boldsymbol{W}}{\partial t} + \mathscr{L} = \mathrm{RHS}_4 \tag{3.75}$$

with

$$\mathscr{L} = \begin{pmatrix} \lambda^1 \left(\frac{\partial \rho}{\partial x_n} - \frac{1}{a^2} \frac{\partial P}{\partial x_n} \right) \\ \lambda^2 \left(\frac{\partial u_n}{\partial x_n} + \frac{1}{\rho a} \frac{\partial P}{\partial x_n} \right) \\ \lambda^3 \left(-\frac{\partial u_n}{\partial x_n} + \frac{1}{\rho a} \frac{\partial P}{\partial x_n} \right) \\ \lambda^4 \frac{\partial u_{t1}}{\partial x_n} \\ \lambda^5 \frac{\partial u_{t2}}{\partial x_n} \\ \lambda^6 \frac{\partial \psi_1}{\partial x_n} \\ \ldots \\ \lambda^{5+n} \frac{\partial \psi_n}{\partial x_n} \end{pmatrix} \tag{3.76}$$

Finally, PDE of non-conservative and conservative variables are expressed using the characteristic wave amplitude variations:

- **Non-conservative variables in normal frame**

$$\frac{\partial \boldsymbol{V_n}}{\partial t} + \boldsymbol{R}\mathscr{L} = \mathrm{RHS}_3 \tag{3.77}$$

- **Non-conservative variables**

$$\frac{\partial \boldsymbol{V}}{\partial t} + \boldsymbol{\Omega_V R}\mathscr{L} + \boldsymbol{A}_{t1} \frac{\partial \boldsymbol{V}}{\partial x_{t1}} + \boldsymbol{A}_{t2} \frac{\partial \boldsymbol{V}}{\partial x_{t2}} = \mathrm{RHS}_2 \tag{3.78}$$

- **Conservative variables**

$$\frac{\partial \boldsymbol{U}}{\partial t} + \boldsymbol{R_U}\mathscr{L} + \frac{\partial \boldsymbol{F}^{t1}}{\partial x_{t1}} + \frac{\partial \boldsymbol{F}^{t2}}{\partial x_{t2}} + \frac{\partial \boldsymbol{F}_d^j}{\partial x_j} = \boldsymbol{S} \tag{3.79}$$

where $\boldsymbol{R_U} = \boldsymbol{M\Omega_V R}$ and $\boldsymbol{F}^{t1}$, $\boldsymbol{F}^{t2}$ are the Eulerian fluxes in tangential directions. Relations between characteristic waves and conservative variables are summarized in Tab. 3.1. Intermediate transformations have been introduced: from conservative to non-conservative variables, then to non-conservative variables in the referential normal to the boundary patch and finally to characteristic form. Global transformation matrices are therefore combined from other matrices:

$$\boldsymbol{L_U} = \boldsymbol{L\Omega_V^{-1} M^{-1}} \tag{3.80}$$

$$\boldsymbol{R_U} = \boldsymbol{M\Omega_V R} \tag{3.81}$$

The following sections give intermediate matrices then global transformation matrices, $\boldsymbol{L_U}$ and $\boldsymbol{R_U}$.

Conservative		Non-conservative		Non-conservative in normal frame		Characteristic
$\partial \boldsymbol{U}$		$\partial \boldsymbol{V}$		$\partial \boldsymbol{V_n}$		$\partial \boldsymbol{W}$
$\begin{pmatrix} \partial\rho \\ \partial(\rho u) \\ \partial(\rho v) \\ \partial(\rho w) \\ \partial(\rho e_t) \\ \partial(\rho\psi_1) \\ \vdots \\ \partial(\rho\psi_n) \end{pmatrix}$	$\boldsymbol{M}^{-1}$ $\rightarrow$ $\leftarrow$ $\boldsymbol{M}$	$\begin{pmatrix} \partial\rho \\ \partial u \\ \partial v \\ \partial w \\ \partial P \\ \partial\psi_1 \\ \vdots \\ \partial\psi_n \end{pmatrix}$	$\boldsymbol{\Omega_V^{-1}}$ $\rightarrow$ $\leftarrow$ $\boldsymbol{\Omega_V}$	$\begin{pmatrix} \partial\rho \\ \partial u_n \\ \partial u_{t1} \\ \partial u_{t2} \\ \partial P \\ \partial\psi_1 \\ \vdots \\ \partial\psi_n \end{pmatrix}$	$\boldsymbol{L}$ $\rightarrow$ $\leftarrow$ $\boldsymbol{R}$	$\begin{pmatrix} \partial\rho - \frac{\partial P}{a^2} \\ \partial u_n + \frac{\partial P}{\rho a} \\ -\partial u_n + \frac{\partial P}{\rho a} \\ \partial u_{t1} \\ \partial u_{t2} \\ \partial\psi_1 \\ \vdots \\ \partial\psi_n \end{pmatrix}$
		$\boldsymbol{L_U}$ $\rightarrow$				
		$\leftarrow$ $\boldsymbol{R_U}$				

Table 3.1: *Wave decomposition from conservative to characteristic variables and transformation matrices.*

Intermediate matrices

$$\boldsymbol{L_V} = \boldsymbol{L\Omega_V^{-1}} = \begin{pmatrix} 1 & 0 & 0 & 0 & -\frac{1}{a^2} & 0 & \cdots & 0 \\ 0 & n_x & n_y & n_z & \frac{1}{\rho a} & 0 & \cdots & 0 \\ 0 & -n_x & -n_y & -n_z & \frac{1}{\rho a} & 0 & \cdots & 0 \\ 0 & t_{1x} & t_{1y} & t_{1z} & 0 & 0 & \cdots & 0 \\ 0 & t_{2x} & t_{2y} & t_{2z} & 0 & 0 & \cdots & 0 \\ 0 & 0 & 0 & 0 & 0 & 1 & \cdots & 0 \\ \vdots & \vdots & \vdots & \vdots & \vdots & \vdots & \ddots & \vdots \\ 0 & 0 & 0 & 0 & 0 & 0 & \cdots & 1 \end{pmatrix}$$

$$\boldsymbol{R_V} = \boldsymbol{\Omega_V R} = \begin{pmatrix} 1 & \frac{\rho}{2a} & \frac{\rho}{2a} & 0 & 0 & 0 & \cdots & 0 \\ 0 & \frac{n_x}{2} & -\frac{n_x}{2} & t_{1x} & t_{2x} & 0 & \cdots & 0 \\ 0 & \frac{n_y}{2} & -\frac{n_y}{2} & t_{1y} & t_{2y} & 0 & \cdots & 0 \\ 0 & \frac{n_z}{2} & -\frac{n_z}{2} & t_{1z} & t_{2z} & 0 & \cdots & 0 \\ 0 & \frac{\rho a}{2} & \frac{\rho a}{2} & 0 & 0 & 0 & \cdots & 0 \\ 0 & 0 & 0 & 0 & 0 & 1 & \cdots & 0 \\ \vdots & \vdots & \vdots & \vdots & \vdots & \vdots & \ddots & \vdots \\ 0 & 0 & 0 & 0 & 0 & 0 & \cdots & 1 \end{pmatrix}$$

Global transformation matrice $\boldsymbol{L_U}$

$$\boldsymbol{L_U} = \boldsymbol{L_V}\boldsymbol{M}^{-1}$$

$$\boldsymbol{L_U} = \begin{pmatrix} 1-\frac{1}{a^2}\left(\beta e_c+\Pi-\sum_l \psi_l\vartheta_{\psi_l}\right) & \frac{\beta u}{a^2} & \frac{\beta v}{a^2} & \frac{\beta w}{a^2} & -\frac{\beta}{a^2} & -\frac{\vartheta_{\psi_1}}{a^2} & \cdots & -\frac{\vartheta_{\psi_n}}{a^2} \\ -\frac{u_n}{\rho}+\frac{1}{\rho a}\left(\beta e_c+\Pi-\sum_l \psi_l\vartheta_{\psi_l}\right) & \frac{an_x-\beta u}{\rho a} & \frac{an_y-\beta v}{\rho a} & \frac{an_z-\beta w}{\rho a} & \frac{\beta}{\rho a} & \frac{\vartheta_{\psi_1}}{\rho a} & \cdots & \frac{\vartheta_{\psi_n}}{\rho a} \\ \frac{u_n}{\rho}+\frac{1}{\rho a}\left(\beta e_c+\Pi-\sum_l \psi_l\vartheta_{\psi_l}\right) & \frac{-an_x-\beta u}{\rho a} & \frac{-an_y-\beta v}{\rho a} & \frac{-an_z-\beta w}{\rho a} & \frac{\beta}{\rho a} & \frac{\vartheta_{\psi_1}}{\rho a} & \cdots & \frac{\vartheta_{\psi_n}}{\rho a} \\ -\frac{u_{t1}}{\rho} & \frac{t_{1x}}{\rho} & \frac{t_{1y}}{\rho} & \frac{t_{1z}}{\rho} & 0 & 0 & \cdots & 0 \\ -\frac{u_{t2}}{\rho} & \frac{t_{2x}}{\rho} & \frac{t_{2y}}{\rho} & \frac{t_{2z}}{\rho} & 0 & 0 & \cdots & 0 \\ -\frac{\psi_1}{\rho} & 0 & 0 & 0 & 0 & \frac{1}{\rho} & \cdots & 0 \\ \vdots & \vdots & \vdots & \vdots & \vdots & \vdots & \ddots & \vdots \\ -\frac{\psi_n}{\rho} & 0 & 0 & 0 & 0 & 0 & \cdots & \frac{1}{\rho} \end{pmatrix} \tag{3.82}$$

where the three velocity components in the boundary referential are computed as:

$$\begin{aligned} u_n &= un_x+vn_y+wn_z \\ u_{t1} &= ut_{1x}+vt_{1y}+wt_{1z} \\ u_{t2} &= ut_{2x}+vt_{2y}+wt_{2z} \end{aligned}$$

Global transformation matrice $\boldsymbol{R_U}$

$$\boldsymbol{R_U} = \boldsymbol{M}\boldsymbol{R_V}$$

$$\boldsymbol{R_U} = \begin{pmatrix} 1 & \frac{\rho}{2a} & \frac{\rho}{2a} & 0 & 0 & 0 & \cdots & 0 \\ u & \frac{\rho}{2a}(u+an_x) & \frac{\rho}{2a}(u-an_x) & \rho t_{1x} & \rho t_{2x} & 0 & \cdots & 0 \\ v & \frac{\rho}{2a}(v+an_y) & \frac{\rho}{2a}(v-an_y) & \rho t_{1y} & \rho t_{2y} & 0 & \cdots & 0 \\ w & \frac{\rho}{2a}(w+an_z) & \frac{\rho}{2a}(w-an_z) & \rho t_{1z} & \rho t_{2z} & 0 & \cdots & 0 \\ e_c - \frac{\Pi}{\beta} & \frac{\rho}{2a}(\alpha+au_n) & \frac{\rho}{2a}(\alpha-au_n) & -\rho u_{t1} & -\rho u_{t2} & -\frac{\rho}{\beta}\vartheta_{\psi_1} & \cdots & -\frac{\rho}{\beta}\vartheta_{\psi_n} \\ \psi_1 & \frac{\rho\psi_1}{2a} & \frac{\rho\psi_1}{2a} & 0 & 0 & \rho & \cdots & 0 \\ \vdots & \vdots & \vdots & \vdots & \vdots & \vdots & \ddots & \vdots \\ \psi_n & \frac{\rho\psi_n}{2a} & \frac{\rho\psi_n}{2a} & 0 & 0 & 0 & \cdots & \rho \end{pmatrix} \tag{3.83}$$

where

$$\alpha = e_c + \frac{a^2 - \Pi}{\beta}$$

3.5.8 NSCBC treatment

In the case of Local One Dimensional Inviscid (LODI) approximation, source terms, tangential and diffusive fluxes are neglected in Eq. 3.77, 3.78, 3.79. In such a case, the time variation of any quantity can be expressed in terms of $\mathscr{L}_m$:

$$\frac{\partial \rho}{\partial t} + \left[\mathscr{L}_1 + \frac{\rho}{2a}(\mathscr{L}_2 + \mathscr{L}_3)\right] = 0 \tag{3.84}$$

$$\frac{\partial u_n}{\partial t} + \frac{1}{2}(\mathscr{L}_2 - \mathscr{L}_3) = 0 \tag{3.85}$$

$$\frac{\partial u_{t1}}{\partial t} + \mathscr{L}_4 = 0 \tag{3.86}$$

$$\frac{\partial u_{t2}}{\partial t} + \mathscr{L}_5 = 0 \tag{3.87}$$

$$\frac{\partial P}{\partial t} + \frac{\rho a}{2}(\mathscr{L}_2 + \mathscr{L}_3) = 0 \tag{3.88}$$

$$\frac{\partial \psi_l}{\partial t} + \mathscr{L}_{5+l} = 0 \tag{3.89}$$

$$...$$

At a boundary interface, some waves enter the computational while other are leaving it. Outgoing waves can be computed inside the domain and ingoing waves that are unknown must be prescribed. NSCBC treatment consists in specifying entering characteristic waves from other known waves and time variation of relevant variables. The treatment depends on the kind of boundary conditions (Poinsot and Veynante, 2005). Once all $\mathscr{L}_m$ are known, boundary conditions can be applied to conservative variables $\boldsymbol{U}$ (Eq. 3.79).

NSCBC was first written for one-component flow (Poinsot and Lele, 1992) then extended to multi-component systems (Baum et al., 1995). There are several techniques to set wave amplitudes $\mathscr{L}_m$ depending on the boundary condition and the level of accuracy. LODI provides simple relations but can lead to errors when the flow is strongly three-dimensional. In this case, Lodato et al. (2008) have established three-dimensional boundary conditions. In comparison to NSCBC treatment for multi-component description, tabulated chemistry does not change the way to impose waves amplitudes. Indeed, the method to specify species characteristic waves is similarly applied to the ψ_l variables. Let's consider for instance species characteristic waves $\mathscr{L}'_{5+k} = \lambda^{5+k}\frac{\partial Y_k}{\partial x_n}$ chosen so that species mass fraction Y_k would relax to a target composition Y_k^t at an inflow boundary:

$$\mathscr{L}'_{5+k} = K(Y_k - Y_k^t) \tag{3.90}$$

where the relaxation factor K controls the time to reach Y_k^t. In tabulated chemistry, ψ_l characteristic waves are then similarly chosen as:

$$\mathscr{L}_{5+l} = K(\psi_l - \psi_l^t) \tag{3.91}$$

The major modification introduced by TTC formalism in boundary conditions treatment are the transformation matrices that have been rewritten to take into account variation of energy due to a composition change.

3.5.9 Tabulation of ϑ_{ψ_l}

Transformation matrices show new factors ϑ_{ψ_l} that need to be computed at the boundary but cannot be directly tabulated since they depend on temperature and energy which are sensitive to compressible effects:

$$\vartheta_{\psi_l} = \sum_{k=1}^{N} \left(\frac{RT}{W_k} - \beta e_k \right) \frac{\partial Y_k}{\partial \psi_l}$$

As done for temperature in Eq. 3.17, ϑ_{ψ_l} is compared to its tabulated value:

$$\begin{aligned} \vartheta_{\psi_l} - \vartheta_{\psi_l}^{tab}(\psi_1, ..., \psi_n) &= \sum_{k=1}^{N} \left(\frac{RT}{W_k} - \beta e_{sk} \right) \frac{\partial Y_k}{\partial \psi_l} \\ &\quad - \sum_{k=1}^{N} \left(\frac{RT}{W_k} T^{tab} - \beta^{tab} e_{sk}^{tab} \right) \frac{\partial Y_k}{\partial \psi_l}^{tab} \end{aligned}$$

Composition is assumed given by the database:

$$\begin{aligned} \beta &= \beta^{tab}(\psi_1, ..., \psi_n) \\ \frac{\partial Y_k}{\partial \psi_l} &= \frac{\partial Y_k}{\partial \psi_l}^{tab}(\psi_1, ..., \psi_n) \end{aligned}$$

Therefore, the difference $\Delta\vartheta_{\psi_l} = \vartheta_{\psi_l} - \vartheta_{\psi_l}^{tab}(\psi_1, ..., \psi_n)$ is:

$$\begin{aligned} \Delta\vartheta_{\psi_l} &= \sum_{k=1}^{N} \left[\frac{R}{W_k}(T - T^{tab}) - \beta^{tab}(e_{sk} - e_{sk}^{tab}) \right] \frac{\partial Y_k}{\partial \psi_l}^{tab} \\ &= \sum_{k=1}^{N} \left[\frac{R}{W_k}(T - T^{tab}) - \beta^{tab} \int_{T^{tab}}^{T} C_{vk}(T) \mathrm{d}T \right] \frac{\partial Y_k}{\partial \psi_l}^{tab} \end{aligned} \quad (3.92)$$

As done in section 3.4, if $C_{vk}(T)$ is assumed constant on the interval $[T^{tab}, T]$, Eq. 3.92 becomes:

$$\Delta\vartheta_{\psi_l} = \sum_{k=1}^{N} \left[\frac{R}{W_k}(T - T^{tab}) - \beta^{tab} C_{vk}^{tab}(T - T^{tab}) \right] \frac{\partial Y_k}{\partial \psi_l}^{tab}$$

or

$$\Delta\vartheta_{\psi_l} = \sigma_{\psi_l}^{tab}(\psi_1, ..., \psi_n)(T - T^{tab}) \quad (3.93)$$

where

$$\sigma^{tab}_{\psi_l}(\psi_1, ..., \psi_n) = \sum_{k=1}^{N} \left(\frac{R}{W_k} - \beta C_{vk} \right) \frac{\partial Y_k}{\partial \psi_l} \tag{3.94}$$

is stored as a function of $(\psi_1, ..., \psi_n)$. Consequently, in order to introduce compressible effects in the simulation, variables ϑ_{ψ_l} are computed from the stored quantities $\vartheta^{tab}_{\psi_l}$ and $\sigma^{tab}_{\psi_l}$ as:

$$\vartheta_{\psi_l} = \vartheta^{tab}_{\psi_l}(\psi_1, ..., \psi_n) + \sigma^{tab}_{\psi_l}(\psi_1, ..., \psi_n) \left[T - T^{tab}(\psi_1, ..., \psi_n) \right] \tag{3.95}$$

3.6 Implementation of TTC formalism in the AVBP code

The TTC formalism which allows to couple tabulated chemistry with compressible CFD solvers is implemented in the unstructured explicit solver AVBP (Moureau et al., 2005). The code AVBP solves compressible Navier-Stokes equations for multi-component mixture using the ideal gas law. The code was modified to compute the temperature using Eq. 3.17 and NSCBC treatment for tabulated chemistry was enhanced by adding characteristic boundary conditions for ψ_l variables and changing the already implemented transformation matrices $\boldsymbol{L_U}$ and $\boldsymbol{R_U}$. To compare AVBP computations to tabulated chemistry formulation, the choice of reference temperature is discussed. Then, differences with the initial multi-component formulation are listed.

3.6.1 Temperature reference in thermodynamics

The AVBP code thermodynamics is defined for a reference temperature $T_0 = 0$ K. Species molar sensible enthalpies, h^m_{sk}, are tabulated from 0 to 5000 K every 100 K to match the JANAF database (Stull and Prophet, 1971) for each transported species. However, tabulated chemistry models such as flamelets are often based on the CHEMKIN package thermodynamics (Kee et al., 1985b) whose reference temperature is 298 K. In CHEMKIN's thermodynamics, molar heat capacities C^m_{pk} are approximated by polynomials and h^m_{sk} are computed by integration of these polynomials adding an integration constant to provide species formation enthalpies. In order to couple the compressible solver with tabulated chemistry, two choices are then possible:

- Change AVBP reference temperature to $T_0 = 298K$. Thermo-chemistry tabulation is read straightforwardly from CHEMKIN.
- Keep AVBP reference temperature $T_0 = 0K$. Thermo-chemistry is first read from CHEMKIN but must be modified before generating the database.

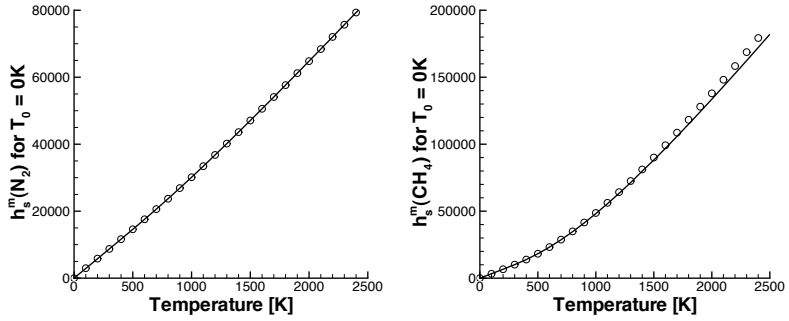

(a) (b)

Figure 3.1: *Molar sensible enthalpy for a reference temperature of 0K plotted for nitrogen (a) and methane (b). Line: tabulated enthalpy given in the code AVBP. Symbols: CHEMKIN enthalpy computed from Eq. 3.96.*

In the second case, conversion from sensible enthalpies to different reference temperature is done as follows:

$$h_{sk}^{AVBP}(T) = h_{sk}^{CK}(T) - h_{sk}^{CK}(T = 0K) \tag{3.96}$$

where h_{sk}^{AVBP} stands for species sensible enthalpy (mass or molar) at AVBP reference temperature of 0 K and h_{sk}^{CK} for CHEMKIN reference temperature of 298 K. Figure 3.1 shows that sensible enthalpies are well reproduced.
Formation enthalpies are also dependent on the reference temperature. Given the reference point, it is defined as the enthalpy released by formation of species k from its elements in their stable state at the reference temperature. To link AVBP formation enthalpies, $\Delta h_{f,k}^{0,AVBP}$, to CHEMKIN ones, $\Delta h_{f,k}^{0,CK}$, four transformations are considered. The formation of species k at $T = 0K$ (transformation A) is considered in three steps:

- Transformation B: heating of elements to their stable states at $T = 298K$.
- Transformation C: formation of species k at $T = 298K$.
- Transformation D: cooling of species k at $T = 0K$.

$\Delta h_{f,k}^{0,AVBP}$ can be computed as the sum of enthalpies released by transformations B, C and D:

$$\begin{array}{ccc} \text{Elements at } 0K & \xrightarrow[A]{\Delta h_{f,k}^{0,AVBP}} & \text{Species } k \text{ at } 0K \\ \sum_{elements} \Delta h_{elt}|_0^{298K} \Big\downarrow B & & D \Big\uparrow -\Delta h_k|_0^{298K} \\ \text{Elements at } 298K & \xrightarrow[\Delta h_{f,k}^{0,CK}]{C} & \text{Species } k \text{ at } 298K \end{array}$$

This requires the knowledge of enthalpy variation from $T = 298$ K down to $T = 0$ K for species and elements, however polynomials used to describe CHEMKIN thermodynamics are not valid down to 0 K. AVBP formation enthalpies can therefore not be computed from CHEMKIN ones precisely. A solution could be to provide these quantities to CHEMKIN. However, the first solution, changing AVBP reference temperature to $T_0 = 298$ K, is retained instead for its simplicity of implementation.

3.6.2 Differences introduced by tabulated chemistry

Implantation of the TTC formalism in the CFD code AVBP modifies some key steps in the simulation process. Major modifications are synthesized in Tab. 3.2.

3.7 TTC formalism: validation tests

3.7.1 Tests description

The present method to introduce tabulated chemistry into a compressible CFD solver is validated. For that purpose, the temperature computation and characteristic boundary condition reformulations presented in sections 3.4 and 3.5 are tested. First, correct implementation of ψ_l balance equations is verified by performing one-dimensional convection and diffusion simulations. Then, the temperature computation method is validated in the case of an acoustic wave traveling a gas mixture at rest. The NSCBC terms evaluation is validated by sending acoustic and entropic waves through boundaries. Finally, a turbulent jet and a laminar premixed flame are simulated to illustrate the model performances. Two simulations are performed for each test case. The first one uses multi-component transport formulation for species present in the mixture (reference simulation), while the other one uses the TTC formalism. All simulations are done with the compressible CFD solver AVBP (Moureau et al., 2005) using a third-order numerical scheme (Colin and Rudgyard, 2000).
Simple molecular transport is retained in multi-component simulation by considering Fick law with unity Lewis number:

$$V_{k,i}Y_k = -D\frac{\partial Y_k}{\partial x_i} \quad \text{with} \quad D = \frac{\lambda}{\rho C_p} \tag{3.97}$$

Species balance equation are therefore given by Eq. 1.44. In tabulated chemistry simulations, database coordinates balance equations are described by Eq. 3.2. In both descriptions, energy balance equation is simplified using simple transport description: Eq. 1.56 and 1.55 are respectively used for multi-component and tabulated formulation.

		Standard AVBP	AVBP with TTC formalism
Transport equations		ρu_i ρE $(T_0 = 0K)$ ρY_k, $k = 1, N$	ρu_i ρe_t $(T_0 = 298K)$ ρ $(Y_0 = 1)$ $\rho\psi_l$, $l = 1, n < N$
Before iterating		Read thermodynamical data: $C_{vk}(T)$, $\Delta h^0_{f,k}$, ...	Read database: $C_v^{tab}(\psi_1, ..., \psi_n)$, $T^{tab}(\psi_1, ..., \psi_n)$, ...
For each iteration	Compute mixture thermodynamics	$C_v = \sum_{k=1}^{N} C_{vk} Y_k$ $C_p = \sum_{k=1}^{N} C_{pk} Y_k$ $W = 1/\sum_{k=1}^{N} \frac{Y_k}{W_k}$	$C_v = C_v^{tab}(\psi_1, ..., \psi_n)$ $C_p = C_p^{tab}(\psi_1, ..., \psi_n)$ $W = 1/(1/W)^{tab}(\psi_1, ..., \psi_n)$
	Temperature computation	$e_s = E - \frac{u_i^2}{2}$ T is found by inversion of $e_s = \sum_{k=1}^{N} e_{sk}(T) Y_k$	$e = e_t - \frac{u_i^2}{2}$ $T = T^{tab}(\psi_1, ..., \psi_n) + \frac{e - e^{tab}(\psi_1, ..., \psi_n)}{C_v}$
	Other thermodynamical variable	$P = \rho r T$ with $r = R/W$ $a = \sqrt{\gamma r T}$ with $\gamma = C_p/C_v$	$P = \rho r T$ with $r = R \cdot (1/W)^{tab}(\psi_1, ..., \psi_n)$ $a = \sqrt{\gamma r T}$ with $\gamma = C_p^{tab}/C_v^{tab}$
	Compute chemical source terms	$\dot{\omega}_k$, $\dot{\omega}_T$	$\dot{\omega}^{tab}_{\psi_l}(\psi_1, ..., \psi_n)$
	Boundary conditions treatment	NSCBC for ρu_i, ρE, ρY_k	NSCBC for ρu_i, ρe_t, ρ, $\rho\psi_l$ Additional terms: $\vartheta^{tab}_{\psi_l}(\psi_1, ..., \psi_n)$ $\sigma^{tab}_{\psi_l}(\psi_1, ..., \psi_n)$
Post-processing		-	Extract $Y_k^{tab}(\psi_1, ..., \psi_n)$

Table 3.2: *Differences introduced by TTC formalism in comparison to a multi-component formulation.*

Database	ψ_i	Database description
A	z	Mixing between two dummy species with identical properties
B	z	Mixing between two dummy species with different properties
C	z	Mixing between a rich CH_4/air mixture and a hot vitiated air mixture
D	c	Stoichiometric CH_4/air premixed flame

Table 3.3: *Description of the different database used in the studied configurations.*

Except for the one-dimensional premixed flame case, transport properties are described with empirical laws. A constant Prandtl number (Pr = 0.75) is provided to compute the mixture thermal conductivity $\lambda = \frac{\mu Cp}{\Pr}$ where the dynamic viscosity μ is given by:

$$\mu = c_1 \left(\frac{T}{T_{ref}} \right)^b \tag{3.98}$$

with $T_{ref} = 300$ K, $c_1 = 1.788\ 10^{-5}$ kg.m^{-1}.s^{-1} and $b = 0.686$.
Non-reactive test cases are first considered. All thermo-chemical quantities are stored in a look-up table in term of a unique coordinate: $n = 1$ and $\psi_1 = z$ where z is the mixture fraction. In order to validate the implementation of the method step by step, the mixing description complexity is increased in three successive database A,B and C described in Tab. 3.3. First, mixing between two dummy species with identical properties (molar mass, heat capacities) is tested with database A before considering two dummy species with different properties in database B. Then, a more realistic case is investigated with database C where a rich methane/air mixture mixes with a hot vitiated air mixture. Although only mixing and no combustion is considered in these tests, the term "tabulated chemistry" is retained.
Finally, to demonstrate the application of the method in a reactive case, a one-dimensional premixed flame is computed with tabulated chemistry. All thermo-chemical quantities are then stored in the look-up table D in term of a unique coordinate: $n = 1$ and $\psi_1 = c$ where c is the progress variable.

3.7.2 Database A (Tab. 3.3)

Mixing is first considered between two dummy species, Y_1 and Y_2, without combustion. Species are characterized by their respective molar weight, W_1 and W_2, and heat capacities at constant pressure, C_{p_1} and C_{p_2}, which are assumed independent of temperature. Heat capacities at constant volume, C_{v_1} and C_{v_2}, are computed from Eq. 1.14.
Multi-component simulations solve balance equations for species Y_1 and Y_2 and are used as reference solutions. Initial temperature in both mixtures is a constant parameter T_{init}. Tabulated chemistry is tackled with the mixture fraction defined as $z = Y_1$ which describes all thermodynamics and

Parameters : $A = 1.0$ and $d = 0.5mm$	
multi-component	Tabulated chemistry
$P = 101325$ Pa $u = 0$ m/s $T = 300$ K $Y_1 = 1 - A\exp\left(-\frac{(x-x_0)^2}{d^2}\right)$ $Y_2 = A\exp\left(-\frac{(x-x_0)^2}{d^2}\right)$	$P = 101325$ Pa $u = 0$ m/s $T = 300$ K $z = 1 - A\exp\left(-\frac{(x-x_0)^2}{d^2}\right)$

Table 3.4: *Initial solution for species diffusion validation using tabulated chemistry.*

composition:

$$\begin{aligned} Y_1^{tab}(z) &= z \\ Y_2^{tab}(z) &= 1 - z \\ T^{tab}(z) &= T_{init} \end{aligned}$$

In order to validate the implementation of the method step by step, thermochemical properties are first assumed independent of species mass fractions. Hence, species properties are taken identical:

$$\begin{array}{|lllllll|} \hline W_1 & = & W_2 & = & W & = & 0.01 \text{ kg/mol} \\ C_{p_1} & = & C_{p_2} & = & C_p & = & 1000.0 \text{ J/K/kg} \\ \hline \end{array}$$

The thermodynamical properties are then constant in database A:

$$\begin{aligned} C_v^{tab}(z) &= C_v \\ W^{tab}(z) &= W \end{aligned}$$

In AVBP, balance equations for species and for ψ_l use different part of the code. Hence, database A allows to verify that these parts give identical results when multi-component or tabulated chemistry formalism is chosen. The transport through diffusion and convection is tested.

Diffusion validation with database A (Tab. 3.3)

The first validation test is conducted on a one-dimensional periodic domain of length 5 mm and discretized on 100 cells. Diffusion of species in multi-component formalism is compared to diffusion of mixture fraction in tabulated chemistry simulation. The default AVBP transport description was replaced by a simple Fick law (Eq. 3.97). Initial conditions are indicated in Tab. 3.4.
Figure 3.2 shows that the initial gaussian profile of Y_2 decreases due to the effect of molecular diffusion until perfect mixing between species is achieved.

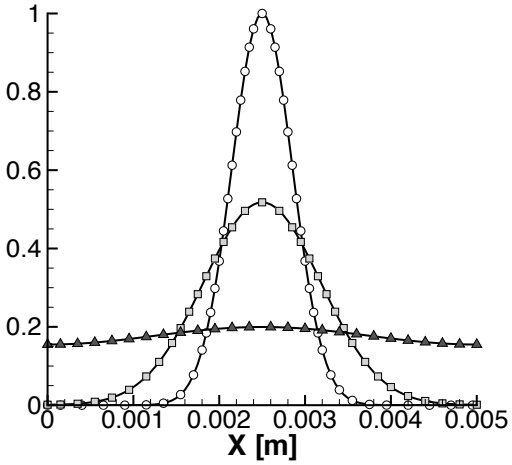

Figure 3.2: *Profiles of Y_2 in multi-component simulation (symbols) and extracted from tabulated chemistry simulation with database A (line) at different time: t = 0 ms ; t = 2.5 ms ; t = 25 ms.*

Parameters : $A = 33.0$, $d = 0.5mm$, $x_0 = 0.0025$	
multi-component	Tabulated chemistry
$P = 101325$ Pa	$P = 101325$ Pa
$u = 0$ m/s	$u = 0$ m/s
$T = 300 + A \exp\left(-\frac{(x-x_0)^2}{d^2}\right)$	$T = 300 + A \exp\left(-\frac{(x-x_0)^2}{d^2}\right)$
$Y_1 = 1$; $Y_2 = 0$	$z = 1$

Table 3.5: *Initial solution for temperature diffusion validation using tabulated chemistry.*

In order to be compared with the multi-component, profiles of $Y_2^{tab} = 1 - z$ are extracted from the database. The profiles plotted in Fig. 3.2 perfectly match the reference solution. Hence, the implementation of balance equations for species and for the database coordinates in AVBP is consistent.

Another diffusion case is considered to assess the correct implementation of energy diffusion in tabulated chemistry simulation (Eq. 1.54). Initial profiles are given in Tab. 3.5 where a gaussian profile is set for temperature. Temperature profiles for multi-component and tabulated chemistry solution are shown in Fig. 3.3. As both solutions are identical, it validates the energy diffusion implementation.

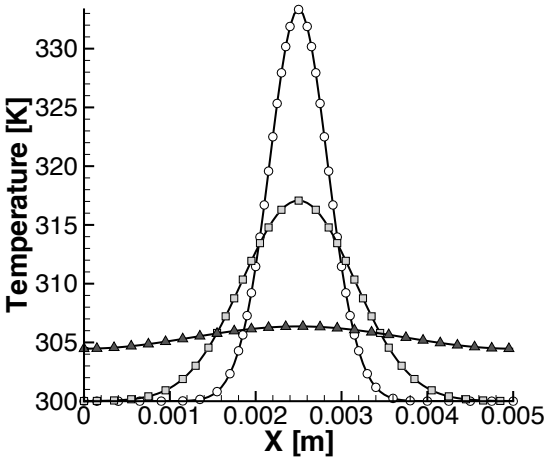

Figure 3.3: *Profiles of temperature in multi-component simulation (symbols) and in TTC formalism with database A (line) at different time: t = 0 ms ; t = 2.5 ms ; t = 25 ms.*

Convection validation with database A (Tab. 3.3)

Convection of dummy species, respectively mixture fraction profiles is considered without taking into account diffusion in both multi-component and tabulated chemistry simulations. Profiles are similar to those given in Tab. 3.4 except for velocity: $u = 10$ m/s. The convective time is $\tau_c = \frac{L}{u} = 0.5$ ms. Hence, the profile travels across the periodical domain every 0.5 ms. Figure 3.4 shows that after 50 cycles, profiles of Y_2 for both formulations match perfectly.

3.7.3 Database B (Tab. 3.3)

Before using CHEMKIN libraries to build the thermo-chemical database, a simpler case is considered where mixing occurs between only two dummy species, Y_1 and Y_2, with different properties:

W_1	=	0.01 kg/mol
W_2	=	0.04 kg/mol
C_{p_1}	=	1000.0 J/K/kg
C_{p_2}	=	500.0 J/K/kg

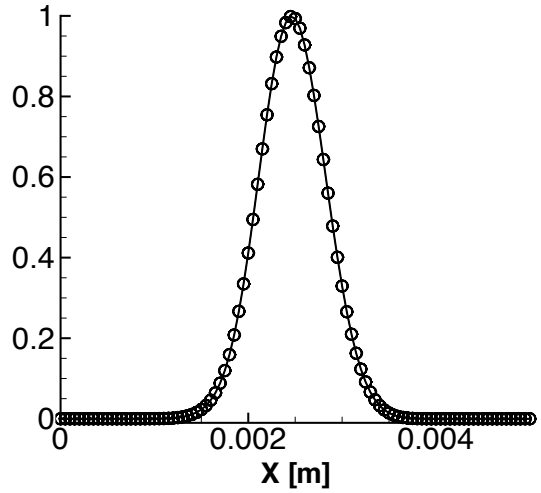

Figure 3.4: *Profiles of Y_2 in multi-component simulation (symbols) and extracted from tabulated chemistry simulation with database A (line) after 50 cycles of the gaussian profile. Species properties are identical and only convection is considered.*

Database B is therefore built as follows[§]:

$$\begin{aligned} Y_1^{tab}(z) &= z \\ Y_2^{tab}(z) &= 1-z \\ T^{tab}(z) &= T_{init} \\ C_p^{tab}(z) &= zC_{p_1} + (1-z)C_{p_2} \\ C_v^{tab}(z) &= zC_{v_1} + (1-z)C_{v_2} \\ (1/W)^{tab}(z) &= z/W_1 + (1-z)/W_2 \\ e^{tab}(z) &\ ... \end{aligned}$$

In TTC formalism, temperature is computed from Eq. 3.17 which is here exact since C_{vk} are independent of temperature. Characteristic boundary conditions require to compute ϑ_z given by Eq. 3.95 which, as for temperature, is exact. The terms σ_z^{tab} and ϑ_z^{tab} are added to the look-up table.

Diffusion and convection validation with database B (Tab. 3.3)

As the mass density depends on the local composition, species transport is coupled with the aerodynamic field from now on. A supplemental validation test of the coded balance equations is performed where initial solution profiles given by Tab. 3.4 are convected with the initial velocity $u = 10$ m/s. As molecular diffusion is also considered, the initial profile travels across the

[§]Note that the tabulation of (1/W) instead of W leads to smaller interpolation error

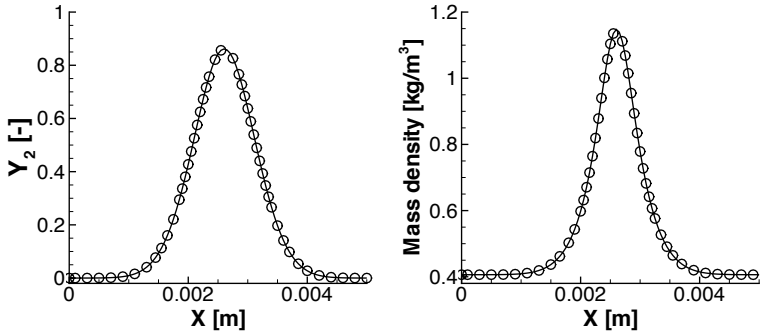

(a) (b)

Figure 3.5: *Comparison between multi-component simulation (symbols) and TTC formalism with database B (line) after* 3 *cycles. (a): mass fraction* Y_2*. (b): mass density. Species properties are different (Eq. 3.99) and convection and diffusion are considered.*

Parameters : $A = 0.02a_0$, $d = 0.5mm$, $x_0 = 0.0025$ $u_0 = 10$ m/s, $P_0 = 101325$ Pa, $T_0 = 300$ K, $\rho_0 = P_0/(rT_0)$	
multi-component	Tabulated chemistry
$\Delta u = A \exp\left(-\frac{(x-x_0)^2}{d^2}\right)$	$\Delta u = A \exp\left(-\frac{(x-x_0)^2}{d^2}\right)$
$u = u_0 + \frac{1}{2}\Delta u$	$u = u_0 + \frac{1}{2}\Delta u$
$P = P_0 + \frac{\rho a_0}{2}\Delta u$	$P = P_0 + \frac{\rho a_0}{2}\Delta u$
$\rho = \rho_0 + \frac{\rho}{2a_0}\Delta u$	$\rho = \rho_0 + \frac{\rho}{2a_0}\Delta u$
$T = \frac{P}{\rho r}$	$T = \frac{P}{\rho r}$
$Y_1 = 1$; $Y_2 = 0$	$z = 1$

Table 3.6: *Initial solution with an acoustic wave traveling downstream superimposed to a constant solution* (ρ_0, u_0, P_0, T_0)*.* a_0 *is the sound speed in the initial solution.*

periodical domain and diffuses along time. As presented in Fig. 3.5, tabulated chemistry solution matches the reference multi-component solution after three cycles. This results enables to verify the correct interpolation of mixture properties in the database during the tabulated chemistry simulation.

Temperature computation validation with database B (Tab. 3.3)

Previous tests confirmed the right implementation of transport equations for the database coordinates ψ_l when thermodynamical properties are given by tabulation. The temperature computation given in Eq. 3.17 to take into account compressible effects is here tested. As C_{v_1} and C_{v_2} are fixed in this example, Eq. 3.17 is exact and is verified by computing an acoustic wave

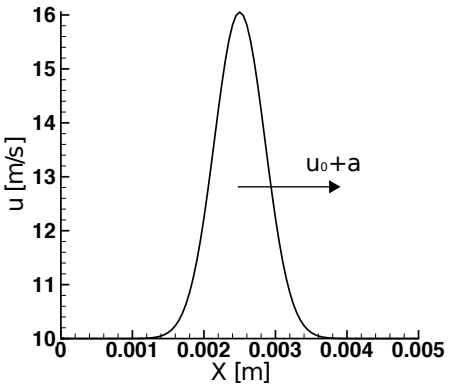

Figure 3.6: *Initial velocity profile, superposition of a constant velocity flow (u_0 = 10 m/s) and an acoustic perturbation.*

traveling towards positive values of x in a constant velocity gas mixture. Initial profiles for both multi-component and tabulated chemistry solutions are given in Tab. 3.6. Fig. 3.6 shows the initial velocity profile. The acoustic velocity perturbation induces a variation of pressure and temperature which travels in the periodical domain.
Time history of different variables is monitored in different points of the domain. Time evolutions of velocity, mass density, pressure and temperature at the point $x = 0$ are plotted in Fig. 3.7. Tabulated chemistry solution follows the same evolution as the multi-component solution and temperature is accurately computed by Eq. 3.17.

Characteristic wave decomposition validation with database B (Tab. 3.3)

In addition to temperature computation, characteristic wave decomposition was reformulated in 3.5 to be compatible with tabulated chemistry framework. The wave decomposition introduced global transformation matrices between conservative and characteristic variables. In order to verify the matrix expressions, initial solution fields are built from given characteristic waves profiles and compared between both multi-component and TTC formalisms. In AVBP multi-component formalism, wave decomposition introduces seven characteristic wave amplitudes when two species are considered:

$$\begin{pmatrix} \mathscr{L}'_1 & = & \mathscr{L}_1 \\ \mathscr{L}'_2 & = & \mathscr{L}_2 \\ \mathscr{L}'_3 & = & \mathscr{L}_3 \\ \mathscr{L}'_4 & = & \mathscr{L}_4 \\ \mathscr{L}'_5 & = & \mathscr{L}_5 \\ \mathscr{L}'_6 & = & u_n \frac{\partial Y_1}{\partial x_n} \\ \mathscr{L}'_7 & = & u_n \frac{\partial Y_2}{\partial x_n} \end{pmatrix}$$

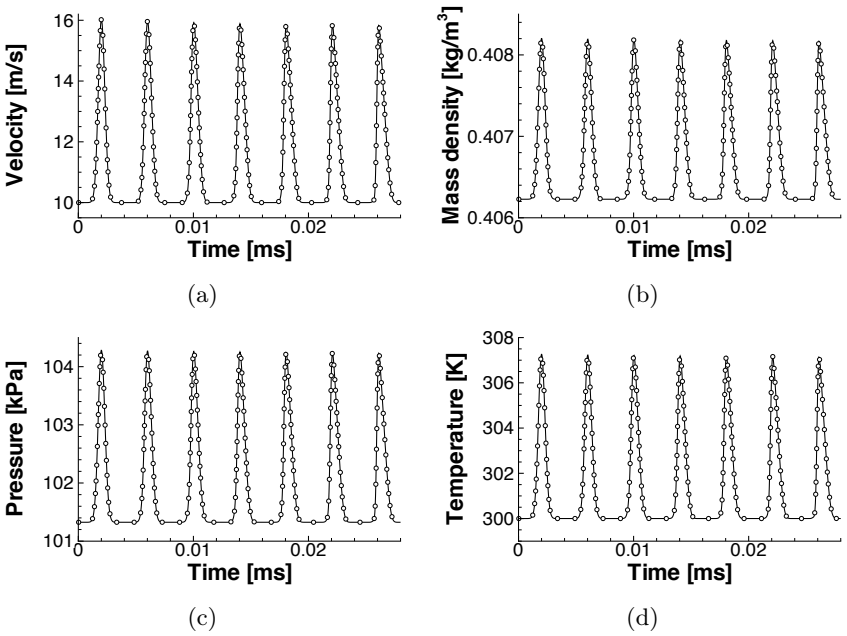

Figure 3.7: *Time evolution of velocity (a), mass density (b), pressure (c) and temperature (d) at the point $x = 0$ m. Symbols: multi-component solution. Line: tabulated chemistry solution.*

The five first waves are identical to those obtained in 3.5 and the two remaining are species characteristic waves. In this particular case, a mixture fraction z is linked to species Y_1 and Y_2 according to $Y_1 = z$ and $Y_2 = 1 - z$, the mixture fraction characteristic wave amplitude $\mathscr{L}_6 = u_n \frac{\partial z}{\partial x_n}$ is linked to species characteristic waves as:

$$\begin{aligned} \mathscr{L}'_6 &= \mathscr{L}_6 \\ \mathscr{L}'_7 &= -\mathscr{L}_6 \end{aligned}$$

In order to verify $\boldsymbol{R_U}$ expression (Eq. 3.83), a characteristic wave is added to an initial homogeneous solution field $(\rho_0, u_0, v_0, w_0, e_{t_0}, z_0)$ with $P_0 = 101325$ Pa, $T_0 = 300$ K, $z_0 = 1$, $u_0 = 10$ m/s and $v_0 = W_0 = 0$ m/s to build a new solution (ρ, u, v, w, e_t, z):

$$\begin{pmatrix} \rho \\ \rho u \\ \rho v \\ \rho w \\ \rho e_t \\ \rho z \end{pmatrix} = \begin{pmatrix} \rho_0 \\ \rho_0 u_0 \\ \rho_0 v_0 \\ \rho_0 w_0 \\ \rho_0 e_{t_0} \\ \rho_0 z_0 \end{pmatrix} + \boldsymbol{R_U} \begin{pmatrix} \mathscr{L}_1 \\ \mathscr{L}_2 \\ \mathscr{L}_3 \\ \mathscr{L}_4 \\ \mathscr{L}_5 \\ \mathscr{L}_6 \end{pmatrix} \tag{3.99}$$

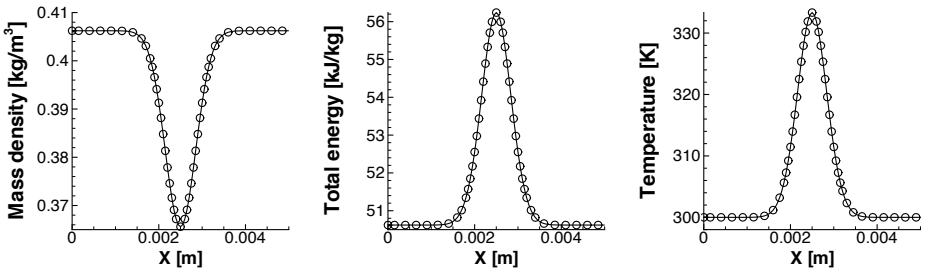

(a) (b) (c)

Figure 3.8: *Initial solution created by superposing an entropic wave through the transformation matrix between conservative and characteristic variables. The gaussian wave amplitude A_1 is $-0.1\rho_0$. Mass density (a), total energy (b) and temperature (c) are represented. Symbols: multi-component solution. Line: tabulated chemistry solution.*

This solution is compared with the equivalent multi-component solution computed as[¶] ($Y_{1_0} = 1$ and $Y_{2_0} = 0$):

$$\begin{pmatrix} \rho \\ \rho u \\ \rho v \\ \rho w \\ \rho e_t \\ \rho Y_1 \\ \rho Y_2 \end{pmatrix} = \begin{pmatrix} \rho_0 \\ \rho_0 u_0 \\ \rho_0 v_0 \\ \rho_0 w_0 \\ \rho_0 e_{t_0} \\ \rho_0 Y_{1_0} \\ \rho_0 Y_{2_0} \end{pmatrix} + \boldsymbol{R}_{\boldsymbol{U}_{AVBP}} \begin{pmatrix} \mathscr{L}'_1 \\ \mathscr{L}'_2 \\ \mathscr{L}'_3 \\ \mathscr{L}'_4 \\ \mathscr{L}'_5 \\ \mathscr{L}'_6 \\ \mathscr{L}'_7 \end{pmatrix} \tag{3.100}$$

where the matrix $\boldsymbol{R}_{\boldsymbol{U}_{AVBP}}$ is the default transformation matrix between conservative and characteristic variables implemented in AVBP for multi-component flow. After specifying identical characteristic waves amplitudes $\mathscr{L}_m$ and $\mathscr{L}'_m$, multi-component and tabulated chemistry solutions built from Eqs. 3.99 and 3.100 must be identical. The superimposed waves, $\mathscr{L}_m$, are set with a gaussian profile:

$$\mathscr{L}_m = A_m \exp\left(-\frac{(x - x_{0m})^2}{d_m^2}\right), \quad \text{here } x_{0m} = 2.5 \text{ mm and } d_m = 0.5 \text{ mm}$$

Initial solutions are built as follows:

- Entropic wave: $\mathscr{L}_1 \neq 0$, $\mathscr{L}_{m\neq 1} = 0$
  The wave is superposed to the homogeneous solution. Figure 3.8 show that mass density, total energy and temperature are well reproduced.

[¶]As chemical reactions are not considered, dummy species enthalpies of formation are set to zero and the total non-chemical energy is identical to the total energy: $E = e_t$.

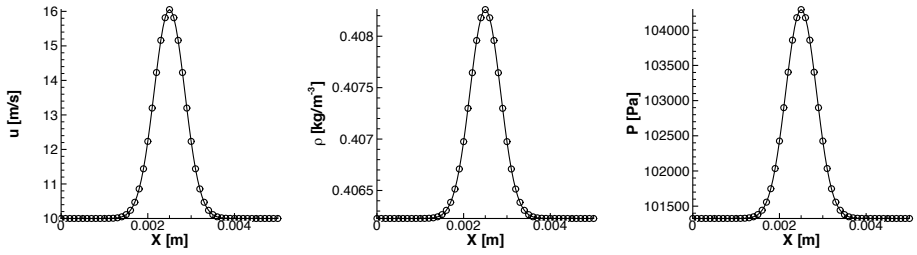

(a) (b) (c)

Figure 3.9: *Initial solution created after adding an acoustic wave through the transformation matrix between conservative and characteristic variables. The gaussian wave amplitude A_2 is $0.01a_0$. Velocity (a), mass density (b) and pressure (c) are represented. Symbols: multi-component solution. Line: tabulated chemistry solution.*

- Acoustic wave: $\mathscr{L}_2 \neq 0$, $\mathscr{L}_{m\neq 2} = 0$
  The wave introduces perturbation of pressure, velocity and mass density. Same initial solutions are retrieved by both methods (Fig. 3.9).

- Acoustic wave: $\mathscr{L}_3 \neq 0$, $\mathscr{L}_{m\neq 3} = 0$
  The test is similar to $\mathscr{L}_2$ and therefore not presented.

- Transverse velocity waves: $\mathscr{L}_4 \neq 0$, $\mathscr{L}_{m\neq 4} = 0$ and $\mathscr{L}_5 \neq 0$, $\mathscr{L}_{m\neq 5} = 0$
  These waves are irrelevant in a one-dimensional configuration.

- Composition wave: $\mathscr{L}_6 \neq 0$, $\mathscr{L}_{m\neq 6} = 0$ in TTC formalism, respectively $\mathscr{L}'_6 \neq 0$ and $\mathscr{L}'_7 \neq 0$ in multi-component formalism
  Species, mass density and temperature profiles presented in Fig. 3.10 are in good agreement between both methods.

These results valid the expression of $\boldsymbol{R_U}$ and therefore the characteristic wave decomposition developed for the TTC formalism.

NSCBC tests with database B (Tab. 3.3)

As characteristic wave decomposition has been validated, Navier-Stokes Characteristic Boundary Conditions (NSCBC) can now be tested. The LODI approximation presented in 3.5.8 is used to specify the unknown characteristic wave amplitudes $\mathscr{L}_m$. NSCBC are then applied to conservative variables as explained in Eq. 3.79. Mixing between two dummy species is still considered and multi-component characteristic wave amplitudes are linked to $\mathscr{L}_m$ as explained in the previous characteristic wave decomposition test. Different characteristic boundary conditions are presented and investigated by

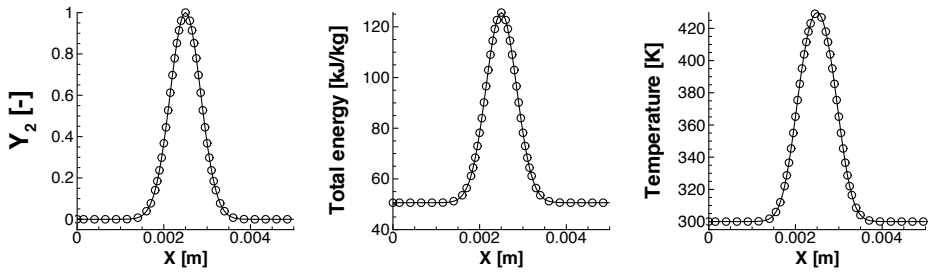

(a) (b) (c)

Figure 3.10: *Initial solution created by superposing a species wave through the transformation matrix between conservative and characteristic variables. The gaussian wave amplitude A_6 is -1.0, which is equivalent for multi-component simulation to $A_{Y_1} = -1.0$ and $A_{Y_2} = 1.0$. Mass fraction of Y_2 (a), total energy (b) and temperature (c) are represented. Symbols: multi-component solution. Line: tabulated chemistry solution.*

injecting acoustic and entropic waves through inflow and outflow boundary conditions.

- Acoustic wave through subsonic non-reflective outlet
  At an outflow boundary, all waves amplitudes are computed inside the domain except for the ingoing acoustic wave $\mathscr{L}_3$. Partially reflective conditions are used to bring information on the mean downstream pressure p_∞ into the computational domain (Poinsot and Lele, 1992) and $\mathscr{L}_3$ is therefore given by

$$\mathscr{L}_3 = K(p - p_\infty) \tag{3.101}$$

  When the relaxation coefficient K is null, the boundary is perfectly non-reflective but the mean pressure is not maintained inside the domain. That is why partially reflective boundary conditions are used instead and the coefficient K must be chosen as small as possible to decrease reflectivity of the boundary while fixing the mean pressure. For that purpose, Rudy and Strikwerda (1980) have proposed that $K = \sigma(1 - \mathscr{M})a/L$ where $\mathscr{M}$ is the maximum Mach number in the flow, L a characteristic size in the computational domain and σ controls the level of reflectivity of the boundary.

  The acoustic wave initial solution built in previous test is sent through a perfectly non-reflective condition ($K = 0$). During the simulation, mean pressure does not have time to decrease significantly. Fig. 3.11 shows velocity and pressure profiles passing through the right boundary without noticeable reflectivity. Identical solutions are observed in both multi-component and tabulated chemistry simulations.

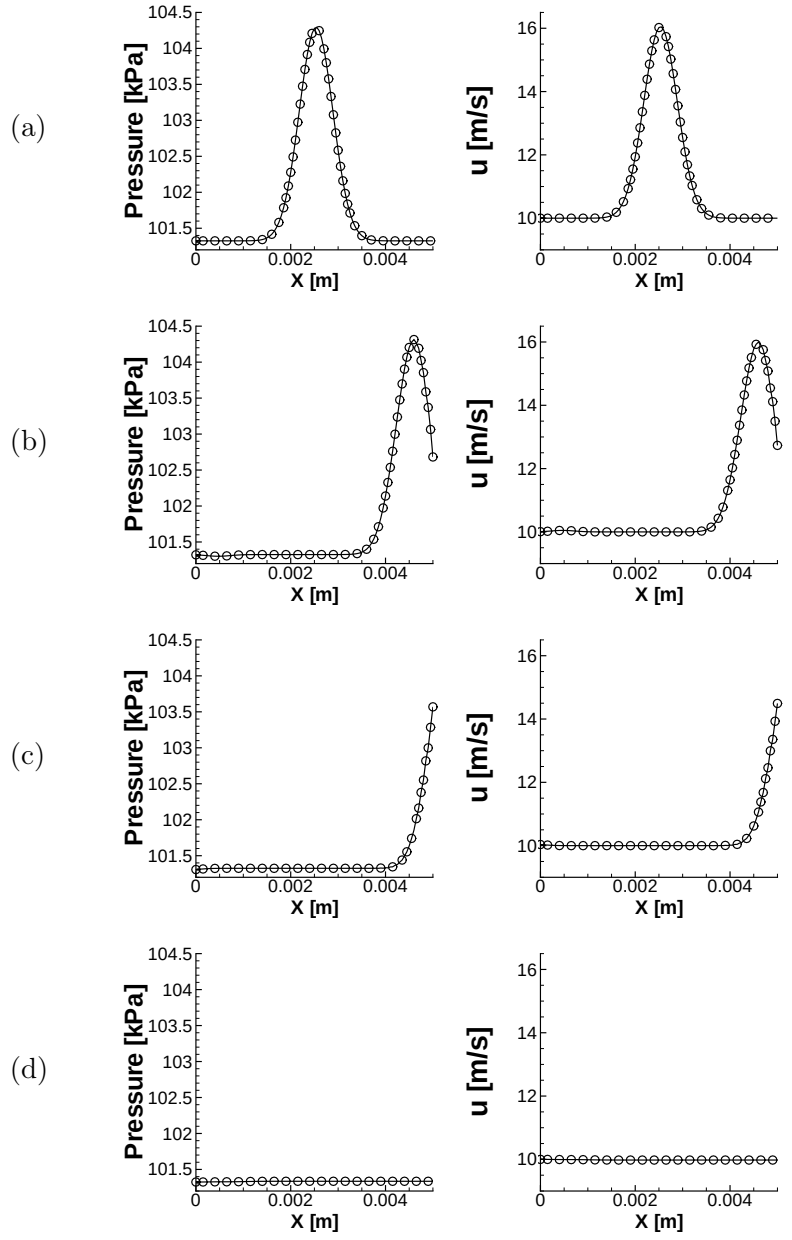

Figure 3.11: *Acoustic wave passing through a non-reflective boundary. Pressure (left) and velocity (right) profiles are plotted for multi-component (symbols) and TTC (line) formalism at different times* $t^+ = tL/a_0$ *in the simulation. (a) Initial solution,* $t^+ = 0$ *; (b)* $t^+ = 0.4$ *; (c)* $t^+ = 0.54$ *; (d)* $t^+ = 1.37$.

Fuel side ($z = 1$)			Oxidizer side ($z = 0$)		
T_f	=	320 K	T_{ox}	=	1350 K
Y_{O2_f}	=	0.195	$Y_{O2_{ox}}$	=	0.142
Y_{N2_f}	=	0.591	$Y_{N2_{ox}}$	=	0.758
Y_{H2O_f}	=	0.0	$Y_{H2O_{ox}}$	=	0.1
Y_{CH4_f}	=	0.214	$Y_{CH4_{ox}}$	=	0.0

Table 3.7: *Temperature and species mass fractions on fuel and oxidizer sides in the Cabra burner (Cabra et al., 2005).*

- Species wave through subsonic non-reflective outlet:
  Same test case is realized with species waves, respectively mixture fraction wave for multi-component, respectively TTC formalism. The composition perturbation is transported through the boundary in the same way for both methods (Fig. 3.12).

- Acoustic wave reflected by a subsonic inflow condition
  Characteristic boundary condition is chosen to fix velocity, temperature and composition at the boundary. The boundary is then purely reflective and the following relations are imposed to characteristic wave amplitudes:

$$\begin{aligned} u = u_0 \Rightarrow \mathscr{L}_2 &= \mathscr{L}_3 \\ T = T_0 \Rightarrow \mathscr{L}_1 &= \frac{\rho\beta}{2a}(\mathscr{L}_2 + \mathscr{L}_3) \\ z = Z_0 \Rightarrow \mathscr{L}_6 &= 0 \end{aligned}$$

  where $\mathscr{L}_3$ is computed inside the domain. Reflectivity of the boundary is compared for both multi-component and tabulated chemistry solutions (Fig. 3.13). As the acoustic wave travels upstream at the speed $u_0 - a_0$, the velocity perturbation is negative. For both solutions, the wave is reflected identically by the inlet boundary.

3.7.4 Database C (Tab. 3.3)

Validations tests are reevaluated by considering real species. The database C is built using CHEMKIN subroutines and a reference temperature of 298 Kelvin as discussed in 3.6.1. All thermo-chemical quantities are stored in a look-up table in term of a unique coordinate: $n = 1$ and $\psi_1 = z$ where z is the mixture fraction. The database C represents a rich methane-air mixture ($z = 1$) injected in a hot vitiated air ($z = 0$) coflow. Table 3.7 details species mass fractions and temperature on the fuel side (Y_{k_f} and T_f) and on the oxidizer side ($Y_{k_{ox}}$ and T_{ox}). Species mass fractions and temperature are stored in the database as:

$$Y_k(z) = (Y_{k_f} - Y_{k_{ox}})z + Y_{k_{ox}} \tag{3.102}$$

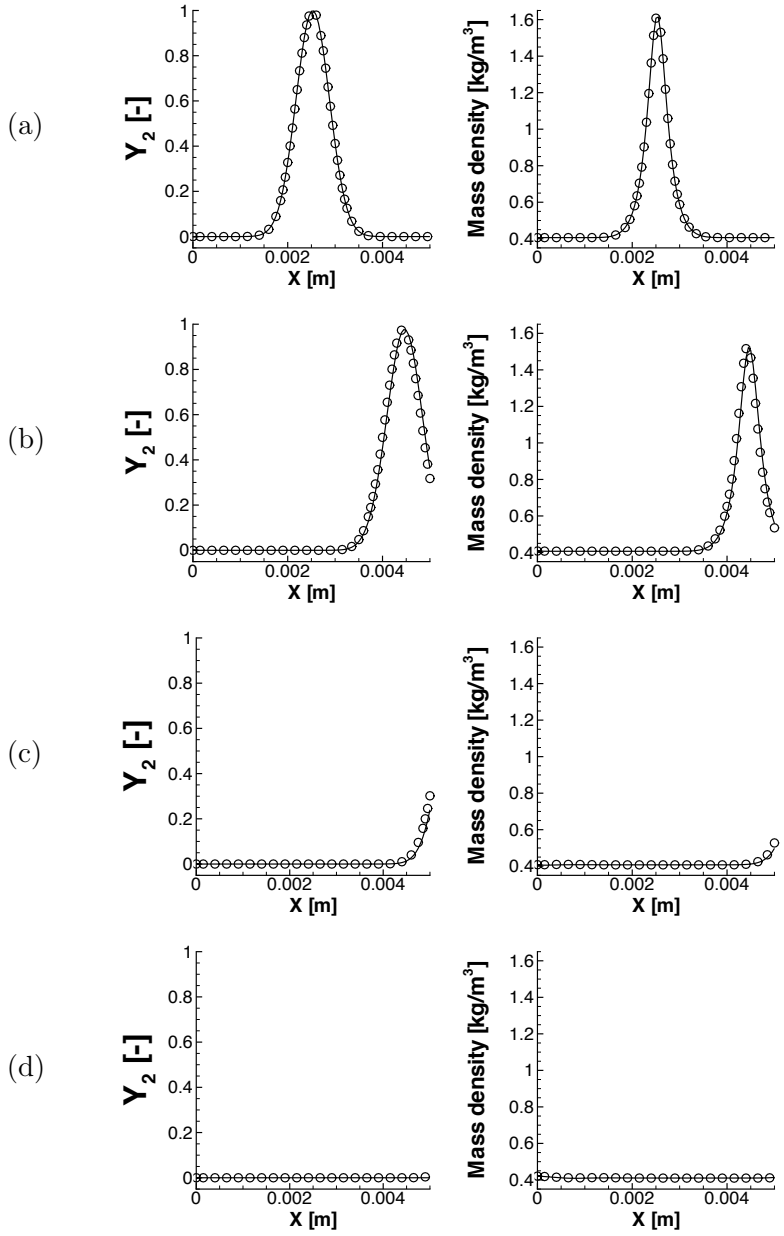

Figure 3.12: *Composition wave passing through a reflective boundary. Mass fractionY_2 (left) and mass density (right) profiles are plotted for multi-component (symbols) and TTC (line) formalism at different times $t^+ = tL/u_0$ in the simulation. (a) Initial solution, $t^+ = 0$; (b) $t^+ = 0.4$; (c) $t^+ = 0.62$; (d) $t^+ = 0.85$.*

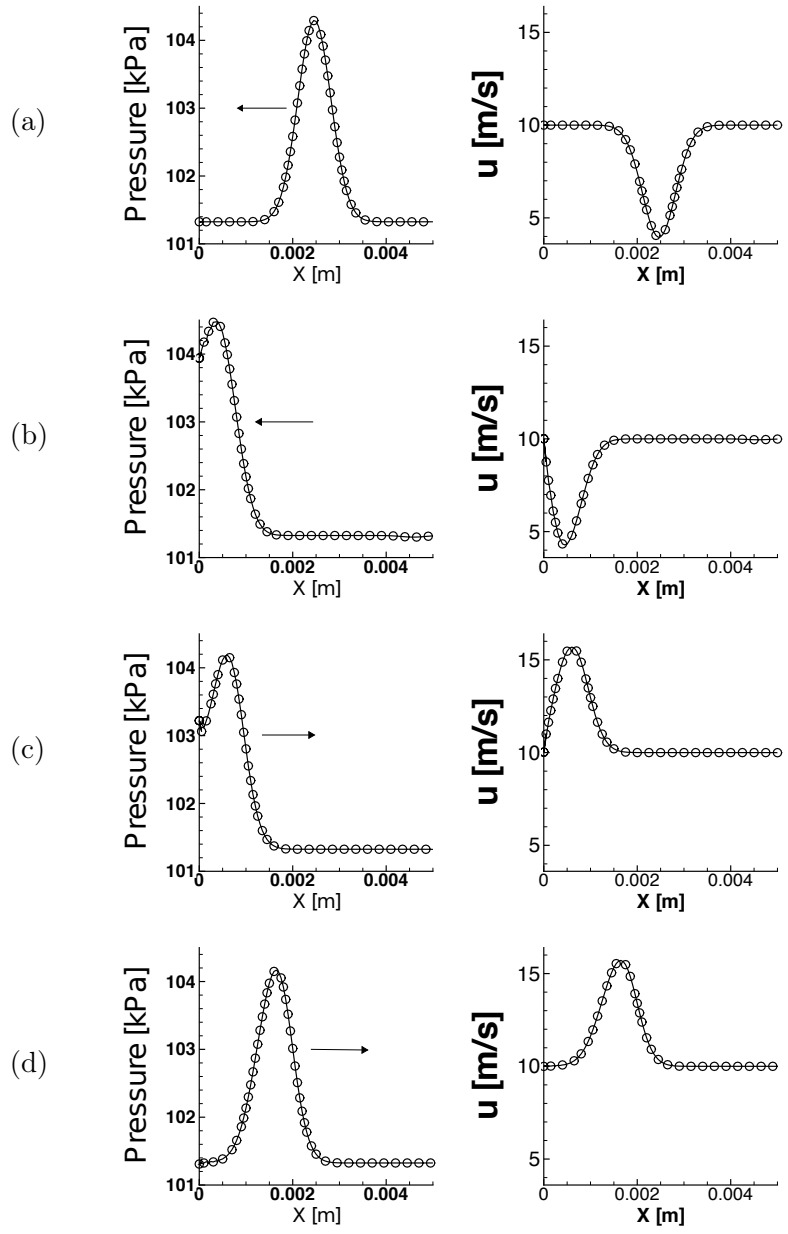

Figure 3.13: *Acoustic wave reflected by an inlet boundary. Pressure (left) and velocity (right) profiles are plotted for multi-component (symbols) and TTC (line) formalism at different times* $t^+ = tL/a_0$ *in the simulation. (a) Initial solution,* $t^+ = 0$ *; (b)* $t^+ = 0.41$ *; (c)* $t^+ = 0.62$ *; (d)* $t^+ = 0.82$.

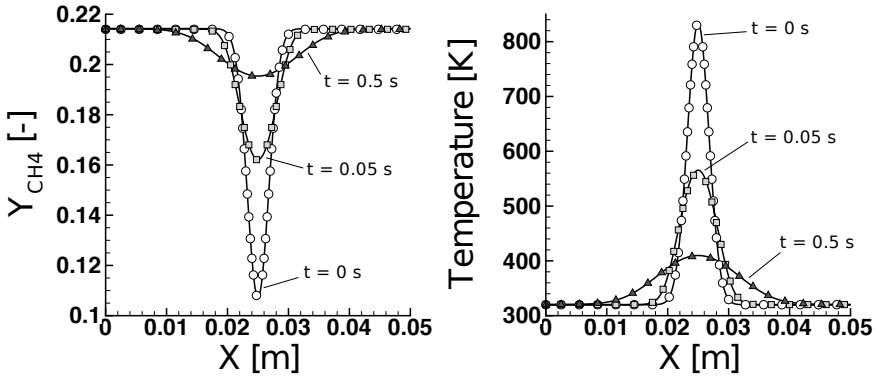

(a) (b)

Figure 3.14: *Diffusion test case with database C. Initial profile ($t = 0$ s) of methane mass fraction (a) and temperature (b) diffuse along time. Two different instants are plotted:* 0.05 *s and* 0.5 *s. Symbols: multi-component solution. Line: tabulated chemistry solution.*

and

$$T(z) = (T_f - T_{ox})z + T_{ox} \tag{3.103}$$

In the present case only one balance equation for the mixture fraction z is added to the mass, momentum and energy balance equations to replace the four species (O_2, N_2, CH_4, H_2O) balance equations solved in the multi-component formulation.

Diffusion validation with database C (Tab. 3.3)

Diffusion test is realized on a one-dimensional 0.05m long mesh discretized with 200 cells. Periodical boundary conditions are used and the initial solution for tabulated chemistry simulation is given by:

$$\begin{aligned} z &= z_0 + z' \quad \text{with} \quad z' = A \exp\left(-\frac{(x - x_0)^2}{d^2}\right) \\ u &= 0 \text{ m/s} \quad , \quad P = 101325 \text{ Pa} \end{aligned} \tag{3.104}$$

Mixture fraction profile is defined with the following parameters: $z_0 = 1$, $A = -1$, $d = 2.5\ 10^{-3}$ m and $x_0 = 0.025$ m. Temperature is initialized according to Eq. 3.103. For the multi-component simulation, initial species mass fraction profiles are deduced by Eq. 3.102. Multi-component and tabulated chemistry solution are depicted in Fig. 3.14. The database extracted value $Y^{tab}_{CH4}(z)$ follows the same evolution as the transported mass fraction of methane. Same results are observed for temperature.

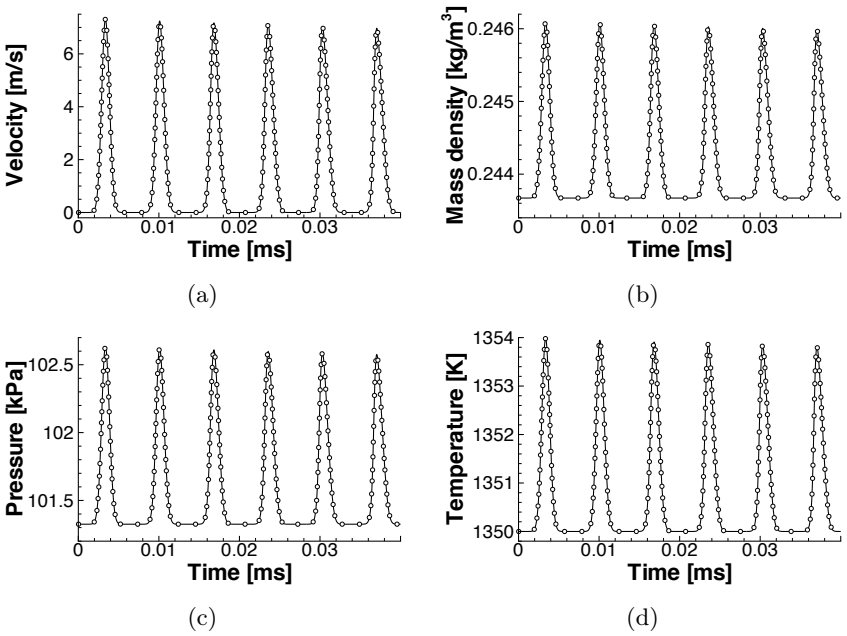

Figure 3.15: *Variation in time at the probe (x = 0 m) of velocity (a), mass density (b), pressure (c) and temperature (d). The initial gaussian profile is parametrized by $A = 0.01a_0$, $d = 5\ 10^{-4}$ m and $x_0 = 0.0025$ m. Symbols: multi-component solution. Line: tabulated chemistry solution.*

Temperature computation validation with database C (Tab. 3.3)

The temperature computation reformulation in Eq. 3.17 for compressible flows is validated by computing an acoustic wave traveling across a periodic domain of length $L = 0.005$ m in a pure oxidizer mixture ($z_0 = 0$, Y_{k_0}, T_0, $P_0 = 1$ atm). The initial solution is given by:

$$\begin{aligned} u &= \pm A \exp\left(-\frac{(x-x_0)^2}{d^2}\right), P = P_0 + \rho_0 a_0 u \\ \rho &= \rho_0 + \frac{\rho_0}{a_0} u \quad , \quad T = \frac{P}{\rho r} \end{aligned} \tag{3.105}$$

where $\rho_0 = 0.24$ kg/m^3 and $a_0 = 734.6$ m/s are the mass density and sound speed in the unperturbed initial solution. The sign of the velocity is chosen so that the wave travels in the domain towards positive x values. Periodic boundary conditions are prescribed. Temperature time evolution at $x = 0$ is plotted in Fig. 3.15(d). The same temperature field is predicted by both tabulated chemistry and multi-component simulations. Similar conclusions are observed for pressure, velocity and mass density time evolutions in Fig. 3.15.

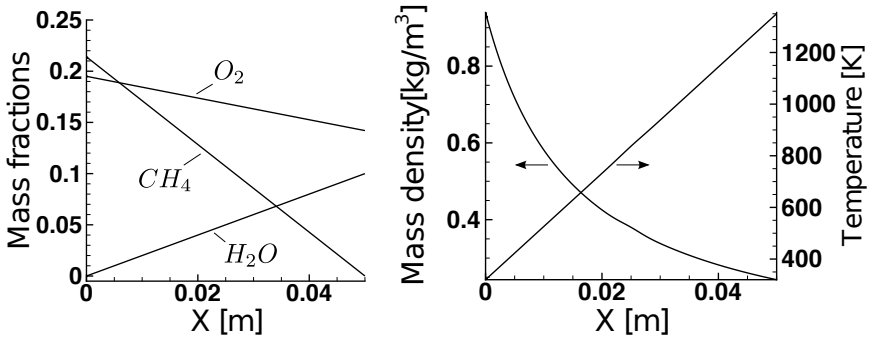

(a) (b)

Figure 3.16: *Initial solution for NSCBC tests with database C before adding characteristic waves. (a) Species mass fraction. (b) Mass density and temperature.*

NSCBC tests with database C (Tab. 3.3)

The NSCBC modifications for tabulated chemistry described in 3.5 are tested with real species by injecting acoustic and entropic waves through inflow and outflow boundary conditions. The wave amplitudes $\mathscr{L}_m$ are imposed as previously. In the proposed test cases, the initial mixture fraction is given by Eq. 3.104 with $z_0 = 1 - \frac{x}{L}$. When the flow is not perturbed by acoustic, species and temperature profiles are deduced using Eqs. 3.102 and 3.103, respectively. Figure 3.16 shows species and temperature profiles in this situation, without mixture fraction perturbation ($z' = 0$).

- Acoustic wave through subsonic non-reflective outlet
  An acoustic wave defined by Eq. 3.105 with parameters: $A = 0.01a_0$, $d = 2.5\ 10^{-3}$ m and $x_0 = 0.025$ m is superimposed. In this first case, the mixture fraction field is not perturbed: $z' = 0$. Fig. 3.17 shows velocity and pressure profiles passing through the right boundary. Identical solutions are observed in both multi-component and tabulated chemistry simulations.

- Acoustic wave reflected by a subsonic inflow condition
  An acoustic wave is defined with the parameters $A = -0.01a_0$, $d = 2.5\ 10^{-3}$ m and $x_0 = 0.025$ m in order to travel upstream towards a reflective inflow boundary with fixed velocity. Fig. 3.19 shows velocity and pressure profiles reflected by the left boundary. The same reflection is found in both multi-component and tabulated chemistry simulations.

- Species wave through subsonic non-reflective outlet
  The flow velocity is now uniformly initialized: $u = 20$ m.s^{-1} and $P = 1$ atm. The mixture fraction is perturbed with a gaussian profile of

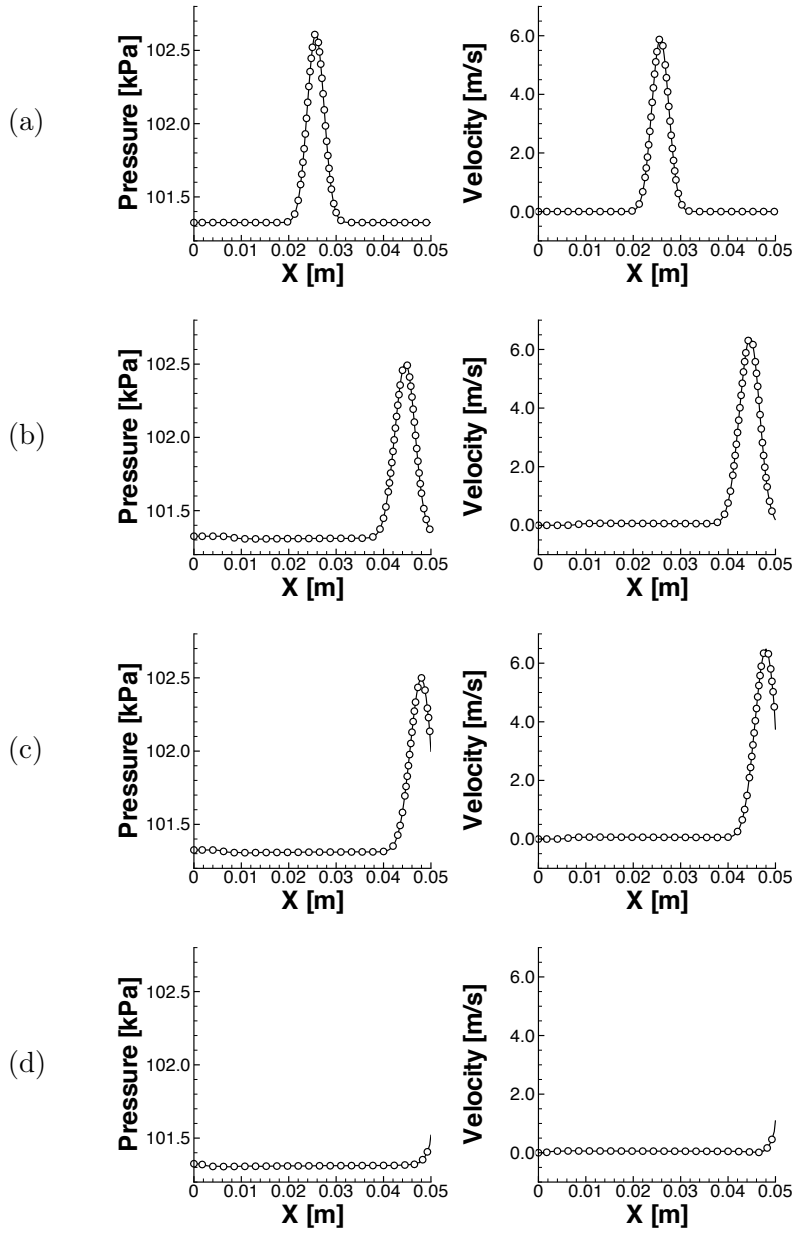

Figure 3.17: *Acoustic wave passing through a non-reflective boundary. Pressure (left) and velocity (right) profiles are plotted for multi-component (symbols) and TTC (line) formalism at different times* $t^+ = tL/a_0(x = L/2)$ *in the simulation. (a) Initial solution,* $t^+ = 0$ *; (b)* $t^+ = 0.35$ *; (c)* $t^+ = 0.4$ *; (d)* $t^+ = 0.51$.

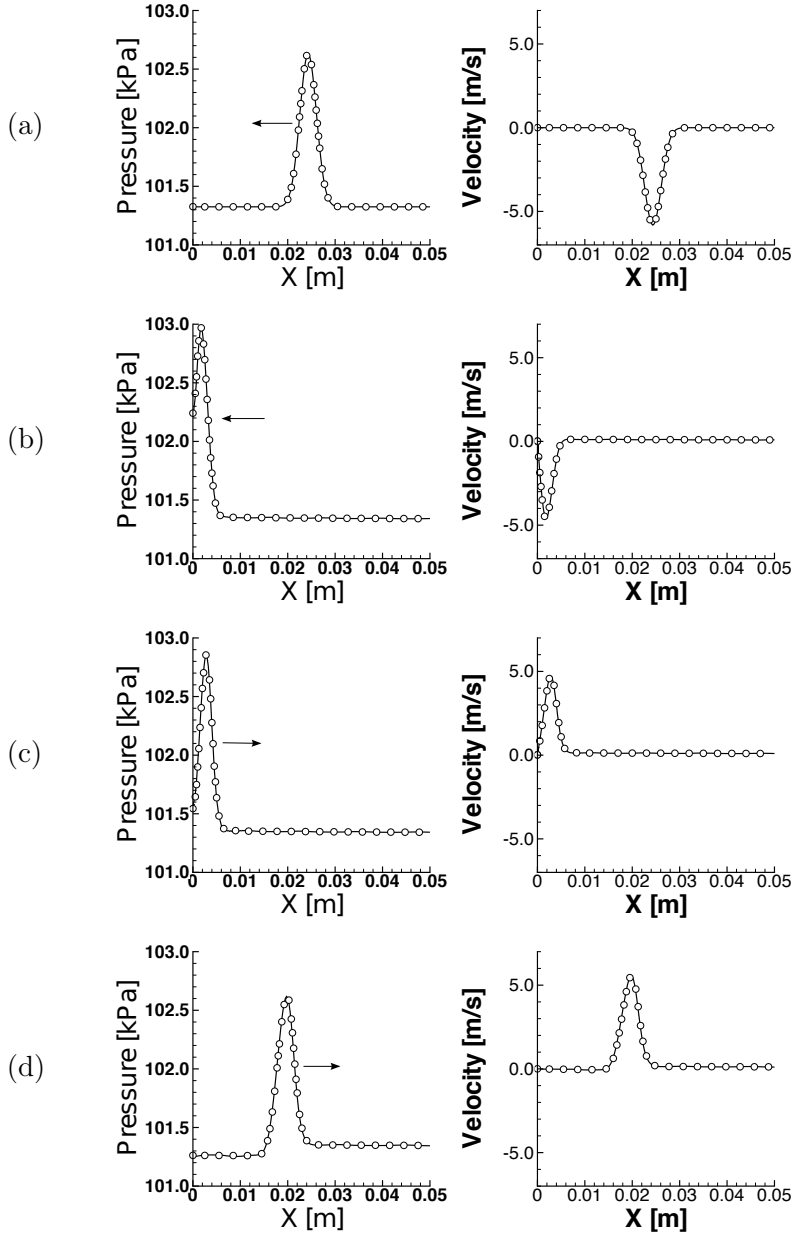

Figure 3.18: *Acoustic wave reflected by a reflective boundary using database C. Pressure (left) and velocity (right) profiles are plotted for multi-component (symbols) and TTC (line) formalism at different times* $t^+ = tL/a_0(x = L/2)$ *in the simulation. (a) Initial solution,* $t^+ = 0$ *; (b)* $t^+ = 0.53$ *; (c)* $t^+ = 0.67$ *; (d)* $t^+ = 1.06$.

z' where $A = -0.5$, $d = 2.5\ 10^{-3}$ m and $x_0 = 0.025$ m. Fig. 3.19 shows methane mass fraction, temperature and density at different instants. Species mass fractions are transported in the multi-component simulation and extracted from the look-up table in the tabulated chemistry simulation. The entropic wave exits properly the computational domain without introducing numerical artifacts in both multi-component and tabulated chemistry simulations.

3D large eddy simulation of a round jet with database C (Tab. 3.3)

Validation of the method is addressed here on a three-dimensional simulation of a round jet impinging in a vitiated coflow. The configuration is identical to the one described by Cabra et al. (2005). The fuel jet diameter d is 4.57 mm and the bulk velocity U_{jet} is 100 m/s (Reynolds number is 28,000). The coflow velocity is 5.4 m/s. Composition of the fuel jet and the coflow are the same as specified in Tab. 3.7. Large Eddy Simulation (LES) is performed with multi-component and TTC formulations without taking combustion into account. Therefore, only the mixing phenomenon is studied here. The subgrid LES flux is modeled using the WALE model (Nicoud and Ducros, 1999). Scalar and energy subgrid turbulent fluxes are modeled with Boussinesq approximation and respectively with turbulent Schmidt and Prandtl number set equal to 0.9. The domain of length $L = 0.7$ m and of 0.35 m diameter is discretized on a non-uniform mesh composed of 30 million tetrahedra. In order not to disturb the jet entrainment, boundary conditions are put far from the domain of interest which extends up to $l = 40$ d in the non-reactive simulation. Characteristic boundary conditions are used and turbulence is injected through in the fuel pipe with an intensity of 1%. An instantaneous mixture fraction isosurface obtained by the tabulated chemistry method is represented in Fig. 3.22.

Comparisons are made between two simulations: the first one denoted as case (1) is made using multi-component description with four species (CH_4, N_2, O_2 and H_2O) ; the second one denoted as case (2) uses tabulated chemistry with mixture fracture as the only input parameter of the table. Instantaneous data are averaged during a physical time of 5 ms higher than twice the convective time l/U_{jet}, to compute mean and root-mean-square (rms) quantities. Figure 3.21(a) shows that mean axial temperature and rms profiles obtained by both simulations are similar. Same behavior are observed in Fig. 3.21(b) for radial profiles of mean species mass fraction. Consequently, mixing is well described using the new coupling technique with the same accuracy as the multi-component formalism.

Assumptions made to derive Eq. 3.17 are now verified: the difference between the tabulated temperature and the temperature computed from Eq. 3.17 must be small for the Taylor series truncation to be valid. The denomination "small" is relative to the temperature sensitivity of the heat capacity C_v.

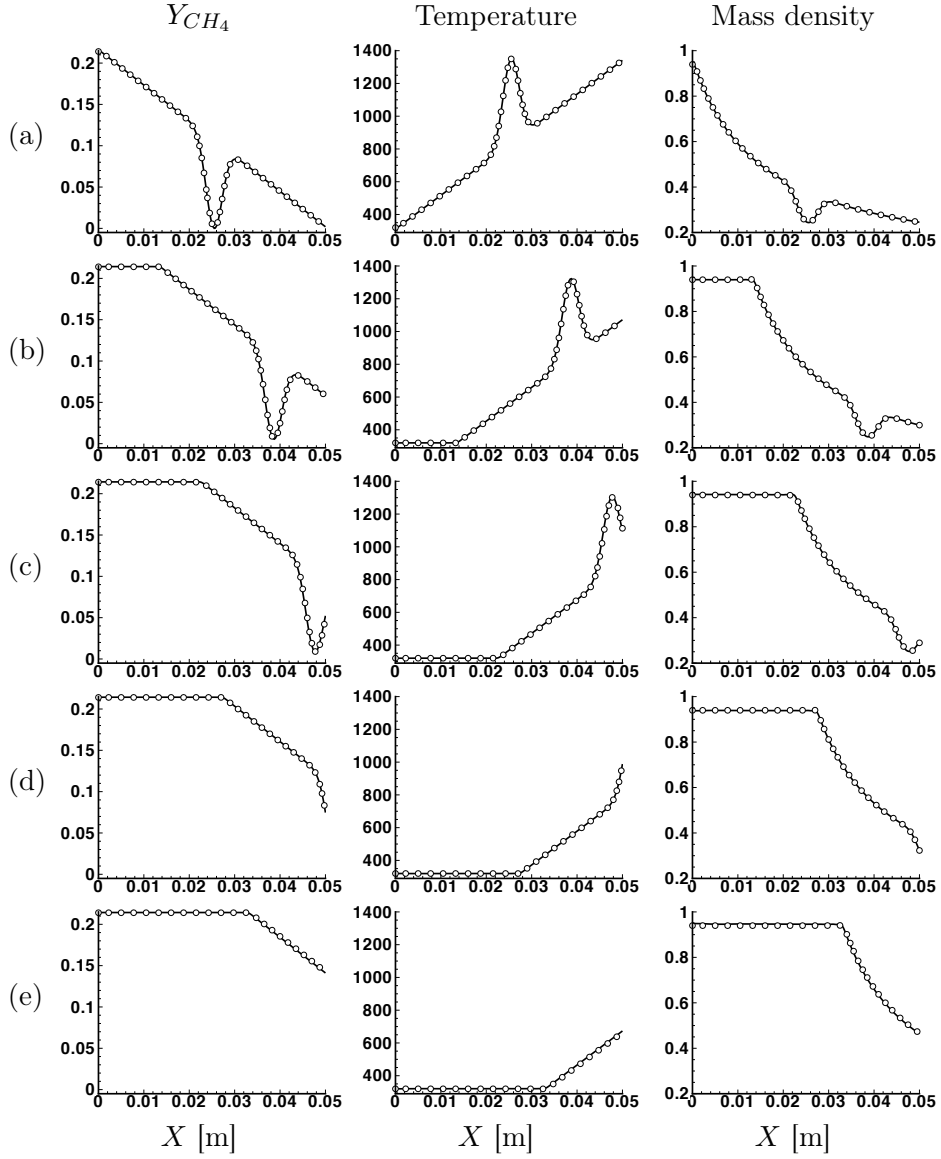

Figure 3.19: *Composition wave passing through a reflective boundary. Methane mass fraction, temperature [K] and mass density [kg/m^3] profiles are plotted for multi-component (symbols) and TTC (line) formalism at different times $t^+ = tL/u_0$ in the simulation. (a) Initial solution, $t^+ = 0$; (b) $t^+ = 0.27$; (c) $t^+ = 0.45$; (d) $t^+ = 0.54$; (e) $t^+ = 0.63$.*

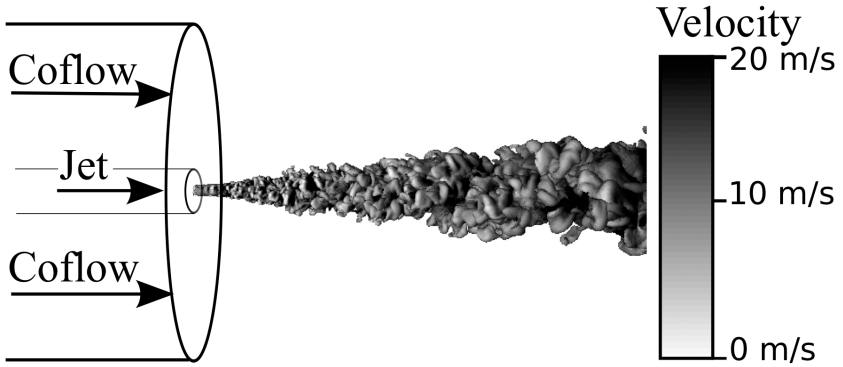

Figure 3.20: *Mixture fraction isosurface $z = 0.1$ colored by longitudinal velocity.*

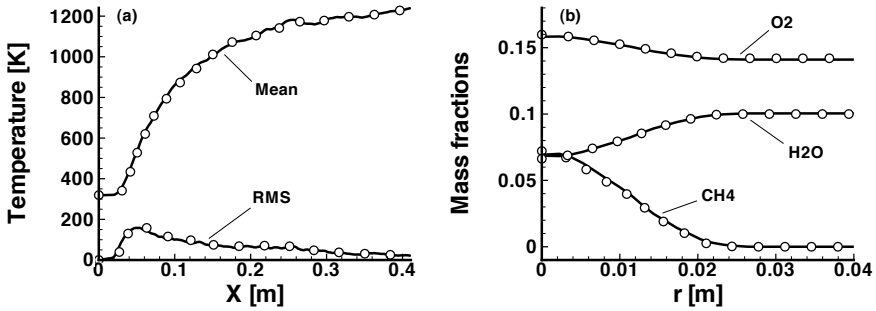

Figure 3.21: *LES Comparison using multi-component (symbols) and tabulated chemistry (line) formulation. (a) Longitudinal mean and root-mean-square (rms) temperature profile. (b) Radial profiles of mean species mass fractions extracted at the axial distance $X = 30d$.*

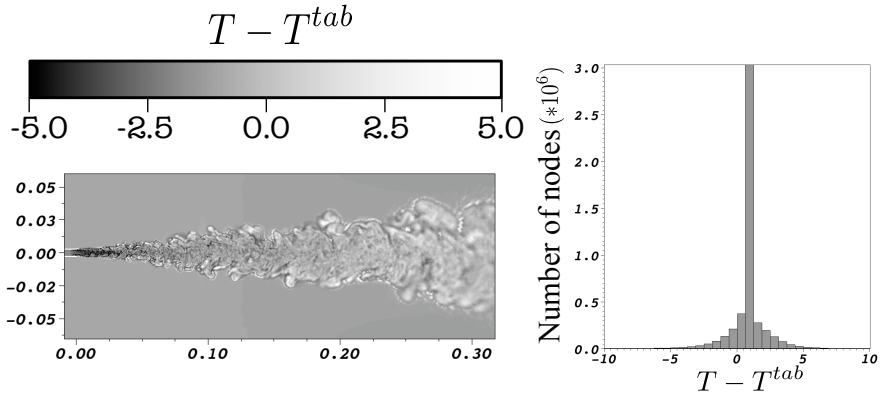

(a) (b)

Figure 3.22: *Difference between the tabulated temperature T^{tab} and the computed temperature T in the tabulated chemistry simulation. (a) Cut plane colored by ΔT. (b) Scattering of ΔT in histograms.*

Fig. 3.22 shows that this difference is less than 5 Kelvin in the most part of the computational domain. In comparison, AVBP thermodynamics for multi-component flow gives species heat capacities C_{vk} as constant on 100K-wide intervals. Therefore, the hypothesis made to compute temperature in tabulated chemistry framework from Eq. 3.17 is valid.
The modified code performance are investigated by comparing different simulations in non-reactive and reactive configuration. Two cases for non-reactive configurations have already been described:

- **Case (1)**. Multi-component formulation is used to compute the Cabra burner without combustion. Hence, four species (CH_4, N_2, O_2 and H_2O) balance equations have been considered.

- **Case (2)**. Tabulated chemistry is addressed with mixture fraction. The four species transport equations of case (1) are replaced by one balance equation for mass density and another one for mixture fraction.

- **Case (3)**. The case is purely multi-component without combustion. Eight species (CH_4, N_2, O_2, H_2O, CO, CO_2, OH, H_2) balance equations are considered. This number of species is still small compared to the number of balance equations that would require a detailed chemical mechanism and is chosen to be compared with the case (4).

Reactive cases have also been computed in order to reproduce the lifted flame associated to the Cabra burner configuration. The turbulent combustion model will be described in chapters 5, 6 and **??**. The cost of tabulated chemistry is presented here in terms of performance through the number of

	Non-reactive simulations			Reactive simulations	
Case	(1)	(2)	(3)	(4)	(5)
Chemistry	4 Y_k	1 Y_k + 1 ψ_l	8 Y_k	8 Y_k + 4 ψ_l	1 Y_k + 4 ψ_l
CPU cost	1	0.81	1.26	1.97	1.12

Table 3.8: *CPU cost comparison between five different simulation cases. Chemistry and thermodynamics are described using a different number of transport equation for species and/or input parameters for a thermochemical database. CPU cost are compared taking case (1) as a reference. Gray columns outline simulations with the new implemented TTC formalism.*

transport equations and of chemical table dimensions. Two different cases using chemistry reduction have been considered to compute the reactive configuration:

- **Case (4)**. Tabulated chemistry for the reactive configuration is addressed with a chemical database where four balance equations are solved for ψ_1, ψ_2, ψ_3 and ψ_4. In this case, the method described by Galpin et al. (2008b) to couple tabulated chemistry in a compressible code is used. Hence, in addition to the four balance equations, eight balance equations for species (CH_4, N_2, O_2, H_2O, CO, CO_2, OH, H_2) are necessary to compute mixture thermodynamics and ensure element conservation.

- **Case (5)**. The same tabulated chemistry model as in case (4) is used except the new coupling method TTC is used instead. There are then only one balance equation for mass density and four others for the parameters ψ_l.

Scalability is first studied for the five different cases. Tests are realized on the Power6 IBM cluster installed at IDRIS. The simulation efficiency E is computed as:

$$E(n) = \frac{T(n)}{N_{iter} \cdot N_{node}(n)} \tag{3.106}$$

where n is the number of CPUs, T(n) is the elapsed time of the simulation, N_{node} is the number of nodes after partitioning of the mesh and N_{iter} is the number of iterations of the computation. If the scalability is perfect, $E(n)$ is linear. Cases performance are investigated on 32, 64, 128, 256, 400 and 512 cores and the speed-up performance is shown in Fig. 3.23. The performance is computed in reference to the 32-cores simulation as $E(n)/E(32)$. For all cases, the speed-up is very good and the new tabulated chemistry coupling model does not penalize the scalability significantly.
Finally, CPUs cost between the different cases is compared on 128-cores simulations. The different CPU costs of each case are given in Tab. 3.8 as

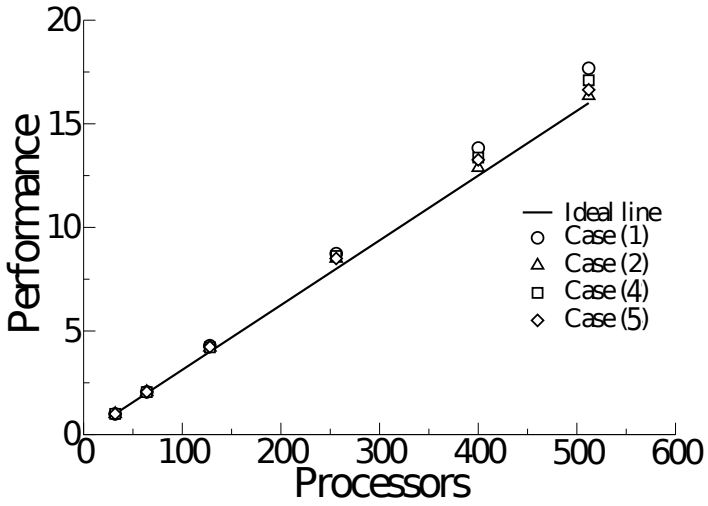

Figure 3.23: *Scalability tests realized for the cases (1), (2), (4) and (5) by taking the 32-cores simulation as a reference. Performance is given by the ratio* $E(n)/E(32)$*. Plain line represents the ideal behavior.*

the ratio between cases efficiency and the efficiency of case (1) taken as a reference: 48,6 μs. The eight species multi-component simulation of case (3) adds four species balance equations to the four already introduced in case (1). The supplemental cost is approximatively 25 %. The tabulated chemistry simulation in non-reactive configuration i.e. case (2) is 20% less expensive in CPU resources than case (1). This shows that even for "cold" simulation tabulation techniques can be interesting to initialize the "hot" simulation.
Efficiencies of the reactive configuration cases are now compared. The main purpose of tabulated chemistry strategies is to reduce the computational cost of detailed kinetics. The case (4) uses the coupling method developed by Galpin et al. (2008b) and introduces 100% additional cost compared to the cold multi-component case. It was enlightened in paragraph 3.3.2 that most of the cost of this method could be reduced. Indeed, the new coupling method used in case (5) requires only 12% additional cost.
The new implementation of tabulated chemistry is, then, very efficient in terms of CPU cost. Besides, many numerical issues relative to the simultaneous transport and tabulation of species disappear:

- For instance, there is no need to artificially modify reaction rates in order to ensure element conservation.

- Supplementary terms to relax species towards the manifold are also

not required anymore.

3.7.5 One-dimensional laminar premixed flame with database D (Tab. 3.3)

A simulation with combustion is now considered with a detailed comparison between multi-component and tabulated chemistry solutions. The method is compatible with any tabulated chemistry model. It is here illustrated with the FPI method (Gicquel et al., 2000; Fiorina et al., 2005b). The objective is to simulate a one-dimensional laminar premixed flame with the TTC formalism in a compressible CFD code. The reference solution with detailed chemistry is computed with the PREMIX code (Kee et al., 1985b) for a stoichiometric methane-air mixture. Pressure is 1 atm and fresh gas temperature is 298K. Transport is described with Fick law and unity Lewis numbers for all species. The detailed mechanism GRI 3.0 (Smith et al., 2000) which involves 53 species is used. The flame structure is tabulated following the FPI methodology (Gicquel et al., 2000). All thermo-chemical quantities are stored in a look-up table in term of a unique coordinate: $n = 1$ and $\psi_1 = c$ where the progress variable c is defined as the coordinate of the chemical database:

$$c = \frac{Y_{CO_2}}{Y_{CO_{2eq}}} \tag{3.107}$$

where $Y_{CO_{2eq}}$ is the equilibrium value of CO_2 in burnt gases. AVBP initial solution is obtained by interpolating the detailed chemistry solution profile of c on a mesh with a length $L = 0.04$ m.
A convective time is defined as $\tau_{conv} = L/S_l$. The tabulated chemistry simulation runs over a physical time equal to $0.2\ \tau_{conv} = 27$ ms. Comparisons between PREMIX and AVBP solutions are shown in Fig. 3.24. Species mass fractions and temperature match perfectly, demonstrating the performance of FPI technique in the TTC formalism. Moreover, CPU saving is important since 53 species transport equations are replaced by one balance equation for progress variable.

3.8 Conclusion

In the present chapter, methods to couple tabulated chemistry with CFD solvers are presented. It was enlightened that compressible solver required specific care since direct reading of the database does not take into account acoustics effects. A new technique called TTC (Tabulated Thermo-chemistry for Compressible flows) formalism was therefore developed to accurately couple tabulated chemistry with compressible flow solvers. The computation of temperature is reformulated to include the deviation from the temperature stored in the chemical database due to compressible effects. NSCBC boundary conditions are also adapted to tabulated chemistry formalism. It

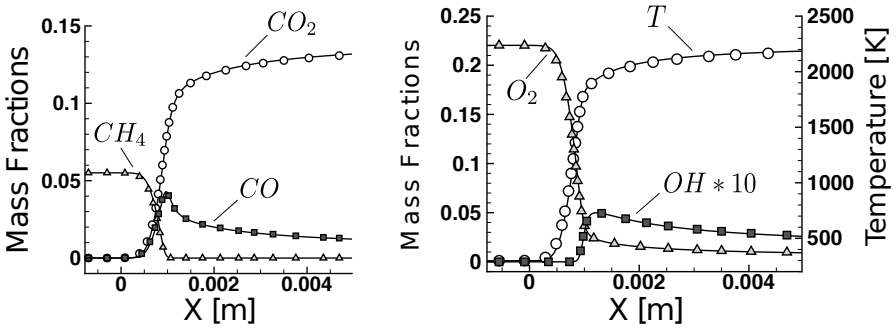

Figure 3.24: *Mass fractions and temperature in a 1-D stoichiometric laminar premixed methane-air flame. Symbols: detailed chemistry solution. Line: TTC solution.*

is shown that acoustic and entropic waves propagations are very well predicted. A LES of a turbulent round jet shows that the mixing is well described using this new coupling technique with the same accuracy as the multi-component formalism. Finally, a laminar flame simulation shows that the method perfectly reproduces premixed combustion phenomena. This new procedure creates a new framework to efficiently introduce tabulated chemistry in compressible flow solvers and therefore to take into account detailed chemistry effects in realistic LES configurations.
The model was written for a general case of tabulated chemistry. Therefore, any flamelets model can now be implemented in AVBP easily:

- In premixed combustion, most AVBP users combine single or two-step chemistry with the thickened flame model (Colin et al., 2000). Keeping the same turbulent combustion model, the chemistry can be tackled by the FPI method to build a TFLES-FPI model (Auzillon et al., 2010a). Finally, the subgrid chemistry-turbulence interaction can be modeled differently using alternative approaches such as the Presumed Conditional Moment (PCM) (Vervisch et al., 2004; Fiorina et al., 2005b; Galpin et al., 2008b) or the Filtered Tabulated Chemistry for Large Eddy Simulation (F-TACLES) model presented in chapter 8. Hence, in addition to the default TFLES model with simple chemistry, other models are now easily implementable and their predictions can be investigated in the same CFD code.

- In non-premixed combustion, the applicability of TFLES in diffusion flames is not trivial. However, the new tabulated chemistry coupling allows to use non-premixed flamelets (Peters, 2000) models straightforwardly by solving balance equations for the filtered mixture fraction and its variance only.

- In partially premixed combustion, different combustion modes can be involved. Usually, models developed for premixed combustion (TFLES, PCM-FPI) are used hoping that the introduced error in some part of the flame are of small importance. However, dedicated models may be developed instead, especially for tabulated chemistry which assumes a fixed flame structure. For instance, in the case of diluted combustion where autoignition occurs, it is necessary to tabulate other kinds of flamelets as it will be shown in the next part.

Part II

Application to diluted combustion

Chapter 4

Flameless combustion

In this chapter, properties of flameless combustion are reviewed. It is outlined that several physical features are involved inside a furnace where flameless combustion occurs. Several authors focused on fundamental studies by simplifying the experimental configuration in order to get a better understanding of the reaction zone structure. Such configurations allow advanced diagnostics through optical access and reduce the number of physical features. Modeling efforts can therefore be conducted on such simplified burners before simulating the whole flameless combustion process in a furnace with confidence in the future.

4.1 Flameless combustion properties

Flameless combustion was developed in order to achieve high thermal efficiency in industrial furnaces keeping low NO_x emission (Wunning and Wunning, 1997; Katsuki and Hasegawa, 1998). In many industrial facilities equipped with recuperative burners, efficiency increases by transferring heat from exhaust gases to the impinging reactants (air and/or fuel). The increase of reactants temperature induces higher temperature peaks inside the combustion chamber. Unfortunately, among the different chemical paths leading to NO_x production, the Zel′dovich thermal NO reaction rate depends exponentially on temperature. Consequently, high temperature peaks lead to massive NO_x emission. This is prevented by enhancing dilution of reactants in order to act as a thermal ballast to keep temperature peaks low. If dilution is large enough, NO_x emission drastically falls and the flame becomes invisible: the flameless combustion mode is reached.
The flameless combustion mode, reviewed by Cavaliere and de Joannon (2004), is characterized by:

- Low NO_x emission
- Thermal efficiency

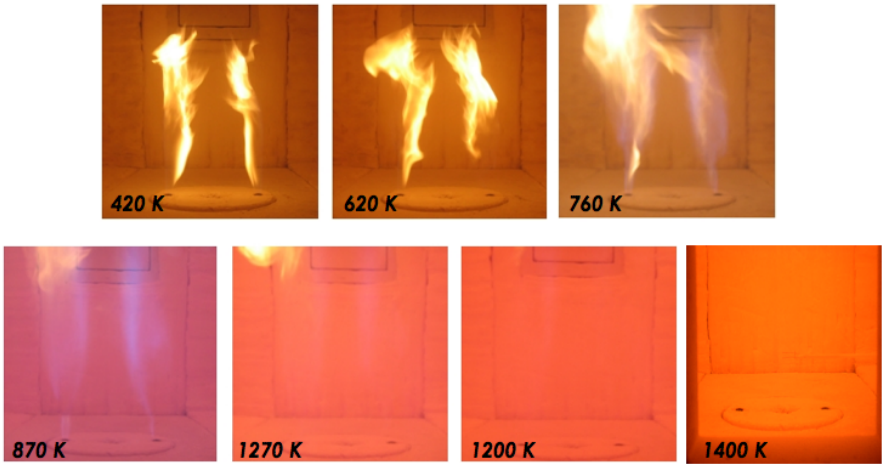

Figure 4.1: *Photographs of a laboratory scale furnace (Rottier, 2010). Transition from a conventional flame to the flameless combustion mode as the furnace power and temperature increase. The nominal power is* 18.6 *kW.*

- No visible flame
- Small gradients of the mean temperature field
- Low flame noise

Different authors have proposed several names and definitions to describe this new combustion mode. A general definition is difficult to obtained as the phenomenon is not fully understood specifically concerning the way combustion occurs at microscales. Instead, the different existing definitions use global parameters or physico-chemical features. Unfortunately, each single definition is not able to fully characterized flameless combustion only and can have some limitations. Consequently, flameless combustion is approximated by the tree following definitions:

- **Flameless Oxidation** or FLOX®. This definition was introduced by (Wunning and Wunning, 1997) and focuses on the visual appearance of the reaction zone: the term "flameless" means there is no visible flame. This point of view is not the most relevant since the light emission is not absolutely null. In fact, as shown by Fig. 4.1, the flame emission becomes less intense than the light radiated by the hot walls of the combustion chamber. The flame light emission decreases because concentrations of species responsible for this emission have become smaller. This is attributed to the species dilution and to a change of chemical reaction paths which do not favor production of light emitting species (Gupta et al., 1999). It should also be noted that some fuel compositions lead to visible flame although the "flameless" combustion

mode, observed when NO_x emission falls, is reached. This shows that the definition based on the flame visibility is not general.

- **High Temperature Air Combustion** or HiTAC (Cavaliere and de Joannon, 2004). This denomination is similar to the Highly Preheated Air Combustion (HPAC) notion defined by Katsuki and Hasegawa (1998). These are systems where the injected air temperature is high enough to enable auto-ignition inside the combustion chamber. Therefore, no particular stabilization mechanism is required inside the combustion chamber such as swirled injection, pilot flame or bluff body. As explained by Cavaliere and de Joannon (2004), the definition concerns a large number of configurations including flameless combustion. Indeed, in many studies, preheating of the oxidant at high temperature is necessary to enhance flameless combustion. However, other studies (Masson, 2005; Szegö et al., 2009) have shown that preheated air is not necessary as long as the furnace temperature is high enough and if the internal mixing of reactants with burnt gases is efficient*.

- **Moderate or Intense Low-oxygen Dilution** or MILD combustion. Oberlack and Peters (2000) defined the mild combustion mode at the flame structure level. After computing perfectly stirred reactors for different parameters, Oberlack and Peters (2000) identified mild combustion as the case where the transition from fresh gases to burnt gases occurs monotonically i.e. without quenching and ignition singular points in the so-called "S" curve. This is encountered when the increase of temperature due the exothermic reaction is relatively small compared to the initial temperature. Cavaliere and de Joannon (2004) outlined that the term "mild" can also be seen as an acronym for moderate or intense low-oxygen dilution which is characteristic of the flameless processes.

These three terms describe different aspects of flameless combustion (flame visibility, high temperature and dilution) whose principal consequence is the significant decrease of NO_x emission. The dilution of reactants is enhanced by designing the combustion chamber so that burnt gases recirculate towards fuel and air injections. The amount of recirculated burnt gases compared the total injected mass is quantified by the recirculation rate K_V defined by:

$$K_V = \frac{\dot{m}_e}{\dot{m}_a + \dot{m}_f}$$

$\dot{m}_e$ is the mass flow rate of recirculating exhaust gases and $\dot{m}_a$ and $\dot{m}_f$ are respectively the injected mass flow rates of air and fuel. In mild combustion

*Such a property is not used in industrial applications where preheating by heat recirculation from exhaust gases is responsible for the thermal efficiency benefit.

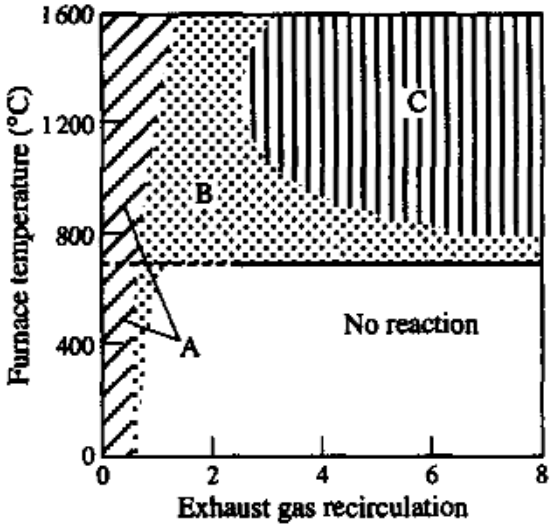

Figure 4.2: *Flameless combustion diagram (Wunning and Wunning, 1997). Furnace temperature is plotted in function of the recirculation ratio K_V. A: conventional flames. B: unstable flame. C: flameless combustion.*

furnaces, K_V is large in order to decrease temperature peaks responsible for NO_x emission. Besides, temperature of the furnace and of reactants (if necessary) must be high enough to promote autoignition inside the combustion chamber and sustain flammability of the mixture. This two requirements are depicted in a diagram realized by Wunning and Wunning (1997) shown in Fig. 4.2. The flameless combustion mode is restrained by two thresholds in the furnace temperature-K_V map. That is why it is located on the upper right corner. There should also be a second practical temperature threshold above which NO_x emission becomes too high, even when operating in mild combustion.

4.2 Several modeling issues

Simulation of industrial applications of mild combustion involves several modeling key features of different physical nature. These different phenomena are schematized in Fig 4.3 where the geometry is representative of the experimental flameless combustion furnace studied by Masson (2005) and Rottier (2010): two fuel pipes and one air pipe impinging in a rectangular combustion chamber. This configuration is similar to other studies and industrial applications[†]. The different circled numbers in Fig 4.3 stand for the following phenomena:

[†]The flow exits sometimes on the same side where the reactants are injected.

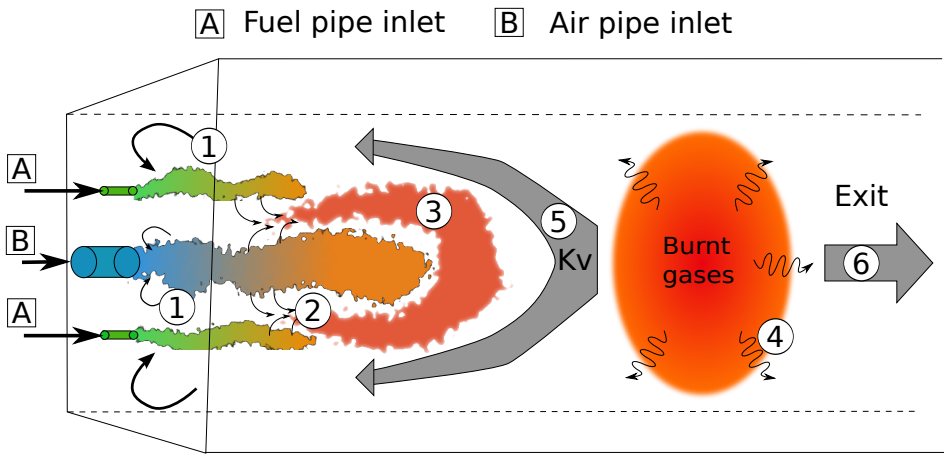

Figure 4.3: *Scheme representing flameless combustion inside a furnace and the different steps. ①: the recirculated burnt gases are entrained by the impinging jets, which dilutes reactants. ②: the diluted air and fuel jets mix. ③: reaction takes place between fuel and air jets. ④: burnt gases loose enthalpy through radiation which is transmitted to the furnace charge. ⑤: a part of burnt gases recirculates downstream towards step ① with the recirculation rate K_V. ⑥: burnt gases exit the furnace.*

① The recirculated burnt gases mix with fuel and air by being entrained by the impinging jets. The amount of dilution of reactants is a key parameter to achieve mild combustion. The prediction of flue gas mixing by entrainment is therefore critical. Reynolds Averaged Navier-Stokes (RANS) simulations showed good prediction of mixing between the air jet and the ambient burnt gases but the fuel jet mixing was poorly predicted (Yimer et al., 2001; Mancini et al., 2007), revealing the limitations of classical turbulent closure models. The discrepancy is due to the difference of momentum between the two jets and is known as the strong-jet/weak-jet problem. As the prediction of the fuel jet dilution is crucial, analytical (Grandmaison et al., 1998) and experimental (Yimer et al., 2001) studies of the problem have been conducted.

② Most mild combustion systems operate in non-premixed configurations. Indeed, separated fuel and air injections enable both mixtures to be diluted by burnt gases before they react downstream. The mixing inside the furnace is therefore a three-streams mixing problem composed of air, fuel and burnt gases. Beyond the computational challenge on an aerodynamic point of view, such configuration influences the turbulent combustion modeling. In flamelet models for instance, two different mixture fractions are necessary in order to tackle the three-streams

mixing problem (Hasse, 2004; Hasse and Peters, 2005).

③ Reaction takes place between fuel and air streams. The turbulent combustion modeling efforts are dedicated to this part of the flow. It influences the prediction of temperature and formation of species including pollutants.

④ The purpose of a furnace is to transfer most of hot gases heat to the furnace charge. Hence, the combustion is not adiabatic and burnt gases created by the fuel oxidation loose enthalpy mainly through radiation but also through heat loss near the furnace walls. The prediction of the temperature field is then also conditioned to the good prediction of radiation and wall heat loss in turbulent flows.

⑤ A part of burnt gases recirculates downstream with the recirculation rate K_V. The amount of recirculated gases is fixed by the computed aerodynamical field.

⑥ Finally, burnt gases exit the furnace. Due to its slow chemistry, the final NO_x concentration is dependent on the residence time inside the furnace. It enlightens that the computed aerodynamic field in addition to turbulent chemistry modeling influences the prediction of pollutant formation.

The different steps presented outline that the simulation of a mild combustion furnace involves complex and multi-physical problems. It requires the accurate prediction of aerodynamics, mixing, combustion and radiation. If liquid fuels or solid fuels like coal are used, multiphase combustion must also be considered. Using detailed models to describe each phenomenon would penalize the computational cost of the simulation too much. Hence, different levels of complexity are usually retained depending on the study's focus. Tab. 4.1 lists several publications where numerical simulations of realistic flameless combustion installation were conducted. The different models chosen to simulate turbulent mixing and aerodynamics, heat losses due to radiation and turbulent combustion are given as well. Several kinds of models for each physical area are identified and given below.

- **Aerodynamics/Mixing**: the standard $k-\varepsilon$ model (Jones and Launder, 1972) and its modified versions are both RANS models. Modified versions change the fixed coefficients in order to limit the standard model discrepancies such as the round jet anomaly for instance. More detailed approaches such as Reynolds Stress Models (RSM) or Large Eddy Simulations (LES) exist.

- **Radiation**: the optically thin assumption combined with approximated grey gas properties is the less costly model since a single term is

added to the energy balance equation of the form $\sigma(T^4 - T_0^4)$. It is more accurate to solve the Radiative Transfer Equation (RTE) in order to compute the radiative heat flux. The Discrete Ordinates Model (DOM) (Fiveland, 1984) and the Discrete Transfer Method (Shah, 1979) are used to solve the RTE in many heat transfer applications. More expensive methods consists in Monte-Carlo algorithms.

- **Chemistry**: in many industrial configurations, combustion is tackled by models that are already implemented in commercial codes such as the Eddy Break-Up (EBU) model (Magnussen and Hjertager, 1976) or its extension to multi-step mechanism, the Eddy Dissipation Concept (EDC). Flamelet models associated to presumed PDF allow to introduce detailed chemistry effects at low CPU cost. Finally, turbulence-chemistry interaction can alternatively be computed with significant additional cost by solving balance equation for the PDF.

The combination of standard $k - \varepsilon$ model with DOM and EDC clearly emerges from Tab. 4.1. Given the limitations of the $k - \varepsilon$ model, the confidence in mixing and dilution of reactants predictions is low. Modifying the model coefficients corrects the intrinsic round jet overspreading of the standard model but cannot be given for general configurations. No works using more detailed description of turbulence such as RSM or LES were found. Concerning the radiation description, the use of DOM or DTM outlines the importance of radiative heat transfer inside the combustion chamber in order to predict the temperature field in burnt gases. Galletti et al. (2007) explained that small difference were observed with Monte-Carlo simulations, which indicates that DOM/DTM are good CPU cost/accuracy compromises. Finally, combustion is mainly described with models such as EBU or EDC with simple chemistry (one or two steps) (Galletti et al., 2007; Schaffel et al., 2009), skeletal (Yang and Blasiak, 2005) or detailed (Parente et al., 2008) mechanisms. As auto-ignition is believed to take place inside the combustion chamber, detailed chemical effects should be included in numerical simulations through detailed mechanisms or reduction methods.

4.3 Necessity of simplified experimental configurations for numerical simulation validation

The comparison of numerical simulations listed in 4.1 with experimental data is often poor and/or limited because of the configuration which does not allow full optical access and advanced diagnostics. Such limitations and the presence of many challenging modeling features motivated research efforts to design simplified configurations in order to gain a deeper fundamental understanding of the combustion mode but also in order to allow reliable modeling validation.

References	Aerodynamics/Mixing		
	$k-\varepsilon$ standard	$k-\varepsilon$ modified	RSM/ LES
a. Coelho and Peters (2001)	x		
b. Dally et al. (2004)		x	
c. Yang and Blasiak (2005)	x		
d. Kumar et al. (2007)	x		
e. Galletti et al. (2007)		x	
f. Kim et al. (2007)	x		
g. Parente et al. (2008)	x		
h. Schaffel et al. (2009)	x		
References	**Radiation**		
	optically thin	DOM/ DTM	Monte-Carlo
a. Coelho and Peters (2001)	x	x	
b. Dally et al. (2004)	?	?	?
c. Yang and Blasiak (2005)		x	
d. Kumar et al. (2007)	?	?	?
e. Galletti et al. (2007)		x	x
f. Kim et al. (2007)		x	
g. Parente et al. (2008)		x	
h. Schaffel et al. (2009)		x	
References	**Chemistry**		
	EBU/ EDC	Flamelet	PDF transport
a. Coelho and Peters (2001)		x	
b. Dally et al. (2004)		x	
c. Yang and Blasiak (2005)	x		
d. Kumar et al. (2007)	x		
e. Galletti et al. (2007)	x		
f. Kim et al. (2007)	x		
g. Parente et al. (2008)	x		
h. Schaffel et al. (2009)	x		

Table 4.1: *Modeling approaches in several studies (a, b, c, d, e, f, g and h) on numerical simulation of mild combustion furnaces. The mark x shows which models were used in the considered publication. Question marks are used when no information was found.*

The Cabra burner (Cabra et al., 2002, 2005; Wu et al., 2006; Gordon et al., 2008), the Jet in Hot Coflow (JHC) burner (Dally et al., 2002; Medwell et al., 2007, 2008) and the experimental set up designed by Choi et al. (2009) are examples of such simplified configurations. The flames are unconfined jet flames isolated by a co-flow from the laboratory ambient air. Fuel or air streams are diluted with vitiated gases before being injected and the air stream is heated either by its pre-mixing with hot gases or by a pre-heater. This set-up enables to eliminate the three streams mixing problem and to neglect heat losses in the flame. The study is therefore focused on the mixing of diluted fuel and air and on the combustion at high temperature i.e. phenomena ② and ③ described in Fig. 4.3.
Given the level of fresh gases dilution by products, these flames do not necessary operate in the mild combustion mode: diluted combustion in a large sense is studied. In the following chapters, a tabulated chemistry model is developed for diluted combustion configurations with simplified geometry where auto-ignition is involved. This work is a first step towards a global model for flameless combustion furnace where enthalpy variation and variable hot gases dilution must be considered.

Chapter 5

A tabulated chemistry model for diluted combustion

A general modeled configuration is presented. Auto-igniting one-dimensional flamelets are chosen to represent self-igniting non-premixed flames. The behavior of the flamelets solutions is illustrated by examples that correspond to a laboratory flame issuing in a vitiated co-flow (Cabra et al., 2005). The impact of differential diffusion is discussed. Then, a chemical database is built from the non-premixed flamelet solutions in order to include detailed chemistry effects at low CPU cost in numerical simulations. The turbulence-chemistry interaction is not treated at this stage. Finally, the steady scalar dissipation rate assumption to build the database is evaluated and a source term correction is proposed to predict the auto-ignition delays.

5.1 Introduction

In many combustion devices, such as Diesel internal-combustion (IC) engines or SCRAMJET combustor, auto-ignition initiates the transformation of a fuel/oxidizer mixture to a fully burnt state. This phenomenon is also of great importance in new technologies where exhaust gas are mixed with fresh gases in order to reduce NO_x emission while high thermal efficiency is maintained. Indeed, in industrial furnaces operating in the MILD combustion mode (Cavaliere and de Joannon, 2004), the dilution of fresh gases with burnt gases is large enough to promote auto-ignition

In such industrial configurations, fuel, oxidizer and burnt gases are not premixed before entering in the combustion chamber. Therefore, auto-ignition takes place in a turbulent non-premixed environment. Mastorakos (2009) recently reviewed and highlighted the complexity of such flames structure where auto-ignition competes with diffusion. It was previously showed that the presence of multiple physical phenomena makes mathematical modeling a very challenging feature. The different modeling issues are:

- Auto-ignition delay times are very sensitive to the radical build-up during the preignition phase and then require an accurate description of the chemistry. Including detailed chemical kinetics in calculations is therefore essential.

- Many studies (Hilbert and Thevenin, 2002; Hilbert et al., 2004; Mastorakos, 2009) showed that ignition in non-premixed systems starts under specific mixing conditions corresponding to the "most-reactive mixture fraction", $z = z_{MR}$. The prediction of mixing between fuel and oxidizer streams is therefore of great importance.

- As burnt gases are reinjected, the local composition and, consequently, the combustion properties are affected by the additional mixing between flue gases and reactants.

- Recirculation of cooled burnt gases due to heat losses impacts combustion and variation of enthalpy must then be included in tabulated chemistry models (Fiorina et al., 2003).

Consequently, a proper description of the detailed kinetics, the mixing between fuel, oxidizer and burnt gases, and heat losses is necessary to perform accurate simulations of diluted combustion.
To facilitate understanding of auto-ignition in non-premixed flame diluted by recirculating burnt gases, laboratory scale flames (Cabra et al., 2002; Dally et al., 2002; Medwell et al., 2007) were designed in simpler configurations: a fuel jet issues in a coflow diluted with burnt gases produced by a secondary burner. Such experiments are very useful to develop and validate turbulent combustion models. The burner designed by Cabra et al. (2002, 2005) was studied for two fuels and investigated with multiscalar one-point diagnostics. These data are useful in order to validate tabulated chemistry model. That is why, this configuration was chosen to validate the future combustion model. The central fuel jet is surrounded by a hot co-flow composed of air and water vapor. Therefore, combustion occurs between fuel and oxidizer pre-diluted with burnt gases. The resulted lifted flame is the consequence of only two remaining physical features: detailed chemistry and mixing between the jet and the vitiated co-flow. Indeed, as radiation is neglected, no heat loss will impact the flame structure.
The experiment investigated two fuels respectively composed of hydrogen and nitrogen (25% H_2, 75% N_2 in volume), and of methane and air (33% CH_4, 67% air in volume). High sensitivity of the flame lift-off height in respect to the co-flow temperature evidenced the role of auto-ignition in the flame stabilization (Cabra et al., 2002; Wu et al., 2003; Cabra et al., 2005; Gordon et al., 2005). Sensitivity analysis to jet and co-flow inlet velocities are smoother and evidenced linear dependence of the flame lift-off height. Multiscalar measurements were used to draw scatter plots of reactive scalar

in both configurations. Significant differences were found and led to assume different flame stabilization mechanism. However, information is not sufficient to draw conclusions regarding the flame stabilization structures.
That is why Gordon et al. (2008) realized 2D-imaging of reactive scalars in order to give better insight into the stabilization region. Different flame stuctures representative of a transient non-premixed flamelets were identified:

- A pool of chemical precursors is first built up.
- Then, fast ignition proceeds in flame kernels.
- Finally a "steady" diffusion flame is formed downstream.

In order to reproduce these effects and to capture the flame lift-off, interactions between chemistry, micro-mixing and turbulence must be included in numerical simulations.
A natural way to introduce chemistry-turbulence interactions is to use transport equations for Probability Density Function (PDF) (Haworth, 2010). With this method, detailed kinetics features may be introduced through the direct use of detailed chemical mechanisms. However, such strategy is expensive and modeling efforts remain to be done towards micro-mixing. Nonetheless, efficiency of PDF methods to tackle auto-ignition has been demonstrated in the hydrogen/nitrogen case (Cabra et al., 2002; Masri et al., 2004; Cao et al., 2005; Gordon et al., 2007a; Jones and Navarro-Martinez, 2007) and the methane/air case (Cabra et al., 2005; Gkagkas and Lindstedt, 2007; Gordon et al., 2007b). Analysis of the lift-off height sensitivity to the flow temperature were conducted. Despite experimental uncertainties, transport PDF fairly predict the trend.
Hence, confident in their results, Gordon et al. (2007a,b) post-process their computations to find out which mechanism was responsible for the flame stabilization. The analysis is based on balance between advection, diffusion and chemistry, and species indicator to discriminate auto-ignition from propagative deflagration flame. Indeed, auto-ignition is expected to display chemical precursors of ignition such as CH_2O and H_2O_2 and balance between chemistry and advection only. In opposite, deflagration does not yield to the production of low temperature precursors and is characterized by a balance of advection and diffusion in low temperature regions and a balance of chemistry and diffusion at high temperature. After analyzing their results, Gordon et al. (2007a,b) argued auto-ignition is the phenomenon responsible for the stabilization of the flame rather than premixed flame propagation.
Unfortunately, transported PDF methods remain too expensive in CPU resources, especially for industrial applications. Flamelets based tabulated chemistry is an alternative strategy which allow considerable CPU saving compared to PDF methods:

- Detailed kinetics effects are introduced at low cost using few controlling parameters.

- Turbulent combustion modeling is addressed using presumed PDF.

This approach was applied to the Cabra methane/air flame by Domingo et al. (2008) and later by Michel et al. (2009). Domingo et al. (2008) used homogeneous auto-ignition and laminar premixed flamelets to build a look-up table for LES context. Michel et al. (2009) performed RANS computations with a table of unsteady flamelets. However, these flamelets were not exact and were approximated from homogeneous auto-ignition computations (Michel et al., 2008). In both models, micro-mixing i.e. diffusion is necessary in the flamelets generation to ignite cold mixtures: Michel et al. (2008) introduced diffusion between different mixture fraction layers while Domingo et al. (2008) tabulation involved premixed flamelets where burnt gases diffuse towards fresh ones. In fact, in the Cabra burner configuration, only hot lean mixtures can quickly ignite spontaneously and rich mixtures auto-ignition delays are too large without taking into account diffusion in the flamelets solutions.
Consequently, several results point unsteady laminar flamelets solutions as a good candidate to describe the flame structure. In this chapter, such flamelets are computed and examined to understand the physical phenomena responsible for ignition. The solutions are then stored in a database parametrized by mixture fraction, progress variable and scalar dissipation rates. This representation of auto-ignition in non-premixed turbulent flame is called Unsteady flamelets Tabulated Chemistry (UTaC).

5.2 Modeling configuration

The investigated flame configuration is depicted in Fig. 5.1. The ignition and the flame stabilization take place while fuel and oxidizer streams mix. The sketched turbulent flame shows ignition kernels which grow and form a steady diffusion flame as they move downstream. It is assumed that:

- Mixing occurs between only two streams, fuel and oxidizer. By considering only two streams, the impact of recirculating burnt gases by locally changing the composition is neglected.

- Conditions to promote auto-ignition as a flame stabilization mechanism are fulfilled: for instance, one or both mixtures are vitiated with hot gases such as in the Cabra burner*.

Following Peters (2000) analysis, the turbulent flame structure can be modeled by a collection of strained laminar flamelets of which boundary conditions correspond to fuel and air conditions. Hence, flamelet boundary conditions are prescribed by mixture compositions on the fuel (Y_k^{fuel}, T^{fuel})

*In IC engine such as HCCI, auto-ignition is promoted by high pressure.

and oxidizer (Y_k^{ox}, T^{ox}) sides where Y_k are species mass fraction and T the temperature. Different flamelet structures corresponding to different locations in the reactive shear layer are sketched in Fig. 5.1. The temperature profile evolves from a line characteristic of pure mixing to the profile of a steady burning diffusion flamelet. During intermediate states, ignition starts at the most-reactive mixture fraction z_{MR} and spreads to other mixtures.
Deflagration may occur in such combustion regimes. However, it has been shown in different studies (Gordon et al., 2007b,a, 2008; Yoo et al., 2009) that the influence of these phenomena in the flame stabilization is negligible compared to auto-ignition events that are promoted by the elevated air stream temperature. Furthermore, it was recently demonstrated experimentally by Choi et al. (2009) that tribrachial edge structures vanish when the level of dilution is high i.e. in the mild combustion mode. Therefore we will assume that chemical flame structure can be mapped by a collection of self-igniting non-premixed flamelets and premixed flame front propagation effects will be neglected.
Heat losses are neglected to propose first an adiabatic model.

5.3 Equations of unsteady laminar non-premixed flamelets

Assuming constant species Lewis number, Le_k, transient flamelets equations for species mass fractions, Y_k and temperature, T, are written in mixture fraction space (Pitsch and Peters, 1998; Peters, 2000):

$$\rho\frac{\partial Y_k}{\partial \tau} = \frac{\rho\chi}{2}\frac{1}{Le_k}\frac{\partial^2 Y_k}{\partial z^2} + \rho\dot{\omega}_k \tag{5.1}$$

$$\rho\frac{\partial T}{\partial \tau} = \frac{\rho\chi}{2}\frac{\partial^2 T}{\partial z^2} + \sum_{k=1}^{N}\frac{\rho h_k\dot{\omega}_k}{c_p} + \frac{\rho\chi}{2}\frac{1}{c_p}\frac{\partial c_p}{\partial z}\frac{\partial T}{\partial z} + \sum_{k=1}^{N}\frac{\rho\chi}{2}\frac{c_{p_k}}{c_p}\frac{1}{Le_k}\frac{\partial Y_k}{\partial z} \tag{5.2}$$

ρ, $\dot{\omega}_k$, h_k and c_{p_k} are respectively the mass density, the chemical species reaction rates, species enthalpies and species mass heat capacities at constant pressure. C_p is the mixture heat capacity and λ is the mixture thermal conductivity. $\chi = 2D_z\left(\frac{\partial z}{\partial x_i}\frac{\partial z}{\partial x_i}\right)$ is the scalar dissipation rate where $D_z = \frac{\lambda}{\rho c_p}$. χ is function of flow conditions and must be modeled. In steady strained counter-flow, the scalar dissipation rate is expressed in terms of mixture fraction and a, the flame strain rate, through the following analytical function (Peters, 2000):

$$\chi(z) = \frac{a}{\pi}\exp\left(-2[\mathrm{erf}^{-1}(2z-1)]^2\right) = aF(z) \tag{5.3}$$

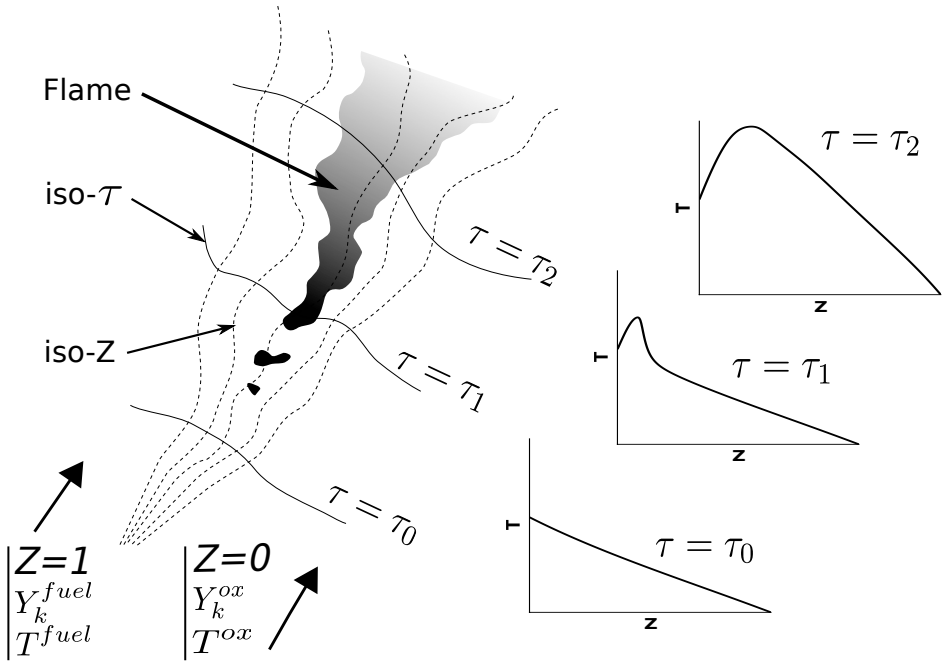

Figure 5.1: *Schematic of auto-ignition in a partially non-premixed turbulent flow (left) and the corresponding non-premixed flamelets (right). Left: the flame (in grey) is stabilized between fuel ($z = 1$) and oxidizer ($z = 0$) streams ; isolines of lagragian time (plain curves) and isolines of mixture fraction (dashed curves) are plotted. Right : temperature versus mixture fraction in a laminar non-premixed flamelet at three different times $\tau = \tau_0, \tau_1, \tau_2$.*

With the introduction of the stoichiometric scalar dissipation rate, $\chi_{st} = \chi(z = z_{st})$, Eq. 5.3 becomes:

$$\chi(z) = \chi_{st} \frac{F(z)}{F(z_{st})} \tag{5.4}$$

Numerical computations of transient equations 5.1-5.2 require an initial solution in mixture fraction space. At $t = 0$, fuel and oxidizer are mixed and reaction does not occur yet. Species mass fractions, $Y_k(t = 0)$, and enthalpy $h(t = 0)$ are then linear functions of z:

$$Y_k(z, t = 0) = z Y_k^{fuel} + (1 - z) Y_k^{ox} \tag{5.5}$$

$$h(z, t = 0) = z h^{fuel} + (1 - z) h^{ox} \tag{5.6}$$

where *fuel* and *ox* superscripts refer to fuel and oxidizer respectively. The initial temperature profile, $T(z, t = 0)$, is deduced from the local composition, $Y_k(z, t = 0)$ and the enthalpy, $h(z, t = 0)$. The unsteady flamelet equations are solved with the *FLAMEMASTER* code (Pitsch, 1998). Pressure and χ_{st} are not time dependent.
In the specific case where $\chi_{st} = 0$ s^{-1}, equations 5.1-5.2 reduce to homogeneous auto-ignition configurations:

$$\rho \frac{dY_k}{dt} = \rho \dot{\omega}_k \tag{5.7}$$

$$\rho \frac{dT}{dt} = \sum_{k=1}^{N} \frac{\rho h_k \dot{\omega}_k}{c_p} \tag{5.8}$$

where initial compositions remain defined by Eq. 5.5-5.6. This set of equations is solved using the SENKIN program from the CHEMKIN package (Kee et al., 1985b) in constant pressure mode.

5.4 Analysis of laminar flamelets results in the methane/air case

Simulations of flamelets representative of the methane/air case are performed using the GRI 3.0 mechanism (Smith et al., 2000) involving 53 species and 341 reactions. Solutions are analyzed to understand the auto-ignition phenomenon and its dependence on the simulation parameters. Fuel and oxidizer mixture compositions and temperature are listed in Tab. 5.1. Species Lewis number are assumed equal to unity. A collection of flamelets is computed under atmospheric pressure for different values of the parameter χ_{st}.

	Central Jet	Coflow
T (K)	320	1,350
X_{O2}	0.15	0.12
X_{N2}	0.52	0.73
X_{H2O}	0.0029	0.15
X_{CH4}	0.33	0.003

Table 5.1: *CH_4/Air experimental boundary conditions (temperature and species molar fractions). These conditions are retained to define the flamelet boundary conditions.*

5.4.1 Temperature and species mass fractions evolution

Figure 5.2 shows the evolution of temperature in mixture fraction space from the frozen initial solution to the steady diffusion flamelet solution. Between $t = 0$ and $t = 3.5$ ms, auto-ignition starts preferentially in a lean and hot temperature mixture. Here, the stoichiometric mixture is $z_{st} = 0.175$ and the most-reactive mixture z_{MR} is 0.0015. z_{MR} is defined as the mixture with the minimal ignition delay. Following the early ignition of lean mixtures, a combustion wave propagates in z-space quickly from z_{MR} to $z \approx 0.2$ between $t = 3.5$ ms at $t = 5$ ms. Afterwards, the temperature keeps increasing in rich mixtures very slowly until the steady solution is reached. In fact, rich mixtures are poorly reactive and mainly controlled by diffusion. It explains the combustion slow down.
Major species mass fractions are plotted in figure 5.3. Mass fractions follow the same pattern than temperature profiles: reaction starts at $z = z_{MR}$, a wave propagates across iso-z and a steady flame solution is reached. Note that Y_{O_2} is higher on the fuel side because methane is premixed with air. Pre-ignition precursors such as H_2O_2, HO_2 or CH_2O are plotted in Fig. 5.4. These radicals are first created during ignition stage (Gkagkas and Lindstedt, 2007; Gordon et al., 2007b) and accumulated close to z_{MR} before following the combustion wave in z-space.

5.4.2 Auto-ignition delay analysis

In the present study, the auto-ignition delay τ_{ai} is defined by the instant where the derivative $|\frac{\partial T}{\partial \tau}|$ is maximal. These delays are computed for unsteady diffusion flamelets as function of z and χ_{st}. Note that the extreme situation where scalar dissipation rate is equal to zero corresponds to a collection of independent homogeneous reactors. Figure 5.5 (a) and (b) shows the variation of ignition delay for different values of stoichiometric scalar dissipation rate. In order to analyze the effect of χ_{st} on the unsteady flamelet structure, we first focus around $z = z_{MR}$ (Fig. 5.5(b)). The smallest τ_{ai} is

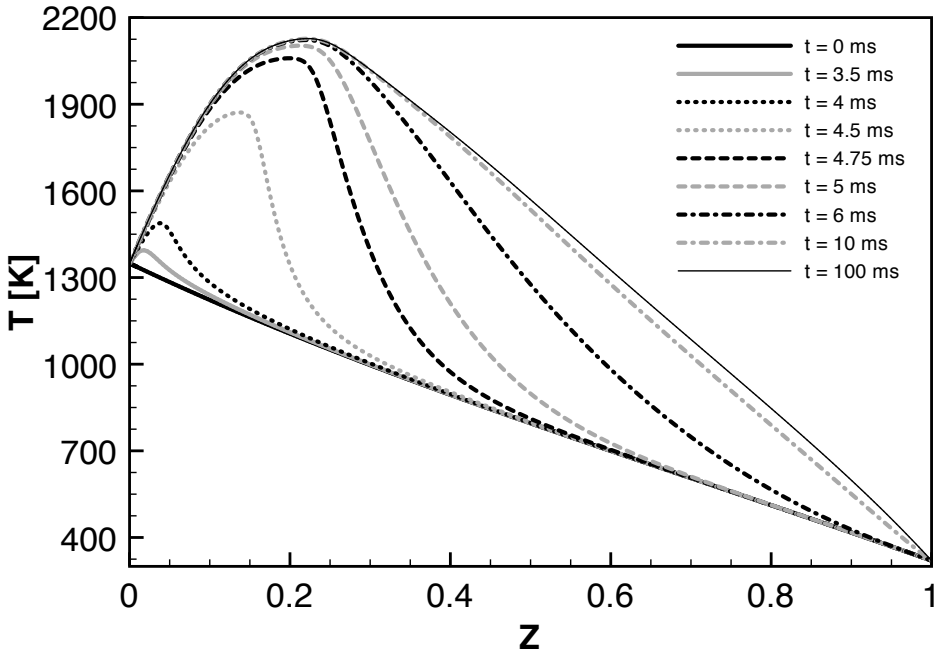

Figure 5.2: *Unsteady temperature profile in mixture fraction space. The flamelet was generated with χ_{st} fixed to 30 s^{-1}.*

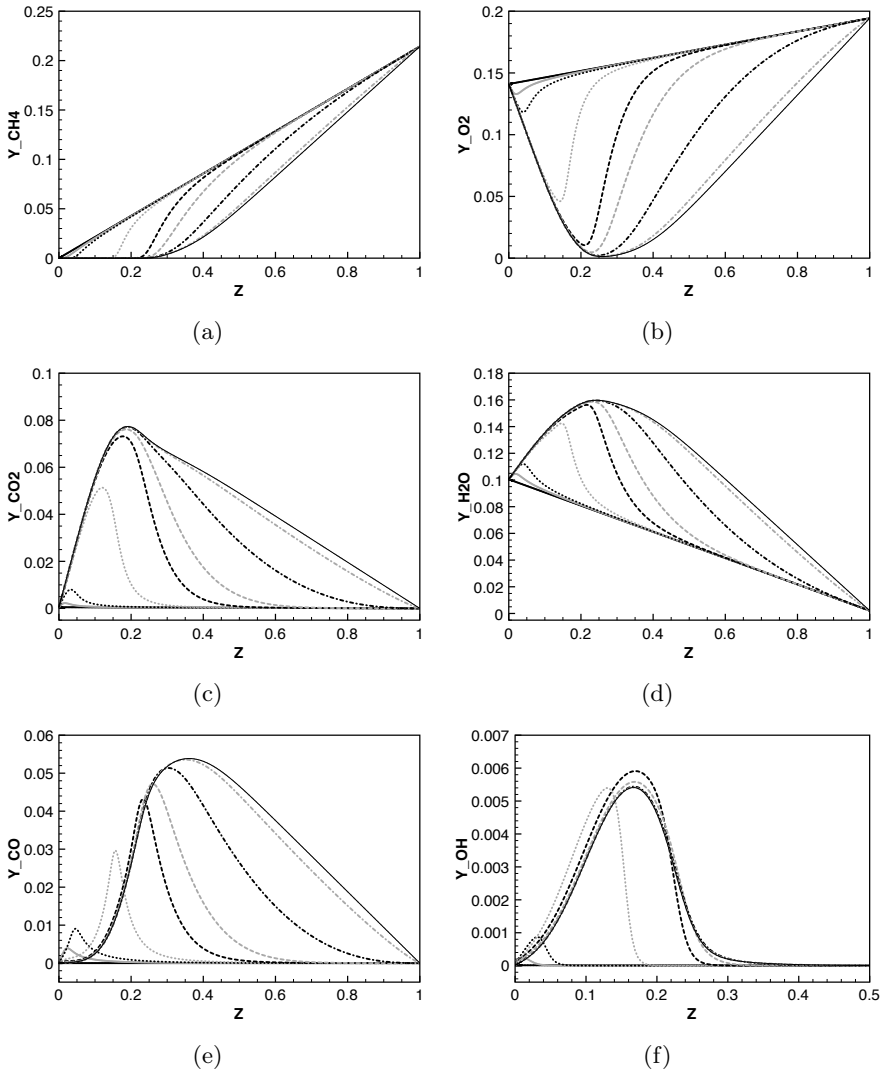

Figure 5.3: *Unsteady species mass fractions profile in mixture fraction space: (a) CH_4 (b) O_2 (c) CO_2 (d) H_2O (e) CO (f) OH. The flamelet was generated with χ_{st} fixed to 30 s^{-1}. The legend is the same as in Fig. 5.2.*

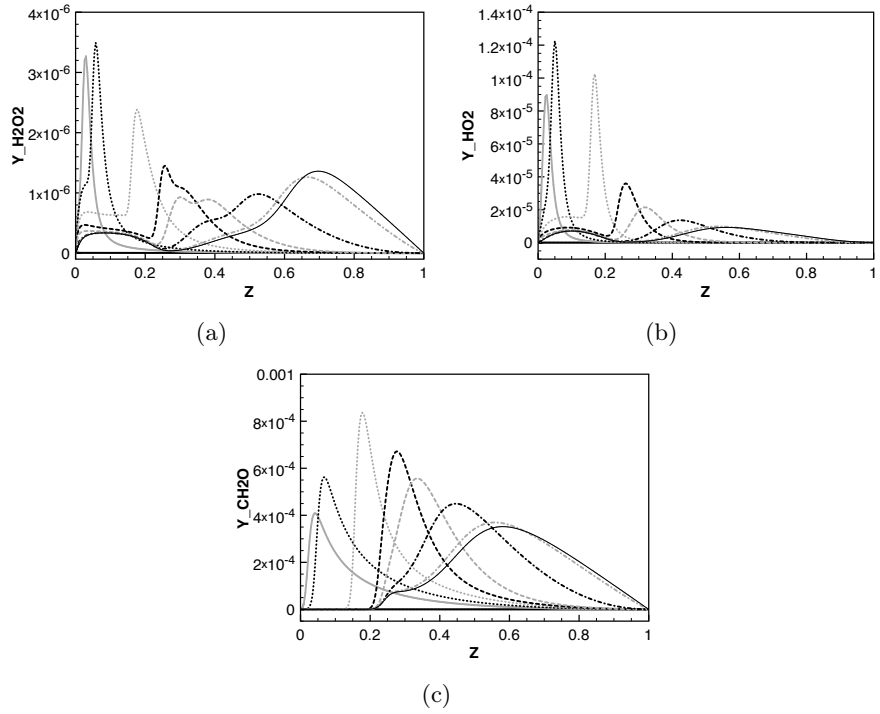

Figure 5.4: *Unsteady mass fractions profile of precursors species in auto-ignition in mixture fraction space: (a) H_2O_2 (b) HO_2 (c) CH_2O. The flamelet was generated with χ_{st} fixed to 30 s^{-1}. The legend is the same as in Fig. 5.2.*

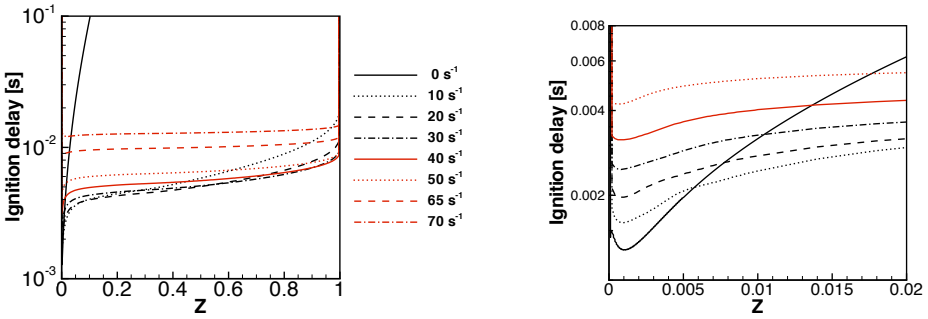

(a) All mixture fraction range (b) Zoom in lean region: $z \in [0; 0.02]$

Figure 5.5: *Variation of ignition delays as a function of mixture fraction for several χ_{st} values. The left scale is logarithmic.*

observed in homogeneous ignition (χ_{st} is null). An increase of χ_{st} from 0 s^{-1} to 70 s^{-1} delays ignition until a critical value, $\chi_i = 80$ s^{-1}, where combustion never starts. Indeed diffusion of heat and radical species from $z = z_{MR}$ to unburnt neighboring mixtures will slow down combustion process. Note that this observation is consistent with literature on DNS of auto-ignition (Mastorakos, 2009).
For other mixture fractions, the phenomenon is more complex: when χ_{st} increases, $\tau_{ai}(z)$ first decreases then goes up until no combustion occurs at $\chi_{st} = \chi_i$ (Fig. 5.5(a)). For instance at $z = z_{st}$, τ_{ai} first falls down from 100 ms to 3 ms when χ_{st} varies between 0 s^{-1} and 20 s^{-1}. The ignition of unburnt mixtures is promoted by heat and radical species diffusion from ignited lean mixtures, which, at the same time, have been slightly delayed. Nonetheless, the overall diffusion benefit is positive and makes the whole flamelet ignite a little moment after lean mixtures. Then, when χ_{st} varies between 20 s^{-1} and 70 s^{-1}, τ_{ai} at stoichiometric mixture increases from 3 ms to 10 ms. Hence, as hot mixtures ignition is more delayed, all mixtures follow the same trend. Ultimately, once $\chi_{st} = \chi_i$, no combustion takes place.

Figure 5.6 plots τ_{ai} of different mixtures in terms of χ_{st}. Scalar dissipation increase always penalizes ignition of lean hot mixtures whereas rich and cold mixtures ignition first benefits of diffusion before being also delayed. The line $\chi_{st} = \chi_i$ is an asymptotic line as no combustion stars spontaneously after this value.

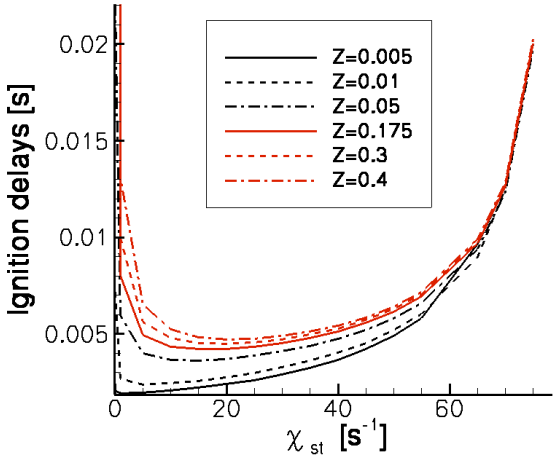

Figure 5.6: *Variation of ignition delays as a function of χ_{st} for different mixtures (lean: z =0.005, 0.01, 0.05 ; stoichiometric: z =0.175 ; rich: z =0.3, 0.4). Ignition time becomes infinity for $\chi_{st} > \chi_i$.*

5.5 Effect of differential diffusion

The effect of differential diffusion is now studied by considering non-unity species Lewis number: $\mathrm{Le}_k \neq 1$. In order to estimate Le_k numbers, we use two important properties observed by Pitsch and Peters (1998). They first showed that steady flamelet computations with detailed transport properties are well approximated by flamelets computed using constant Lewis number for each species. The numbers Le_k are evaluated at a specific point in the flamelet with full transport description and this value is imposed to all other points: $\mathrm{Le}_k(z) = cte$. Secondly, Pitsch and Peters (1998) found that, once the species Lewis numbers are computed for a specific configuration, the choice is valid for other configurations.
In the present case, species Lewis numbers are computed at the point of maximal temperature in a steady diffusion flamelet with $\chi_{st} = 20$ s^{-1}. The list of Le_k is given in Tab. 5.2 for each species of the chemical mechanism GRI 3.0. The influence of species Lewis numbers is first investigated on steady state diffusion flamelets (Fig. 5.7). The maximum temperature is decreased by approximately 100 K when non-unity Le_k are considered. The enthalpy profile $h(z)$ (Fig. 5.7(b)) is also sensitive to differential diffusion. If $\mathrm{Le}_k = 1$, h remains a linear function of mixture fraction in opposition to the case where $\mathrm{Le}_k \neq 1$. Different species mass fractions are plotted in Fig. 5.7 and show that the more different from unity Le_k is, the more the species profile changes in comparison with the unity-Lewis-number solution.
In the present CH_4/air configuration, differential diffusion in steady flamelet

Species	Lewis Number	Species	Lewis Number
$N2$	1.130	AR	1.101
O	0.699	O_2	1.071
H	0.181	OH	0.712
H_2	0.300	HO_2	1.077
H_2O_2	1.085	CH	0.654
CO	1.089	CH_2	0.963
HCO	1.236	$CH_2(S)$	0.963
CH_3	0.984	CH_2O	1.246
CH_4	0.988	CO_2	1.356
CH_2OH	1.271	CH_3O	1.271
CH_3OH	1.274	C_2H	1.274
C_2H_2	1.286	$HCCO$	0.858
C_2H_3	1.298	CH_2CO	1.470
C_2H_4	1.297	C_2H_5	1.415
C_2H_6	1.427	H_2O	0.790
C	0.748	$HCCOH$	1.470
N	0.787	NO	1.097
N_2O	1.352	NO_2	1.227
NH	0.663	HNO	1.080
NH_2	0.676	NNH	1.115
CN	1.108	NCO	1.340
HCN	1.244	$HOCN$	1.346
$HNCO$	1.346	H_2CN	1.255
$HCNN$	0.858	$HCNO$	1.346
NH_3	0.873	CH_2CHO	1.477
CH_3CHO	1.483	C_3H_8	1.839
C_3H_7	1.831		

Table 5.2: *Species Lewis numbers computed in a steady diffusion flamelet with* χ_{st}*=20* s^{-1} *for the methane/air case.*

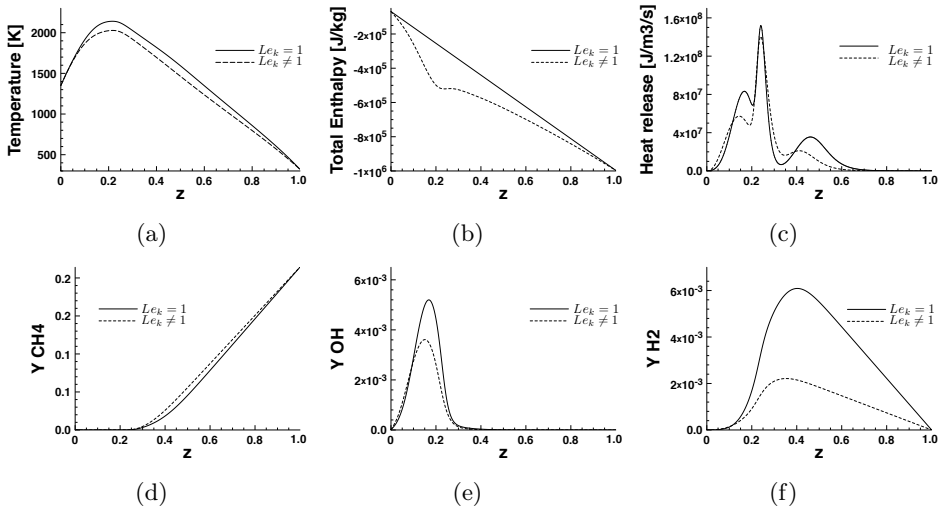

Figure 5.7: *Effect of species Lewis numbers in a steady diffusion flamelet for the methane/air case with $\chi_{st} = 20\ s^{-1}$ on: (a) temperature ; (b) enthalpy (chemical + sensible) ; (c) heat release ; (d) CH_4mass fraction ; (e) OH mass fraction ; (f) H_2 mass fraction. Plain line: $Le_k = 1$. Dashed line: non-unity Le_k given in Tab. 5.2.*

	Central Jet	Coflow
T (K)	305	1045
X_{O2}	0.0	0.15
X_{N2}	0.75	0.75
X_{H2O}	0.0	0.1
X_{H2}	0.25	0.0

Table 5.3: *H_2/N_2r experimental boundary conditions (temperature and species molar fractions). These conditions are retained to define the flamelet boundary conditions.*

computations has a noticeable but small impact on temperature and major species. It can therefore be neglected. Would species for which Le_k is highly different from unity participate to the fuel composition, differential diffusion effects are expected to be amplified. This is investigated by computing a steady diffusion flamelet for the H_2/N_2 configuration whose compositions are given in Tab. 5.3.

All H_2/N_2 flamelets are computed using the hydrogen oxidation mechanism developed by Ó Conaire et al. (2004). Species Lewis numbers are evaluated as previously and given in Tab. 5.4. Two steady flamelet are depicted in Fig. 5.8: the first one is computed with $\mathrm{Le}_k = 1$ and the second one with $\mathrm{Le}_k \neq 1$. The temperature profile is very different between the two flamelets. The first flamelet has a temperature maximum of 1600 K close to the stoichiometric

Species	Lewis Number
N_2	1.170
AR	1.054
H	0.173
O_2	1.025
O	0.668
OH	0.681
H_2	0.288
H_2O	0.764
HO_2	1.030
H_2O_2	1.037

Table 5.4: *Species Lewis numbers computed in a steady diffusion flamelet with χ_{st}=20 s^{-1} for the hydrogen/nitrogen case.*

mixture fraction $z_{st} = 0.475$ while the second flamelet temperature maximum is 2030 K and is located around $z = 0.2$. Other quantities shown in Fig. 5.8 are highly sensitive to species Lewis numbers.
In order to derive Eqs. 5.1 and 5.2, the mixture fraction z was defined as solution a passive scalar balance equation where the diffusivity coefficient D_z is computed from a unity mixture fraction Lewis number (Pitsch and Peters, 1998). When all species Lewis numbers are equal to unity, this definition is coherent with other mixture fraction definitions based on each single element mass fractions z_i (Eq. 2.2). Indeed, for each element, a mixture fraction Z_i can be defined by normalization of z_i between its value in fuel (z_{if}) and oxidizer (z_{ox}):

$$Z_i = \frac{z_i - z_{io}}{z_{if} - z_{io}} \tag{5.9}$$

With unity species Lewis numbers, all definitions are equivalent and are solution of the same balance equation. This is not true anymore once $\mathrm{Le}_k \neq 1$: the mixture fraction z defined by its balance equation and the local fuel/oxidizer ratio are not related anymore. Consequently, the stoichiometric mixture fraction point $z = z_{st}$ in flamelet solutions becomes irrelevant when differential diffusion is important, and that is why the maximum temperature location changes in Fig. 5.8(a).
In order to retrieve the stoichiometric notion using mixture fraction framework, Bilger et al. (1990) have defined a mixture fraction z_{Bilger} from the combination of elemental element mass fraction. For the oxidation of methane, z_{Bilger} is given by:

$$z_{Bilger} = \frac{Z - Z_o}{Z_f - Z_o} \quad \text{with} \quad Z = 2\frac{Y_C}{W_C} + \frac{Y_H}{2W_H} - \frac{Y_O}{W_O} \tag{5.10}$$

Y_C, Y_H and Y_O are the element mass fractions for respectively carbon, hydro-

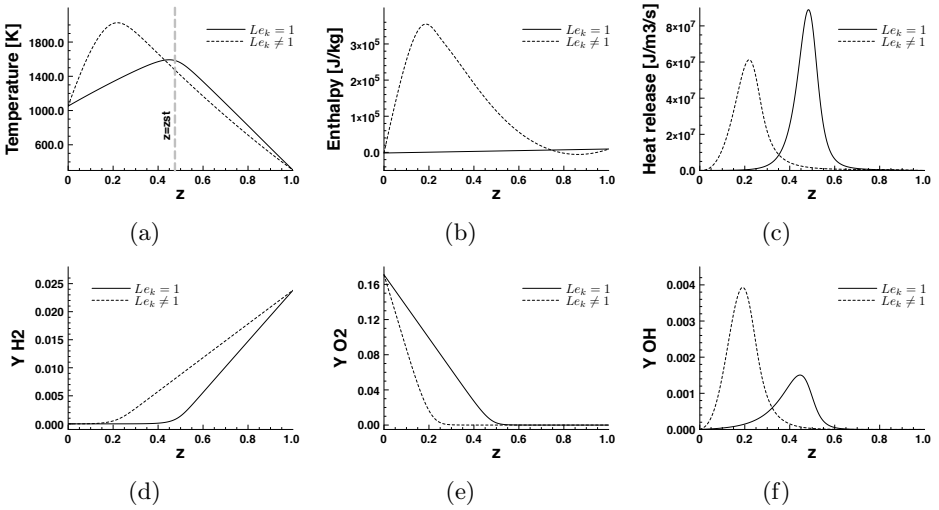

Figure 5.8: *Effect of species Lewis numbers in a steady diffusion flamelet for the hydrogen/nitrogen case with $\chi_{st} = 20\ s^{-1}$ on: (a) temperature ; (b) enthalpy (chemical + sensible) ; (c) heat release ; (d) H_2 mass fraction ; (e) O_2 mass fraction ; (f) OH mass fraction. Plain line: $Le_k = 1$. Dashed line: non-unity Le_k given in Tab. 5.4. The location of z_{st} is indicated by a thick vertical grey line.*

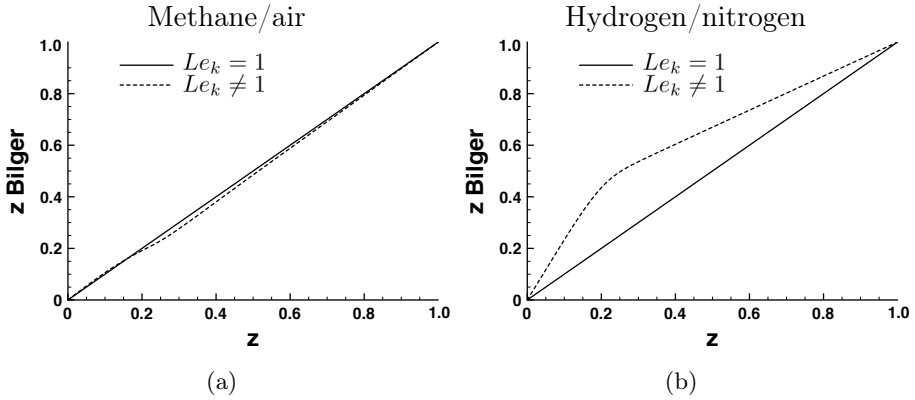

Figure 5.9: *Mixture fraction defined by Bilger z_{Bilger} is plotted versus z in both Cabra flame configurations: methane/air (a) and hydrogen/nitrogen (b). Plain line: unity Lewis numbers. Dashed line: non-unity Lewis numbers.*

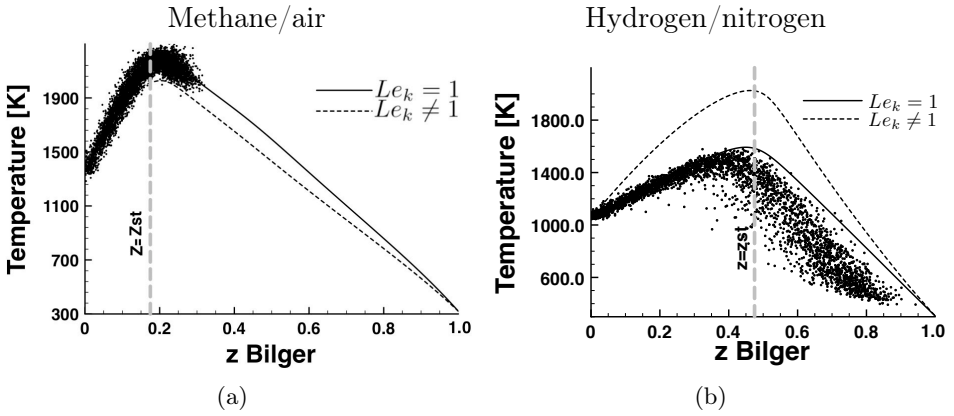

Figure 5.10: *Temperature versus z_{Bilger} for methane/air (a) and hydrogen/nitrogen (b) configuration. Two steady diffusion flamelets computed with $\chi_{st} = 20\ s^{-1}$ are plotted: non-unity Le_k (plain line) and unity Le_k (dashed line). Scattor plots of experimental data are represented by dots at $x/d = 70d$ for the CH_4/air case and $x/d = 14d$ for the H_2/N_2 case. The location of z_{st} is indicated by a thick vertical grey line.*

gen and oxygen. These quantities are weighted by the element molar mass. f and o subscripts denote respectively values of Z in fuel and oxidizer. For hydrogen oxidation, definition of z_{Bilger} reduces to:

$$z_{Bilger} = \frac{Z - Z_o}{Z_f - Z_o} \quad \text{with} \quad Z = \frac{Y_H}{2W_H} - \frac{Y_O}{W_O} \tag{5.11}$$

When differential diffusion effects are significant, only the equality $z_{Bilger} = z_{st}$ makes sense, while $z = z_{st}$ does not. The mixture fraction z_{Bilger} is plotted in flamelets with and without unity species Lewis numbers for both configurations in Fig. 5.9. When $\mathrm{Le}_k = 1$, z and z_{Bilger} are identical as expected. In the case where $\mathrm{Le}_k \neq 1$, z_{Bilger} remains close to the diagonal identity line in the CH_4/air configuration in opposition to the $\mathrm{H_2/N_2}$ configuration. This explains the shift of the temperature maximum in z-space which was observed in the hydrogen/nitrogen flamelet computed with differential diffusion. It is verified by representing temperature as a function of z_{Bilger} instead of z in Fig. 5.10. In the CH_4/air configuration (Fig. 5.10(a)), the figure does not significantly change from Fig. 5.7(a). In the opposite way, the H_2/N_2 temperature profile for which $\mathrm{Le}_k \neq 1$ is changed and the temperature maximum is now located at $z_{Bilger} = z_{st}$.
Direct numerical simulations (Hilbert and Thevenin, 2002; Mastorakos, 2009) have shown that the level of transport description can significantly change the ignition delays. Hence, influence of differential diffusion is now studied in the transient flamelet computations. For both fuel configurations, auto-igniting flamelets are computed with and without unity species Lewis numbers. The auto-ignition delay profiles in mixture fraction space are first

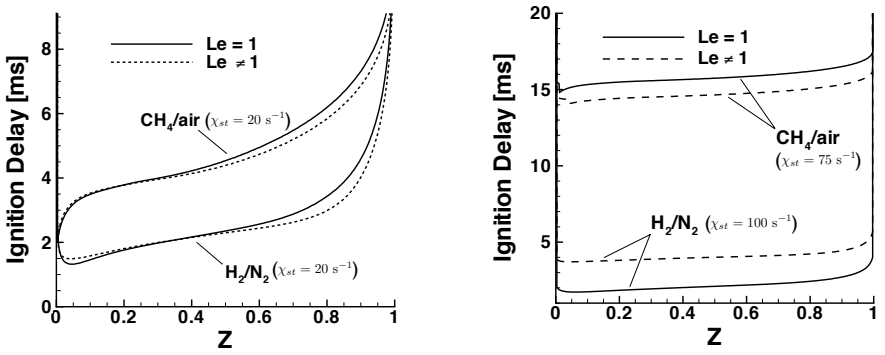

Figure 5.11: *Impact of species Lewis numbers on auto-ignition delays computed at different mixture fraction z in a transient flamelet computation. (a) CH_4/air and H_2/N_2 cases are computed with $\chi_{st} = 20\ s^{-1}$. (b) CH_4/air and H_2/N_2 cases are respectively computed with $\chi_{st} = 75\ s^{-1}$ and $\chi_{st} = 100\ s^{-1}$. Plain line: $Le_k = 1$. Dashed line: non-unity Le_k.*

shown in Fig. 5.11(a) with $\chi_{st} = 20\ \mathrm{s}^{-1}$. It is observed that ignition delays of the H_2/N_2 configuration are shorter than those for the CH_4/air configuration. This is consistent with the fact that the lift-off height is shorter in the H_2/N_2 flame ($H/d = 10$) than the one in the CH_4/air flame ($H/d = 35$), knowing that similar injection velocity was used in both configurations (Cabra et al., 2002, 2005). There is also a difference in the value of z_{MR} between both configurations: in the H_2/N_2 flame, z_{MR} is close to 0.01 while it is 0.0015 in the CH_4/air configuration. Concerning the effect of species Lewis numbers, both configurations present only a small deviation from the case where $\mathrm{Le}_k = 1$. This observation is different from other results in the literature (Hilbert and Thevenin, 2002; Mastorakos, 2009). However, it appears that numerical solutions were initialized with large gradients of mixture fractions, the effect of differential diffusion might then be reinforced. This point is investigated by computing transient flamelets with higher stretch. Results are shown in Fig. 5.11(b) and clearly demonstrate that the variation of auto-ignition delays when $\mathrm{Le}_k \neq 1$ depends on χ_{st}: in the CH_4/air configuration, the ignition delays changes over a small percentage while it doubles in the H_2/N_2 case.

It was shown that differential diffusion has a relatively small impact on the CH_4/air configuration in comparison to the hydrogen/nitrogen case. It could then be expected to retain non-unity species Lewis numbers to build the chemical database when the fuel is composed of hydrogen, however this choice turns out to be inaccurate in turbulent flows (Peters, 2000). This is shown for the present configuration in Fig. 5.10 where experimental scatter plots have been added to the flamelets profiles. As described by Cabra et al. (2002) and Cabra et al. (2005), the scatter data are close to the unity

species Lewis numbers solution for both fuel configurations. In fact, the scale separation assumption to derive flamelet models is not valid on the entire mixture fraction range from zero to one: small vortices are able to enter the diffusive layer, which create a turbulent flux in z-space. This term appears in Conditional Moment Closure (CMC) species balance equations (Bilger, 1993). Peters (2000) shows that the laminar and turbulent fluxes in z-space can be gathered using an effective Lewis number. The fact that this number is close to unity explains why laminar flamelets computed with $\mathrm{Le}_k = 1$ are able to match experimental data from turbulent non-premixed flames.
In some configurations, experimental measurements exhibit an effect of differential diffusion. Pitsch (2000) pictured three different mechanism leading to such effects. The first one is due to the presence of laminar regions around the jet potential core. The second mechanism explains that the laminar diffusion coefficient might be of same order as the turbulent diffusivity. Finally, the third explanation indicates that the scale separation assumption is actually valid on the whole mixture fraction range in some regions. These regions are identified by analyzing different turbulent scales and the diffusive thickness. In the Cabra experiment, scatter plots shown in Fig. 5.10 demonstrate that the flow is turbulent enough for laminar fluxes to be negligible. This rules out the occurrence of second and third mechanisms. Finally, the first mechanism can not occur because the flame is lifted and hence, is not attached close to the jet exit where the laminar regions exist. Consequently, the different chemical databases are built with unity species Lewis numbers.

5.6 Tabulation of laminar flamelets solutions

In order to generate the chemical table, flamelet equations are solved from unburnt mixtures up to the steady state flamelet solution.
χ_{st} is assumed constant in time when building-up the chemical database. This assumption has two consequences:

- First, some steady flamelets solutions are not reached. Indeed, Fig. 5.12 represents the so-called S-curve: maximal temperature and heat release of steady state diffusion flamelet are plotted against $1/\chi_{st}$. Building a look-up table from unsteady igniting flamelets implies that any situation where $\chi_{st} > \chi_i$ remain cold. In reality for $\chi_i < \chi_{st} < \chi_q$, where χ_q is the steady state quenching limit, steady state burning solutions exist that cannot be reached starting from an initial frozen solution. However, this assumption has a very small impact in the studied configuration since high scalar dissipation rates are located close to the jet nozzle where no combustion occurs[†].

[†]Another scenario where transient high values of χ_{st} may stretch steady burning flamelets above χ_i is possible. It is however unlikely to occur in the studied configuration since the flame is lifted far away from the nozzle where χ_{st} is weak. For other

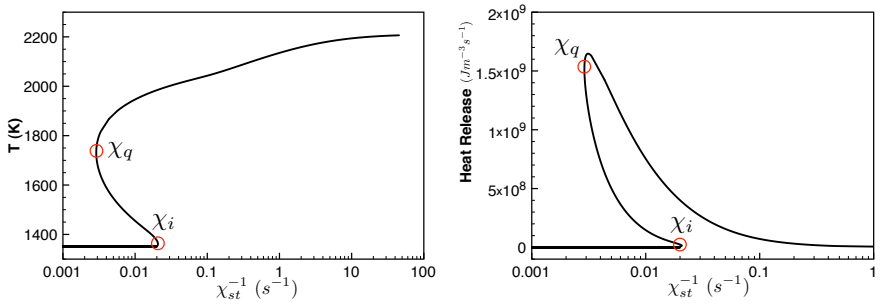

(a) (b)

Figure 5.12: *The maximum temperature (a) and the maximum heat release (b) of the steady solution flamelets is plotted in function of the inverse of the stoichiometric scalar dissipation rate. Two singular points are represented by circles: χ_i the ignition scalar dissipation rate and χ_q the quenching scalar dissipation rate.*

- During ignition and afterwards, flamelets undergo a time variable χ_{st}. By construction of the library, such unsteady effects in the table generation are neglected since χ_{st} was fixed.

Each flamelet solution is a function of mixture fraction, time and stoichiometric scalar dissipation rate. Any relevant variable can therefore be written as $\varphi(z, t, \chi_{st})$. The time variable is substituted by a reaction progress variable, c:

$$c = \frac{Y_c(z, t, \chi_{st}) - Y_{c_u}(z)}{Y_{c_b}(z, \chi_{st}) - Y_{c_u}(z)} \tag{5.12}$$

where Y_c is the non-normalized progress variable. In Eq. 5.12, maximal and minimal values of Y_c, Y_{c_b} and Y_{c_u}, are introduced for c to vary between zero and unity for each flamelet solution. Y_{c_u} is the initial solution with unburnt mixtures, which depends on z only, and when steady state is reached, Y_c is the steady state burning solution Y_{c_b} function of z and χ_{st}. Eq. 5.12 is different from Eq. 2.37 where the equilibrium profile $Y_{c_{eq}}(z)$ is used instead. However, when χ_{st} is null, the steady state solution is the equilibrium solution:

$$Y_{c_b}(z, \chi_{st} = 0) = Y_{c_{eq}}(z) \tag{5.13}$$

Laminar flamelets quantities are then tabulated as $\varphi(z, c, \chi_{st})$. FPI methods (Fiorina et al., 2003, 2005b) have proposed the following definition for the progress variable:

$$Y_c = Y_{CO_2} + Y_{CO} \tag{5.14}$$

configurations, assuming quenching for $\chi_{st} > \chi_i$ instead of χ_q might be a second order approximation.

This definition maps combustion reactions once CO and CO_2 are significantly produced in the flamelet. Therefore, the first stage where ignition precursors are created is not captured by the progress variable. Indeed, in order to enable auto-ignition, $\dot{\omega}_{Y_c}(c = 0)$ must be strictly positive. CH_4 species is then also considered in a revised definition of the progress variable Y_c:

$$Y_c = Y_{CO} + Y_{CO_2} - Y_{CH_4} + Y_{c_0}(z) \tag{5.15}$$

where $Y_{c_0}(z) = Y_{CH_{4_u}}(z)$ is added to the definition of Y_c in order to ensure that Y_c remains positive. By construction, Y_c is null in fresh gases and Eq. 5.12 is simplified:

$$c = \frac{Y_c(z, t, \chi_{st})}{Y_{c_b}(z, \chi_{st})} \tag{5.16}$$

Without taking into account turbulence-chemistry interactions yet, the present formulation of tabulated chemistry is available for laminar or Direct Numerical Simulation (DNS). Any variable of interest φ is tabulated as $\varphi(z, c, \chi_{st})$.

5.7 Unsteady mixing effects

It was previously outlined that the tabulation method neglects the effect of time dependency of χ_{st}. To investigate the error introduced by not considering this phenomenon, a non-reactive Large Eddy Simulation (LES) is performed and post-treated to extract a realistic function $\chi_{st}(\tau)$ representative of the unsteady scalar dissipation rate that undergoes a flamelet in the turbulent flow. The profile $\chi_{st}(\tau)$ is then used to compute an unsteady flamelet ignition with time varying χ_{st}, this solution is finally compared with the already generated database by a priori tests.

5.7.1 Extracting the profile $\chi_{st}(\tau)$

In chapter 3, a non-reactive LES of the Cabra burner was performed by solving balance equations for mass density, momentum, energy and mixture fraction. The balance equation for the mass-weighted filtered mixture fraction $\tilde{z}$ reads:

$$\frac{\partial \overline{\rho}\tilde{z}}{\partial t} + \frac{\partial}{\partial x_j}\left(\overline{\rho}\tilde{u}_j\tilde{z}\right) = \frac{\partial}{\partial x_j}\left(\overline{\rho}(D + D_t)\frac{\partial \tilde{z}}{\partial x_j}\right) \tag{5.17}$$

$\overline{\rho}$, $\tilde{u}_j$ are respectively the filtered mass density and the mass-weighted filtered velocity components. Subgrid mixture fraction flux is modeled by introducing the turbulent diffusivity D_t.
The LES is post-treated to define a Lagrangian flamelet time τ. At $\tau = 0$ s, the flamelet, defined as the stoichiometric mixture fraction iso-surface, is located at the fuel pipe lips. As depicted in Fig. 5.1, the flamelet starts with

the pure mixing solution, it is transported by the turbulent flow, ignites after a certain delay time and finally reaches a full burning state. Along the flamelet trajectory, different values of the scalar dissipation rate χ_{st} are encountered.

The flamelet time τ is computed following the method used by Pitsch and Steiner (2000). Velocity of resolved mixture fraction iso-surfaces is given by

$$\tilde{\boldsymbol{u}}_{\tilde{z}}(\boldsymbol{x},t) = \tilde{\boldsymbol{u}}(\boldsymbol{x},t) - \frac{\boldsymbol{\nabla}\cdot(\overline{\rho}(D+D_t)\boldsymbol{\nabla}\tilde{z})}{\overline{\rho}|\boldsymbol{\nabla}\tilde{z}|}\boldsymbol{i}_z \tag{5.18}$$

where $\boldsymbol{i}_z = \boldsymbol{\nabla}\tilde{z}/|\boldsymbol{\nabla}\tilde{z}|$. The axial component is obtained by multiplying $\tilde{\boldsymbol{u}}_{\tilde{z}}$ by the unit vector $\boldsymbol{e}_x$ oriented along the jet axis. It is then conditionally averaged for several planes at different distance from the fuel pipe exit and written for stoichiometric mixture fraction $\tilde{z} = z_{st}$ to compute the resolved velocity of flamelet sheets:

$$\langle\tilde{u}_{\tilde{z}}|\tilde{z}=z_{st}\rangle(x,t) = \langle\tilde{u}|\tilde{z}=z_{st}\rangle(x,t) - \left\langle\frac{\boldsymbol{\nabla}\cdot(\overline{\rho}(D+D_t)\boldsymbol{\nabla}\tilde{z})}{\overline{\rho}|\boldsymbol{\nabla}\tilde{z}|^2}\frac{\partial\tilde{z}}{\partial x}\Big|\tilde{z}=z_{st}\right\rangle \tag{5.19}$$

The flamelet Lagrangian time is then computed as

$$\tau(x,t) = \int_0^x \frac{1}{\langle\tilde{u}_{\tilde{z}}|\tilde{z}=z_{st}\rangle(x',t)}\,\mathrm{d}x' \tag{5.20}$$

For each instantaneous LES solution, a profile $\tau(x)$ can be computed. Pitsch and Steiner (2000) showed that instantaneous and time averaged profiles of $\tau(x,t)$ are similar. Figure 5.13 shows the profile $\langle\tilde{u}_{\tilde{z}}|\tilde{z}=z_{st}\rangle(x)$ computed from an instantaneous solution and the resulted profile $\tau(x)$. Similarly to the results of Pitsch and Steiner (2000), $\langle\tilde{\boldsymbol{u}}_{\tilde{z}}|\tilde{z}=z_{st}\rangle(x)$ stays close to a constant value, 20 m/s here, in the self-similar zone of the round jet. This independence from the axial distance can be shown analytically (Peters, 2000) and was verified experimentally (Donbar et al., 2001).

Next step consists in evaluating the stoichiometric scalar dissipation rate χ_{st} seen by the flamelet at the subgrid level along the axis. The obtained profile $\chi_{st}(x)$ is then expressed in function of the Lagrangian flamelet time as $\chi_{st}(\tau)$. The mass-weighted filtered scalar dissipation rate $\tilde{\chi}$ is first modeled following Girimaji and Zhou (1996):

$$\tilde{\chi} = 2(D_z + D_t)\frac{\partial\tilde{z}}{\partial x_i}\frac{\partial\tilde{z}}{\partial x_i} \tag{5.21}$$

Pitsch and Steiner (2000) computed the subgrid conditional mean $\langle\chi|z\rangle(\boldsymbol{x},t)$ and the flamelet scalar dissipation rate profile was approximated by $\chi(z,\boldsymbol{x},t) = \langle\chi|z\rangle(\boldsymbol{x},t)$ leading to $\chi_{st}(\boldsymbol{x},t) = \langle\chi|z=z_{st}\rangle(\boldsymbol{x},t)$. As we are only interested in the unsteady behavior of χ_{st} and not its precise value, χ_{st} is computed from the conditional mean of the resolved scalar dissipation rate:

$$\chi_{st}(x,t) = \langle\tilde{\chi}|\tilde{z}=z_{st}\rangle(x,t) \tag{5.22}$$

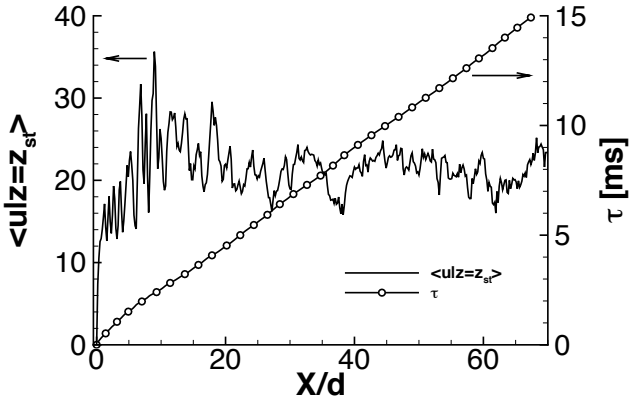

Figure 5.13: *The conditional mean $\langle \tilde{u}_{\tilde{z}} | \tilde{z} = z_{st} \rangle$ (plain line) and the flamelet Lagragian time τ (line + symbols) are plotted in function of the axial coordinate x/d where d the fuel pipe diameter.*

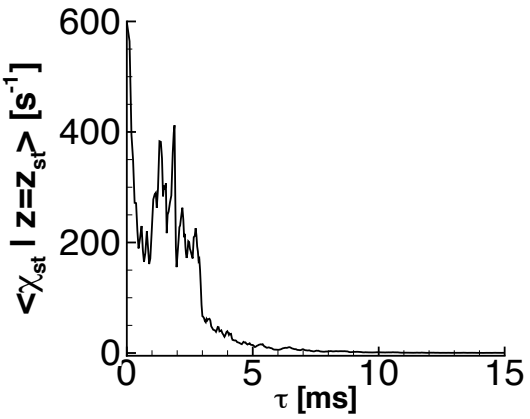

Figure 5.14: *Profile of $\chi_{st}(\tau)$ computed from Eq. 5.22.*

The profile $\chi_{st}(x)$ is computed for an instantaneous LES solution. The function $\chi_{st}(\tau)$ is plotted in Fig. 5.14 and is used in the following as an input to the *FLAMEMASTER* code to compute a flamelet ignition solution.

5.7.2 Comparison between flamelet and database

The function $\chi_{st}(\tau)$ is used to compute a reference solution including scalar dissipation rate unsteadiness. Any quantity (temperature, species mass fraction, ...) is a function of mixture fraction and time: $\varphi^{ref}(z, \tau)$. A priori comparisons with the tabulated quantities $\varphi^{tab}(z, c, \chi_{st})$ where χ_{st} was kept constant during the whole simulation are conducted. For each mixture fraction

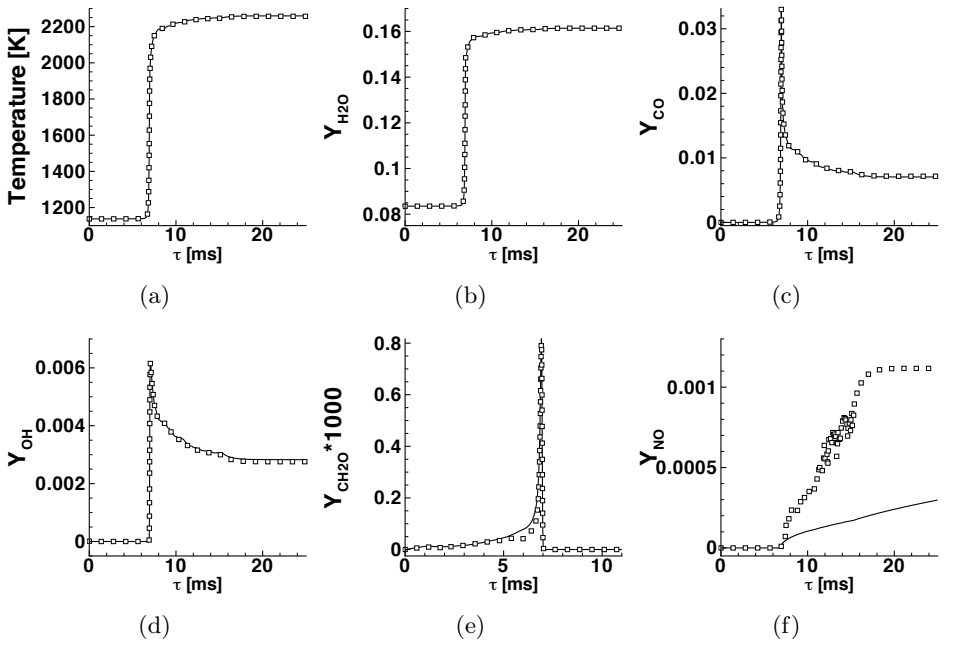

Figure 5.15: *Time evolution at $z = z_{st}$ of temperature (a) and species mass fractions: Y_{H_2O} (b), Y_{CO} (c), Y_{OH} (d), Y_{CH_2O} (e) and Y_{NO} (f). Plain line: reference solution computed with $\chi_{st}(\tau)$. Square symbols: solution interpolated in the database built for steady scalar dissipation rates.*

z and time τ of the reference solution, the corresponding progress variable $c^{ref}(z,\tau)$ is computed:

$$\begin{aligned} c^{ref}(z,\tau) &= \frac{Y_c^{ref}(z,\tau)}{Y_{c_b}^{tab}(z,\chi_{st}(\tau))} \qquad (5.23) \\ \text{where} \quad Y_c^{ref}(z,\tau) &= Y_{CO}^{ref}(z,\tau) + Y_{CO_2}^{ref}(z,\tau) - Y_{CH_4}^{ref}(z,\tau) + Y_{c_0}^{tab}(z) \end{aligned}$$

The variables $\varphi^{ref}(z,\tau)$ are then compared with the corresponding tabulated values $\varphi^{tab}(z, c^{ref}(z,\tau), \chi_{st}(\tau))$. The database was built from different flamelets with different χ_{st} values which are (in s^{-1}): 0.1 ; 0.5 ; 1.0 ; 3.0 ; 5.0 ; 10.0 ; 20.0 ; 30.0 ; 40.0 ; 50.0 ; 60.0 ; 70.0. Figure 5.15 shows time evolution at $z = z_{st}$ for different variables. The temperature profiles indicate that ignition of the mixture occurs around $\tau = 7$ ms. At the beginning, χ_{st} is above the non-ignition critical value $\chi_i = 80$ s^{-1} as shown in Fig. 5.14. This prevents the flamelet from auto-igniting. Then, on the one hand, at $\tau \approx 3$ ms, χ_{st} drops below the non-ignition limit. On the other hand, Fig. 5.5 shows the ignition delay is about 5 ms for $z = z_{st}$. This points towards an auto-ignition time of 8 ms for the flamelet solution computed with transient χ_{st}. This value is close but higher than the 7 ms deduced from Fig. 5.15.

In fact, ignition occurs sooner than expected for the following reason: although early stage of the simulation prevents full ignition of the flamelet since $\chi_{st} > \chi_i$, chemical precursors such as CH_2O (Fig. 5.15(e)) are built nonetheless. Consequently, once χ_{st} becomes lower than χ_i, a pool of radicals is already present, which fastens the ignition process.
Figure 5.15 also presents comparisons between the solution solved with $\chi_{st}(\tau)$ and the solution extracted from the generated database. Temperature, major species such as H_2O, intermediate species such as CO or OH and ignition precursors such as CH_2O profiles are well retrieved by interpolation in the database. Following Eq. 5.1, three different time scales can be defined corresponding to the different physical processes: unsteadiness, transport, chemistry. The Lagrangian time τ accounts for the unsteady term. A characteristic diffusion time τ_χ is defined as (Pitsch et al., 1998; Peters, 2000):

$$\tau_\chi = \frac{\Delta z^2}{\chi_{st}} \tag{5.24}$$

τ_χ is an estimation of the time required to transport mass and energy in z-space over a distance Δz. Finally, a chemical time scale τ_c is introduced. Comparisons between these different time scales enable to know which phenomenon is predominant and in particular when unsteady effects can not be neglected (Pitsch et al., 1998; Pitsch, 2000; Ihme and Pitsch, 2008a). Unsteady effects become important when $\tau_\chi > \tau$ (Pitsch et al., 1998; Peters, 2000). The temporal variation of χ_{st} is then too fast for the flamelet to adapt because diffusion in z-space is slower than unsteadiness. As τ_χ is inversely proportional to χ_{st}, this occurs when χ_{st} is small i.e. far downstream in the flow. As for Pitsch et al. (1998), in the studied case, gases are already close to equilibrium when such effects become noticeable. However for species involved in slow chemical processes such as NO in Fig. 5.15(f), species mass fractions cannot be retrieved from the database built with steady scalar dissipation rates.
Further comparisons in z-space are given in Fig. 5.16 for three instants: one at the early stage of ignition ($\tau = 6.5$ ms), another at a more advanced stage ($\tau = 7$ ms) and the last one corresponding to the final burning state where changes are not noticeable anymore ($\tau = 20$ ms). Temperature and progress variable source term profiles are shown to be well retrieved from the tabulation technique for all mixture fractions. It should be noticed that as the flamelet travels downstream, χ_{st} tends towards zero, which tends to almost freeze the reaction front propagation in z-space. Hence, the flamelet profile in Fig. 5.16 changes very slowly after $\tau = 20$ ms. In fact, even when $\chi_{st} = 0$ s^{-1}, rich mixtures auto-ignite very slowly, which causes the reaction front to propagates, even a little, towards $z = 1$.

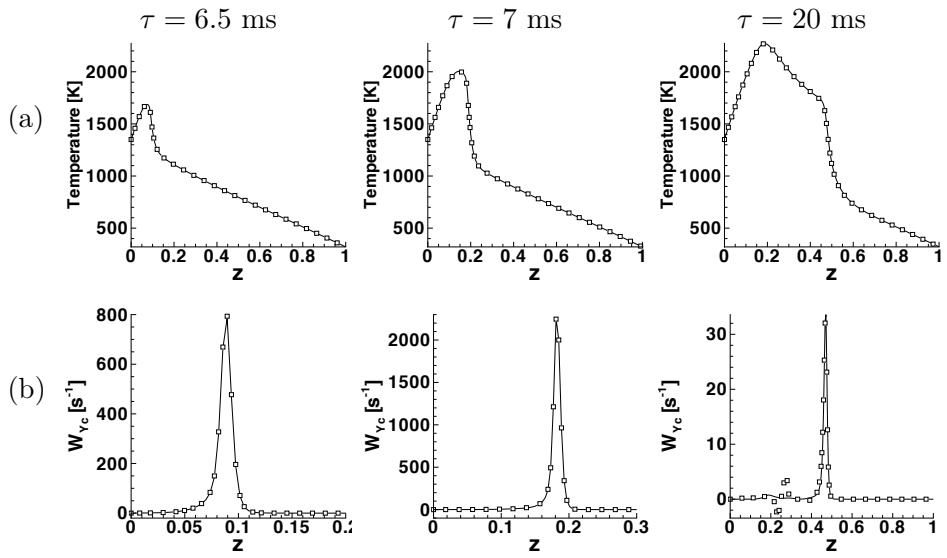

Figure 5.16: *Profiles of temperature (a) and source term $\dot{\omega}_{Y_c}$ in s^{-1} (b) at different instants: τ=6.5 ms ; 7 ms ; 20 ms. Plain line: reference solution computed with $\chi_{st}(\tau)$. Square symbols: solution interpolated in the database built for steady scalar dissipation rates.*

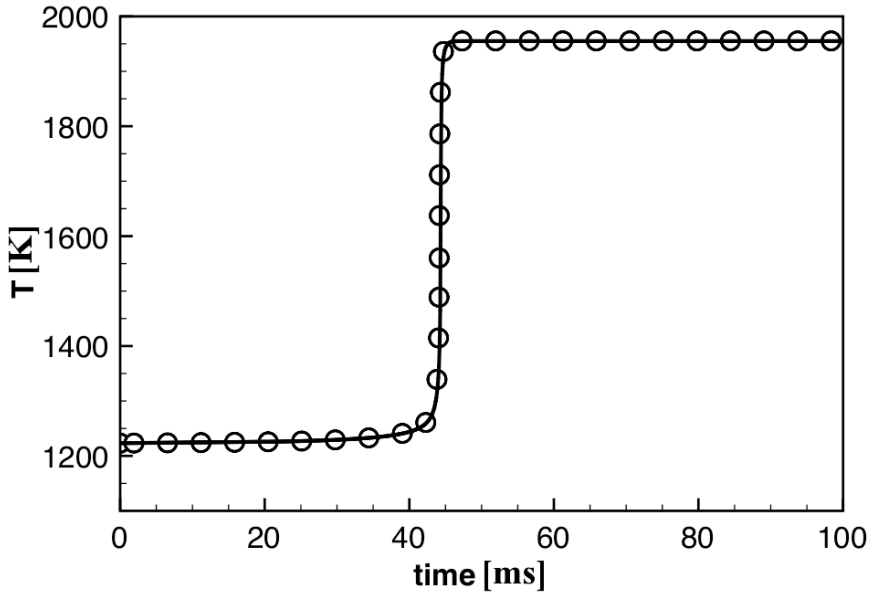

Figure 5.17: *Computation of homogeneous auto-ignition at $z = 0.1$. symbols : reference solution with a detailed chemical mechanism. line : simulation with tabulated chemistry.*

5.8 Source term correction

The progress variable reaction rate, $\dot{\omega}_{Y_c} = \dot{\omega}_{CO_2} + \dot{\omega}_{CO} - \dot{\omega}_{CH_4}$, is a key tabulated quantity. Auto-ignition is very sensitive to the induction period that precedes the abrupt temperature increase. If the table is not refined enough in c-space, especially for small c values, ignition delays are badly predicted. To illustrate this numerical issue, a homogeneous auto-ignition case using tabulated chemistry is investigated. The combustion problem reduces then to one progress variable ODE:

$$\frac{dY_c}{dt} = \dot{\omega}_{Y_c}^{tab}(z, c, \chi_{st} = 0) \tag{5.25}$$

where $\dot{\omega}_{Y_c}^{tab}(z, c, \chi_{st} = 0)$ is the tabulated progress variable reaction rate from a detailed chemistry homogeneous auto-ignition simulation.
For example, at $z = 0.1$, if the source term is equally discretized with 201 points in the progress variable dimension, the ignition delay is found to be 23 ms by solving Eq. 5.25 instead of 44.1 ms in the detailed chemical computation using the GRI 3.0 mechanism. High refinement of the mesh in c direction corrects the deviation but this technique demands large memory space.
Another technique is to hold the source term $\dot{\omega}_{Y_c}$ constant between the first two points of the database, $c = 0$ and $c = \epsilon$ (Embouazza, 2005; Galpin et al., 2008a):

$$\dot{\omega}_{Y_c} = \begin{cases} \dot{\omega}_{Y_{c_0}}(z, \chi_{st}) & \text{if } 0 \leq c \leq \epsilon \\ \dot{\omega}_{Y_c}^{tab}(z, c, \chi_{st}) & \text{if } \epsilon \leq c \leq 1 \end{cases} \tag{5.26}$$

where

$$\dot{\omega}_{Y_{c_0}}(z, \chi_{st}) = \frac{\epsilon}{t_\epsilon(z, \chi_{st})} \tag{5.27}$$

It ensures that c reaches ϵ at the same time, t_ϵ, as the exact detailed chemistry solution. The efficiency of this method is shown in Fig. 5.17 where temperature computed from tabulated chemistry (circles) is compared to reference detailed chemistry solution (solid line). The effect of constant $\dot{\omega}_{Y_{c_0}}$ on the temporal solution is shown at early stage of ignition in Fig. 5.18. Both temporal evolution of source terms (Fig. 5.18(a)) and progress variable profiles (Fig. 5.18(b)) do not match the detailed chemistry solution for $c < \epsilon$. However the profiles perfectly match afterwards for $c \geq \epsilon$.
Fig. 5.19 shows reference ignition delay computations (solid line) compared to the tabulated chemistry prediction (symbols) as a function of mixture fraction z. The good agreement validates the method. The source term correction is also retained for unsteady strained flamelets.

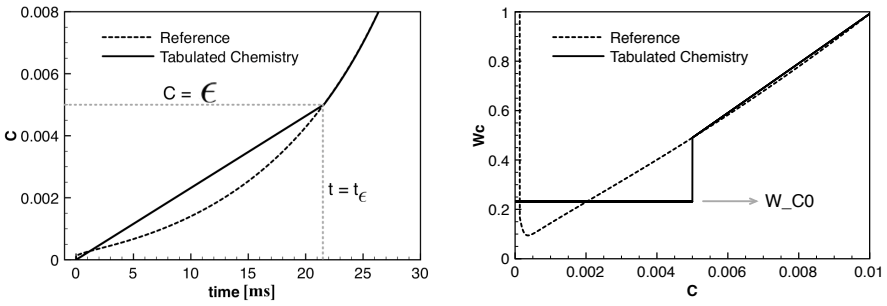

(a) (b)

Figure 5.18: *Comparison of tabulated chemistry simulation with the reference solution at* $z = 0.1$ *at small values of progress variable.* $\epsilon = 0.005$

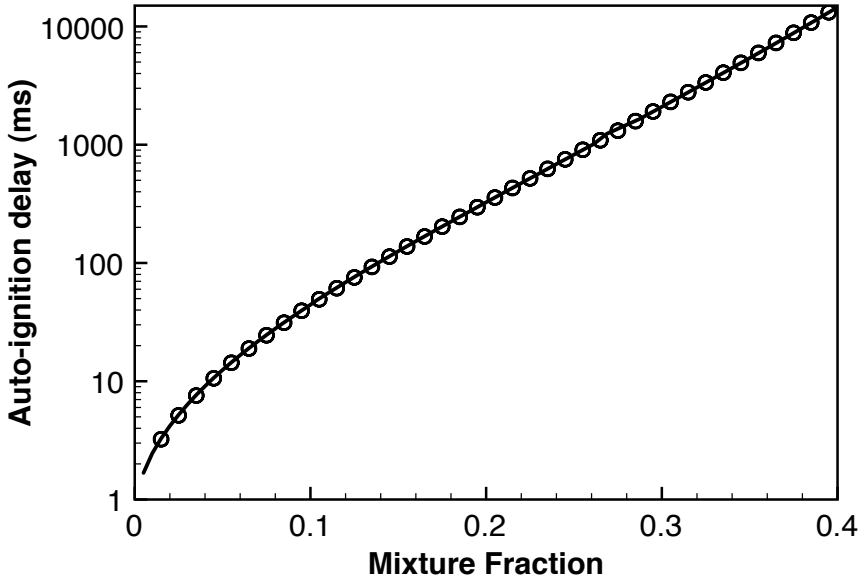

Figure 5.19: *Comparison of ignition delays from 0D computations. Symbols: detailed chemistry. Line: tabulated chemistry.*

Boundary conditions	$z = 1$	$z = 0$
T (K)	1400	1400
Y_{CH4}	0.048	0.0
Y_{O2}	0.0	0.011
Y_{N2}	0.690	0.727
Y_{H2O}	0.118	0.118
Y_{CO2}	0.144	0.144

Table 5.5: *Typical flameless combustion experimental boundary conditions (temperature and species mass fractions).*

5.9 Conclusion

A tabulated chemistry model was proposed in order to include detailed chemistry effect in configurations where dilution with hot gases promotes auto-ignition. The turbulent flame structure is approximated by a family of auto-igniting strained non-premixed flamelets. They are computed, then stored in a look-up table assuming unity species Lewis numbers and steady scalar dissipation rates. Both assumptions were analyzed and validated. The "laminar" database has three coordinates: the mixture fraction z, the progress variable c and the stoichiometric scalar dissipation rate χ_{st}.
The model is developed for the general case of diluted combustion including mild combustion. We give here a short view of the model in such a configuration to investigate if any presented flamelet properties are changed in flameless combustion. This was done by changing the flamelet boundary conditions and imposing highly diluted fuel and air conditions. Here is an example:

- Pure methane ($Y_{CH_4} = 1.0$) and air ($Y_{O_2} = 0.233$, $Y_{N_2} = 0.767$) mixtures are first considered and are going to be mixed with burnt gases.
- Burnt gases are set as products issued from stoichiometric combustion of methane and air.
- Burnt gases are mixed with fuel and air mixtures with a ratio 20/1. The temperature is changed to account for burnt gases heat losses and is fixed to 1400K in both sides of the flamelet. The obtained mixture compositions are given in Tab. 5.5.

Like previous computations, the flamelet auto-ignites but the big difference resides in the shape of the "S" curve shown in Fig. 5.20. First, the temperature change due to combustion is small (less than 100 K) compared to the ambient temperature of 1400 K, as expected from mild combustion. Secondly, the two singular points χ_i and χ_q tend to merge and disappear. The

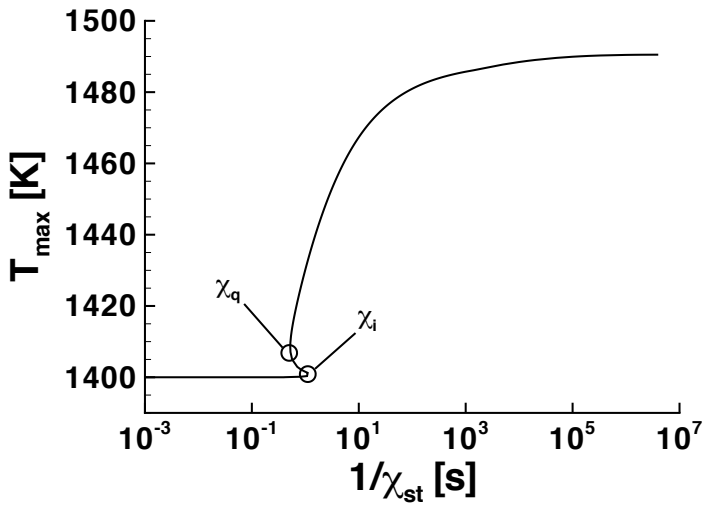

Figure 5.20: *The maximum temperature of the steady solution flamelets is plotted in function of the inverse of the stoichiometric scalar dissipation rate in a mild combustion configuration. The two singular points χ_i and χ_q tend to merge and disappear.*

maximal temperature profile becomes a monotonic function as explained by Oberlack and Peters (2000). Therefore, the database can be built similarly to other diluted combustion cases with an additional feature: the error consisting in neglecting burning state for $\chi_{st} > \chi_i$ decreases and becomes true when the mild combustion is reached.

In order to be coupled with Reynolds averaged Navier-Stokes and large eddy simulations, the turbulence-chemistry interaction remains to be modeled. This is presented in the next chapters.

We thank Pr. Heinz Pitsch for providing the code *FLAMEMASTER*.

Chapter 6

Numerical simulation of a jet issuing in a vitiated coflow: RANS

The tabulated chemistry model UTaC is applied to the Cabra burner configuration in RANS computations. Experimental results on the CH_4/air case are first summed up. RANS equations are then presented and a turbulent combustion model for UTaC is derived using presumed Probability Density Functions (PDFs). Finally, RANS simulations are performed on CH_4/air and H_2/N_2 cases.

6.1 Experimental configuration of the Cabra burner

This laboratory scale flame was been designed to reproduce the stabilization of turbulent flames in a vitiated coflow. The authors wanted a configuration where auto-ignition could participate to the stabilization mechanism. The burner was used to study two kinds of unconfined flames: the main jet was either composed of hydrogen-nitrogen (Cabra et al., 2002) or methane-air (Cabra et al., 2005). Both jets were injected in a hot coflow composed of a vitiated air mixture. The burner is composed of a perforated plate surrounding the central pipe where a multitude of lean premixed H_2/air flames are anchored. This produces the high temperature mixture composed of air and water vapor.
For the methane case, a methane/air jet is issuing in this environment 70 mm above the perforated plate. A lifted flame is stabilized approximately 35 diameters above the pipe as depicted in Fig. 6.1. The plate diameter is large enough (210 mm) to isolate the flame from the laboratory ambient air. Experimental conditions for the methane/air configuration are given in Tab. 6.1 (respectively for the hydrogen/nitrogen case in Tab. 6.2).
The Cabra configuration does not fully reproduce mild combustion but em-

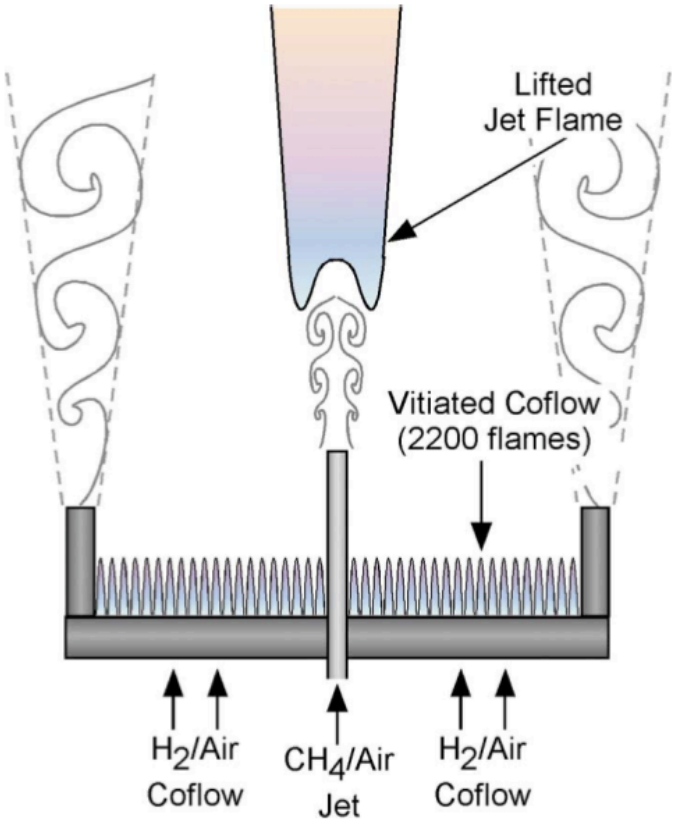

Figure 6.1: *Lifted CH_4/air jet into a coflow of hot products from a lean H_2/air flame (Cabra et al., 2005).*

phasizes the impact of fresh gases dilution by burnt gases on the flame structure. The stabilization mechanism and the reaction zone structure of the Cabra flame are therefore representative of mild combustion. In terms of numerical simulation, the Cabra burner is much simpler than furnaces as depicted in chapter 4: the flame is unconfined, radiation can be neglected, there is no complex recirculation zone and the mixing problem is limited to two streams.

Experimental results of the methane/air case obtained by Cabra et al. (2005) are now presented. Multiscalar points measurements were performed using Raman-Rayleigh scattering. CH_4, O_2, CO, CO_2, H_2, OH and temperature data were collected. For a better precision, mass fractions of CO and OH were deduced from laser-induced fluorescence (LIF). Favre averaged quantities were reconstructed by post-processing of these data. A mixture fraction which is zero in the coflow and one in the methane/air jet is computed from element mass fractions (Bilger et al., 1990). Figure 6.2(a) shows the axial profile of mixture fraction and temperature from the jet exit plane up to

Central Jet		Coflow	
Q_{CH4} (slm)	30	Q_{H2} (slm)	360
Q_{Air} (slm)	60	Q_{Air} (slm)	2100
T_{JET} (K)	320	T_{COFLOW} (K)	1350
V_{JET} (m/s)	100	V_{COFLOW} (m/s)	5.4
Re_{JET}	28000	Re_{COFLOW}	23300
d_{JET} (mm)	4.57	D_{COFLOW} (mm)	210
X_{CH4}	0.33	X_{H2O}	0.15
X_{O2}	0.15	X_{O2}	0.12
X_{N2}	0.52	X_{N2}	0.73

Q: volumetric flow rate; X: mole fraction;
Re: Reynolds number; d and D: diameter

Table 6.1: *CH_4/air experimental conditions (Cabra et al., 2002)*

Central Jet		Coflow	
Q_{H2} (slm)	25	Q_{H2} (slm)	225
Q_{N2} (slm)	75	Q_{Air} (slm)	2100
T_{JET} (K)	305	T_{COFLOW} (K)	1045
V_{JET} (m/s)	107	V_{COFLOW} (m/s)	3.5
Re_{JET}	23600	Re_{COFLOW}	18600
d_{JET} (mm)	4.57	D_{COFLOW} (mm)	210
X_{H2}	0.25	X_{H2O}	0.099
X_{N2}	0.74	X_{O2}	0.15
		X_{N2}	0.75

Q: volumetric flow rate; X: mole fraction;
Re: Reynolds number; d and D: diameter

Table 6.2: *H_2/N_2 experimental conditions (Cabra et al., 2005).*

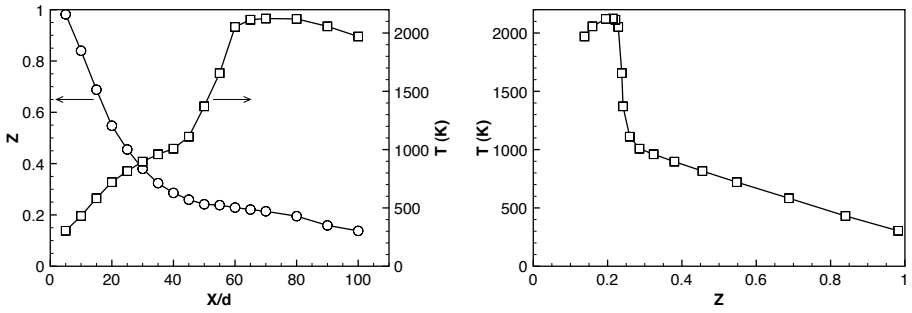

(a) (b)

Figure 6.2: *Axial profile of Favre averaged mixture fraction and temperature (a) and axial temperature versus mixture fraction (b). d is the pipe diameter (Cabra et al., 2005).*

one hundred diameters above. When the averaged mixture fraction decays, the temperature rises from the jet temperature up to 2200 K. The profiles outline that temperature increases in two stages. First, between X/d=0 and X/d≈35, the mixture fraction starts from one and decreases to 0.3. In mixture fraction space (Fig. 6.2(b)), the temperature profile follows a straight line between the two points (z=0, T=320K) and (z=0.3, T=1000K). This emphasizes a pure mixing without reaction between the jet and the hot coflow. Then, the departure of temperature from the pure mixing line for z<0.3 is due to combustion.

Several transverse plans were analyzed to get radial information on the flame structure. Figure 6.3 shows the radial temperature profiles. The mean profiles exhibit the combustion progress from the pure mixing line (Fig. 6.3(b), profile X/d=1) to a fully burnt mixture (Fig. 6.3(b), profile X/d=70) with intermediate states. Average information could point to a smooth ignition process. Nonetheless, scatter data of instantaneous temperature and OH mass fraction as function of mixture fraction (Fig. 6.4) and root-mean square (rms) data do not allow any obvious conclusion. Around the flame stabilization plane (X/d=40 and Z/d=50), temperature shows a bimodal behavior with few intermediate states. Thus, mean intermediate values of temperature are the result of the superposition of burnt and frozen mixtures. This result for the methane/air configuration is very different from the hydrogen/nitrogen where the scatter data are far more equally distributed (Cabra et al., 2005). Distributed scatter data favor random ignition in a homogeneous turbulent reactive flow whereas bimodality is usually observed in ambient air lifted flames stabilized by flame propagation. However, data dispersion can be interpreted differently: it may be observed in a turbulent thickened premixed flame. Therefore the data distribution is not sufficient to reveal the flame

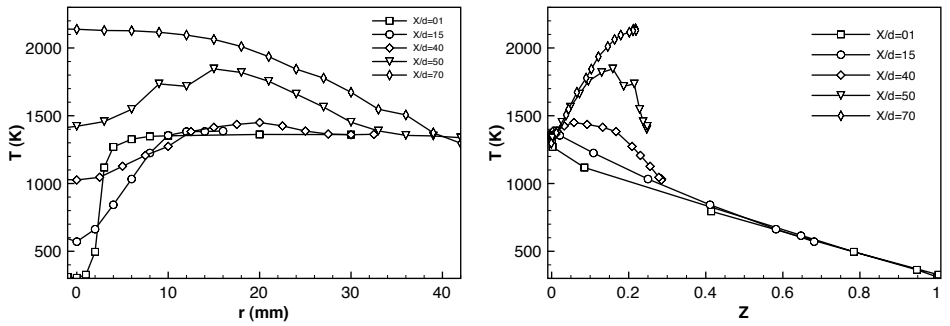

(a) (b)

Figure 6.3: *Radial profile of Favre averaged temperature for different position (a) and as function of mixture fraction (b) (Cabra et al., 2005).*

structure. Consequently, the different behavior of scatter data between the methane/air and hydrogen cases does not necessarily indicate different flame stabilization mechanisms. In the methane case, the distribution bimodality usually attributed to a propagating flame front can reflect thin intermittent igniting pockets.

The detailed experimental data brought some clarifications on the flame but is not sufficient to conclude definitely on the stabilization mechanism : auto-ignition, propagation or both. Sensibility of the flame lift-off height to the jet velocity, to the coflow velocity and to the coflow temperature was studied (Cabra, 2004; Cabra et al., 2005). The flame showed a high sensitivity to the coflow temperature with a linear dependence. The flame stabilizes closer to the jet exit plane when the coflow temperature increases. This behavior is largely underestimated by classic correlation of flame liftoff height based on laminar flame speed (Cabra et al., 2005). Tests on velocity sensibilities showed that the coflow velocity changes had more impact than variations of the jet velocity. This family of test cases are useful to test robustness of models. In papers where sensitivities comparison are included, the model parameters are fixed to reproduce correctly the reference case, then sensitivity of the experimental conditions is studied and compared without changing the model parameters.

Presented results are one-point composition measurements available on the website `http://www.me.berkeley.edu/cal/vcb/index.htm` (Cabra, 2002), published in two papers (Cabra et al., 2002, 2005) and in a detailed technical report (Cabra, 2004). Laser doppler velocimetry has also been performed on the hydrogen/nitrogen configuration by Wu et al. (2006) to add aerodynamics information for comparison. Other works have used Cabra-like burners with a central jet and a vitiated coflow to reproduce the combustion under burnt gas dilution. An example is a burner (Masri, 2003; Gordon et al., 2005,

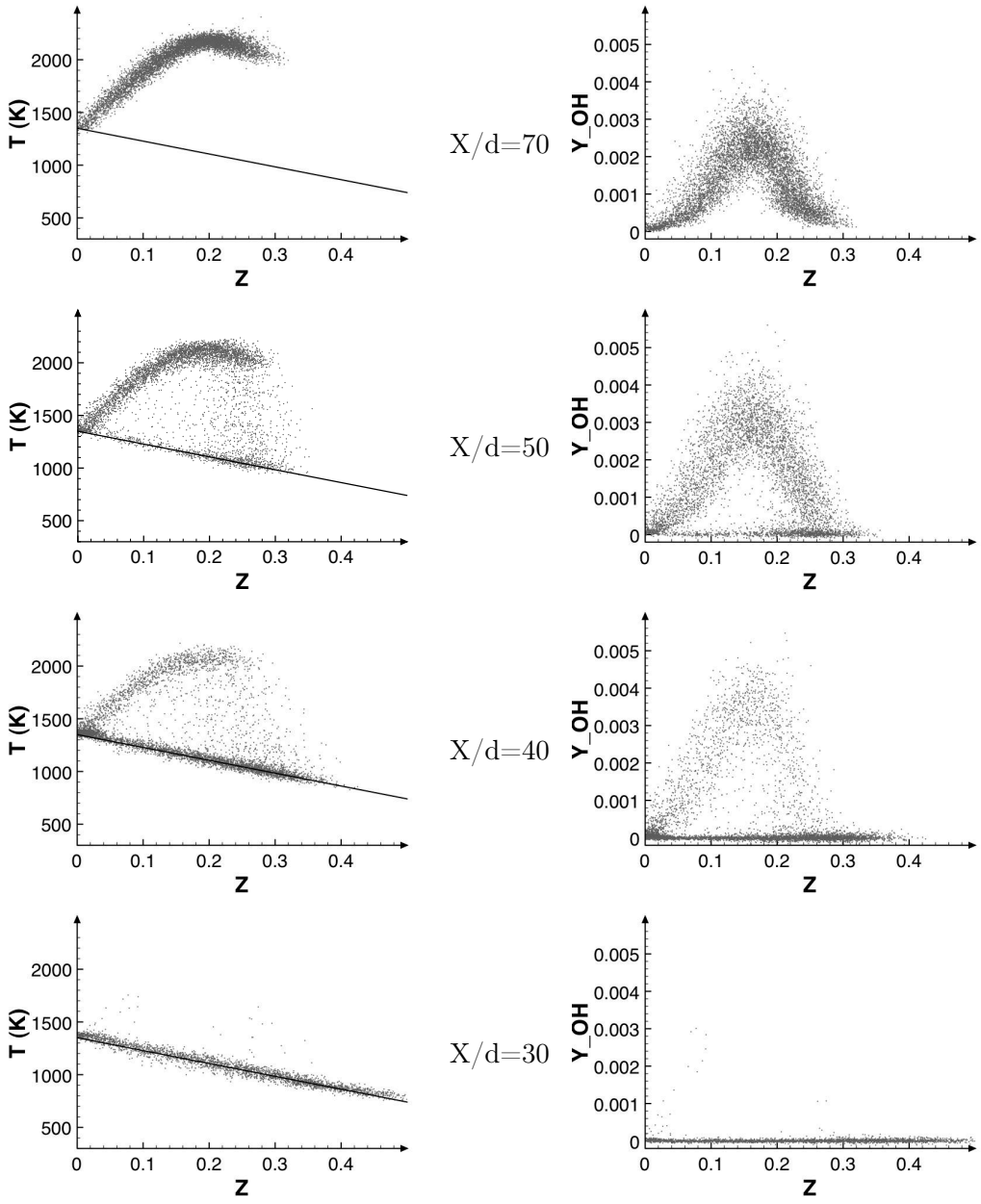

Figure 6.4: *Scatter plots of temperature and OH mass fraction for different plane positions (Cabra et al., 2005). The solid line on the temperature plots represents the pure mixing line.*

2008) that is functionally similar to the Cabra burner but only geometric dimensions are slightly different. Same conclusions as for the original Cabra burner were found in the reference case and in the sensitivity analysis. A different sensitivity of the hydrogen/nitrogen case to the coflow temperature was noticed (Gordon et al., 2005). There is first an area where the liftoff height is extremely sensitive (exponentially) followed by a stable height at high temperature, maybe promoted by flame propagation. Finally, a recent work from Gordon et al. (2008) used 2D-imaging of CH_2O and OH on the methane/air configuration to clearly asses the presence of auto-ignition events in this flame. The authors identified three categories of events occurring in the turbulent flame: build-up of a radical pools of CH_2O (and other precursors), ignition kernels and formation of steady flame flame. These events were compared with transient laminar non-premixed flamelets and show a good agreement. Thus, auto-ignition is indeed a key parameter of the stabilization and transient laminar non-premixed flamelets should reproduce this mechanism.

6.2 Reynolds Averaged Navier Stokes equations

Reynolds Averaged Navier Stokes (RANS) equations are obtained by averaging the Navier Stokes equations. Any quantity φ is written as:

$$\varphi = \overline{\varphi} + \varphi' \tag{6.1}$$

where $\overline{\varphi}$ and φ' are respectively the mean and fluctuating parts of φ. For variable density flows such as reactive flows, a mass-weighted average quantity $\tilde{\varphi}$, called Favre average, is defined:

$$\tilde{\varphi} = \frac{\overline{\rho\varphi}}{\overline{\rho}} \tag{6.2}$$

and φ is then split into Favre mean and fluctuation:

$$\varphi = \tilde{\varphi} + \varphi'' \tag{6.3}$$

The governing equations described in chapter 1 are averaged to find the RANS equations. The set of equations is reduced by assuming low Mach-number flow and adiabatic configurations. Moreover, tabulated chemistry from chapter 5 is used to include detailed chemistry at low computational cost. Therefore, energy equation is not required since temperature is read directly from the chemical database and species balance equation are replaced by balance equations for mixture fraction and progress variable. The set of RANS equations is therefore given by:

Mass balance

$$\frac{\partial \overline{\rho}}{\partial t} + \frac{\partial}{\partial x_j}\left(\overline{\rho}\tilde{u}_j\right) = 0 \tag{6.4}$$

In low Mach-number, Eq. 6.4 is replaced by the Poisson equation for mean pressure:

$$\frac{\partial^2 \overline{P}}{\partial x_j \partial x_j} = \frac{\partial^2 \overline{\rho}}{\partial t^2} - \frac{\partial^2}{\partial x_i \partial x_j}\left(\overline{\rho}\tilde{u}_i\tilde{u}_j\right) - \frac{\partial^2}{\partial x_i \partial x_j}\left(\overline{\rho}\widetilde{u_i'' u_j''}\right) + \frac{\partial^2 \overline{\tau}_{ij}}{\partial x_i \partial x_j} \tag{6.5}$$

Momentum balance

$$\frac{\partial \overline{\rho}\tilde{u}_i}{\partial t} + \frac{\partial}{\partial x_j}\left(\overline{\rho}\tilde{u}_i\tilde{u}_j\right) = -\frac{\partial \overline{P}}{\partial x_i} + \frac{\partial}{\partial x_j}\left(\underbrace{\overline{\tau}_{ij}}_{I} - \overline{\rho}\underbrace{\widetilde{u_i'' u_j''}}_{II}\right) \tag{6.6}$$

Mixture fraction balance

$$\frac{\partial \overline{\rho}\tilde{z}}{\partial t} + \frac{\partial}{\partial x_j}\left(\overline{\rho}\tilde{u}_j\tilde{z}\right) = \frac{\partial}{\partial x_j}\left(\underbrace{\overline{\rho D \frac{\partial z}{\partial x_j}}}_{III} - \overline{\rho}\underbrace{\widetilde{u_j'' z''}}_{IV}\right) \tag{6.7}$$

Progress variable balance

$$\frac{\partial \overline{\rho}\tilde{Y}_c}{\partial t} + \frac{\partial}{\partial x_j}\left(\overline{\rho}\tilde{u}_j\tilde{Y}_c\right) = \frac{\partial}{\partial x_j}\left(\underbrace{\overline{\rho D \frac{\partial Y_c}{\partial x_j}}}_{V} - \overline{\rho}\underbrace{\widetilde{u_j'' Y_c''}}_{VI}\right) + \overline{\rho}\underbrace{\widetilde{\dot{\omega}_{Y_c}}}_{VII} \tag{6.8}$$

Several terms in RANS equations are unknown and require closure model. Averaged laminar diffusive fluxes for momentum (I) and scalars (III, V) are modeled as (Poinsot and Veynante, 2005):

$$\overline{\tau}_{ij} = \overline{\mu}\left(\frac{\partial \tilde{u}_i}{\partial x_j} + \frac{\partial \tilde{u}_j}{\partial x_i}\right) - \frac{2}{3}\overline{\mu}\frac{\partial \tilde{u}_k}{\partial x_k}\delta_{ij} \tag{6.9}$$

$$\overline{\rho D \frac{\partial z}{\partial x_j}} = \overline{\rho} D \frac{\partial \tilde{z}}{\partial x_j} \quad \text{and} \quad \overline{\rho D \frac{\partial Y_c}{\partial x_j}} = \overline{\rho} D \frac{\partial \tilde{Y}_c}{\partial x_j} \tag{6.10}$$

The Reynolds stress $\widetilde{u_i'' u_j''}$ (II) is modeled with a Boussinesq assumption:

$$\overline{\rho}\widetilde{u_i'' u_j''} = \mu_t\left(\frac{\partial \tilde{u}_i}{\partial x_j} + \frac{\partial \tilde{u}_j}{\partial x_i} - \frac{2}{3}\delta_{ij}\frac{\partial \tilde{u}_k}{\partial x_k}\right) + \frac{2}{3}\overline{\rho}k \tag{6.11}$$

where $k = \sum_i \widetilde{u_i''^2}/2$ is the turbulent kinetic energy and μ_t, the turbulent viscosity is given by the $k-\varepsilon$ model (Jones and Launder, 1972) as:

$$\mu_t = \rho C_\mu \frac{k^2}{\varepsilon} \tag{6.12}$$

where C_μ is a model constant and balance equations are solved for k and the turbulent energy dissipation rate ε.
Turbulent fluxes of scalars (IV, VI) are modeled using a gradient assumption:

$$\overline{\rho}\widetilde{u_j''z''} = -\frac{\mu_t}{Sc_t}\frac{\partial \tilde{z}}{\partial x_j} \quad \text{and} \quad \overline{\rho}\widetilde{u_j''Y_c''} = -\frac{\mu_t}{Sc_t}\frac{\partial \tilde{Y}_c}{\partial x_j} \tag{6.13}$$

where Sc_t is a turbulent Schmidt number. The last unclosed term is the mean chemical reaction rate (VII). The laminar reaction rate was tabulated in chapter 5 as:

$$\dot{\omega}_{Y_c} = \dot{\omega}_{Y_c}^{tab}(z, c, \chi_{st}) \tag{6.14}$$

Due to high non-linearity of the source term, the average reaction rate cannot be read as in Eq. 6.14 using averaged quantities as input parameters in the database:

$$\widetilde{\dot{\omega}_{Y_c}} \neq \dot{\omega}_{Y_c}^{tab}(\tilde{z}, \overline{c}, \tilde{\chi}_{st}) \tag{6.15}$$

6.3 Turbulent combustion model

In order to use tabulated chemistry in RANS equations, a new chemical table is built by considering presumed Probability Density Functions (PDFs) of input parameters.

6.3.1 Turbulent combustion closure through presumed PDFs

Solutions of self-igniting non-premixed flamelets have been stored in a look-up table $\phi(z, c, \chi_{st})$ where ϕ is any thermodynamical or chemical variable such as temperature, mass fractions, reaction rates, ... The Favre mean quantities are expressed from the joint mass weighted Probability Density Function (PDF) $\tilde{P}(z^*, c^*, \chi_{st}^*)$:

$$\tilde{\phi} = \int_0^{+\infty}\int_0^1\int_0^1 \phi(z^*, c^*, \chi_{st}^*)\tilde{P}(z^*, c^*, \chi_{st}^*)dz^*\ dc^*\ d\chi_{st}^* \tag{6.16}$$

where z^*, c^* and χ_{st}^* are respectively sample space variables for mixture fraction, progress variable and scalar dissipation rate. $\tilde{P}$ is defined from the joint PDF $P(z^*, c^*, \chi_{st}^*)$ as:

$$\tilde{P}(z^*, c^*, \chi_{st}^*) \quad = \quad \frac{\rho(z^*, c^*, \chi_{st}^*)}{\overline{\rho}}P(z^*, c^*, \chi_{st}^*) \tag{6.17}$$

$\tilde{P}$ is expressed by introducing the conditional PDF $\tilde{P}(z^*, c^*|\chi_{st}^*)$:

$$\tilde{P}(z^*, c^*, \chi_{st}^*) = \tilde{P}(z^*, c^*|\chi_{st}^*)P(\chi_{st}^*) \tag{6.18}$$

where $P(\chi_{st}^*)$ is the marginal PDF of the stoichiometric scalar dissipation rate. Assuming that z and c are independent from χ_{st}, the PDF $\tilde{P}$ reads:

$$\tilde{P}(z^*, c^*, \chi_{st}^*) = \tilde{P}(z^*, c^*)P(\chi_{st}^*) \tag{6.19}$$

The conditional PDF $P(c^*|z^*)$ is introduced in the joint PDF $\tilde{P}(z^*, c^*)$:

$$\tilde{P}(z^*, c^*, \chi_{st}^*) = \tilde{P}(z^*)P(c^*|z^*)P(\chi_{st}^*) \tag{6.20}$$

If the dependency of c on z is neglected, then:

$$\tilde{P}(z^*, c^*, \chi_{st}^*) = \tilde{P}(z^*)P(c^*)P(\chi_{st}^*) \tag{6.21}$$

PDF of a passive scalar is well approximated by a β-function (Girimaji, 1992). Hence, $\tilde{P}(z^*)$ is modeled as:

$$\tilde{P}(z^*) = \beta_{\tilde{z},S_z}(z^*) = \frac{z^{*a-1}(1-z^*)^{b-1}}{\int_0^1 u^{a-1}(1-u)^{b-1}du} \tag{6.22}$$

$$\text{where } a = \tilde{z}\left(\frac{1}{S_z} - 1\right); \quad b = a\left(\tfrac{1}{\tilde{z}} - 1\right); \quad S_z = \frac{z_v}{\tilde{z}(1-\tilde{z})}$$

$\tilde{z}$ and $z_v = \widetilde{z^2} - \tilde{z}^2 = \widetilde{z''^2}$ are the mixture fraction mean and variance, respectively. The mixture fraction segregation factor S_z is a normalized variance: it varies between zero and unity whatever the mean mixture fraction is. In a similar way, $P(c^*)$ is also modeled as a β-function determined by $\overline{c}$ and $S_c = \frac{c_v}{\overline{c}(1-\overline{c})}$ where c_v is the progress variable variance. The validity of β-PDF for reactive scalar has not been fully verified but the β-function has a correct phenomenological behavior. Recently, Ihme and Pitsch (2008b) have proposed another candidate called the Statically Most Likely Distribution (SMLD).
$P(\chi_{st}^*)$ is modeled by a log-normal distribution:

$$\begin{aligned} P(\chi_{st}^*) &= \frac{1}{\chi_{st}^*\sigma\sqrt{2\pi}} exp\left(-\frac{(ln\chi_{st}^* - \mu)^2}{2\sigma^2}\right) \\ \text{where } \mu &= \ln(\tilde{\chi}_{st}) - \frac{\sigma^2}{2} \end{aligned} \tag{6.23}$$

where the standard deviation σ is set to 1.0 according to experimental measurements of Effelsberg and Peters (1989) in turbulent flows.
After integration of $\tilde{P}(z^*)$ and $P(c^*)$, Eq. 6.16 reads in term of the conditional mean $\phi|(\chi_{st} = \chi_{st}^*) = \int_0^1 \int_0^1 \phi(z^*, c^*, \chi_{st}^*)\tilde{P}(z^*)P(c^*)dz^*\ dc^*$ as:

$$\tilde{\phi} = \int_0^{+\infty} \phi|(\chi_{st} = \chi_{st}^*)P(\chi_{st}^*)d\chi_{st}^* \tag{6.24}$$

When, $\chi_{st} > \chi_i$, the autoignition limit, thermo-chemical quantities remain unburnt and $\phi = \phi_u(z)$ where ϕ_u is the pure mixing line solution for species mass fractions and temperature. Therefore, $\tilde{\phi}$ is split into two contributions, one using igniting flamelets and the other using the unburnt solution ϕ_u:

$$\tilde{\phi} = \int_0^{\chi_i} \phi|(\chi_{st} = \chi_{st}^*) P(\chi_{st}^*) d\chi_{st}^* + \tilde{\phi}_u \int_{\chi_i}^{+\infty} P(\chi_{st}) d\chi_{st} \tag{6.25}$$

Note that $\tilde{\phi}$ can be different from unburnt solution when the Favre mean scalar dissipation rate $\tilde{\chi}_{st}$ is larger than χ_i. Indeed, using log-normal distribution for $P(\chi_{st}^*)$, probability of finding $\chi_{st} < \chi_i$ when $\tilde{\chi}_{st} > \chi_i$ are small but not null. Hence, partially burning states can be met even if $\tilde{\chi}_{st} > \chi_i$. Averaged thermo-chemical quantities $\tilde{\phi}$ are computed from Eq. 6.16 and stored in a five entries look-up table:

$$\tilde{\phi} = \tilde{\phi}(\tilde{z}, S_z, \overline{c}, S_c, \tilde{\chi}_{st}) \tag{6.26}$$

6.3.2 Balance equations for the database coordinates

The five database entries are known from four additional transport equations:

- **Averaged mixture fraction**, $\tilde{z}$

$$\begin{aligned} \frac{\partial \overline{\rho}\tilde{z}}{\partial t} + \frac{\partial}{\partial x_j}\left(\overline{\rho}\tilde{u}_j\tilde{z}\right) &= \frac{\partial}{\partial x_j}\left(\overline{\rho}(D + D_t)\frac{\partial \tilde{z}}{\partial x_j}\right) \\ \text{with} \quad D_t &= \frac{\mu_t}{Sc_t} \end{aligned} \tag{6.27}$$

- **Mixture fraction variance**, z_v. $S_z = z_v/(\tilde{z}(1-\tilde{z}))$ is computed from its definition. Indeed, solving a balance equation for S_z is unpractical. S_z is relevant for the database storage only and a balance equation is solved for mixture fraction variance instead. This equation can be written as (Veynante and Vervisch, 2002):

$$\begin{aligned} \frac{\partial \overline{\rho} z_v}{\partial t} + \frac{\partial}{\partial x_j}\left(\overline{\rho}\tilde{u}_j z_v\right) &= \frac{\partial}{\partial x_j}\left(\overline{\rho}(D + D_t)\frac{\partial z_v}{\partial x_j}\right) \\ &\quad + 2\overline{\rho} D_t \frac{\partial \tilde{z}}{\partial x_i}\frac{\partial \tilde{z}}{\partial x_i} - \overline{s_{\chi_z}} \end{aligned} \tag{6.28}$$

  The second term on the right hand side is a production term. The mean scalar dissipation rate is split into two parts:

$$\overline{\rho}\tilde{\chi} = \overline{\rho} D \frac{\partial \tilde{z}}{\partial x_i}\frac{\partial \tilde{z}}{\partial x_i} + \overline{s_{\chi_z}} \tag{6.29}$$

  The first one is a laminar dissipation term computed from gradients of mean mixture fraction while the last one is the turbulent scalar dissipation rate $\overline{s_{\chi_z}} = \overline{\rho D \frac{\partial z''}{\partial x_i}\frac{\partial z''}{\partial x_i}}$. Only the turbulent part of mixture fraction scalar dissipation rate appears in the variance balance equation.

- **Averaged progress variable**, $\tilde{Y}_c$. Transport equation for the normalized progress variable $\overline{c}$ introduces additional terms (Bray et al., 2005). That is why a balance equation for $\tilde{Y}_c$ is preferred:

$$\frac{\partial \overline{\rho}\tilde{Y}_c}{\partial t} + \frac{\partial}{\partial x_j}\left(\overline{\rho}\tilde{u}_j\tilde{Y}_c\right) = \frac{\partial}{\partial x_j}\left(\overline{\rho}(D+D_t)\frac{\partial \tilde{Y}_c}{\partial x_j}\right) + \overline{\rho\dot{\omega}_{Y_c}} \quad (6.30)$$

Then, $\overline{c}$ is computed from $\tilde{Y}_c$ (Fiorina et al., 2005b):

$$\overline{c} = \frac{\widetilde{Y_c}}{\widetilde{Y_{c_b}}} \quad (6.31)$$

where the mean quantity $\widetilde{Y_{c_b}}$ is computed as

$$\widetilde{Y_{c_b}} = \int_0^{+\infty}\int_0^1 Y_{c_b}(z^*,\chi_{st}^*)\tilde{P}(z^*)P(\chi_{st}^*)dz^*d\chi_{st}^* \quad (6.32)$$

and stored in the database.

- **Mean of the square progress variable**, $\widetilde{Y_c^2}$. As for mixture fraction, progress variable variance $Y_{cv} = \widetilde{Y_c^2} - \tilde{Y}_c^2$ could be used. However, Galpin (2007) has shown that numerical errors could be decreased by transporting $\widetilde{Y_c^2}$ instead.

$$\frac{\partial \overline{\rho}\widetilde{Y_c^2}}{\partial t} + \frac{\partial}{\partial x_j}\left(\overline{\rho}\tilde{u}_j\widetilde{Y_c^2}\right) = \frac{\partial}{\partial x_j}\left(\overline{\rho}(D+D_t)\frac{\partial \widetilde{Y_c^2}}{\partial x_j}\right) - \overline{\rho}\tilde{\chi}_{Y_c} + 2\overline{\rho\widetilde{Y_c\dot{\omega}_{Y_c}}} \quad (6.33)$$

The mean scalar dissipation rate of the progress variable $\tilde{\chi}_{Y_c}$ was introduced with $\chi_{Y_c} = 2D\frac{\partial Y_c}{\partial x_i}\frac{\partial Y_c}{\partial x_i}$. $\tilde{\chi}_{Y_c}$ is written as:

$$\overline{\rho}\tilde{\chi}_{Y_c} = 2\overline{\rho}D\frac{\partial \tilde{Y}_c}{\partial x_i}\frac{\partial \tilde{Y}_c}{\partial x_i} + \overline{s_{\chi_{Y_c}}} \quad \text{with} \quad \overline{s_{\chi_{Y_c}}} = \overline{2\rho D\frac{\partial Y_c''}{\partial x_i}\frac{\partial Y_c''}{\partial x_i}} \quad (6.34)$$

S_c is then approximated from $\widetilde{Y_c^2}$ (Fiorina et al., 2005b):

$$S_c = \frac{\overline{c^2} - \overline{c}^2}{\overline{c}(1-\overline{c})} \quad (6.35)$$

$$\text{with } \overline{c^2} \approx \frac{\widetilde{Y_c^2}}{\widetilde{Y_{c_b}^2}} \quad (6.36)$$

where the mean quantity $\widetilde{Y_{c_b}^2}$ is computed as

$$\widetilde{Y_{c_b}^2} = \int_0^{+\infty}\int_0^1 Y_{c_b}(z^*,\chi_{st}^*)^2\tilde{P}(z^*)P(\chi_{st}^*)dz^*d\chi_{st}^* \quad (6.37)$$

and stored in the database.

- **Mean stoichiometric scalar dissipation rate** $\tilde{\chi}_{st}$. It is not transported but deduced from $\tilde{\chi}$ which is computed by:

$$\overline{\rho}\tilde{\chi} = 2\overline{\rho}D\frac{\partial\tilde{z}}{\partial x_i}\frac{\partial\tilde{z}}{\partial x_i} + \overline{s_{\chi_z}} \quad \text{with} \quad \overline{s_{\chi_z}} = \overline{2\rho D\frac{\partial z''}{\partial x_i}\frac{\partial z''}{\partial x_i}} \tag{6.38}$$

  $\tilde{\chi}_{st}$ is then related to $\tilde{\chi}$ by writing χ as a function of mixture fraction (Eq. 5.4):

$$\tilde{\chi} = \tilde{\chi}_{st}\int_0^1 \frac{F(z^*)}{F(z_{st})}\tilde{P}(z^*)dz^* = \tilde{\chi}_{st}\mathscr{F}\left(\tilde{z}, S_z\right) \tag{6.39}$$

The term $\mathscr{F}\left(\tilde{z}, S_z\right)$ is added in the chemical table.
Closure models are required for the turbulent scalar dissipation rates $\overline{s_{\chi_z}}$ and $\overline{s_{\chi_{Y_c}}}$. These quantities are estimated from the flow field by algebraic relations. They are here modeled with a linear relaxation model (Veynante and Vervisch, 2002):

$$\overline{s_{\chi_z}} = 2\overline{\rho}c_\chi\frac{z_v}{(k/\varepsilon)} \quad \text{and} \quad \overline{s_{\chi_{Y_c}}} = 2\overline{\rho}c_\chi\frac{Y_{cv}}{(k/\varepsilon)} \tag{6.40}$$

where k is the turbulent kinetic energy, ϵ is the turbulence dissipation rate. c_χ is the model parameter, which is taken to unity.

6.3.3 Scheme of the model UTaC in RANS simulations

Figure 6.5 represents the different steps during one iteration of the RANS simulation:

① Balance equations are solved for mass, momentum, turbulent kinetic energy and dissipation rate. Detailed chemistry is introduced by adding balance equation for the mean mixture fraction, its variance, the mean progress variable and the mean of its square. In order to complete the iteration, some terms such as chemical reaction rates must be provided at each node of the computational domain. These terms are given in step ⑤ after several intermediate computations.

② One of the database coordinate is the mean stoichiometric scalar dissipation rate $\tilde{\chi}_{st}$. It is computed from $\tilde{\chi}$ known from the transported variables and the factor $\mathscr{F}(z, S_z)$ interpolated in the database.

③ The knowledge of $\tilde{z}$, z_v and $\tilde{\chi}_{st}$ allows to read the normalization terms $\widetilde{Y_{c_b}}$ and $\widetilde{Y_{c_b}^2}$ in the database. Both coordinates $\overline{c}$ and S_c are then evaluated from these normalization terms and the transported variables $\widetilde{Y_c}$ and $\widetilde{Y_c^2}$.

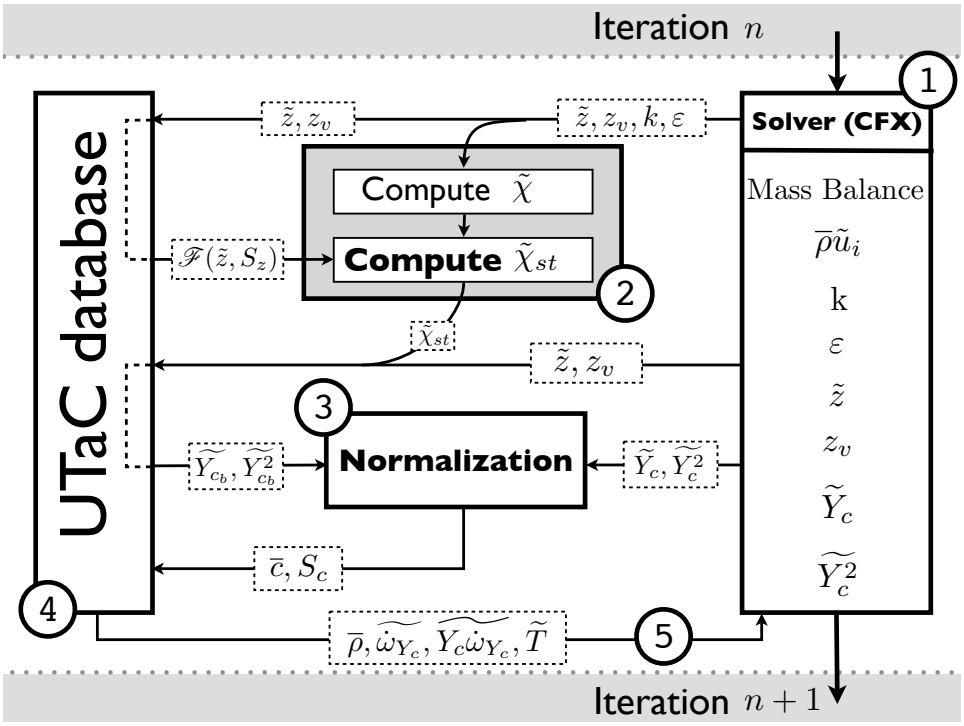

Figure 6.5: *Scheme of the coupling between the UTaC database and the RANS solver between two iterations. Main steps are indicated by circled numbers.*

④ All five entries of the look-up table are now known at each node of the computational domain and any tabulated quantities can be read by interpolation in the UTaC database.

⑤ The terms required to advance the numerical simulation in step ① are sent to the solver to terminate the current iteration.

These process takes place during each iteration until the numerical solution is converged.

6.4 RANS simulations results

All RANS simulations are performed with the CFD code CFX (ANSYS, 2010).

6.4.1 Methane/air configuration

6.4.1.1 Numerical simulation configuration

A known shortcoming of the standard $k-\varepsilon$ model is its overestimation of the round jet spreading, known as the round jet anomaly (Pope, 1978). The error can be corrected by changing and specifying ad hoc coefficients in the k and ε balance equations. Here, we retain the set of parameters used by Gordon et al. (2007b): all coefficients are fixed by their standard values except for $C_{\varepsilon 1}$ which is set to 1.6.
The turbulent Schmidt number Sc_t in balance equation for $\tilde{z}$, z_v, $\widetilde{Y_c}$ and $\widetilde{Y_c^2}$ is fixed to 0.9.

6.4.1.2 Mesh

As the configuration geometry is axisymmetric, RANS solutions have the same property. This allows a large reduction of the mesh size, however the CFX solver cannot perform 2D axisymmetric simulation. That is why a pseudo-two-dimensional mesh shown in Fig. 6.6 is used instead. The axisymmetric geometry is meshed on a 5° small sector with symmetric boundary conditions on both sides that delimit the sector. The mesh is structured with 69000 rectangular elements in the X-Y plane and only one element in the sector width. This procedure gives the same solution as a true 2D axisymmetric simulation.
Figure 6.7 shows a comparison between two simulations of the same jet. The first simulation is done with the code Fluent which can resolve 2D axisymmetric configuration and the second one is the CFX computation. Both codes are used to solve the two-dimensional jet and the axisymmetric jet problems. In the CFX case, the previously described procedure is applied

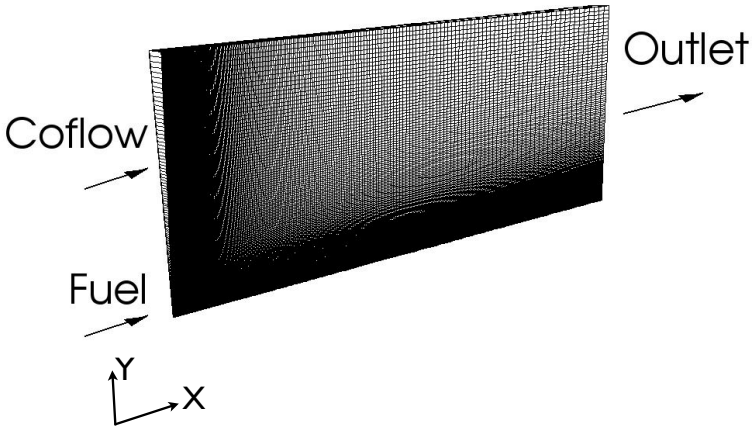

Figure 6.6: *Pseudo two-dimensional structured mesh with 69000 elements.*

	Central Jet	Coflow
Bulk velocity (m/s)	5.4	100.0
$\tilde{z}$	1.0	0.0
$\tilde{Y_c}$	0.0	0.0
$\widetilde{z^2}$	1.0	0.0
$\widetilde{Y_c^2}$	0.0	0.0
k ($m^2.s^{-2}$)	150	0.11
ε ($m^2.s^{-3}$)	66050	5.6

Table 6.3: *CH_4/air boundary conditions in RANS simulation.*

for the axisymmetric configuration. The agreement between Fluent and CFX profiles validates the developed procedure*.
The number of elements was chosen to ensure grid independence of the solution.

6.4.1.3 Boundary conditions

Boundary conditions on the fuel and coflow inlets are set by imposing values given in Tab. 6.3 for velocity components, $\tilde{z}$, $\tilde{Y_c}$, $\widetilde{z^2}$, $\widetilde{Y_c^2}$, k and ε. Uniform velocity profile are used for both inlets by giving their bulk velocity. z, Y_c, z^2, Y_c^2 are fixed by injecting homogeneous fresh mixtures at the corresponding inlet faces. Finally, the values of k and ε are chosen as in Gordon et al. (2007b).

*For both Fluent and CFX to resolve the same balance equations, an additional term must be added to CFX $k-\varepsilon$ equations. Indeed, for stability reasons, the production term $P_k = -\overline{\rho}\widetilde{u_i''u_j''}\frac{\partial \tilde{u}_j}{\partial x_i}$ is modeled as $2\overline{\rho}(\nu+\nu_t)S_{ij}S_{ij}$ in Fluent instead of $2\overline{\rho}\nu_t S_{ij}S_{ij}$ as usual.

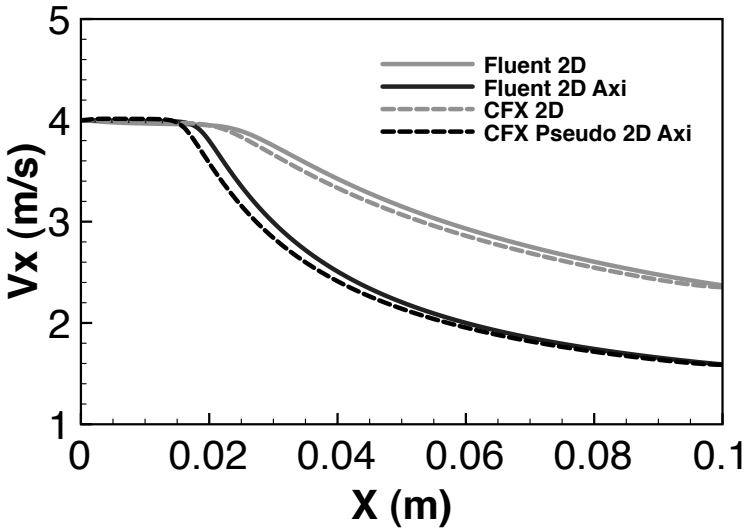

Figure 6.7: *Axial profile of the axial velocity in a constant density jet with a bulk velocity of 4 m/s. Fluent and CFX simulations are realized to simulate the two-dimensional jet and the axisymmetric jet.*

Outlet flow is imposed on the opposite face of inlets by specifying a mean pressure of 1 atm. As explained previously symmetric boundary conditions are used for both faces that delimit the sector angle. The upper face is a slipping wall that is sufficiently far from the jet axis in order not to disturb the flow.

6.4.1.4 Study of the reference case with $T_{coflow} = 1350$ K

Numerical results are compared with measurements of Cabra and co-workers (Cabra et al. (2005) and `http://www.me.berkeley.edu/cal/vcb/index.htm`)

Cold simulation A non-reactive simulation is first performed. As the turbulent flame is lifted above 30 diameters, the flow is not perturbed by combustion between $X/d = 0$ and $X/D = 30$. It is then possible to compare and validate the mixing between the fuel jet and the hot coflow upstream of the flame. Figure 6.8 shows mean mixture fraction and mixture fraction variance in the two-dimensional plane. The experimental measurements of z_{Bilger} can be compared directly to the computed mixture fraction because the database was built assuming unity species Lewis numbers. The axial mean mixture fraction profile (Fig. 6.9(a)) is well reproduced by the RANS simulation thanks to the adequate value of $C_{\varepsilon 1} = 1.6$ in the $k - \varepsilon$ model. The root-mean-square (RMS) axial profile of mixture fraction is also well retrieved (Fig. 6.9(b)). Note that these comparisons are valid for $X/d < 35$

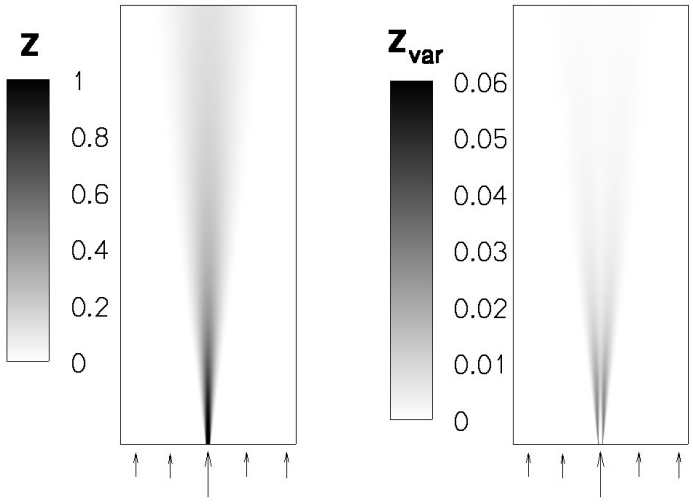

Figure 6.8: *Planar contour of mean mixture fraction $\tilde{z}$ (a) and mixture fraction variance $z_v = \widetilde{z''^2}$ (b).*

where no combustion occurs as colored in grey in Fig. 6.9(c)†. As expected from mixture fraction results, the temperature extracted from the database matches fairly the experimental profile in the non-reactive part of Fig. 6.9(c). The computed temperature is slightly underestimated which is coherent with the overestimation of mixture fraction in Fig. 6.9(a).
Radial profiles upstream of the flame are presented in Fig. 6.10 at three locations: X/D =1, 15 and 30. Experimental and numerical profiles of mean mixture fraction, its RMS and mean temperature are close.

†Although the temperature profile in Fig. 6.9(c) steps away from the non-reactive simulation for $X/d \approx 45$, combustion starts earlier in lean mixtures which set the lift-off height to 35 diameters.

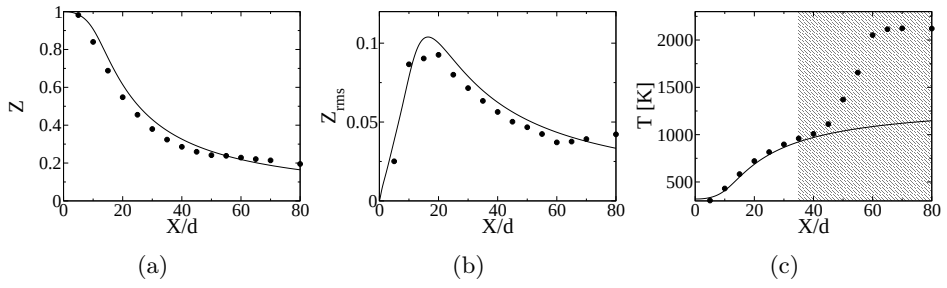

Figure 6.9: *Axial profile of mean mixture fraction (a), RMS mixture fraction (b) and mean temperature (c) in non-reactive RANS simulation (plain line). Symbols: experimental data.*

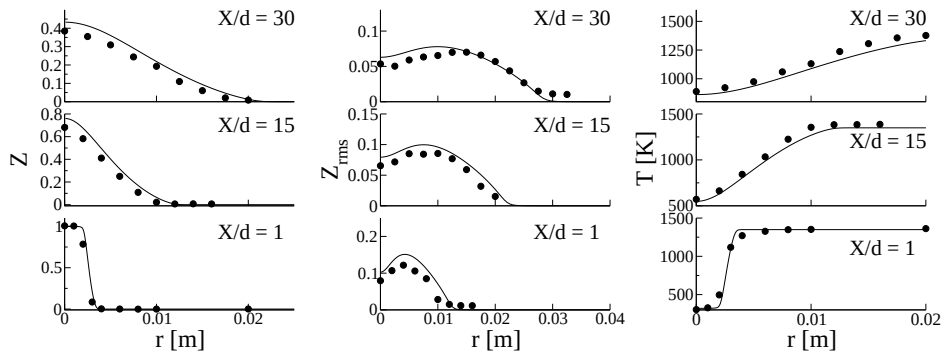

Figure 6.10: *Radial profiles at three axial location ($X/d = 1$, $X/d = 15$ and $X/d = 30$) of mean mixture fraction (a), RMS mixture fraction (b) and temperature (c) in non-reactive RANS simulation (plain line). Symbols: experimental data.*

Hot simulation The model UTaC is now tested by enabling combustion. Figure 6.11 shows a color map of mean temperature and OH mass fraction extracted from the chemical database. Cabra et al. (2005) chose C_2H_2 and C_2H_4 as indicators to determine the flame lift-off but Gkagkas and Lindstedt (2007) showed that different species indicators lead to comparable lift-off height definition. Here, we choose the criterion $Y_{OH} = 0.0005$. The computed lift-off height $H = 20d$ is smaller than the experimental one (35 diameters) based on the flame light emission. This conclusion is also found in detailed comparisons between numerical and experimental profiles.
Axial profiles of mean mixture fraction and temperature are depicted in Fig. 6.12. The temperature profile (Fig. 6.12(b)) first follows the previous non-reactive solution. Then, it steps away due to the misprediction of ignition around $X/d = 30$. Finally, the numerical simulation profile matches again the experimental temperature profile in fully burnt gases. In fact, the zones upstream and downstream of the flame are well predicte. In spite of the flame lift-off height underestimation, during the transition from fresh to burnt gases, the temperature profiles have similar slopes.
The prediction of a smaller flame lift-off height implies a slope change of the mixture fraction profile (Fig. 6.12(a)) due to thermal dilatation sooner than measured. If the temperature profile is sketched in mixture fraction space (Fig. 6.12(c)), one can see that the early ignition of mixture occur in rich mixtures.
Radial profiles of mean mixture fraction (Fig. 6.13(a)) and temperature (Fig. 6.13(b)) are plotted at three axial locations: $X/d = 40$, 50 and 70. As observed in Fig 6.11(a), ignition does not start on the jet axis. At $X/d = 40$, mixtures are already burnt while experimental data shows only a small increase of temperature. Radial profiles of mean temperature are represented

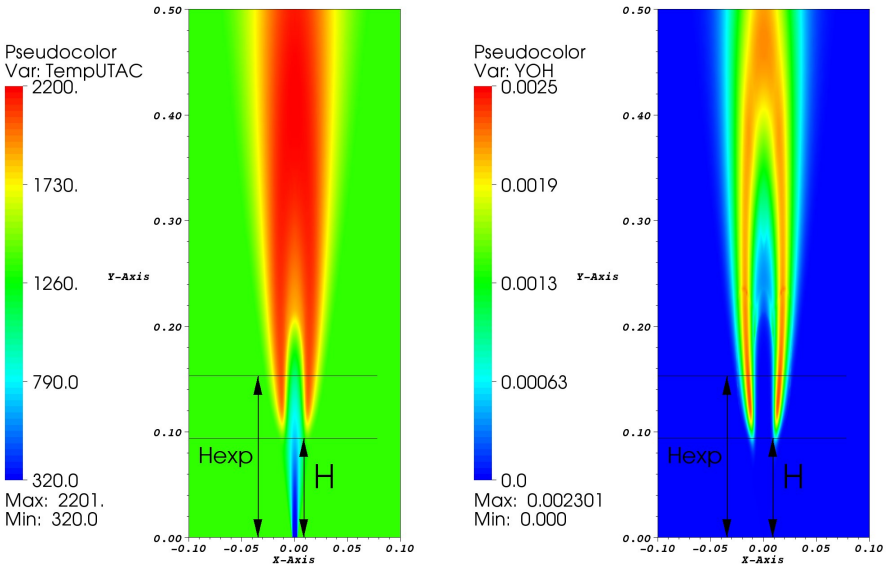

(a) (b)

Figure 6.11: *Planar contours of mean temperature (a) and OH mass fraction (b).*

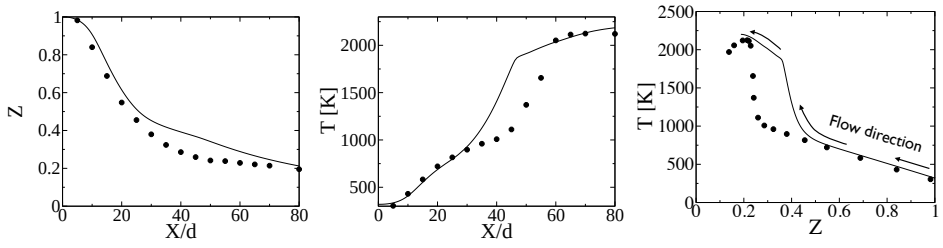

(a) (b) (c)

Figure 6.12: *Axial profile of mean mixture fraction (a) and mean temperature (b) in reactive RANS simulation (plain line). Symbols: experimental data. (c) Mean temperature profile is plotted as function of mean mixture fraction.*

in mixture fraction space in Fig. 6.13(c). As observed previously, ignition starts too early but first and last profiles which correspond to the pure mixing line and the steady state burning flamelet are well retrieved.
Thanks to the tabulated chemistry technique, any species of the detailed mechanism used to build the chemical database can be extracted from the numerical solution. Figure 6.14 shows axial and radial profiles of mean species mass fractions. All comparisons suffer from the underestimation of the flame lift-off height. However, experimental and numerical radial profiles have a fair agreement in burnt gases at $X/d = 70$ even for intermediate species such as OH. Same conclusions are drawn from RMS radial profiles plotted in Fig. 6.15

6.4.1.5 Sensitivity to the configuration parameters.

Sensitivity to the configuration parameters such as the coflow temperature, the jet and coflow bulk velocities is now analyzed. The sensitivity to the coflow temperature is conducted by performing simulations with two different databases. The first one is the same chemical table as previously, i.e. computed from the detailed mechanism GRI 3.0. Another detailed mechanism was retained to build the second database. This mechanism, GDFKin 4.0, is an upgraded version of GDFKin 3.0 (de Ferrières et al., 2008) and has been developed in collaboration with the Pôle CHENE in GDF SUEZ and academic laboratories (PC2A, Lille and LCSR, Orléans). GDFKin 4.0 is composed of 88 species involved in 652 elementary reactions (NO chemistry was removed from GDFKin for this study). Auto-ignition delays of both mechanisms in an unsteady flamelet are compared in Fig. 6.16. Although GDFKin 4.0 predicts a higher ignition time, both mechanisms give the same order of magnitude.
Different simulations are performed with both chemical tables and the dependence of the flame lift-off height H on coflow temperature is depicted in Fig. 6.17(a). In comparison to experimental data, the predicted flame sensitivity to the coflow temperature is underestimated. This might be attributed to the model hypothesis: flamelet structure, independence between z and c, β-PDF. Furthermore, the difference of ignition delays between both detailed mechanism is not retrieved in the difference of lift-off heights. This could indicate that numerical errors are introduced in the simulations. Indeed, the most-reactive mixture fraction z_{MR} is very lean, making auto-ignition very difficult to be captured by numerical simulation.
Two sets of experimental data on the temperature sensitivity of H are available: the one measured by Cabra et al. (2005) and the other one given by Gordon et al. (2005). Although both burners operate in the same conditions, a lift-off height of approximatively 35 diameters was found for different coflow temperature: 1350 K (Cabra et al., 2005) and 1420 K (Gordon et al., 2005). This difference can be attributed to the experimental incertitude on the mea-

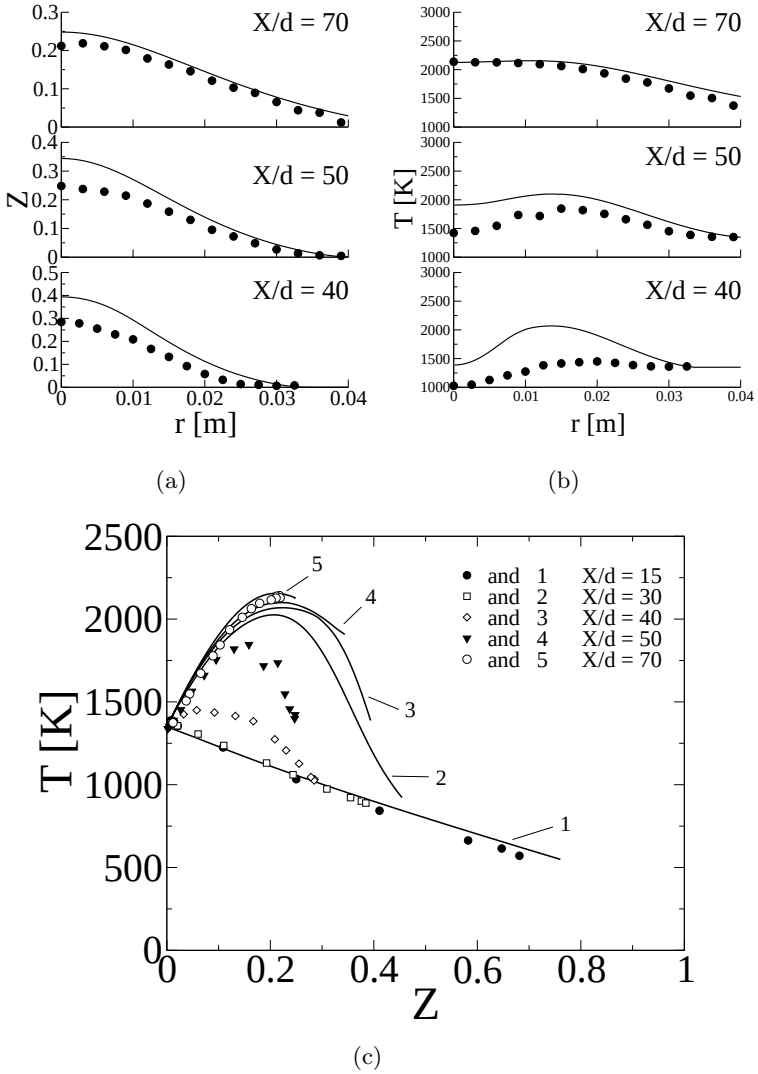

(a) (b)

(c)

Figure 6.13: *Radial profiles at three axial location ($X/d = 40$, $X/d = 50$ and $X/d = 70$) of mean mixture fraction (a) and temperature (b) in reactive RANS simulation (plain line). Symbols: experimental data. (c) Mean temperature profiles are plotted as function of mean mixture fraction.*

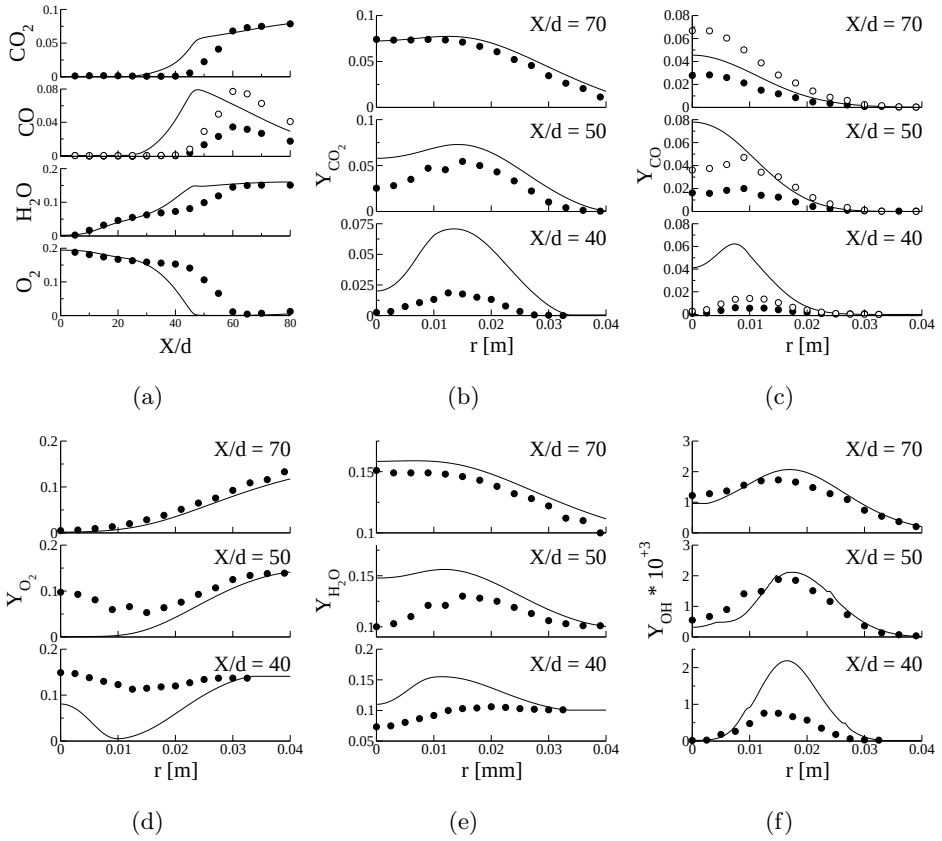

Figure 6.14: *Profiles of mean species mass fractions tabulated in the UTaC database (plain line) and measured (symbols). (a) Axial profiles of several species. (b) Radial profiles of CO_2. (c) Radial profiles of CO (two sets of measurements are available: black (Raman) and white (LIF) circles). (d) Radial profiles of O_2. (e) Radial profiles of H_2O. (f) Radial profiles of OH.*

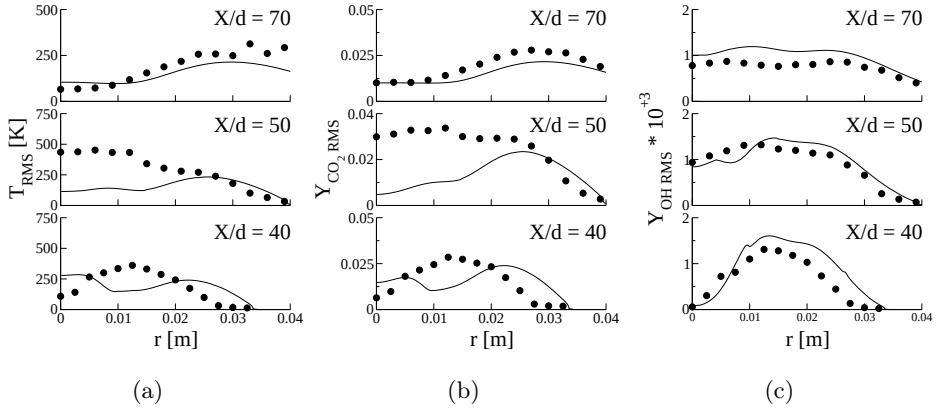

Figure 6.15: *Radial profiles of temperature (a), CO_2 and OH mass fraction RMS in reactive RANS simulation (plain line). Symbols: experimental data.*

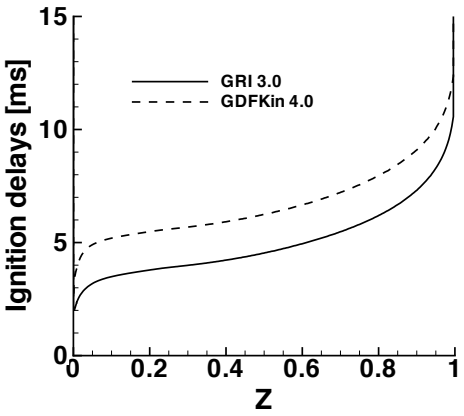

Figure 6.16: *Difference of auto-ignition delays between GRI 3.0 and GDFKin 4.0 in a transient non-premixed flamelet computed with* $\chi_{st} = 20\ s^{-1}$.

sured temperature. This double sets of data is troublesome regarding model validation in numerical simulation. Indeed, Gkagkas and Lindstedt (2007) retrieved the flame lift-off heights found by Cabra et al. (2005) through numerical simulations but, therefore, cannot match those found by Gordon et al. (2005), and vise versa, numerical results of Gordon et al. (2007b) agree with experimental data obtained by the same team (Gordon et al., 2005) but not with Cabra et al. (2005). Nonetheless, although the lift-off heights differ at absolute temperature, the tendency is identical for both experimental set-up: H doubles within 80 K. This behavior was not predicted with the UTaC model in the present configuration.
Sensitivity of the lift-off height to the fuel jet velocity is reported in Fig. 6.17(b). Experimental points of Cabra et al. (2005) and Gordon et al. (2005) are added. Although the exact height is not found, numerical simulation predict the same behavior as the jet velocity increases. Similarly, the same study is conducted on the coflow velocity (Fig. 6.17(c)). The computed sensitivity from RANS simulations is closer to the one found by Gordon et al. (2005).

6.4.2 Hydrogen/nitrogen configuration

Numerical simulation configuration

RANS simulations are performed on the H_2/N_2 configuration (Cabra et al., 2002). Small changes are introduced to the previous case:

- **Mesh**: it as the same configuration (sector with one element width). As the flame length is shorter than the CH_4/air case, the domain length is 55 diameters.

- **Boundary conditions**: the same faces as previously are present and the same boundary conditions are then applied. The imposed values

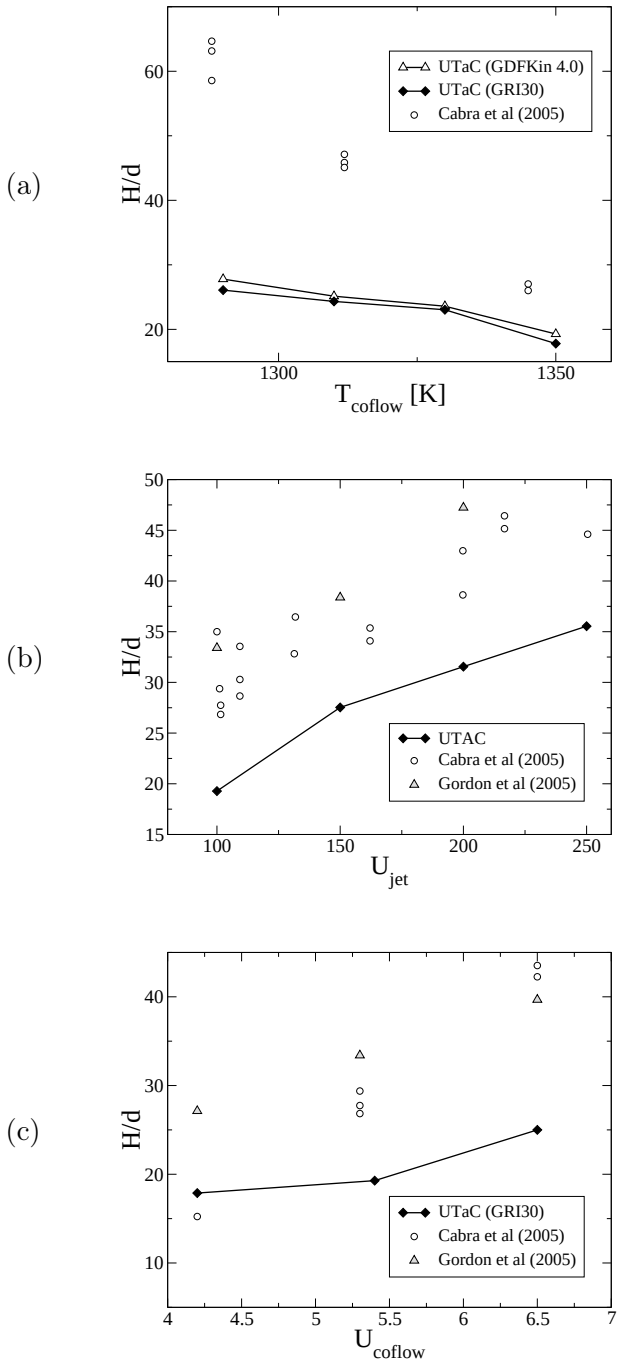

Figure 6.17: *Sensitivity of the lift-off height H to the configuration parameters. (a) Sensibility to the coflow temperature. (b) Sensitivity to the jet bulk velocity. (c) Sensitivity to the coflow bulk velocity. Symbols and plain line: RANS simulations. Symbols only: experimental flames.*

	Central Jet	Coflow
Bulk velocity (m/s)	3.5	107.0
$\tilde{z}$	1.0	0.0
$\tilde{Y_c}$	0.0	0.0
$\widetilde{z^2}$	1.0	0.0
$\widetilde{Y_c^2}$	0.0	0.0
k ($m^2.s^{-2}$)	150	0.11
ε ($m^2.s^{-3}$)	66050	5.6

Table 6.4: *H_2/N_2 boundary conditions in RANS simulation.*

at inlets are given in Tab 6.4.

- **RANS turbulence model**: the value of $C_{\varepsilon 1}$ is still set to 1.6 to compensate the round jet anomaly.

- **UTaC**: The same tabulated chemistry model is used with a different look-up table built in the hydrogen/nitrogen configuration. The detailed mechanism is the one published by Ó Conaire et al. (2004).

The major difference with the previous simulation is the chemical database. Unsteady igniting non-premixed flamelets are set with the boundary conditions at $z = 0$ and $z = 1$ given in Tab. 6.2. The flamelets are computed with the detailed mechanism of Ó Conaire et al. (2004) developed for hydrogen/air combustion. It is composed of 10 species and 21 elementary reactions. Then, flamelet solutions are stored in a database and combined with presumed PDF to build the UTaC table. As the fuel is not composed of carbon elements, the progress variables must be redefined. The non-normalized progress variable is defined as:

$$Y_c = Y_{H_2O} - Y_{H_2} \tag{6.41}$$

Cabra et al. (2002) specified a coflow temperature of 1045 K, which leads to a flame lifted at $H/d \approx 10$. However, Wu et al. (2003) and Gordon et al. (2005) found that H is highly sensitive to the coflow temperature: the lift-off height doubles within 20K. As Cabra et al. (2002) reported an experimental uncertainty of 3 % on temperature, the value of 1045 K cannot be trusted to set the numerical simulation. Therefore, the coflow temperature in numerical simulations should be first fitted to find the same lift-off height of 10 diameters before quantitative comparisons (Cao et al., 2005; Gordon et al., 2007a; Jones and Navarro-Martinez, 2007). In the present work, a coflow temperature of 1052K was chosen to compute the reference H_2/N_2 case. It belongs to the experimental uncertainty range of 3 %.

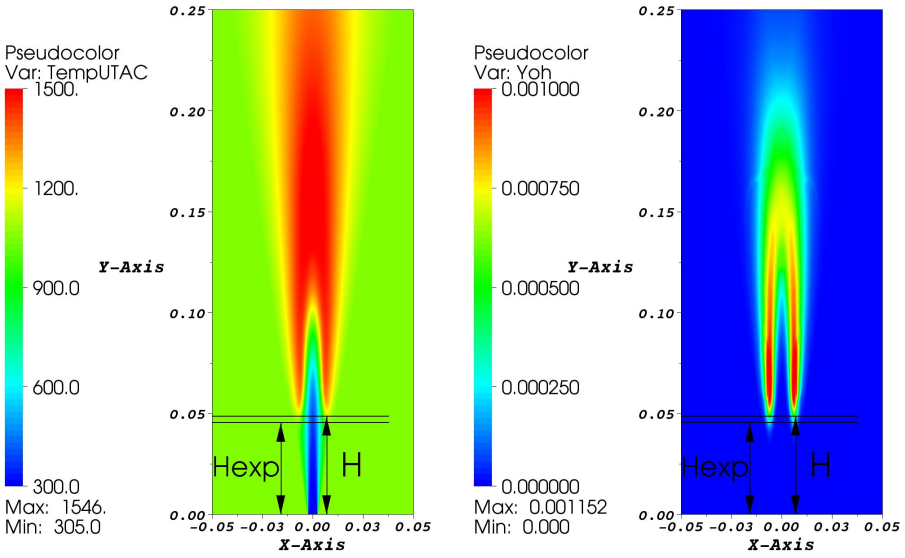

(a) (b)

Figure 6.18: *Planar contours of mean temperature (a) and OH mass fraction (b) in the H_2/N_2 case.*

Study of the reference case with $T_{coflow} = 1052$ K

Color maps of mean temperature and OH mass fraction in the RANS simulation are given in Fig. 6.18. As found experimentally, the flame lift-off height is much shorter than in the CH_4/air case. Although levels of OH mass fractions change depending which fuel is used, the value $Y_{OH} = 0.0005$ remains a good indicator to compute the lift-off height H. When T_{coflow} is fixed to 1052 K to build the chemical database, H is close to the target value of ten diameters. Numerical results are now compared with measurements of Cabra and co-workers (Cabra et al. (2002) and `http://www.me.berkeley.edu/cal/vcb/index.htm`)

Axial profile of mean mixture fraction is plotted in Fig. 6.19(a). As observed with the methane/air jet, the corrected value of $C_{\varepsilon 1}$ allows to predict the right mixing of the central jet. The axial mean temperature profile (Fig. 6.19(b)) shows a fair agreement between numerical and experimental results. Discrepancies at the jet basis are due to inconsistency in measurements: the measured jet temperature falls to 184 K.

Figure 6.19(c) shows the mean temperature profile as a function of the mean mixture fraction along the axis line. Starting from the jet origin at $\tilde{z} = 1$, temperature first follow the frozen mixing line in rich mixtures. Then, numerical simulation shows the same transition as measured experimentally

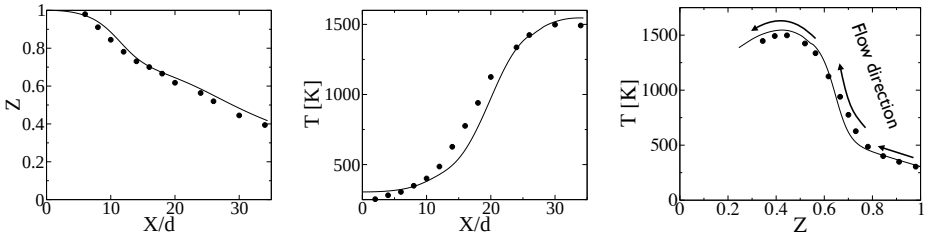

(a) (b) (c)

Figure 6.19: *Axial profile of mean mixture fraction (a) and mean temperature (b) in reactive RANS simulation (plain line) of the H_2/N_2 Cabra flame. Symbols: experimental data. (c) Mean temperature profile is plotted as function of mean mixture fraction.*

between fresh and burnt gases. Finally, the fully burning state is reached. As the numerical domain spreads further than experimental data, the mean temperature curve extends towards leaner mixtures.

Radial profiles of mean mixture fraction (Figs. 6.20(a,d)) and its RMS (Figs. 6.20(b,e)) are plotted at six axial locations: X/d = 8, 9, 10, 11, 14 and 26. The very good agreement between numerical and experimental profiles emphasizes the good prediction of mixing between the central jet and the surrounding coflow. Radial profiles of mean temperature are shown in Figs. 6.20(c,f). At the first three locations (X/d = 8, 9 and 10), combustion has not started yet or is not noticeable on temperature profiles. Hence, as pure mixing is well predicted (Fig. 6.20(d)), the fresh gases temperature extracted from the database agrees similarly to experimental profiles. Then, at higher locations (X/d = 11, 14 and 26), temperature increases first in lean mixtures before ignition spreads to the neighborhood, finishing the transition form fresh to burnt gases. This transition is almost identical in both numerical and experimental profiles.

This result is depicted in Fig. 6.21 where mean temperature profiles are plotted against the mean mixture fraction. The correct prediction of the flame structure while ignition occurs appears clearly in mixture fraction space.

Favre mean species mass fractions are extracted from the look-up table and compared to experimental profiles. Figure 6.22 shows that species axial profiles of OH, H_2O, H_2 and O_2 are fairly predicted. The behavior of the dioxygen profile is due to jet mixing with the coflow where Y_{O_2} is higher: i) downstream of the flame, O_2 mass fraction on the jet axis increases as mixing advances ; ii) Y_{O_2} drops because combustion takes place on the jet axis ; iii) finally, O_2 concentration goes up again while burnt gases mixes with the coflow.

The corresponding radial profiles of Favre mean mass fractions are plotted in 6.23. The agreement between numerical and experimental profiles is very good. Even during the ignition phase, intermediate species profiles such as

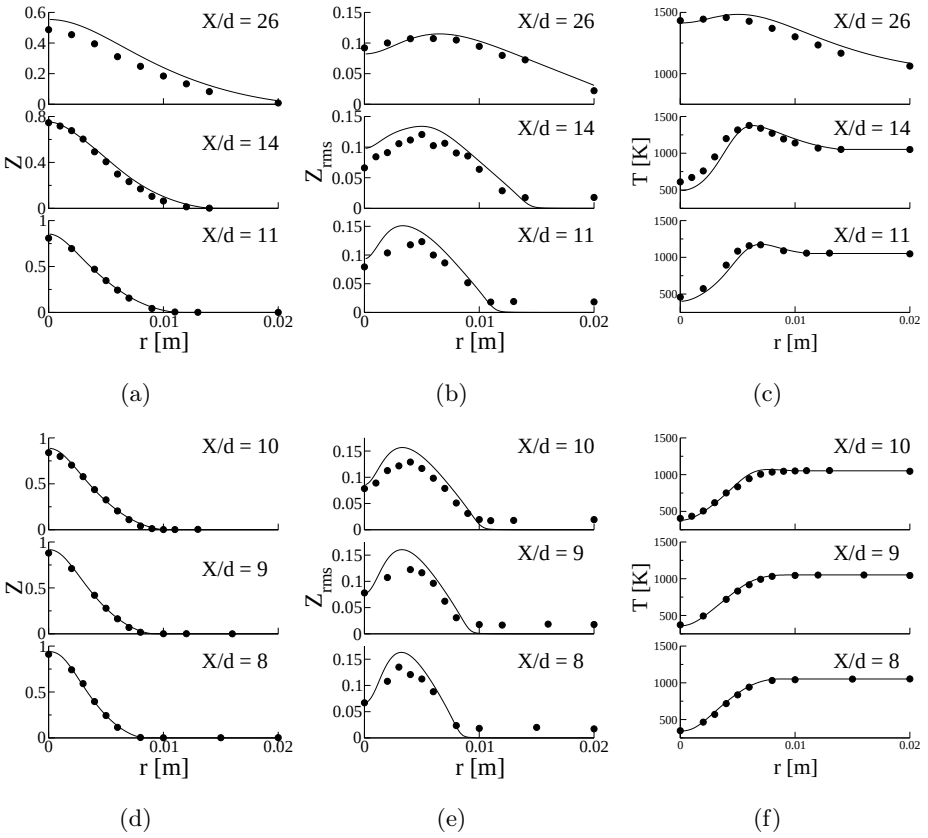

Figure 6.20: *Radial profiles at six axial locations (X/d = 8, 9, 10, 11, 14 and 26) of mean mixture fraction (a,d), its RMS (b,e) and mean temperature (c,f) in reactive RANS simulation (plain line) of the H_2/N_2 Cabra flame. Symbols: experimental data.*

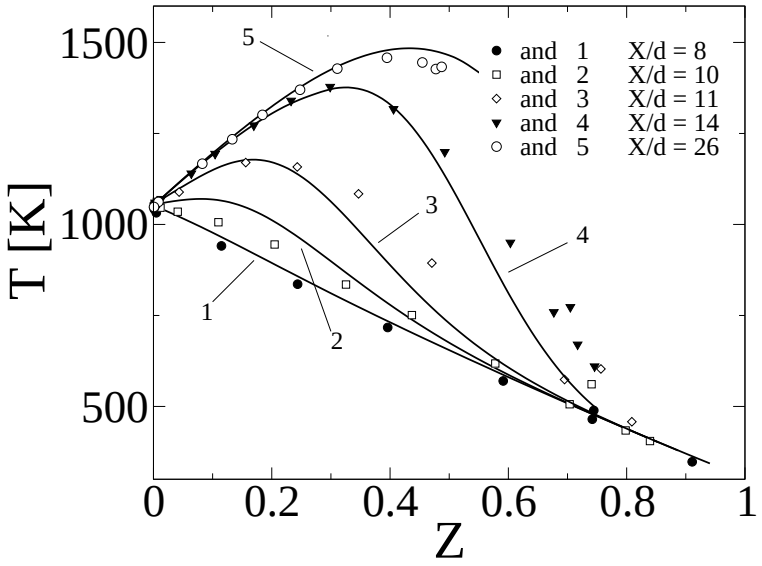

Figure 6.21: *Radial profiles of mean temperature are plotted against mean mixture fraction. Plain line: RANS simulation of the H_2/N_2 Cabra flame. Symbols: experimental data.*

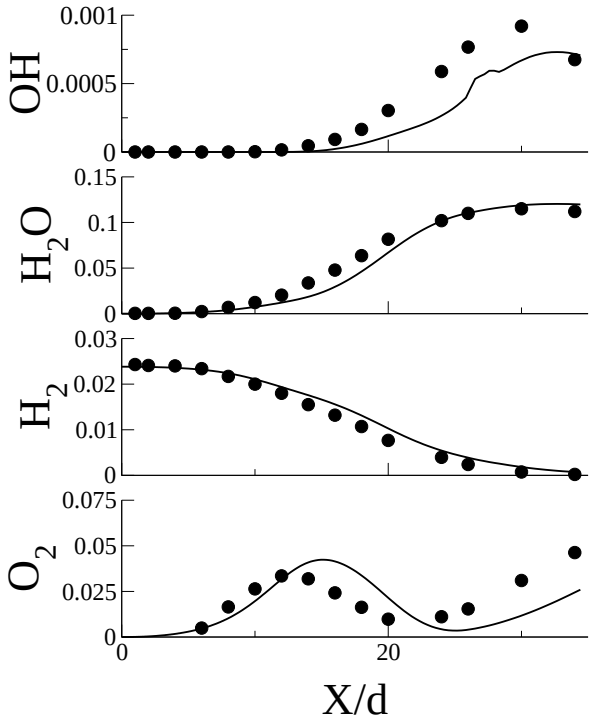

Figure 6.22: *Axial profiles of species. Plain line: RANS simulation of the H_2/N_2 Cabra flame. Symbols: experimental data.*

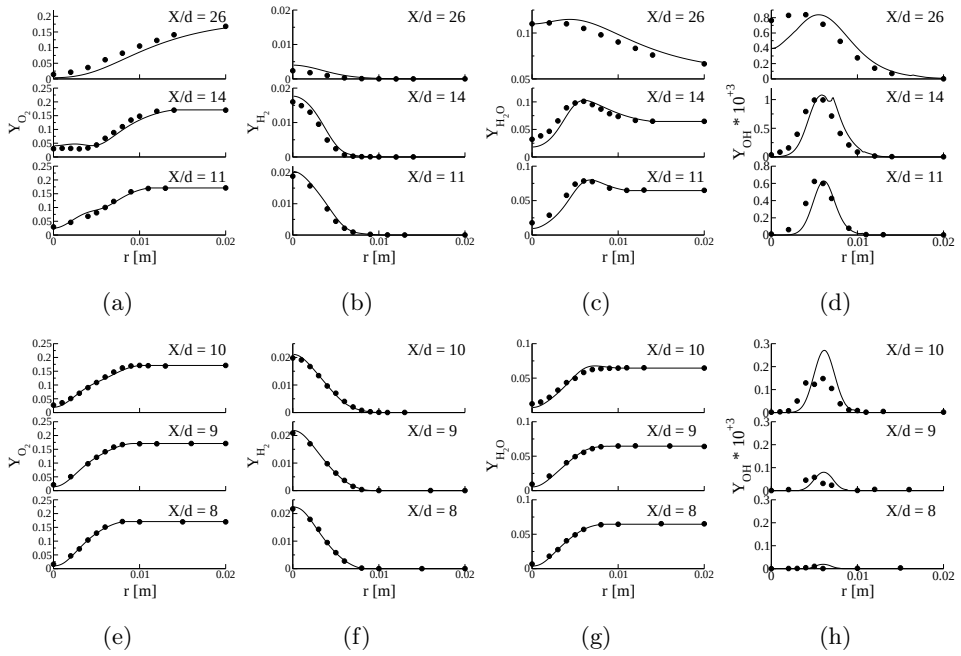

Figure 6.23: *Profiles of Favre mean species mass fractions tabulated in the UTaC database (plain line) and measured (symbols). (a,e) Radial profiles of O_2. (b,f) Radial profiles of H_2. (c,g) Radial profiles of H_2O. (d,h) Radial profiles of OH.*

OH are well retrieved, indicating a good representation of the turbulent lifted flame with a library of unsteady non-premixed flamelets.
The computed RMS of temperature (Fig. 6.24) and species mass fraction (Fig. 6.25) match the measured profiles in the entire domain.

Sensitivity to the coflow temperature

When the coflow temperature is chosen to be 1052 K instead of 1045 K as estimated by Cabra et al. (2002), the right flame lift-off height is found and quantitative comparisons with measured temperature and species profiles prove that the combustion mode is well predicted. The coflow temperature was changed because experimental uncertainties does not allow to know precisely its value whereas the flame is highly sensitive to this configuration parameter. However, as outlined by Gordon et al. (2005), the experimental uncertainty on relative variation of temperature is much lower. It makes then sense to test the aptitude of numerical simulation to recover the flame lift-off height sensitivity to temperature.
Different RANS simulations are then performed with five chemical databases that differ by the imposed temperature at $z = 0$: 1030 K, 1038 K, 1045 K, 1052 K (used for the reference case) and 1060 K. The resulted lift-off height H for each simulation is plotted in Fig. 6.26(a) versus the coflow temperature

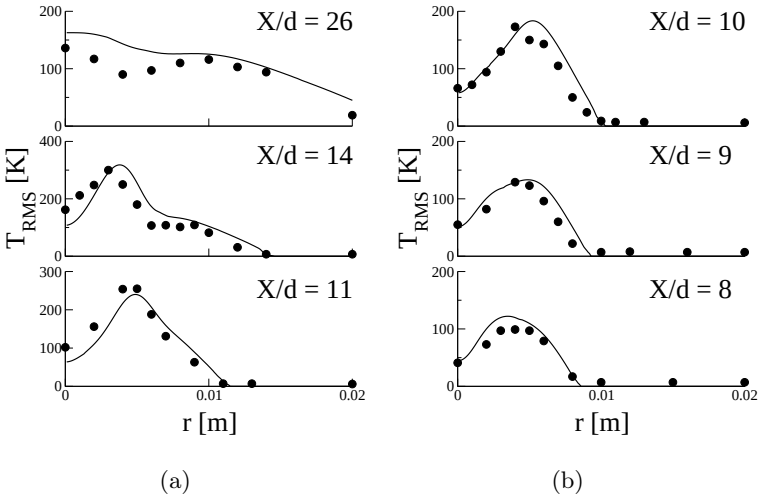

Figure 6.24: *Radial profiles of temperature RMS at different axis locations. Plain line: RANS simulation of the H_2/N_2 Cabra flame. Symbols: experimental data.*

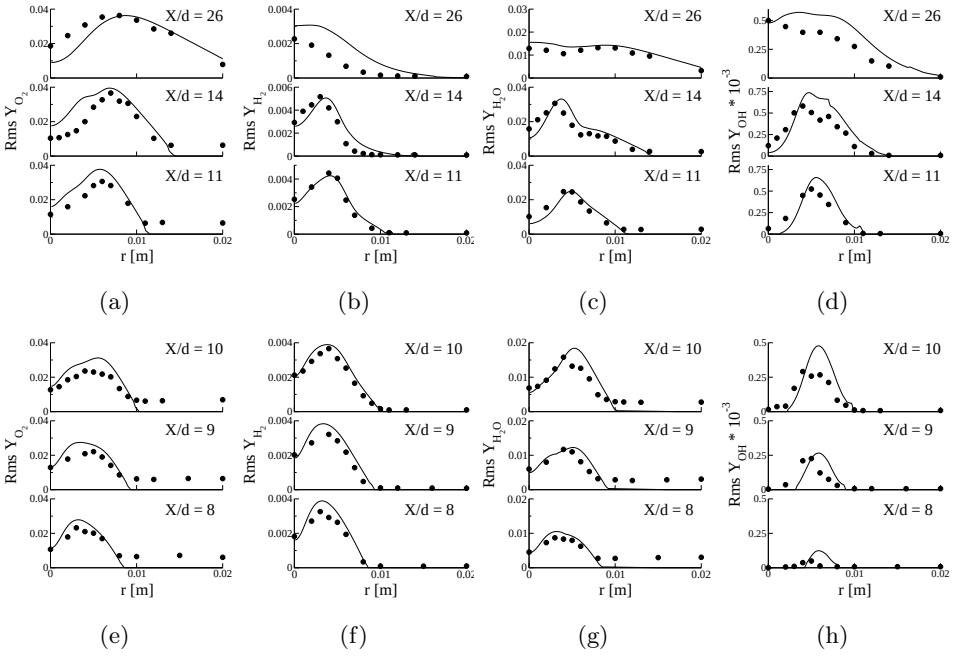

Figure 6.25: *Profiles of species mass fractions RMS tabulated in the UTaC database (plain line) and measured (symbols). (a,e) Radial profiles of O_2. (b,f) Radial profiles of H_2. (c,g) Radial profiles of H_2O. (d,h) Radial profiles of OH.*

T_{coflow}. The measured point of Wu et al. (2003) and Gordon et al. (2005) are represented. The numerical profile demonstrates that the computed flame is very sensitive to the coflow temperature: H/d varies between 8.5 and 28.5 while T_{coflow} decreases from 1060 K to 1030 K. Experimental profiles follow the same trend.
In order to facilitate quantitative comparison, H is plotted in terms of coflow temperature variation $\Delta T_{coflow} = Tcoflow - T_{ref}$. T_{ref} is chosen such as all configurations agree on the same lift-off height when $\Delta T_{coflow} = 0$. The result is given in Fig. 6.26(b). All curved approximatively merge into a single one, even the one computed from the UTaC model. Consequently, the predictive ability of UTaC on the H_2/N_2 is confirmed by the previous quantitative comparisons for $T_{coflow} = 1052$ K and by the coflow temperature sensitivity.

6.5 Conclusion

RANS simulations of the Cabra burner were performed for two fuel configurations: a mixing of methane/air and another one of hydrogen/nitrogen. Results in the CH_4/air case showed the flame lift-off was underestimated. Comparisons are poor since ignition occurs earlier than observed experimentally. Nonetheless, mixing upstream and downstream of the flame stabilization zone is correct. This points out that agreement would have been greater, if the right lift-off height had been found.
In the H_2/N_2 case, numerical results showed very good agreement with experimental data. This is quite disturbing, considering the same turbulent combustion model was used in both fuel configurations. The cause of this difference is not cleared and several reasons are proposed:

- **The flame structure i.e. the combustion mode is different between both cases**. Cabra et al. (2005) observed that H_2/N_2 case had a broaden scatter plot of temperature whereas the CH_4/air case showed a more bimodal distribution. The former has been attributed to auto-igniton while, without excluding autoignition, the latter could be due to another combustion mode such as premixed propagation. If premixed flamelets do take place in the methane/air case, this cannot be taken into account by the UTaC model. Indeed, by computing a series of unsteady non-premixed flamelets, deflagration events are neglected. However, this assumption cannot a priori correct the lift-off height that was underestimated: indeed the introduction of premixed propagation effects in the UTaC database would increase the mixtures reactivity and it would not make the flame lift-off height increase.

- **The proposed flame structure is the right one but some hypothesis in the model derivation are not valid in both cases**.

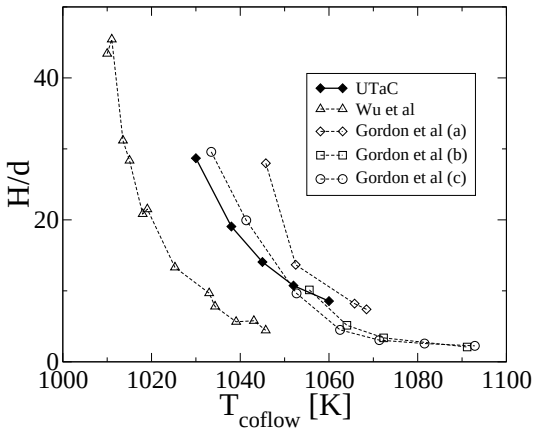

(a)

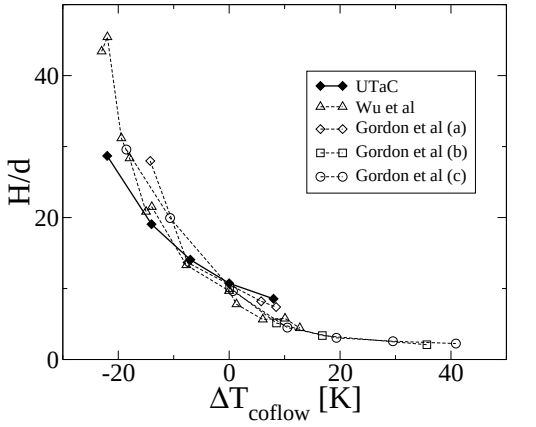

(b)

Figure 6.26: *Sensitivity of the lift-off height H to the coflow temperature. Measurements of Wu et al. (2003) and Gordon et al. (2005) are included.*

Even if the flame description as a group of unsteady flamelets was correct, several additional hypothesis were made to derive the UTaC model: i) z and c were assumed independent ; ii) PDF were presumed with specific functions ; iii) several terms in balance equations for the database coordinates required closure models. It is possible that one or several hypothesis become critical in the methane/air case.

- **The model should work in both cases but this is prevented by numerical errors**. For instance, the most-reactive mixture z_{MR} where autoignition begins is different depending on the fuel configuration: 0.0015 for CH_4/air and 0.01 for H_2/N_2 case. z_{MR} is much leaner in the methane case and this could have led to several numerical difficulties during the RANS simulation.

Chapter 7

Numerical simulation of a jet issuing in a vitiated coflow: LES

A Large Eddy Simulation (LES) of the methane/air Cabra flame is performed. The model UTaC is implemented with the compressible solver AVBP following the coupling method developed in chapter 3. First, the equations for compressible LES are given before specifying how the UTaC model is implemented in AVBP. Numerical parameters of the simulation are then given and the solution is compared with both experimental and RANS simulation data.

7.1 Equations for compressible large eddy simulation

7.1.1 Introduction to large eddy simulation

Large Eddy Simulation (LES) allows a better description of turbulence than the RANS approach. In the RANS approach, an ensemble or time average is used. Consequently, all turbulent scales are unknown and must be modeled. In LES, large turbulent eddies are solved in space and time, only the smaller ones, from a filter cut-off scale down to the Kolmogorov scale, are modeled. Both methods transform the Navier-Stokes equations into balance equations for averaged or filtered quantities. The resulted equations are formally identical, they require models for unclosed terms but they are very different conceptually. In LES context, the quantity $\overline{\varphi}$ is obtained by space filtering of the variable φ:

$$\overline{\varphi} = \int \varphi(\boldsymbol{x'}) F(\boldsymbol{x} - \boldsymbol{x'}) d\boldsymbol{x'} \tag{7.1}$$

where F is a normalized filtering function. Different filter functions (gaussian, box, ... profiles) can be used to compute filtered fields but, in practice, the

	RANS	LES
Time-averaged variables	$\overline{\varphi}$	$\langle\varphi\rangle$
Favre time-averaged variables	$\tilde{\varphi}$	$\{\varphi\}$
Filtered variables	-	$\overline{\varphi}$
Mass-weighted filtered variables	-	$\tilde{\varphi}$

Table 7.1: *Differences of notations for time-averaging and filtering between RANS and LES approaches.*

filtering function becomes implicit by solving balance equations for filtered variables. Similarly to the Favre average operator in RANS, a mass-weighted filtered quantity $\tilde{\varphi}$ is defined as:

$$\overline{\rho}\tilde{\varphi} = \int \rho(\boldsymbol{x'})\varphi(\boldsymbol{x'})F(\boldsymbol{x}-\boldsymbol{x'})d\boldsymbol{x'} = \overline{\rho\varphi} \tag{7.2}$$

In comparison to RANS context, definitions of $\overline{\varphi}$ and $\tilde{\varphi}$ have been modified for simplicity. In LES context, time averaged quantities are noted $\langle\varphi\rangle$. The Favre temporal mean is noted $\{\varphi\} = \langle\rho\varphi\rangle/\langle\rho\rangle$. The different notations used in RANS and LES context are gathered in Tab. 7.1.

7.1.2 Filtered balance equations for LES coupled with UTaC

Transport equations for compressible LES are solved using the tabulated chemistry model UTaC. Hence, equations written in chapter 3 are expressed specifically for UTaC and filtered:

Mass balance $\overline{\rho}$

$$\frac{\partial\overline{\rho}}{\partial t} + \nabla\cdot\overline{\rho}\tilde{\boldsymbol{u}} = 0 \tag{7.3}$$

Momentum balance $\overline{\rho}\tilde{\boldsymbol{u}}$

$$\frac{\partial\overline{\rho}\tilde{\boldsymbol{u}}}{\partial t} + \nabla\cdot(\overline{\rho}\tilde{\boldsymbol{u}}\tilde{\boldsymbol{u}}) = -\nabla\overline{P} + \nabla\cdot\overline{\tau} + \nabla\cdot\tau_{\boldsymbol{u}} \tag{7.4}$$

Mixture fraction balance $\tilde{z}$

$$\frac{\partial\overline{\rho}\tilde{z}}{\partial t} + \nabla\cdot(\overline{\rho}\tilde{\boldsymbol{u}}\tilde{z}) = \nabla\cdot(\overline{\rho}D\nabla\tilde{z}) - \nabla\cdot\tau_z \tag{7.5}$$

Mixture fraction variance balance $z_v = \widetilde{z^2} - \tilde{z}^2$

$$\frac{\partial\overline{\rho}z_v}{\partial t} + \nabla\cdot(\overline{\rho}\tilde{\boldsymbol{u}}z_v) = \nabla\cdot(\overline{\rho}D\nabla z_v) - \nabla\cdot\tau_{z_v} - 2\tau_z\cdot\nabla\tilde{z} - \overline{s_{\chi_z}} \tag{7.6}$$

Progress variable balance $\tilde{Y}_c$

$$\frac{\partial \overline{\rho}\tilde{Y}_c}{\partial t} + \nabla \cdot (\overline{\rho}\tilde{\boldsymbol{u}}\tilde{Y}_c) = \nabla \cdot (\overline{\rho}D\nabla\tilde{Y}_c) - \nabla \cdot \tau_{Y_c} + \overline{\rho}\widetilde{\dot{\omega}}_{Y_c} \tag{7.7}$$

Progress variable square balance $\widetilde{Y_c^2}$

$$\frac{\partial \overline{\rho}\widetilde{Y_c^2}}{\partial t} + \nabla \cdot (\overline{\rho}\tilde{\boldsymbol{u}}\widetilde{Y_c^2}) = \nabla \cdot (\overline{\rho}D\nabla\widetilde{Y_c^2}) - \nabla \cdot \tau_{Y_c^2} - \overline{\rho\chi_{Y_c}} + 2\overline{\rho}\widetilde{Y_c\dot{\omega}_{Y_c}} \tag{7.8}$$

Total energy balance $\tilde{e}_t$

$$\frac{\partial \overline{\rho}\tilde{e}_t}{\partial t} + \nabla \cdot (\overline{\rho}\tilde{\boldsymbol{u}}\tilde{e}_t) = -\nabla \cdot (\overline{P}\tilde{\boldsymbol{u}}) + \nabla \cdot (\overline{\tau}\overline{\boldsymbol{u}}) - \nabla \cdot \overline{\boldsymbol{q}} - \nabla \cdot \boldsymbol{q}^t \tag{7.9}$$

Equations for compressible LES introduce notions of macro-pressure and macro-temperature (Lesieur et al., 2005; Lodato et al., 2009) but both are not distinguished here from the thermodynamical pressure $\overline{P}$ and temperature $\widetilde{T}$ for clarity. The filtered equation of state gives $\overline{P} = \overline{\rho}\widetilde{rT}$ which is approximated by neglecting the subgrid term $(\widetilde{rT} - \tilde{r}\tilde{T})$:

$$\overline{P} = \overline{\rho}\tilde{r}\tilde{T} \tag{7.10}$$

Several subgrid tensor and fluxes have been introduced: the subgrid stress tensor $\tau_{\boldsymbol{u}}$, the subgrid fluxes of mixture fraction τ_z, progress variable τ_{Y_c}, progress variable square $\tau_{Y_c^2}$ and heat $\boldsymbol{q}^t$. The subgrid flux of mixture fraction variance τ_{z_v} is a combination of τ_z and of the subgrid flux of mixture fraction square $\overline{\rho}\left(\widetilde{\boldsymbol{u}z^2} - \tilde{\boldsymbol{u}}\widetilde{z^2}\right)$. They are defined as:

$$\begin{aligned}
\tau_{\boldsymbol{u}_{ij}} &= -\overline{\rho}\left(\widetilde{u_i u_j} - \tilde{u}_i\tilde{u}_j\right) \\
\tau_{z_i} &= \overline{\rho}\left(\widetilde{u_i z} - \tilde{u}_i\tilde{z}\right) \\
\tau_{z_{vi}} &= \overline{\rho}\left(\widetilde{u_i z^2} - \tilde{u}_i\widetilde{z^2}\right) - 2\tilde{z}\tau_{z_i} \\
\tau_{Y_{ci}} &= \overline{\rho}\left(\widetilde{u_i Y_c} - \tilde{u}_i\tilde{Y}_c\right) \\
\tau_{Y_{ci}^2} &= \overline{\rho}\left(\widetilde{u_i Y_c^2} - \tilde{u}_i\widetilde{Y_c^2}\right) \\
\boldsymbol{q}_i^t &= \overline{(\rho e_t + P)u_i} - (\overline{\rho}\tilde{e}_t + \overline{P})\tilde{u}_i
\end{aligned}$$

These terms, the subgrid scalar dissipation rates $\overline{s_{\chi_z}} = \overline{\rho}\tilde{\chi} - 2\overline{\rho}D\frac{\partial\tilde{z}}{\partial x_i}\frac{\partial\tilde{z}}{\partial x_i}$ and $\overline{s_{\chi_{Y_c}}} = \overline{\rho\chi_{Y_c}} - 2\overline{\rho}D\frac{\partial\tilde{Y}_c}{\partial x_i}\frac{\partial\tilde{Y}_c}{\partial x_i}$ and the filtered chemical reaction rates require closure models. In the filtered balance equations, filtered laminar viscous terms are simply approximated by $\overline{\rho D\frac{\partial z}{\partial x_j}} = \overline{\rho}D\frac{\partial\tilde{z}}{\partial x_j}$. This was applied to the laminar fluxes of $\tilde{Y}_c$, $\widetilde{Y_c^2}$ and to $\widetilde{z^2}$ to derive Eqs. 7.7, 7.8 and 7.6 respectively.

Laminar stress tensor and heat flux are closed as:

$$\begin{aligned} \overline{\tau}_{ij} &= \overline{\mu}\left(\frac{\partial \tilde{u}_i}{\partial x_j}+\frac{\partial \tilde{u}_j}{\partial x_i}\right)-\frac{2}{3}\overline{\mu}\frac{\partial \tilde{u}_k}{\partial x_k}\delta_{ij} \\ \overline{q}_i &= \frac{\overline{\lambda}}{\tilde{C}_p}\frac{\partial \tilde{h}}{\partial x_i} \end{aligned}$$

The viscous flux $\overline{\tau \boldsymbol{u}}$ in the filtered energy equation is written as $\overline{\tau}\tilde{\boldsymbol{u}}$.

7.1.3 Closure of the subgrid stress tensor

The deviatoric part of the subgrid stress tensor is modeled with an eddy viscosity assumption:

$$\begin{aligned} \tau_{\boldsymbol{u}_{ij}}-\frac{1}{3}\tau_{\boldsymbol{u}_{ll}} &= 2\overline{\rho}\nu_t\left(\widetilde{S}_{ij}-\frac{\delta_{ij}}{3}\widetilde{S}_{kk}\right) \\ \text{where}\quad \widetilde{S}_{ij} &= \frac{1}{2}\left(\frac{\partial \tilde{u}_i}{\partial x_j}+\frac{\partial \tilde{u}_j}{\partial x_i}\right) \end{aligned} \tag{7.11}$$

Different models are available in the literature to express ν_t (Smagorinsky, 1963; Germano et al., 1991; Lesieur et al., 2005). Here, the WALE (Wall-Adapting Local Eddy-viscosity) model developed by Nicoud and Ducros (1999) is retained. The model was built in order to retrieve the right behavior near walls and it can handle turbulent transition. Besides, in contrary to the classic Smagorinsky model, the WALE model does not arbitrary introduce high eddy viscosity levels inside shear regions. Hence, the WALE model is here used in order not to dissipate the shear layer at the round jet basis. ν_t is computed as:

$$\nu_t = (C_w\Delta)^2\frac{(s^d_{ij}s^d_{ij})^{3/2}}{(\widetilde{S}_{ij}\widetilde{S}_{ij})^{5/2}+(s^d_{ij}s^d_{ij})^{5/4}} \tag{7.12}$$

where s^d_{ij} stands for:

$$\begin{aligned} s^d_{ij} &= \frac{1}{2}\left(\tilde{g}^2_{ij}+\tilde{g}^2_{ji}\right)-\frac{1}{3}\tilde{g}^2_{kk}\delta_{ij} \\ \text{with}\quad \tilde{g}^2_{ij} &= \tilde{g}_{ik}\tilde{g}_{kj}\quad\text{and}\quad \tilde{g}_{ij}=\frac{\partial u_i}{\partial x_j} \end{aligned} \tag{7.13}$$

$C_w = 0.4929$ is the model constant.

7.1.4 Closure of the subgrid scalar fluxes

Scalar subgrid fluxes are modeled by introducing a turbulent diffusivity D_t given from the turbulent Schmidt number $\mathrm{Sc}_t = \frac{\nu_t}{\mathrm{Sc}_t}$:

$$\begin{aligned} \tau_z &= -\overline{\rho} D_t \nabla \tilde{z} \\ \overline{\rho}\left(\widetilde{u_i z^2} - \tilde{u}_i \widetilde{z^2}\right) &= -\overline{\rho} D_t \nabla \widetilde{z^2} \Longrightarrow \tau_{z_v} = -\overline{\rho} D_t \nabla z_v \\ \tau_{Y_c} &= -\overline{\rho} D_t \nabla \tilde{Y}_c \\ \tau_{Y_c^2} &= -\overline{\rho} D_t \nabla \widetilde{Y_c^2} \end{aligned} \tag{7.14}$$

The subgrid heat flux $\boldsymbol{q}^t$ is modeled as:

$$\boldsymbol{q}^t = -\frac{\lambda_t}{\widetilde{C_p}} \nabla \tilde{h} \tag{7.15}$$

where the turbulent thermal conductivity λ_t is given by the turbulent Prandtl number $\mathrm{Pr}_t = \frac{\overline{\rho}\nu_t \widetilde{C_p}}{\lambda_t}$.
The new set of equation is then:

$$\frac{\partial \overline{\rho}}{\partial t} + \nabla \cdot \overline{\rho}\tilde{\boldsymbol{u}} = 0 \tag{7.16}$$

$$\frac{\partial \overline{\rho}\tilde{\boldsymbol{u}}}{\partial t} + \nabla \cdot (\overline{\rho}\tilde{\boldsymbol{u}}\tilde{\boldsymbol{u}}) = -\nabla \overline{P} + \nabla \cdot \overline{\tau} + \nabla \cdot \tau_{\boldsymbol{u}} \tag{7.17}$$

$$\frac{\partial \overline{\rho}\tilde{z}}{\partial t} + \nabla \cdot (\overline{\rho}\tilde{\boldsymbol{u}}\tilde{z}) = \nabla \cdot (\overline{\rho}(D + D_t)\nabla \tilde{z}) \tag{7.18}$$

$$\frac{\partial \overline{\rho} z_v}{\partial t} + \nabla \cdot (\overline{\rho}\tilde{\boldsymbol{u}} z_v) = \nabla \cdot (\overline{\rho}(D + D_t)\nabla z_v) + 2\overline{\rho} D_t |\nabla \tilde{z}|^2 - \overline{s_{\chi_z}} \tag{7.19}$$

$$\frac{\partial \overline{\rho}\tilde{Y}_c}{\partial t} + \nabla \cdot (\overline{\rho}\tilde{\boldsymbol{u}}\tilde{Y}_c) = \nabla \cdot \left(\overline{\rho}(D + D_t)\nabla \tilde{Y}_c\right) + \overline{\rho}\widetilde{\dot{\omega}_{Y_c}} \tag{7.20}$$

$$\frac{\partial \overline{\rho}\widetilde{Y_c^2}}{\partial t} + \nabla \cdot (\overline{\rho}\tilde{\boldsymbol{u}}\widetilde{Y_c^2}) = \nabla \cdot \left(\overline{\rho}(D + D_t)\nabla \widetilde{Y_c^2}\right) - \overline{\rho}\widetilde{\chi_{Y_c}} + 2\overline{\rho}\widetilde{Y_c \dot{\omega}_{Y_c}} \tag{7.21}$$

$$\frac{\partial \overline{\rho}\tilde{e}_t}{\partial t} + \nabla \cdot (\overline{\rho}\tilde{\boldsymbol{u}}\tilde{e}_t) = \nabla \cdot \left(\frac{\overline{\lambda} + \lambda_t}{\widetilde{C_p}} \nabla \tilde{h}\right) - \nabla \cdot (\overline{P}\tilde{\boldsymbol{u}}) + \nabla \cdot (\overline{\tau}\tilde{\boldsymbol{u}}) \tag{7.22}$$

7.1.5 Closure of turbulent scalar dissipation rates

The mixture fraction subgrid scalar dissipation rate is modeled using a linear relaxation assumption:

$$\overline{s_{\chi_z}} = 2\overline{\rho} c_\chi D_t \frac{z_v}{\Delta^2} \tag{7.23}$$

where the model constant c_χ is taken as unity. The same model could be used for the subgrid scalar dissipation rate of progress variable $\overline{s_{\chi_{Y_c}}}$, however Eq. 7.23 is valid for small levels of variance, which is not always verified with

reactive scalars. In the opposite case where the variance is high i.e. in the the bimodal-limit (BML), Domingo et al. (2008) derived the following model*:

$$\overline{\rho\widetilde{\chi_{Y_c}}} = 2\overline{\rho}D|\nabla\tilde{Y}_c|^2 + \overline{s_{\chi_{Y_c}}} = 2\overline{\rho}\widetilde{Y_c\dot{\omega}}_{Y_c} - \widetilde{Y_{c_b}\dot{\omega}_{Y_c}} \tag{7.24}$$

Similarly to Mura et al. (2007), Domingo et al. (2008) then mixed both models in a single one by using the segregation factor $S_c = (\overline{c^2}-\overline{c}^2)/(\overline{c}(1-\overline{c}))$ as a weight parameter:

$$\begin{aligned}\overline{s_{\chi_{Y_c}}} &= 2(1-S_c)\overline{\rho}c_\chi D_t\frac{Y_{cv}}{\Delta^2} \\ &\quad +S_c\left(-2\overline{\rho}D|\nabla\tilde{Y}_c|^2 + 2\overline{\rho}\widetilde{Y_c\dot{\omega}}_{Y_c} - \widetilde{Y_{c_b}\dot{\omega}_{Y_c}}\right)\end{aligned} \tag{7.25}$$

This model is chosen and the term $\widetilde{Y_{c_b}\dot{\omega}_{Y_c}}$ is added to the database UTaC.

7.1.6 Closure of filtered chemical reaction rates

Playing the same part as in RANS context, a large-eddy PDF can be defined (Gao and Obrien, 1993). Using UTaC in LES, each filtered quantity is therefore written as:

$$\tilde{\phi} = \int_0^{+\infty}\int_0^1\int_0^1 \phi(z^*,c^*,\chi_{st}^*)\tilde{P}_{LES}(z^*,c^*,\chi_{st}^*)dz^*\ dc^*\ d\chi_{st}^* \tag{7.26}$$

Consequently, the UTaC model for LES can be derived in the same way as it was done in chapter 6 for RANS: z, c and χ_{st} are assumed independent and β-functions are used for $\tilde{P}_{LES}(z^*)$ and $P_{LES}(c^*)$:

$$\begin{aligned}P_{LES}(z^*) &= \beta_{\tilde{z},S_z}(z^*) \\ P_{LES}(c^*) &= \beta_{\overline{c},S_c}(c^*)\end{aligned}$$

Only the large-eddy PDF of the stoichiometric scalar dissipation rate is modeled differently from the RANS approach. Indeed, as the large-eddy simulation is well resolved, the subgrid values of χ_{st} are assumed equal to the resolved scalar dissipation rate $\tilde{\chi}_{st}$. Hence, a Dirac distribution is used in LES for χ_{st} instead of a log-normal distribution in RANS:

$$P_{LES}(\chi_{st}^*) = \delta(\chi_{st}^* - \tilde{\chi}_{st}) \tag{7.27}$$

Input parameters of the LES database are nonetheless identical to the RANS case: $\tilde{z}$, S_z, $\overline{c}$, S_c and $\tilde{\chi}_{st}$. The coupling, including reading of the reaction rates $\widetilde{\dot{\omega}_{Y_c}}$ and $\widetilde{Y_c\dot{\omega}_{Y_c}}$ in the UTaC database, is realized as described in chapter

*The definition of χ_{Y_c} from Domingo et al. (2008) is different by a factor 2.

6. Database entries are computed from the transported variables:

$$\begin{aligned} S_z &= \frac{z_v}{\tilde{z}(1-\tilde{z})} \\ \overline{c} &= \frac{\tilde{Y}_c}{\widetilde{Y_{c_b}}} \\ S_c &= \frac{\overline{c^2}-\overline{c}^2}{\overline{c}(1-\overline{c})} \quad \text{with} \quad \overline{c^2} = \frac{\widetilde{Y_c^2}}{\widetilde{Y_{c_b}^2}} \end{aligned}$$

The mean scalar dissipation rate of mixture fraction is composed of a resolved part and a subgrid part:

$$\tilde{\chi} = 2D|\nabla\tilde{z}|^2 + \frac{\overline{s_{\chi_z}}}{\rho} = 2D|\nabla\tilde{z}|^2 + 2c_\chi D_t \frac{z_v}{\Delta^2} \tag{7.28}$$

Then, the mean stoichiometric scalar dissipation rate is written:

$$\tilde{\chi}_{st} = \frac{\tilde{\chi}}{\mathscr{F}(\tilde{z}, S_z)}$$

where $\mathscr{F}(\tilde{z}, S_z)$ was defined in Eq. 6.39.
Knowing all five entries of the database ($\tilde{z}$, z_v, $\tilde{Y}_c$, $\widetilde{Y_c^2}$, $\tilde{\chi}_{st}$), any tabulated quantity ϕ^{tab} can be read inside the table. Besides, the TTC formalism described in chapter 3 is used: the temperature computation is reformulated to take into account compressible effects and characteristic boundary conditions are reformulated. Additional terms ϑ_{ψ_l} and σ_{ψ_l} are tabulated and plotted in Fig. 7.1.

7.2 Non-reactive large-eddy simulation

A non-reactive simulation is first performed to compare the mixing prediction upstream the lifted flame. Balance equations are solved for filtered mass, momentum, energy and mixture fraction only. All simulations are realized with the third-order numerical scheme TTGC (Colin and Rudgyard, 2000).

7.2.1 Mesh

The mesh used in large-eddy simulation is composed of approximatively 30 million tetrahedra. Although the number of cells is high, this was necessary to predict a correct mixing field on an unstructured grid. Snapshots of the mesh are given in Fig. 7.2. The geometry is similar to a large cylinder. Lateral boundary conditions are located far enough from the jet axis in order to avoid disturbance of the jet entrainment. Hence, the meshed geometry is 150 diameters long and 80 diameters wide. As shown in Fig. 7.2(b), the zone

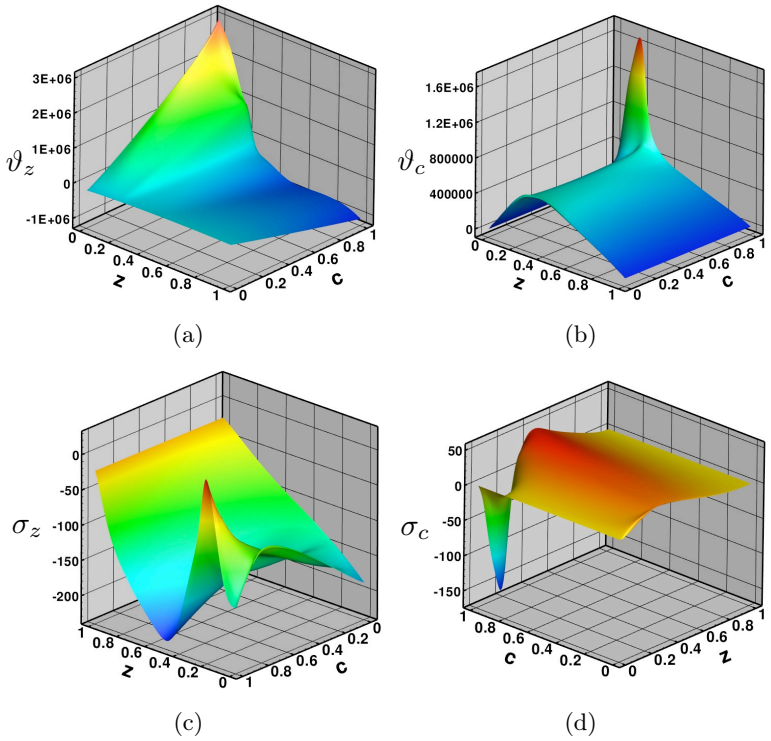

Figure 7.1: *3D view of the surfaces $\vartheta_{\tilde{z}}(\tilde{z},\overline{c})$ (a), $\vartheta_{\overline{c}}(\tilde{z},\overline{c})$ (b), $\sigma_{\tilde{z}}(\tilde{z},\overline{c})$ (c) and $\sigma_{\overline{c}}(\tilde{z},\overline{c})$ (d) with $S_z = S_c = 0$ and $\chi_{st} = 20\ s^{-1}$. The variables ϑ_{ψ_l} are given in $J.kg^{-1}$ and σ_{ψ_l} in $J.kg^{-1}.K^{-1}$. Beware of the change of axis orientation between subfigures.*

of interest between X/d=0 and 80 where experimental data are available is finely discretized.
The jet pipe was meshed on a length of two diameters including the pipe lips. The inner and outer pipe diameters are 4.57 mm and 6.35 mm respectively. The interior of the pipe is discretized using twenty points in the jet diameter. Then, the mesh resolution is kept constant ten diameters above the jet exit plane to capture the jet destabilization which controls the potential core length.

7.2.2 Boundary conditions

Slip adiabatic walls are chosen for the outer cylinder surrounding the coflow. Although the jet destabilization is sensitive to turbulence coming from the pipe boundary layer, resolved near-walls large-eddy simulation remains out of reach in the present case. That is why simple wall boundary conditions are retained inside the fuel pipe, keeping in mind the turbulent boundary layer is not resolved. In this case, slip adiabatic walls are used because they lead to a good estimation of the potential core length.
Characteristic boundary conditions as described in chapter 3 are imposed for both inlet patches and the outflow boundary. Turbulence is injected through the pipe inlet with an intensity of 1% following the method of Smirnov et al. (2001). The mean velocity profile is uniform and given by the jet bulk velocity (100 m/s). The coflow velocity profile is flat (u=5.4 m/s) and the target pressure at the outlet is set to 1 atm.

7.2.3 Numerical results

An instantaneous solution of the filtered mixture fraction field is shown in Fig. 7.3. Close to the pipe exit plane, coherent structure are formed, which destabilizes the jet before the fully turbulent jet develops.
While turbulent viscosity ν_t is given by Eq. 7.12, scalars and heat subgrid fluxes are computed from a turbulent Schmidt Sc_t and Prandlt Pr_t numbers. The influence of their values on the predicted mixing field is first investigated by computing two non-reactive large-eddy simulations: the first one with $\mathrm{Sc}_t = \mathrm{Pr}_t = 0.9$ and the second one with $\mathrm{Sc}_t = \mathrm{Pr}_t = 0.6$. Experimental Favre averaged quantities $\{\varphi\}$ and RMS $\varphi_{RMS} = (\{\varphi^2\} - \{\varphi\}^2)^{1/2}$ are compared with large-eddy simulation statistics:

$$\{\varphi\}^{LES} = \frac{\langle\overline{\rho}\tilde{\varphi}\rangle}{\langle\overline{\rho}\rangle} \quad \text{and} \quad \varphi_{RMS}^{LES} = \left(\frac{\langle\overline{\rho}\widetilde{\varphi^2}\rangle - \langle\overline{\rho}\rangle(\{\varphi\}^{LES})^2}{\langle\overline{\rho}\rangle}\right)^{1/2} \tag{7.29}$$

where $\{\varphi\}^{LES}$ and φ_{RMS}^{LES} are the Favre average and resolved variance of φ computed from LES data, respectively. Time averaging of LES solution fields is conducted on a physical time of 5 ms that corresponds to approximatively twice the convective time l/U_{JET}, where $l = 40d$ is the domain length

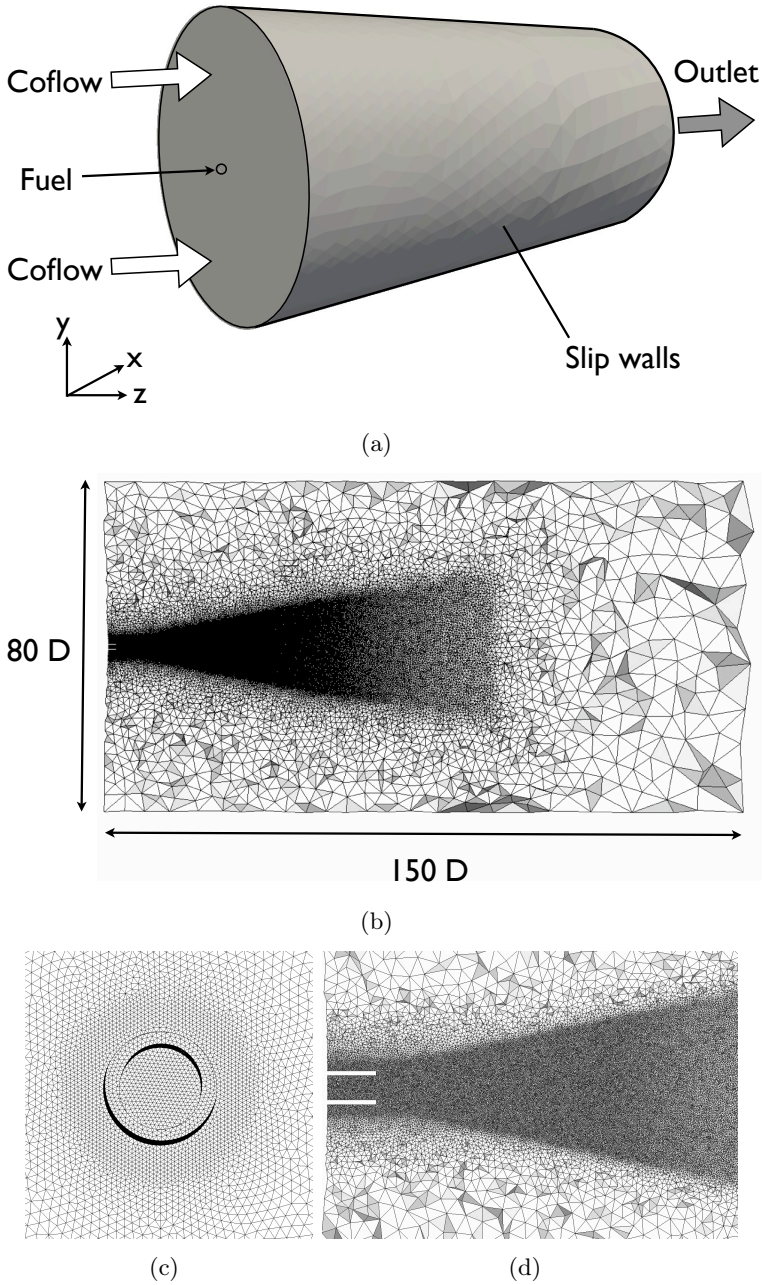

Figure 7.2: *Mesh used in three-dimensional large eddy simulation. (a) 3D view and boundary conditions. (b) Crinkly slice in the y-normal plane. (c) Zoom near the pipe from a x-normal view (d) Zoom near the pipe exit in the y-normal plane.*

Figure 7.3: *Instantaneous solution in the y-normal plane colored by mixture fraction (black: $\tilde{z} = 1$, white: $\tilde{z} = 0$).*

of interest in the non-reactive simulation. Mean variables fields are also averaged in the azimuthal direction to take advantage of the axisymmetric configuration.
Axial profiles of both numerical solutions are compared with the experimental ones in Fig. 7.4. Mixture fraction mean (Fig. 7.4(a)), resolved RMS (Fig. 7.4(b)) and the mean temperature (Fig. 7.4(c)) curves are plotted . Both numerical simulations with different turbulent Schmidt or Prandtl numbers predict similar statistics. Therefore, the influence of value specification for Sc_t and Pr_t is small.
The refinement level of the LES is investigated by comparing the total turbulent kinetic energy with the one resolved on the computational grid. The ratio of both quantities defined the Pope criterion (Pope, 2000, 2004):

$$\mathcal{M} = \frac{\{k_{SGS}\}}{k_{RES} + \{k_{SGS}\}} \tag{7.30}$$

where $k_{RES} = 1/2(\{u_i u_i\} - \{u_i\}\{u_i\})$ is the resolved turbulent kinetic energy and k_{SGS} is the instantaneous subgrid kinetic energy. k_{SGS} is evaluated from the turbulent viscosity (Yoshizawa, 1986) as:

$$k_{SGS} = \frac{\nu_t^2}{(C_{\mathcal{M}}\Delta)^2} \tag{7.31}$$

with the model constant $C_{\mathcal{M}} = 0.069$ and Δ taken as the cube root of the cell volume.
Axial profiles of k_{RES} and $\{k_{SGS}\}$ in Fig. 7.5(a) show that the resolved part of turbulent kinetic energy is much larger than the subgrid part. Radial

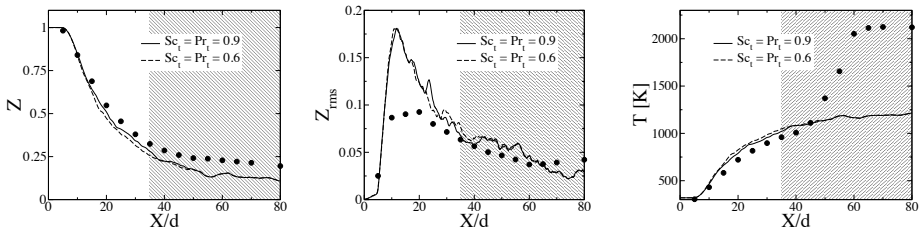

Figure 7.4: *Axial profile of mean mixture fraction (a), mixture fraction variance (b) and mean temperature (c). Numerical simulation:* $Sc_t = 0.9$ *(plain line) and* $Sc_t = 0.6$ *(dashed line). Experimental profile: symbols.*

profiles are also shown in Fig. 7.6. The resulting Pope criterion $\mathcal{M}$ is plotted in 7.5(b): after five diameters, the profile remains around 5-10%. Considering that a level of 20% is often high enough to perform LES (Pope, 2004), the present simulation presents a high level of resolution.
The LES high resolution indicates that turbulent transport is dominated by resolved convection rather than turbulent diffusion. Regarding the mixture fraction balance equation, this explains the reason for both simulations with different turbulent Prandtl and Schmidt numbers to obtain similar results. In the following, the value of 0.9 is chosen for Sc_t and Pr_t in all large-eddy simulations.
Comparisons with experimental profiles in Fig. 7.4 are valid for $X/d < 35$ where no combustion occurs yet. The mean mixture fraction and temperature profiles show that the jet potential core length is fairly retrieved and that the jet mixing is slightly overestimated but the numerical profiles remains close to the experimental ones. Regarding the mixture fraction RMS, levels of mixture fraction fluctuations on the jet axis are first found larger (up to 75%) than those measured by Cabra et al. (2005). Then, the numerical profiles of z_{RMS} get closer to the experimental curve for $X/d > 25$.
Radial profiles are presented in Fig. 7.7 at three axial locations: $X/d =$ 15, 30 and 40. The agreement between LES and experimental data is fair. The prediction of mixing is investigated further by studying the jet similarity. The mean axial profile of mixture fraction $z_0(x) = \{z\}(x, 0, 0)$ is used to normalized the mean mixture fraction field. The radius parameter $r_{1/2}$ defined as the half width of the radial mean mixture fraction profile is also introduced. Experimental and numerical radial profiles of $\{z\}/z_0(x)$ are plotted as function of the normalized radial coordinate $r/r_{1/2}$ in Fig. 7.8(a). Experimental profiles are here included even for $X/d > 40$ where the flame is present. It appears that, even in the presence of a lifted flame, experimental profiles collapse around a single curve. This self-similarity property is also found with numerical simulation profiles except for $X/d = 70$ which may be caused by a too short averaging time.

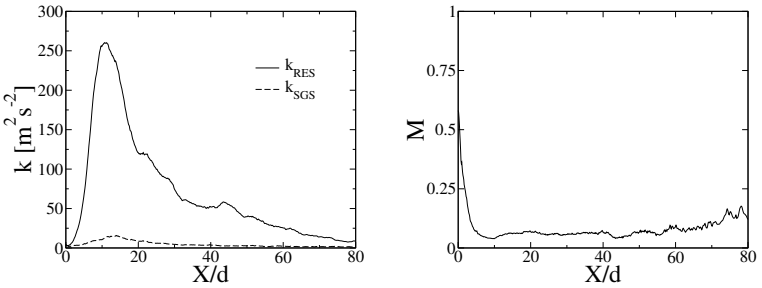

(a) (b)

Figure 7.5: *Axial profile of subgrid and resolved turbulent kinetic energy (a) and Pope criterion (b).*

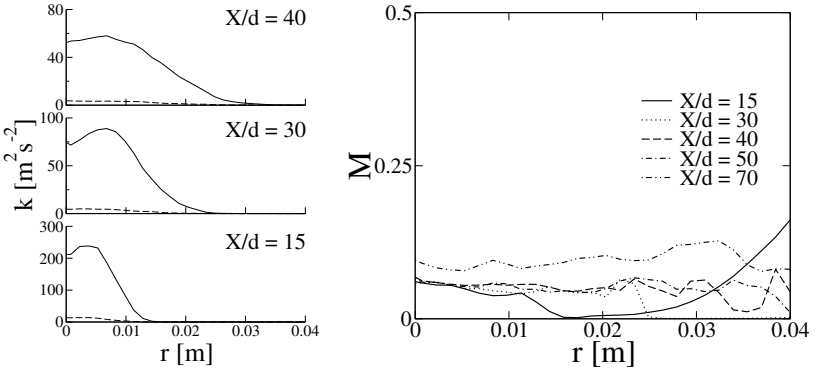

(a) (b)

Figure 7.6: *Radial profiles of subgrid (dashed line) and resolved (plain line) turbulent kinetic energy (a) and Pope criterion (b).*

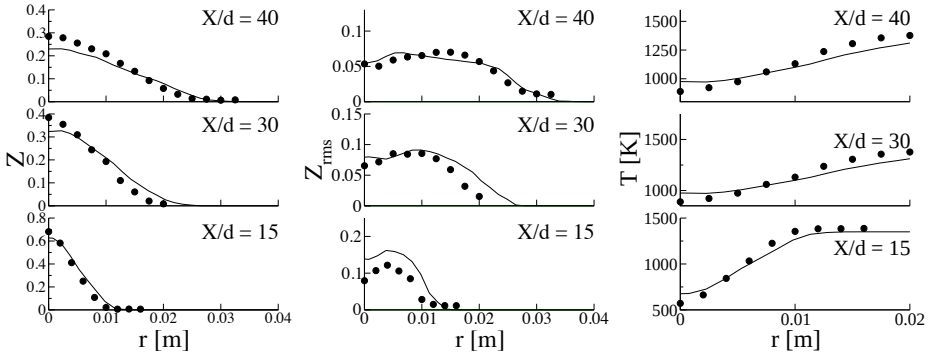

Figure 7.7: *Radial profiles of mean mixture fraction (a), mixture fraction variance (b) and mean temperature (c) at three axis distances: $X/d = 15$, 30 and 40. Numerical simulation: plain line. Experimental profile: symbols.*

Self-similarity is also studied with mixture fraction RMS profiles in Fig. 7.8(b). The collapsing of data is more scattered than previously but except for the $X/d = 70$ profile, the agreement between experimental and numerical profiles is correct. In conclusion, similarity analysis of mean and RMS mixture fraction profiles shows that the turbulent jet mixing properties are well captured by the non-reactive large-eddy simulation.

Finding the right fluctuations of the flame lift-off requires to reproduce the round jet dynamic. That is why the dynamic of the non-reactive jet is finally studied by examining the main frequencies found in the jet destabilization zone. Any jet flow inherently possesses a preferred mode whose frequency is determined by jet diameter d and the jet bulk velocity U_{JET}. The preferred frequency f is expressed in terms of the Strouhal number $S_t = fd/U_{Jet}$ where S_t varies between 0.25 and 0.5 (Gutmark and Ho, 1983). This mode is measured experimentally where the impinging jet destabilizes i.e. around the end of the potential core. In order to retrieve such a property of jet flow, Power Spectral Density (PSD) of the transverse velocity fluctuations v' are realized at different locations shown in Fig. 7.9(a). The PSD frequency resolution is 850 Hz which corresponds to an uncertainty on the Strouhal number of $\Delta S_t = 0.04$.

Probes 1 (Fig. 7.9(b)) and 2 (Fig. 7.9(c)) are located in the shear layer between the fuel jet and the vitiated coflow. High frequency coherent structures similar to those found in planar mixing layers are met. Amplitudes of the PSD peaks doubles between probes 1 and 2. It characterized the growth of shear layer instabilities. A peak at $S_t = 0.67$ is found in both locations and moving from probe 1 to 2, a high frequency peak ($S_t = 0.79$) disappears while a lower frequency mode ($S_t = 51$) appears. This changed of modes from high to lower frequencies inside a shear layer is due to the non-linear

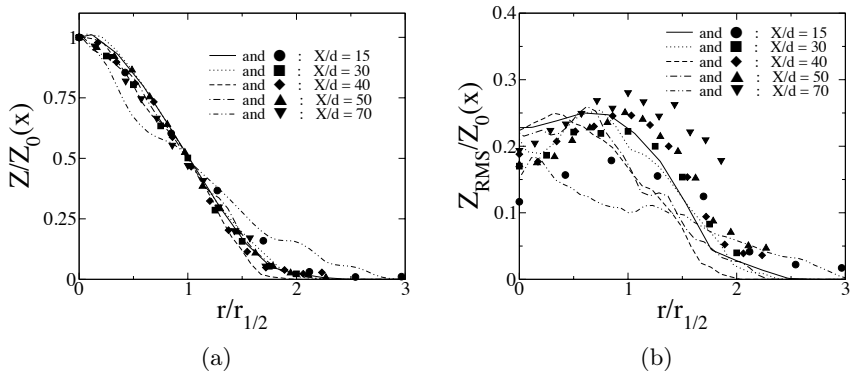

(a) (b)

Figure 7.8: *Self-similarity of radial profiles of mean mixture fraction (a) and mixture fraction variance (b). Time averaged mixture fraction and the resolved mixture fraction variance are scaled by the mean axial profile of mixture fraction $Z_0(x)$. The radius r is scaled by the half-width of the mean mixture fraction profile $r_{1/2}$ at each height. Numerical simulation: lines. Experimental profile: symbols.*

pairing of vortices. When looking downstream in the jet destabilization zone, only one preferred frequency remains at S_t=0.28 which is equivalent to 6130 Hz. This value agrees with the range 0.25-0.5 suggested by Gutmark and Ho (1983).

7.3 Reactive large-eddy simulation

7.3.1 Lift-off height

The reactive simulation is conducted starting from the non-reactive case by adding balance equation for z_v, $\widetilde{Y_c}$ and $\widetilde{Y_c^2}$. Tabulated chemistry parameters are first transported specifying null chemical source terms, which prevents combustion to take place in order to reach the stationary regime for all variables in a cold configuration. Then, the source term constraint is removed to allow auto-ignition. The source term correction specified in section 5.8 allows the LES computation to ignite spontaneously without introducing any kernel of burnt gases. The final lifted flame is shown in Fig. 7.10. Even once the flame is fully established, the source term correction is a key parameter as in RANS computations: it promotes auto-ignition at the flame basis and, hence, participates to the resulting flame lift-off.
LES data are averaged on a physical time of 11.6 ms i.e. almost three times the convective time scale l/U_{JET} where $l = 0.4$ m and $U_{JET} = 100$ m/s. This physical time required 25 000 CPUs hours in terms of computing resources on the IBM Power6 cluster at IDRIS (Institut du Développement et des Ressources en Informatique Scientifique). Data were also averaged in the azimuthal direction in order to benefit from the axisymmetric property of

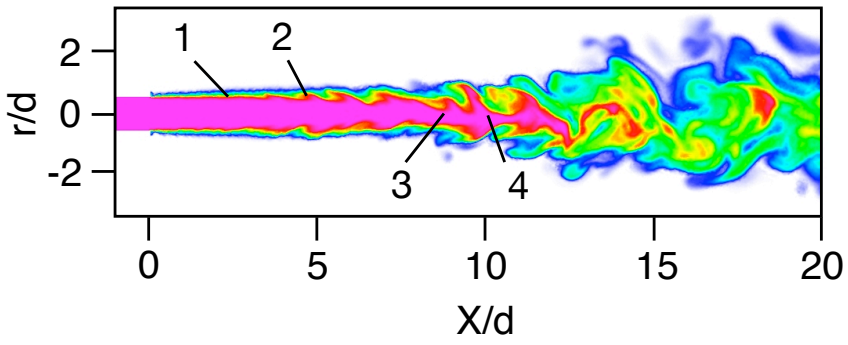

(a) Localisation of probes

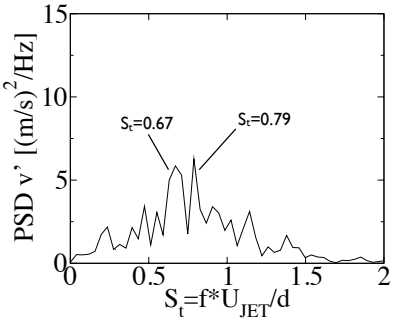

(b) Probe 2

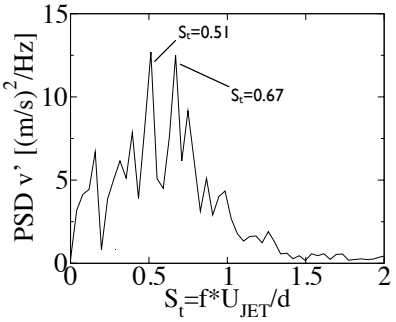

(c) Probe 1

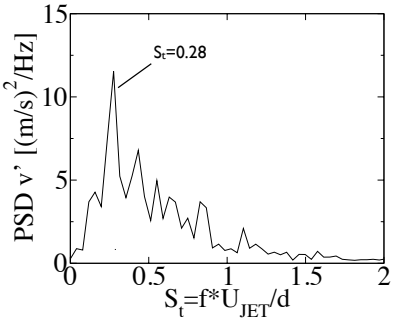

(d) Probe 3

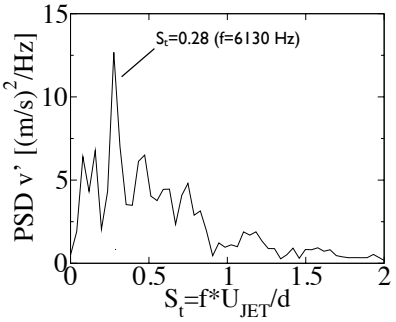

(e) Probe 4

Figure 7.9: *Power spectral density of transverse velocity fluctuations at different locations shown in (a). Probes 1 and 2 are located in the shear layer at $Y/d = 0.5$ while probes 3 and 4 are on the jet axis. Frequency axis is expressed in terms of Strouhal number $S_t = fU_{JET}/d$. The frequency resolution of $\Delta f = 850$ Hz corresponds to $\Delta S_t = 0.04$.*

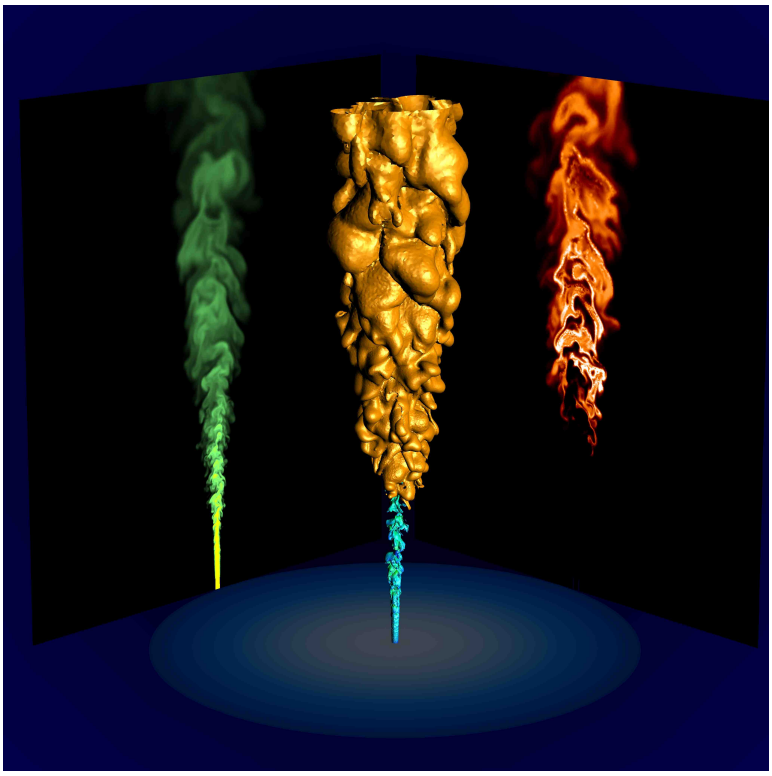

Figure 7.10: *Three-dimensional view of an instantaneous LES solution: isosurfaces of temperature (1600 K) and mixture fraction ($\tilde{z} = 0.5$) ; planar slices colored by mixture fraction (left) and OH mass fraction (right).*

the configuration.
The Favre mean temperature field is shown in Fig. 7.10. As in RANS computations, the isoline $\{Y_{OH}\} = 0.0005$ defines the flame lift-off height H. The large-eddy simulation gives $H/d = 28.8$ which is closer to the experimental value ($H/d = 35$) than the lift-off height found in RANS simulation (Fig. 6.11).

7.3.2 Comparison with experimental and RANS results

Axial profiles of mean mixture fraction $\{z\}$ and temperature $\{T\}$ are depicted in Fig. 7.12. The LES mean mixture fraction profile follows experimental data better than the RANS profile for $X/d > 30$. Hence, mixing prediction of LES is more efficient than RANS simulation with ad hoc coefficients. Indeed, LES subgrid flux modeling applies to small eddies that have a universal behavior, in opposition to large eddies which are resolved in LES and modeled in RANS approach.
Despite mixture fraction profiles in LES and RANS are different, both approaches find similar axial profiles of mean temperature (Fig. 7.12(b)). In

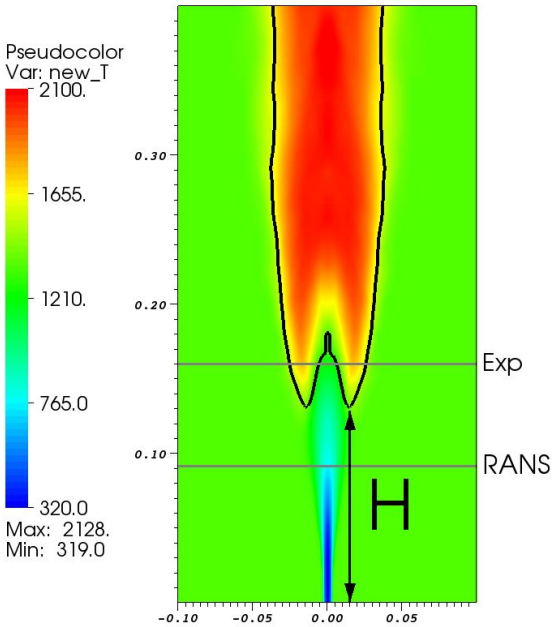

Figure 7.11: *Color map of mean temperature in the reactive large-eddy simulation. The lift-off height H is indicated by the black iso-line $\{Y_{OH}\} = 0.0005$. Lift-off heights found experimentally and in RANS computation are represented by horizontal grey lines.*

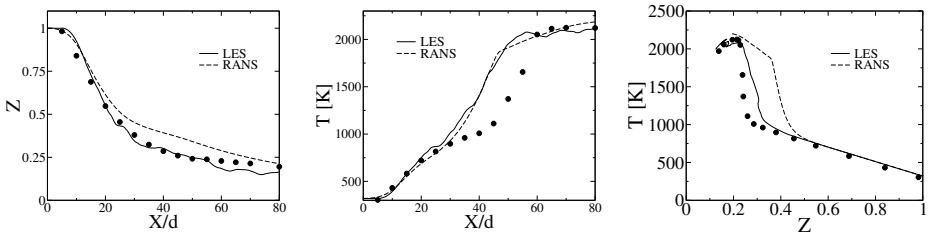

(a) (b) (c)

Figure 7.12: *Axial profiles of Favre mean mixture fraction (a) and mean temperature (b) in reactive LES (plain line) and RANS simulations (dashed line). Symbols: experimental data. (c) Mean temperature profile is plotted as function of mean mixture fraction.*

fact, even if lift-off heights differ, LES and RANS temperature profiles have the same distance with the experimental profile on the jet axis. However, when $\{T\}$ is plotted as a function of $\{z\}$ on the axis (Fig. 7.12(c)), the LES profile is much closer to the experimental one, indicating a better description of the combustion process.
Radial profiles of mean and RMS of mixture fraction are plotted in Fig. 7.13. Agreement between LES and experimental profiles is better than RANS results except for $X/d = 70$. The mean temperature profiles in Figs. 7.13(c) and 7.13(f) shows that combustion starts too soon in RANS and LES and that both approaches prediction are good upstream ($X/D = 15$) and downstream ($X/d = 70$) the flame stabilization zone. Nonetheless, LES finds a better lift-off height by starting to burn above the RANS lift-off height (see profiles at $X/d = 30$).
LES radial profiles of mean temperature are plotted as functions of mean mixture fraction in Fig. 7.14. This figure shows the LES underestimation of the flame lift-off height in mixture fraction space. However, this result is better than the one found with RANS simulation in Fig. 6.13(c).
Mean species profiles of LES and RANS computations are compared with experimental data in Fig. 7.15. Both numerical simulations obtain similar species profile (except for CO mass fraction) because the flame lift-off height is underestimated in both cases. Consequently, progress of reaction is found too high at $X/d = 40$ but numerical profiles retrieve experimental points when fully burning state is reached. RMS radial profiles of temperature, CO_2 and OH mass fraction are plotted in Fig. 7.16. Numerical profiles are in the right order of magnitude and the same tendency as described for mean species profiles is observed.

7.3.3 Analysis of LES results

Scatter plots of temperature

LES results are further investigated in order to understand why RANS and LES approach predict different flame lift-off heights although similar tabulated chemistry models have been used.
Scatter plots are first studied in different planes: $X/d = 10$, 25, 30, 35, 40 and 60. These planes shown in Fig. 7.17 allow to follow the transition from fresh to burnt gases during the large-eddy simulation. For each plane, temperature color map and scatter plot in mixture fraction space are drawn in Fig. 7.18. In the LES computation, combustion takes place as follows:

(a) Fuel jet mixes with the hot vitiated coflow without noticeable reaction. The scatter plot of temperature is identical to the pure mixing line.

(b) Ignition starts in lean hot mixtures. Indeed, departure from the pure mixing line are observed in the scatter plot. In lean mixtures, fresh, burnt and intermediate states are met for the same axis distance.

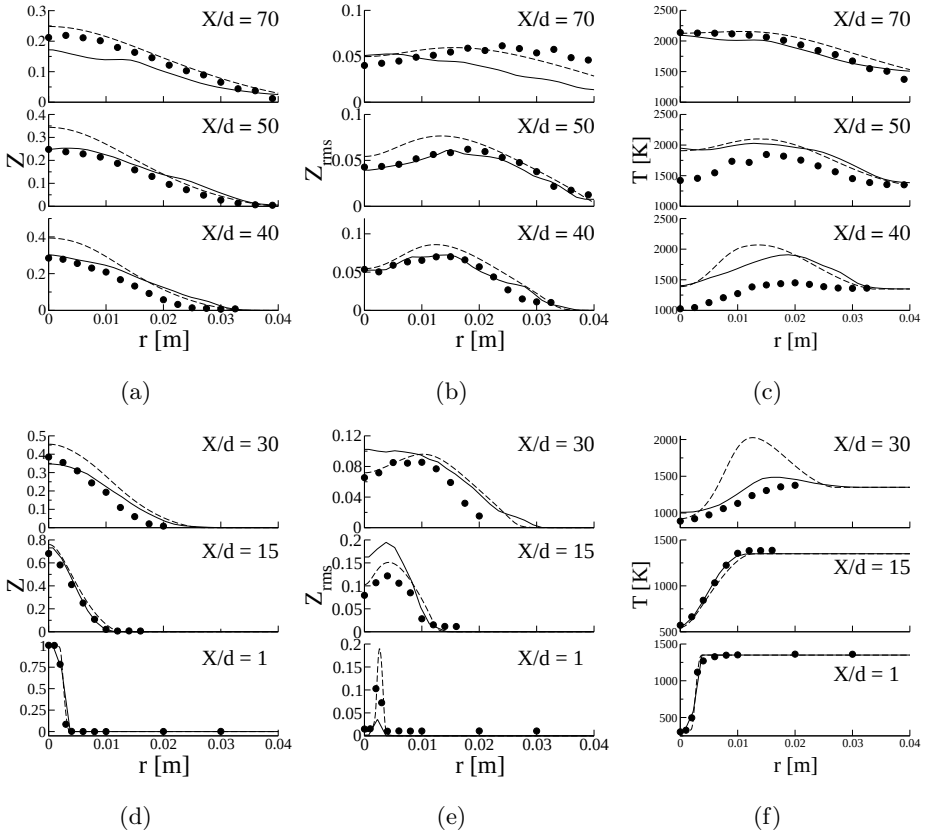

Figure 7.13: *Radial profiles of Favre mean mixture fraction (a), its RMS (b) and Favre mean temperature (c, d) in reactive LES (plain line) and RANS simulations (dashed line). Symbols: experimental data.*

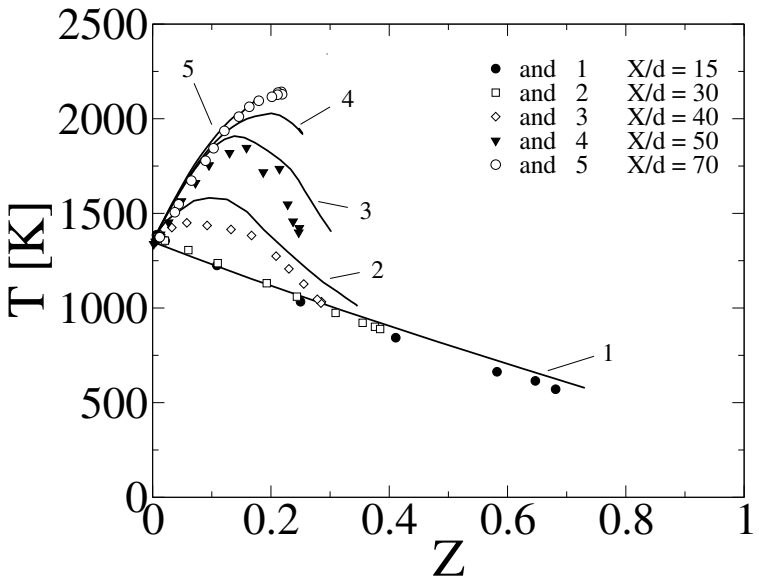

Figure 7.14: *Radial profiles of Favre mean temperature plotted as function of Favre mean mixture fraction. Lines: LES results. Symbols: experimental data.*

(c) Ignition spreads to richer mixtures. During the same time, dilution into the coflow goes on and the maximum mixture fraction encountered decreases.

(d) Lean mixtures are fully burnt while the others close to the jet axis are still burning.

(e) Rich pockets reach the final burning state.

(f) Finally, all points form the steady flamelet solution, indicating a diffusion flame downstream the flame stabilization zone as expected.

Consequently, combustion in LES takes place in the same way as unsteady flamelets in the UTaC database. RANS simulation also follows the same pattern but LES allows to describe much more complex effects. Indeed, auto-ignition is an unsteady phenomenon which should be tackled efficiently by LES. In Fig. 7.18(b) for example, scatter plot shows that different burning states are encountered for a same mixture. This point is investigated more closely in Fig. 7.19 where the source term $\widetilde{\dot{\omega}_{Y_c}}$ is represented. Iso-lines of mixture fraction and mean scalar dissipation rates are also drawn. It appears that combustion does not occur in the left half-part of the figure. It explains the presence of burning and non-burning states in the scatterplot for the same mixture. The mean scalar dissipation rate contour tends to indicate that combustion in identical mixtures is or has been prevented by high strain rates. Consequently, fluctuations of ignition induced by unsteady scalar

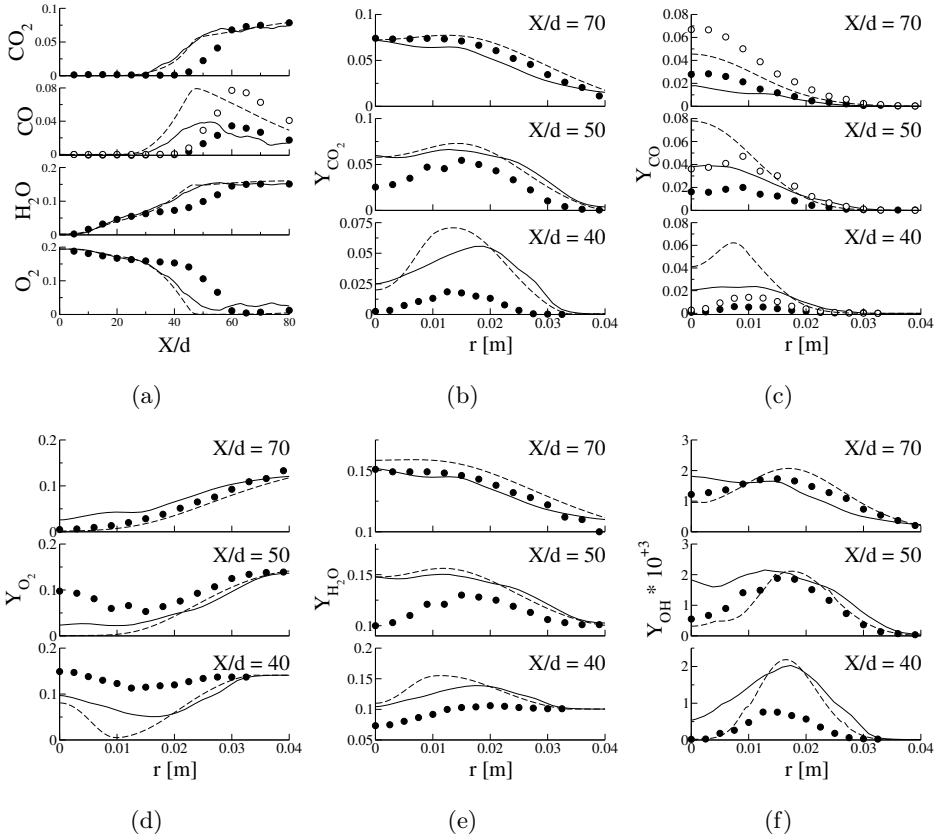

Figure 7.15: *Profiles of Favre mean species mass fractions tabulated in the UTaC database (LES: plain line ; RANS: dashed line) and measured (symbols). (a) Axial profiles of several species. (b) Radial profiless of CO_2. (c) Radial profiles of CO (two sets of measurements are available: black (Raman) and white (LIF) circles). (d) Radial profiles of O_2. (e) Radial profiles of H_2O. (f) Radial profiles of OH.*

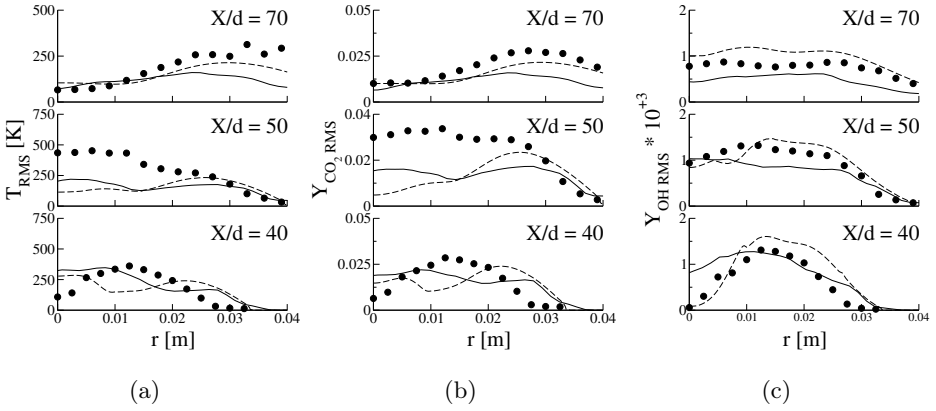

Figure 7.16: *Radial profiles of temperature (a), CO_2 and OH mass fraction RMS in reactive LES (plain line) and RANS simulations (dashed line). Symbols: experimental data.*

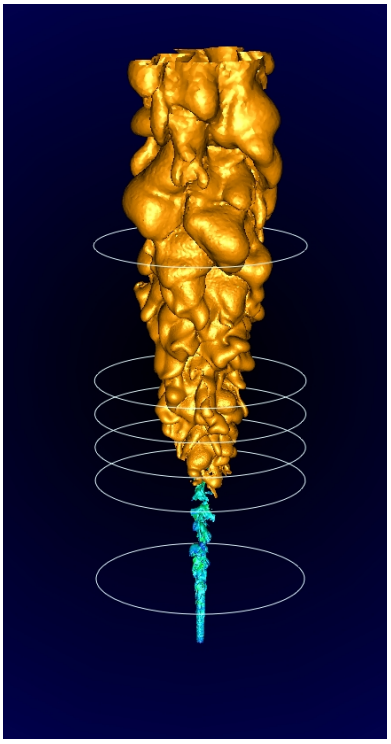

Figure 7.17: *Locations of the different slice planes (X/d = 10, 25, 30, 35, 40, 60) in comparison to the flame position.*

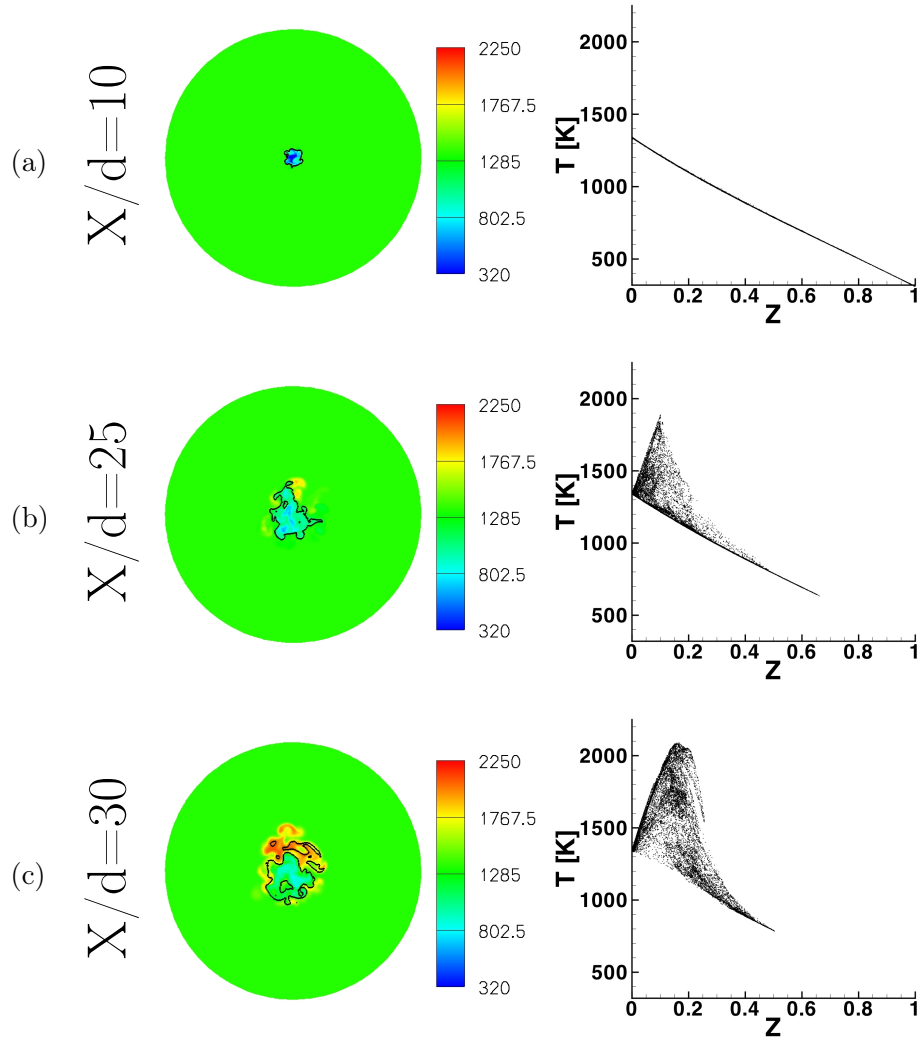

Figure 7.18: *Instantaneous temperature color maps and scatter plots in mixture fraction space at different slice planes: (a) $X/d = 10$; (b) $X/d = 25$; (c) $X/d = 30$; (d) $X/d = 35$; (e) $X/d = 40$; (f) $X/d = 60$. Black line: iso-line $\tilde{z} = z_{st} = 0.175$.*

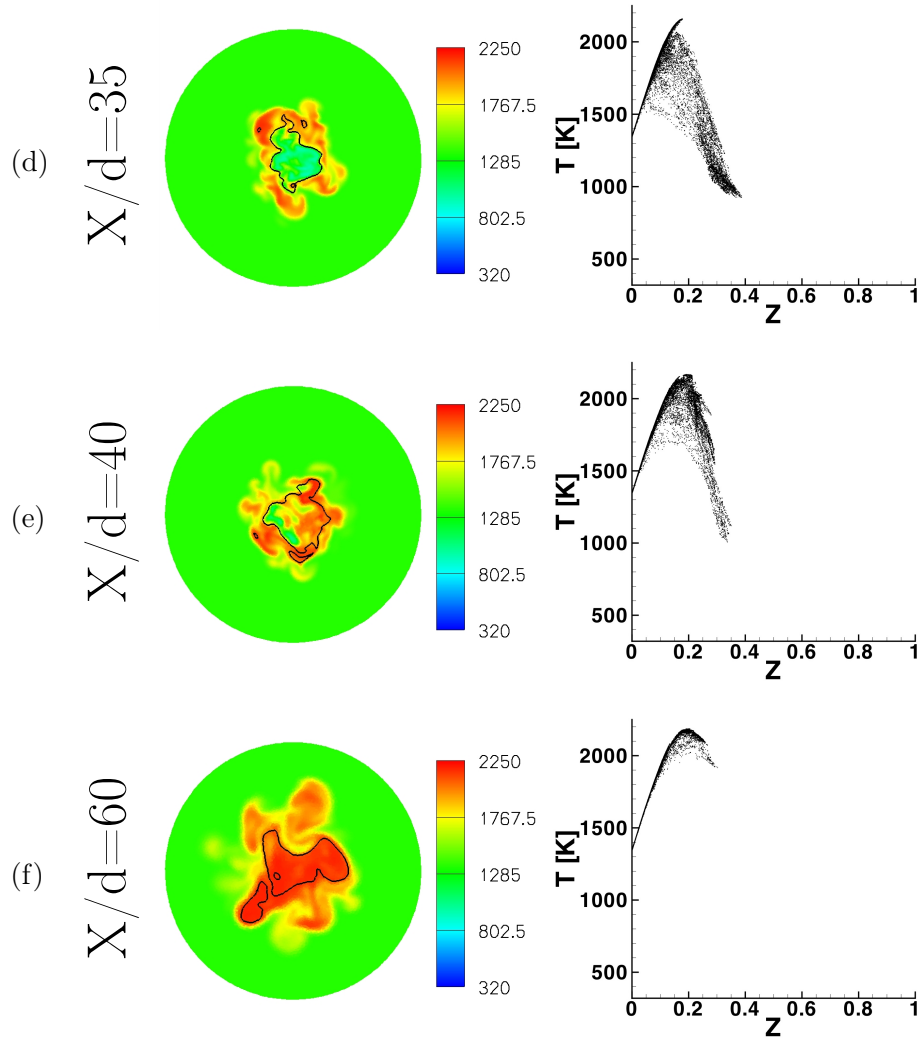

Figure 7.18: *Instantaneous temperature color maps and scatter plots in mixture fraction space at different slice planes: (a) X/d = 10 ; (b) X/d = 25 ; (c) X/d = 30 ; (d) X/d = 35 ; (e) X/d = 40 ; (f) X/d = 60. Black line: iso-line* $\tilde{z} = z_{st} = 0.175$.

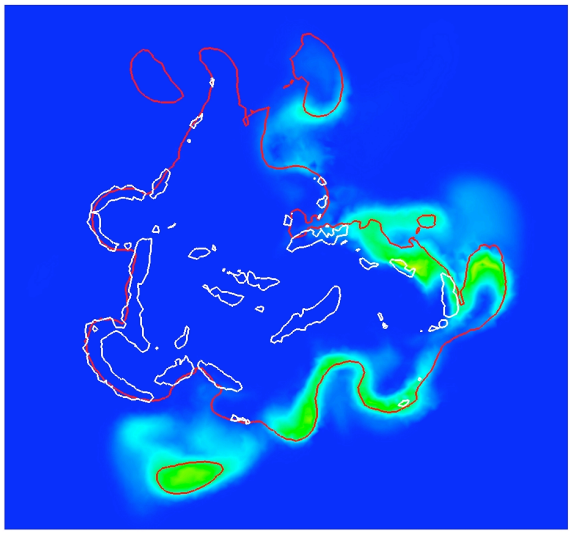

Figure 7.19: *Plane at $X/d = 25$ colored by the source term $\widetilde{\dot{\omega}_{Y_c}}$. White line: iso-line $\tilde{\chi} = 25\ s^{-1}$. Red line: iso-line $\tilde{z} = 0.1$.*

dissipation rates are captured in LES. This is clearly not the case in RANS context where the mean stationary solution is computed and where variation of χ_{st} are taken into account by introducing a log-normal distribution.

Probability density function of scalar dissipation rates

Playing an equivalent part as PDF in RANS, large-eddy PDFs are used in LES. The scalar dissipation rate large-eddy PDF $P_{LES}(\chi_{st})$ was modeled as a Dirac distribution: $P_{LES}(\chi_{st}) = \delta(\chi_{st} - \tilde{\chi}_{st})$. Hence, the actual value χ_{st} at the subgrid scale is assumed identical to the resolved quantity $\tilde{\chi}_{st}$. Consequently, the RANS PDF $P(\chi_{st})$ can be computed from LES by monitoring the signal $\tilde{\chi}_{st}(t)$ at different positions and be compared to the log-normal approximation.
This is done at different points of the large-eddy simulation. Their positions are shown in Fig. 7.20 and the computed PDF $P(\chi_{st})$ are plotted in Fig. 7.21. Each point is indicated by a letter (b, c, d, e, f) which refers to the corresponding subfigure in Fig. 7.21. Figure 7.21(a) shows the signal $\tilde{\chi}_{st}(t)$ registered at the point c for example. Computed PDF (black bins) are compared in Fig. 7.21 with their approximation used in RANS (red curves) i.e. a log-normal distribution whose mean is set to $\langle\tilde{\chi}_{st}\rangle$ and standard deviation σ to unity. The agreement between both PDF is very good in points d, e and f while the comparison is not so good for points closer to the jet exit in points b and c. This result is due to the fact that d, e and f are located in a fully developed turbulent flow whereas points b and c are submitted to scalar dissipation rates fluctuations created by coherent structures. The blue

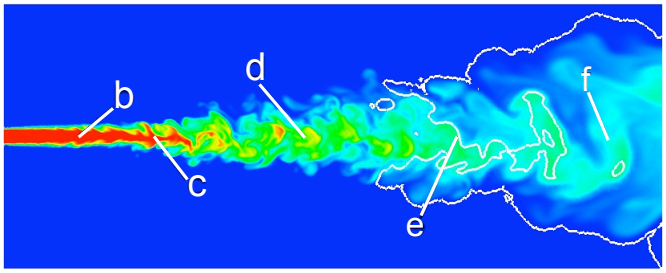

Figure 7.20: *Probes b, c, d, e, f corresponding to subfigures in Fig. 7.21 are located on a color map of mixture fraction. The lifted flame is shown by the iso-line* $\overline{c} = 0.1$.

curve in Fig. 7.21(b) which is the best fitting log-normal distribution shows that the standard deviation, here 0.62, is different from unity.
Consequently, the RANS hypothesis, $\sigma = 1.0$, can be considered as valid although a bias occurs along the potential core.

Study of dependency between $\tilde{z}$ and $\overline{c}$

In LES, z and c are assumed independent at the subgrid scale unlike the RANS model which considers the independency valid at each time and each scale. This latter hypothesis is investigated by computing joint PDF of LES resolved variables $\tilde{z}$ and $\overline{c}$. Results are shown in Fig. 7.22 where time signal of $\tilde{z}$ and $\overline{c}$ (first column) at different location are post-treated to compute the PDF $P(\tilde{z}, \overline{c})$ (second column). $P(\tilde{z}, \overline{c})$ is plotted in the $\tilde{z}$-$\overline{c}$ plane: the progress variable segment [0, 1] is split in ten intervals as well as the mixture fraction segment bounded by its minimum and maximum values. Points in Fig. 7.22 are chosen at different positions on the jet axis: X/d = 20, 30, 40, 50 and 75.
In Fig. 7.22(a), $\overline{c}$ is quasi-null at each moment, leading to a PDF $P(\tilde{z}, \overline{c})$ centered on $\langle\tilde{z}\rangle$ and null for $\overline{c} \neq 0$. The conditional mean of progress variable on mixture fraction, $\langle\overline{c}|\tilde{z} = z^*\rangle$, is also plotted in the third column of Fig. 7.22. In Fig. 7.22(b) where some ignition events are observed, $\langle\overline{c}|\tilde{z} = z^*\rangle$ demonstrates that ignition occurs favorably in lean mixtures. Fluctuations of resolved progress variable are more intense in Fig. 7.22(c). At this point, the joint PDF clearly shows that the function $P(\tilde{z}, \overline{c})$ differs in the mixture fraction direction. The conditional PDF $P(\overline{c}|\tilde{z} = z^*)$ is therefore different from the marginal PDF $P(\overline{c})$, indicating that $\tilde{z}$ and $\overline{c}$ are not independent. Furthermore, for mixture fractions around $\tilde{z}$=0.2, $P(\tilde{z}, \overline{c})$ shows some bimodality behavior in the $\overline{c}$-direction. Dependency between mixture fraction and progress variable is also shown in Fig. 7.22(d) by the form of the joint PDF and the conditional mean. Finally, in Fig. 7.22(e), all mixtures are ignited and form a burning diffusion flame.

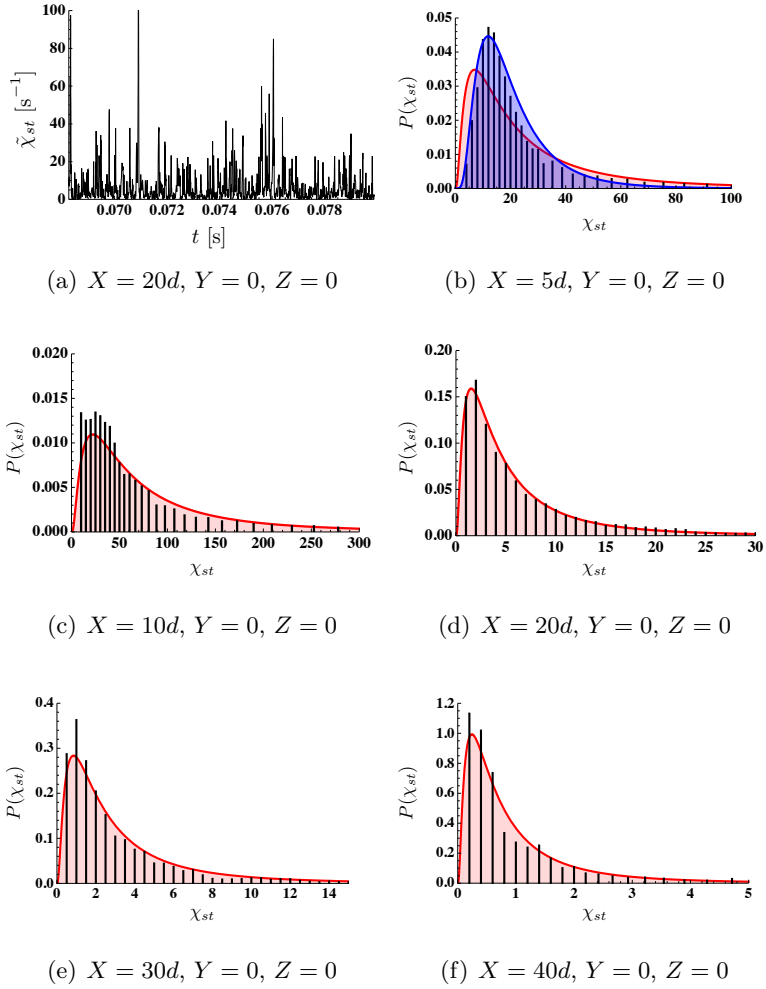

(a) $X = 20d$, $Y = 0$, $Z = 0$ (b) $X = 5d$, $Y = 0$, $Z = 0$

(c) $X = 10d$, $Y = 0$, $Z = 0$ (d) $X = 20d$, $Y = 0$, $Z = 0$

(e) $X = 30d$, $Y = 0$, $Z = 0$ (f) $X = 40d$, $Y = 0$, $Z = 0$

Figure 7.21: *Computed PDF $P(\chi_{st})$ (black bins) compared with log-normal distribution $P(\chi_{st}) = LogNormal(\chi_{st}; \mu, \sigma)$ (red curve) with $\mu = ln(\tilde{\chi}_{st}) - \sigma^2/2$ and $\sigma = 1.0$ at different locations (b, c, d, e, f). The computed mean $\tilde{\chi}_{st}$ are 31.1 (b), 99.0 (c), 6.8 (d), 3.8 (e) and 1.1 s^{-1} (f). An example of the time signal $\tilde{\chi}_{st}(t)$ is given in (a). The best fitting log-normal distribution ($\mu = 2.86$, $\sigma = 0.62$) plotted with a blue curve is added in (b).*

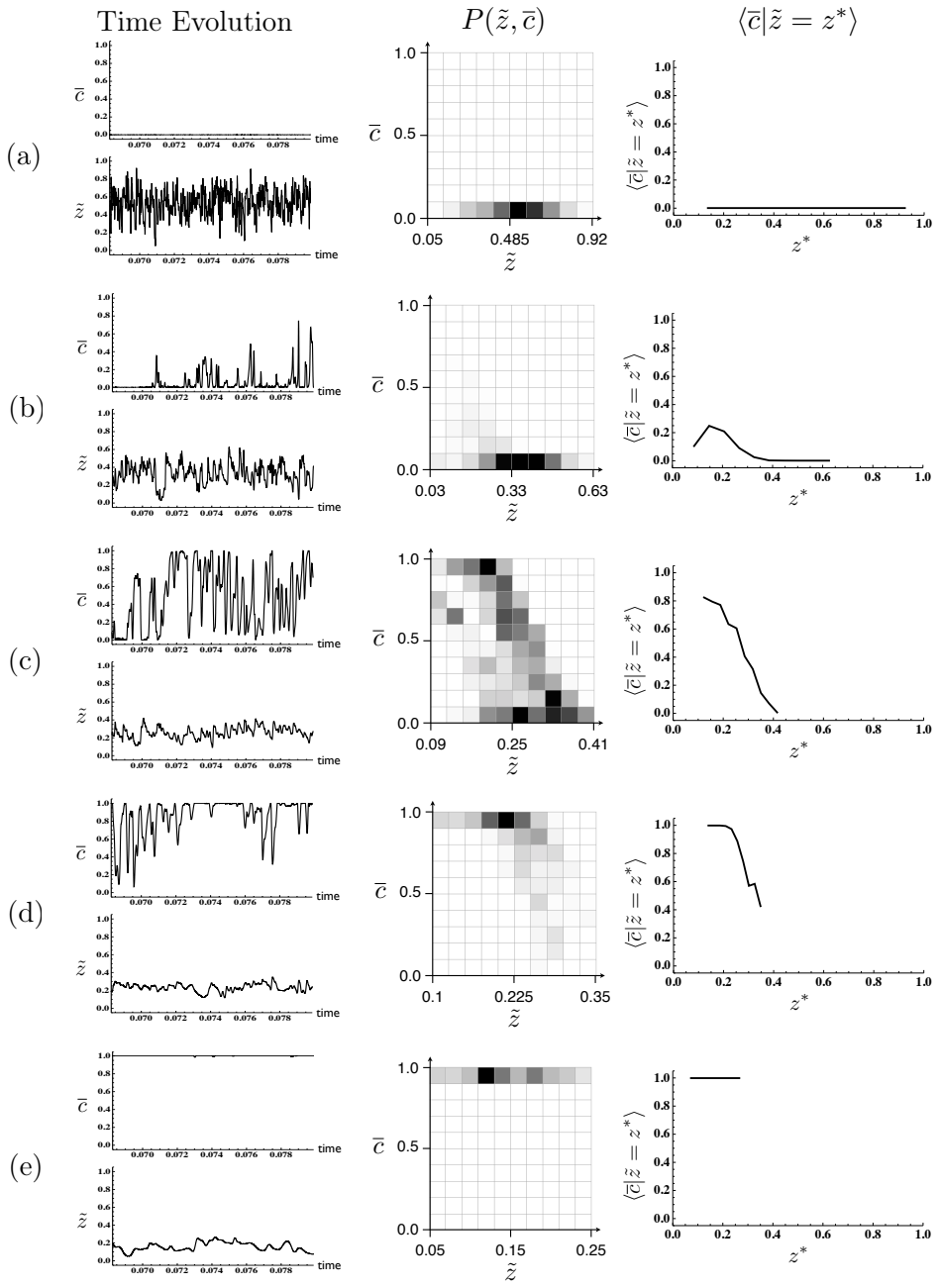

Figure 7.22: *Statistical analysis of time signal of $\overline{c}$ and $\tilde{z}$ at several locations on the jet axis: (a) $X/d = 20$; (b) $X/d = 30$; (c) $X/d = 40$; (d) $X/d = 50$; (e) $X/d = 75$. First column: time signals $\overline{c}(t)$ and $\tilde{z}(t)$. Second column: color maps of the joint PDF $P(\tilde{z},\overline{c})$ in the discretized $\tilde{z}$-$\overline{c}$ plane. Third column: profiles of the progress variable conditional mean $\langle\overline{c}|\tilde{z}=z^*\rangle$.*

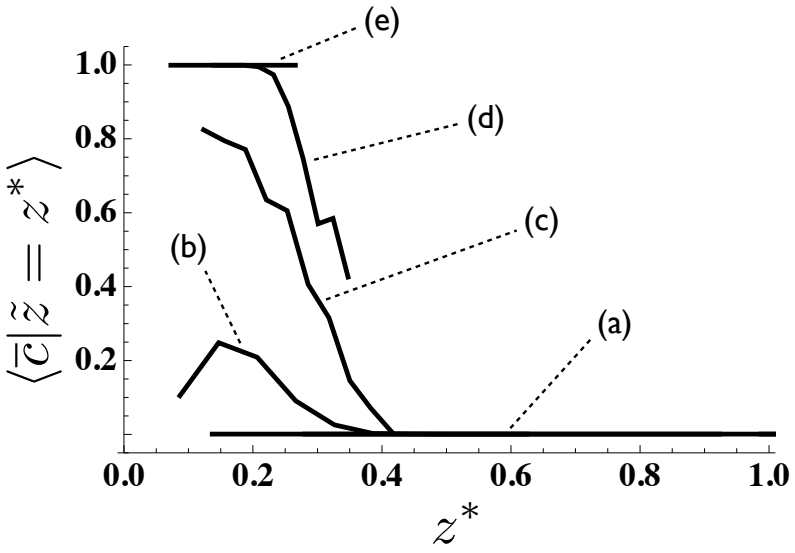

Figure 7.23: *Profiles of the conditional mean $\langle \overline{c}|\tilde{z} = z^* \rangle$ at locations (a), (b), (c), (d) , (e) defined in Fig. 7.22.*

All profiles $\langle \overline{c}|\tilde{z} = z^* \rangle$ of Fig. 7.22 are gathered in Fig. 7.23 showing the evolution of the conditional mean along the jet axis. As already explained, the dependency on mixture fraction of the profile $\langle \overline{c}|\tilde{z} = z^* \rangle$ invalidates the RANS hypothesis: z and c are not independent.

7.4 Conclusion

A large-eddy simulation of a jet issuing in a vitiated coflow was performed with the compressible code AVBP. The model UTaC was coupled with the compressible simulation following the TTC formalism developed in chapter 3. Non-reactive case shows that the mixing field is well predicted upstream of the lifted flame. The reactive case is then realized. Ignition starts spontaneously and leads to a stable lifted flame. The lift-off height found by LES is 28.8 diameters which is half between the experimental value and the one computed in RANS. Comparisons with experimental data suffer from a shift due to the lift-off height underestimation but are good upstream and downstream the flame stabilization zone. Scatter plots have shown that combustion takes place in LES the same way it does in unsteady non-premixed flamelets.
RANS and LES with similar tabulated chemistry models give different results although their predictions of mixing are similar in this case. A first reason for LES to perform better than RANS is that auto-ignition is an

unsteady phenomenon which is well tackled by LES in opposition to steady simulations. Secondly, LES introduces less numerical errors than RANS simulations to capture auto-ignition in lean mixture fractions. Third reason is that some assumptions are made in both approaches but those assumed in LES have a smaller impact since it applies to subgrid scales. Hence, RANS hypotheses are studied by post-processing the LES. The modeling of the scalar dissipation rate PDF by a log-normal distribution with unity standard deviation was shown to be good. However, the presumed independency made in RANS between mixture fraction and progress variable is not valid since combustion first occurs in lean mixtures. This error may explain the underestimated lift-off height found in RANS since when lean mixture starts to burn ($c = 0.1$ for example), all other mixtures are assumed in the same state. This leads the RANS computation to burn in rich mixture regions while LES does not, as shown from mean temperature profile in mean mixture fraction space (Fig. 7.12(c)).

Consequently, a RANS model should be developed in the future without assuming independency between z and c. This can be realized by using a generalized parameter which does not depends on the mixture fraction by its definition, as done by Pierce and Moin (2004) and Ihme and Pitsch (2008b). Michel et al. (2009) derived a model where the joint PDF of z and c is not decoupled and applied it successfully to the Cabra burner. However, this model neglects fluctuations of c at a given mixture fraction, phenomenon which was evidenced by the LES. Results of Michel et al. (2009) tend nonetheless to show that neglecting these fluctuations of c is a smaller error than assuming independency between z and c.

Part III

A new tabulated chemistry model for perfectly premixed combustion in LES

Chapter 8

Derivation and validation of the model F-TACLES (Filtered Tabulated Chemistry for Large Eddy Simulation)

In this part, a new strategy is developed to tackle subgrid combustion modeling in LES. In the previous part, following the FPI-PCM method (Galpin et al., 2008b), subgrid combustion has been modeled by introducing PDF which were approximated by β-functions. This choice is however not valid in premixed combustion when the subgrid wrinkling of the flame vanishes and the LES filter remains larger than the flame thickness. Indeed, Vicquelin et al. (2009) showed that the β-PDF is significantly different from the exact PDF and leads to wrong flame propagation speed. This situation is encountered in several regions of current large eddy simulations. Moreover, this will become more frequent because the growth of computing resources allows to perform more and more resolved LES with a corresponding decreasing contribution of subgrid turbulence. In order to overcome this issue, a new modeling strategy called F-TACLES (Filtered Tabulated Chemistry for Large Eddy Simulation) is developed to introduce tabulated chemistry methods in LES of turbulent premixed combustion. In this model, the filtered flame structure is mapped using 1-D filtered laminar premixed flames. To describe the model and its application, the following publication is inserted: ***Fiorina, B., Vicquelin, R., Auzillon, P., Darabiha, N., Gicquel, O., and Veynante, D. (2010). A filtered tabulated chemistry model for LES of premixed combustion.*** **Combustion and Flame,** ***157(3):465–475.***

A filtered tabulated chemistry model for LES of premixed combustion

Fiorina, B., Vicquelin, R., Auzillon, P., Darabiha, N., Gicquel, O., and Veynante, D.

Combustion and Flame (2010), 157(3):465–475

8.1 Abstract

A new modeling strategy called F-TACLES (Filtered Tabulated Chemistry for Large Eddy Simulation) is developed to introduce tabulated chemistry methods in Large Eddy Simulation (LES) of turbulent premixed combustion. The objective is to recover the correct laminar flame propagation speed of the filtered flame front when subgrid scale turbulence vanishes as LES should tend toward Direct Numerical Simulation (DNS). The filtered flame structure is mapped using 1-D filtered laminar premixed flames. Closure of the filtered progress variable and the energy balance equations are carefully addressed in a fully compressible formulation. The methodology is first applied to 1-D filtered laminar flames, showing the ability of the model to recover the laminar flame speed and the correct chemical structure when the flame wrinkling is completely resolved. The model is then extended to turbulent combustion regimes by including subgrid scale wrinkling effects in the flame front propagation. Finally, preliminary tests of LES in a 3-D turbulent premixed flame are performed.

8.2 Introduction

Flame ignition and extinction or pollutant predictions are crucial issues in LES of premixed combustion and are strongly influenced by chemical effects. Unfortunately, despite the rapid increase in computational power, performing turbulent simulations of industrial configurations including detailed chemical mechanisms will still remain out of reach for a long time. A commonly-used approach to address fluid/chemistry interactions at a reduced computational cost consists in tabulating the chemistry as a function of a reduced set of variables. Some techniques, such as Intrinsic Low Dimensional Manifold (ILDM) developed by Mass & Pope (Maas and Pope, 1992), are based on a direct mathematical analysis of the dynamic behavior of the chemical system response. Alternative approaches are Flame Prolongation of ILDM (FPI) (Gicquel et al., 2000; Fiorina et al., 2003) or Flamelet Generated Manifold (FGM) (van Oijen et al., 2001). Both techniques assume that the chemical flame structure can be described in a reduced phase subspace from elementary combustion configurations. For instance, the chemical subspace of a turbulent premixed flame can be approximated from a collection of

1-D laminar flames. In such simple situations, all thermo-chemical quantities are related to a single progress variable.
To couple tabulated chemistry with turbulent combustion, mean quantities can be estimated with presumed probability density functions. This approach, that does not require prohibitive resources, has been developed for Reynolds Averaged Navier-Stokes (RANS) computations in the past (Vervisch et al., 2004; Fiorina et al., 2005b). Unfortunately, the extension of RANS turbulent combustion models to LES is not straightforward. Indeed, the primary recurrent problem is that the flame thickness is typically thinner than the LES grid size. As the progress variable source term is very stiff, the flame front cannot be directly resolved on practical LES grid meshes, leading to numerical issues. To overcome this difficulty, dedicated models have been developed under simplified chemistry assumptions. A solution to propagate a flame on a coarse grid is to artificially thicken the flame front by modifying the diffusion coefficient and pre-exponential constant (Butler and O'Rourke, 1977; Colin et al., 2000). Following a different strategy and under simplified chemistry assumptions, Boger *et al.* (Boger et al., 1998) and more recently Duwig *et al.* (Duwig, 2007) have introduced a filter larger than the mesh size to resolve the filtered flame structure. An opposite alternative is to solve a large scalar field where a given iso-surface is identified to the instantaneous flame front position. In such technique, called G-equation model, the inner layer is tracked using a level-set technique. Initially developed in a RANS context (Peters, 2000), the G-equation has been reformulated for LES (Menon and Jou, 1991; Chakravarthy and Menon, 2000; Pitsch, 2005). However as level-set techniques provide information only on the thin reaction zone position and not on the filtered flame structure, the coupling with the flow equations is challenging. In particular the knowledge of the temperature field is required for taking into account heat expansion. As recently proposed by Moureau *et al.* under simplified chemistry assumption (Moureau et al., 2009), a solution is to solve an additional progress variable equation to ensure a consistent coupling with a LES flow solver.
The FPI-PCM (Presumed Conditional Moment) model (Galpin et al., 2008b), developed to introduce tabulated chemistry effects in LES, combines presumed Probability Density Functions (PDF) and FPI tables to describe the chemical reaction rate of the filtered progress variable accounting for interactions between turbulence and chemistry at the subgrid scale level. However, as will be shown further, this formulation does not guarantee a proper prediction of regimes where the subgrid scale flame wrinkling vanishes. This regime, observed when the subgrid fluctuations are lower than the laminar flame speed, is encountered in practical LES of premixed combustion (Pitsch, 2006; Moureau et al., 2009). Additionally LES should tend toward DNS when the filter size becomes lower than the Kolmogorov scale. Hawkes & Cant (Hawkes and Cant, 2001) extensively discussed realizability in premixed combustion LES.

In the present work, it is first demonstrated that the β-PDF formalism applied in the context of premixed combustion LES does not guarantee a proper description of a filtered laminar flame front. Therefore an alternative is proposed to include tabulated chemistry in LES approach ensuring the correct propagation speed of the filtered laminar flame front. The resolved flame structure is mapped from 1-D filtered laminar premixed flames. The idea of tabulating filtered quantities has already been introduced (Vreman et al., 2009) but unresolved convective and diffusive terms where neglected. As it will be demonstrated further, these assumptions do not allow a proper description of the filtered flame structure and propagation. Here, closure of filtered flow and progress variable equations are first carefully addressed in regimes where the flame wrinkling is fully resolved. One-dimensional computations are performed to investigate the capability of the proposed model to reproduce the correct propagation speed and the filtered flame structure. The model is then extended to turbulent combustion regimes taking into account subgrid scale flame wrinkling. Finally, simulations of a turbulent swirled premixed flame are performed and compared to experimental data.

8.3 Coupling tabulated chemistry and LES: filtered equations

Low-dimensional trajectories in composition space are identified in FPI framework from the knowledge of the complex chemical structure of 1-D laminar flames (Gicquel et al., 2000). For premixed combustion systems, a 1-D freely propagating flame is first computed using detailed chemical schemes. Thermodynamical and chemical quantities are then tabulated as a function of a unique monotonic progress variable c related to temperature or to a combination of chemical species, where $c = 0$ corresponds to fresh gases and $c = 1$ to fully burnt gases. The chemical database is then coupled to the flow field by adding the progress variable balance equation to the Navier-Stokes equations. The progress variable reaction rate and heat release are extracted from the chemical database. For LES, under unity Lewis numbers assumption, these equations are filtered leading to the following system :

$$\frac{\partial \bar{\rho}}{\partial t} + \nabla \cdot (\bar{\rho}\widetilde{\boldsymbol{u}}) = 0 \tag{8.1}$$

$$\frac{\partial \bar{\rho}\widetilde{\boldsymbol{u}}}{\partial t} + \nabla \cdot (\bar{\rho}\widetilde{\boldsymbol{u}}\widetilde{\boldsymbol{u}}) = -\nabla \overline{P} + \nabla \cdot \overline{\tau} - \nabla \cdot (\bar{\rho}\widetilde{\boldsymbol{u}\boldsymbol{u}} - \bar{\rho}\widetilde{\boldsymbol{u}}\widetilde{\boldsymbol{u}}) \tag{8.2}$$

$$\frac{\partial \bar{\rho}\widetilde{c}}{\partial t} + \nabla \cdot (\bar{\rho}\widetilde{\boldsymbol{u}}\widetilde{c}) = \nabla \cdot \left(\overline{\rho D \nabla c}\right) - \nabla \cdot (\bar{\rho}\widetilde{\boldsymbol{u}c} - \bar{\rho}\widetilde{\boldsymbol{u}}\widetilde{c}) + \bar{\rho}\widetilde{\dot{\omega}}_c \tag{8.3}$$

$$\begin{aligned}\frac{\partial \bar{\rho}\widetilde{E}}{\partial t} + \nabla \cdot (\bar{\rho}\widetilde{\boldsymbol{u}}\widetilde{E}) &= -\nabla \cdot \left(\overline{P\boldsymbol{u}}\underline{\delta}\right) + \nabla \cdot (\overline{\tau \boldsymbol{u}}) - \nabla \cdot \left(\bar{\rho}\widetilde{\boldsymbol{u}E} - \bar{\rho}\widetilde{\boldsymbol{u}}\widetilde{E}\right) \\ &\quad + \nabla \cdot \left(\overline{\rho D \nabla h_s}\right) + \bar{\rho}\widetilde{\dot{\omega}}_E \end{aligned} \tag{8.4}$$

$$\overline{P} = \bar{\rho}\, r\, \widetilde{T} \tag{8.5}$$

where ρ is the density, $\boldsymbol{u}$ the velocity vector, P the pressure, $\underline{\delta}$ the unit tensor, τ the laminar viscous tensor, $E = H - P/\rho$ with H the total non-chemical enthalpy, h_s the sensible enthalpy, D is the diffusivity, $\dot{\omega}_c$ and $\dot{\omega}_E$, respectively, the progress variable and energy source terms. $r = R/W$ where R is the ideal gas constant and W the mean molecular weight. The overbar denotes the spatial filtering operation,

$$\overline{\phi}(\boldsymbol{x}) = \iiint F(\boldsymbol{x} - \boldsymbol{x'})\phi(\boldsymbol{x'})d\boldsymbol{x'}\,, \tag{8.6}$$

where ϕ represents reactive flow variables and velocity components and F the filtering function. The tilde operator denotes the density-weighted filtering defined by $\bar{\rho}\widetilde{\phi} = \overline{\rho\phi}$.

The subgrid scale terms, $-\nabla \cdot (\bar{\rho}\widetilde{\boldsymbol{u}\boldsymbol{u}} - \bar{\rho}\widetilde{\boldsymbol{u}}\widetilde{\boldsymbol{u}})$ and $-\nabla \cdot (\bar{\rho}\widetilde{\boldsymbol{u}\varphi} - \bar{\rho}\widetilde{\boldsymbol{u}}\widetilde{\varphi})$, where φ denotes c or E quantities, the pressure term $\overline{P\boldsymbol{u}}$, as well as the filtered laminar diffusion terms $\overline{\rho D \nabla \varphi}$ and the filtered source terms $\widetilde{\dot{\omega}}_\varphi$, require closure models. The model constraints are both to ensure a correct flame propagation and to recover the chemical structure of the filtered flame under two possible situations : (1) the flame wrinkling is fully resolved at the LES filter size, and (2) wrinkling occurs at the subgrid scale and affects the filtered flame speed.

Different strategies exist to model the filtered progress variable reaction rate $\widetilde{\dot{\omega}}_c$. An approach that does not require extensive CPU resources is to presume the shape of progress variable PDF, generally by a β function. This formalism has been applied to LES of turbulent premixed combustion (Galpin et al., 2008b) but, to our knowledge, the ability of the method to reproduce the propagation speed of filtered flame front has not yet been investigated. In the following section the influence of the PDF shape on the filtered flame properties is discussed when the flame wrinkling is resolved at the LES filter scale i.e. when the subgrid scale flame front remains laminar and planar. The use of a β function is found to introduce errors in the filtered flame front propagation speed. A new modeling alternative based on the tabulation of filtered premixed flame elements is then proposed to correct this drawback.

8.4 *A priori* testing of presumed β-PDF formalism in the laminar regime

An unstretched 1-D filtered laminar premixed flame is considered in this section. If no wrinkling occurs at the subgrid scale, the propagation speed S_Δ of the filtered flame front is identical to the laminar flame speed S_l^0. The following relation then needs to be satisfied:

$$\rho_0 S_\Delta = \int_{-\infty}^{+\infty} \bar{\rho}\widetilde{\dot{\omega}}_c(x)dx = \int_{-\infty}^{+\infty} \rho\dot{\omega}_c(x)dx = \rho_0 S_l^0 \tag{8.7}$$

where ρ_0 is the fresh gases density and x is the spatial dimension.
The ability of presumed β-PDF to satisfy this property is investigated by conducting *a priori* tests on a 1-D stoichiometric freely propagating laminar premixed propane/air flame computed with PREMIX (Kee et al., 1985a) using a modified version of the GRI 3.0 mechanism (Smith et al., 2000). The progress variable c is plotted as a function of the spatial coordinate x in Fig. 8.1(a). The laminar flame thickness, defined by $\delta_l = 1/\max(|dc/dx|)$ is approximately equal to 0.4 mm. Introducing $\widetilde{P}$, the mass weighted PDF defined by $\bar{\rho}\widetilde{P} = \rho\overline{P}$, the progress variable filtered reaction rate reads:

$$\widetilde{\dot{\omega}}_c(x) = \int_0^1 \dot{\omega}_c(c)\widetilde{P}(x,c)dc \tag{8.8}$$

Assuming that c follows a β distribution (Poinsot and Veynante, 2005):

$$\widetilde{P}(x,c) = \frac{c^{a_c-1}(1-c)^{b_c-1}}{\int_0^1 c^{a_c-1}(1-c)^{b_c-1}dc} \tag{8.9}$$

where parameters a_c and b_c are determined from $\widetilde{c}$ and the segregation factor $S_c = (\widetilde{cc} - \widetilde{c}\widetilde{c}) \,/\, (\widetilde{c}(1-\widetilde{c}))$:

$$a_c = \widetilde{c}\left(\frac{1}{S_c} - 1\right); \quad b_c = a_c\left(\frac{1}{\widetilde{c}} - 1\right) \tag{8.10}$$

The knowledge of the first and second moment of the progress variable provides the filtered reaction rate $\widetilde{\dot{\omega}}_c = \widetilde{\dot{\omega}}_c(\widetilde{c}, S_c)$. For the configuration considered here, $\widetilde{c}$ and S_c profiles across the filtered laminar flame front are computed by applying a 1-D Gaussian filter F of size Δ defined by:

$$F(x) = \left(\frac{6}{\pi\Delta^2}\right)^{1/2} e^{-\frac{6x^2}{\Delta^2}} \tag{8.11}$$

on the detailed chemistry laminar flame solution.

Favre-filtered progress variable and the segregation factor are shown in Fig. 8.1(a) for a filter size of $\Delta = 20\delta_l$. According to Eq. 8.9, the presumed β-PDF , $\widetilde{P}(x,c)$, is deduced from these two quantities. The reaction rate $\widetilde{\dot{\omega}}_c$ across the filtered flame front is then estimated from Eq. 8.8. Finally, the integration of the filtered reaction rate according to Eq. 8.7 gives an *a priori* estimation of the filtered flame front propagation speed S_Δ. The ratio S_Δ/S_l^0 (square symbols) is plotted as a function of the ratio Δ/δ_l in Fig. 8.1(b). When $\Delta/\delta_l < 1$ the effect of the β-PDF on the flame structure is moderate and the propagation speed is correctly reproduced. However when the filter size is larger than the flame front, as in LES practical situations, the propagation speed of the filtered progress variable is largely over-estimated by the presumed β function up to a factor of 2.5. In fact, the β-PDF is not relevant when subgrid scale wrinkling is resolved.

A solution to propagate a flame front at the correct speed is to artificially thicken the reaction zone. In the Thickened Flame model for LES (TFLES) (Butler and O'Rourke, 1977; Colin et al., 2000), both reaction rate and diffusion fluxes are affected in order to ensure a correct propagation of the flame front. However the structure of the thickened flame front does not correspond to the filtered flame front.

An alternative to presumed PDF formalism and TFLES is to directly employ a normalized filter function $F(x)$ to estimate the filtered reaction rate. Then the filtered reaction rate reads:

$$\widetilde{\dot{\omega}}_c(x) = \frac{1}{\bar{\rho}} \int_{-\infty}^{+\infty} \rho(x')\dot{\omega}_c(x')F(x-x')dx' \,, \tag{8.12}$$

Since by definition, $F(x)$ satisfies $\int_{-\infty}^{+\infty} F(x)dx = 1$, Eq. 8.7 is then always satisfied:

$$\begin{aligned}
\rho_0 S_\Delta &= \int_{-\infty}^{+\infty} \bar{\rho}\widetilde{\dot{\omega}}_c(x)dx & (8.13)\\
&= \int_{-\infty}^{+\infty}\int_{-\infty}^{+\infty} \rho(x')\dot{\omega}_c(x')F(x-x')dx'dx & (8.14)\\
&= \int_{-\infty}^{+\infty} \rho(x')\dot{\omega}_c(x')\left[\int_{-\infty}^{+\infty} F(x-x')dx\right]dx' & (8.15)\\
&= \int_{-\infty}^{+\infty} \rho(x')\dot{\omega}_c(x')dx' & (8.16)\\
&= \rho_0 S_l^0 & (8.17)
\end{aligned}$$

This property is verified in Fig. 8.1(b) where the propagation speed S_Δ of the filtered flame, is *a priori* computed using Eqs. 8.11 and 8.12.

By taking advantages of this property, a model is proposed in Section 8.5 to ensure the correct propagation of filtered laminar flame front. The closure of unknown terms is carefully addressed and the model is tested on 1-D filtered

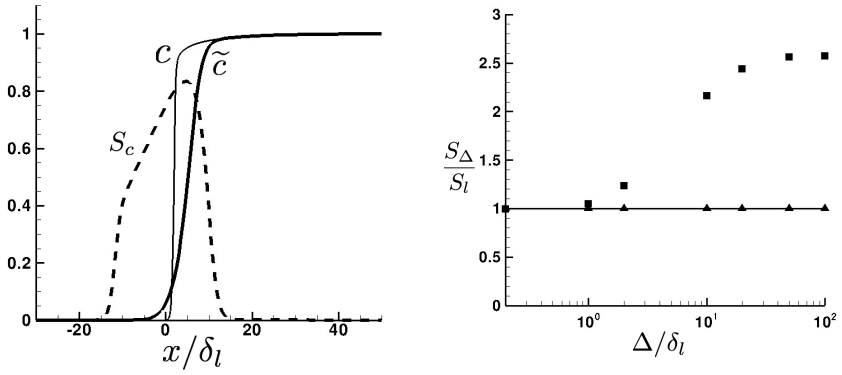

(a) (b)

Figure 8.1: A priori *test of the β-PDF formalism in laminar regime. Left (a): progress variable c (solid line) and filtered progress variable $\widetilde{c}$ (bold line) profiles as a function of the spatial coordinate x. Dashed line is the subfilter progress variable segregation factor S_c. Right (b):* a priori *computations of the filtered progress variable propagation speed for different values of filter size. The filtered progress variable reaction rate is modeled by a β-PDF (squares) or by a Gaussian filter (triangles).*

flame configurations. This approach is extended to turbulent regimes where subgrid flame wrinkling occurs at the subgrid scale level in Section 8.6 by the introduction of the subgrid flame wrinkling factor.

8.5 Filtered laminar premixed flames modeling

8.5.1 Modeling

The flame structure in the direction $\boldsymbol{n}$ normal to the flame front is assumed identical to the structure of a planar 1-D freely propagating premixed laminar flame. A detailed chemical mechanism with N_s species is considered. From this reference flame structure and using the filter operators introduced in Section 8.3, the *a priori* filtered flame structure is determined. For instance, for a given filter size Δ, any filtered fluxes or filtered thermo-chemical quantities of a planar filtered laminar flames are known.
As an example, a 1-D laminar stoichiometric premixed propane/air flame is computed taking into account detailed chemistry effects. The PREMIX (Kee et al., 1992) solver is combined with a modified version of the GRI 3.0 mechanism (Smith et al., 2000) involving $N_s = 70$ species and 463 elementary reactions. The filtered operator given by Eq. (8.11) is then applied to the 1-D laminar flame solution. Figure 8.2 shows all budget terms of the $\widetilde{c}$ balance equation in a steady 1-D laminar premixed flame remapped in the $\widetilde{c}$ coordinate system for different values of Δ. Using these results, a modeling

procedure based on the tabulation of the filtered 1-D laminar flame structure is proposed in the following sections. The closure of each unclosed terms identified in Eqs. 8.2 to 8.4 is first carefully addressed in the situation where no flame wrinkling occurs at the subgrid scale level.

Filtered chemical reaction rates

The filtered source terms for c and the energy equations are directly given by the filtered database:

$$\widetilde{\dot{\omega}}_{\varphi} = \widetilde{\dot{\omega}}^{*}_{\varphi}[\widetilde{c}, \Delta]. \tag{8.18}$$

where φ denotes c or E quantities and the * superscript denotes quantities issued from a 1-D unstretched laminar premixed flame. The notation $\phi[\widetilde{c}, \Delta]$ means that the variable ϕ is tabulated in a 2-D look-up table with coordinates $\widetilde{c}$ and Δ. Figure 8.2 shows that the filter operator affects dramatically both the amplitude and the shape of $\widetilde{\dot{\omega}}_c$ (triangles symbols) profiles.

Filtered laminar diffusion terms $\nabla \cdot (\overline{\rho D \nabla c})$ and $\nabla \cdot (\overline{\rho D \nabla h})$

These terms are usually neglected or approximated as (Poinsot and Veynante, 2005):

$$\nabla \cdot \left(\overline{\rho D \nabla \varphi}\right) \approx \nabla \cdot \left(\overline{\rho} D \, \nabla \widetilde{\varphi}\right). \tag{8.19}$$

This approximation is very rough and may introduce large errors. Indeed, in Fig. 8.2 the exact laminar diffusion fluxes $\frac{\partial}{\partial x^*}\left(\overline{\rho D \frac{\partial c^*}{\partial x^*}}\right)$ (filled diamonds) and the approximation by $\frac{\partial}{\partial x^*}\left(\overline{\rho} D \frac{\partial \widetilde{c}^*}{\partial x^*}\right)$ (empty diamonds) are shown for different values of the filter size Δ. When the filter size is smaller than the laminar flame thickness δ_l, approximation by Eq. 8.19 remains valid. However as soon as the filter size Δ becomes larger than δ_l, important differences are observed between $\frac{\partial}{\partial x^*}\left(\overline{\rho D \frac{\partial c^*}{\partial x^*}}\right)$ and $\frac{\partial}{\partial x^*}\left(\overline{\rho} D \frac{\partial \widetilde{c}^*}{\partial x^*}\right)$. As shown further, these errors impact dramatically the prediction of the propagation speed. In the present work, the filtered diffusion term for the c equation is modeled by:

$$\begin{aligned} \nabla \cdot (\overline{\rho D \, \nabla c}) &= -\nabla \cdot (\overline{\rho D \, |\nabla c|} \boldsymbol{n}) && (8.20) \\ &= -\nabla \cdot \left(\overline{\rho D \left| \frac{\partial c^*}{\partial x^*} \right|} \boldsymbol{n} \right) && (8.21) \\ & && (8.22) \end{aligned}$$

By introducing a corrective factor $\alpha_c(\widetilde{c})$, one can write:

$$\nabla \cdot (\overline{\rho D \, \nabla c}) = \nabla \cdot (\alpha_c[\widetilde{c}, \Delta] \, \overline{\rho} D \, \nabla \widetilde{c}). \tag{8.23}$$

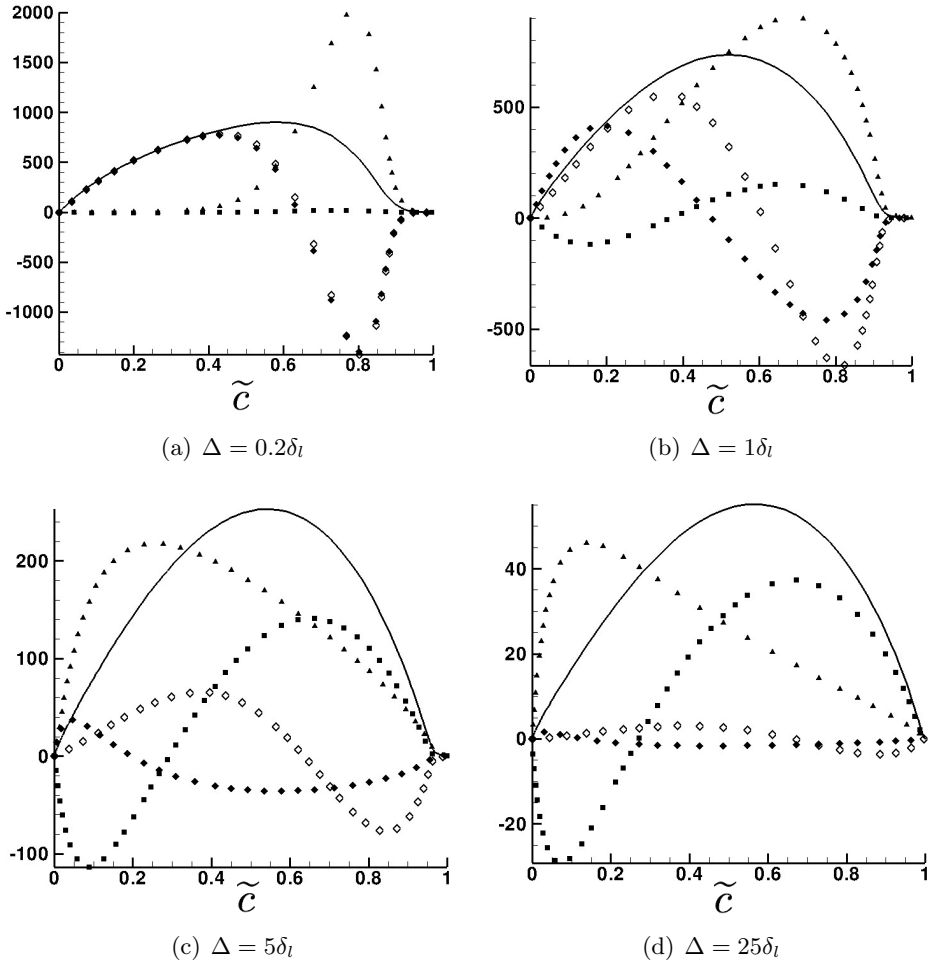

(a) $\Delta = 0.2\delta_l$ (b) $\Delta = 1\delta_l$

(c) $\Delta = 5\delta_l$ (d) $\Delta = 25\delta_l$

Figure 8.2: *Budget terms (in $kg.m^{-3}.s^{-1}$) as a function of $\widetilde{c}$ of the filtered progress variable balance equation of a steady 1-D laminar planar filtered premixed flame for different values of filter size Δ : $\frac{\partial \bar{\rho}\widetilde{\boldsymbol{u}}^*\widetilde{c}^*}{\partial x^*} = \frac{\partial}{\partial x^*}\left(\overline{\rho D \frac{\partial c^*}{\partial x^*}}\right) - \frac{\partial}{\partial x^*}\left(\bar{\rho}\widetilde{\boldsymbol{u}^* c^*} - \bar{\rho}\widetilde{\boldsymbol{u}}^*\widetilde{c}^*\right) + \bar{\rho}\widetilde{\dot{\omega}}_c^*$. — : $\frac{\partial \bar{\rho}\widetilde{\boldsymbol{u}}^*\widetilde{c}^*}{\partial x^*}$. ♦: $\frac{\partial}{\partial x^*}\left(\overline{\rho D \frac{\partial c^*}{\partial x^*}}\right)$. ■: $-\frac{\partial}{\partial x^*}\left(\bar{\rho}\widetilde{\boldsymbol{u}^* c^*} - \bar{\rho}\widetilde{\boldsymbol{u}}^*\widetilde{c}^*\right)$. ▲: $\bar{\rho}\widetilde{\dot{\omega}}_c^*$. ◊: $\frac{\partial}{\partial x^*}\left(\overline{\rho D}\frac{\partial \widetilde{c}^*}{\partial x^*}\right)$. Terms are plotted in the $\widetilde{c}$ coordinate for different values of filter size Δ.*

The normal to the flame front $\boldsymbol{n} = -\nabla\widetilde{c}/|\nabla\widetilde{c}|$ points into the fresh reactants. The correction factor $\alpha_c(\widetilde{c})$ is defined as:

$$\alpha_c[\widetilde{c},\Delta] = \frac{\overline{\rho D \left|\dfrac{\partial c^*}{\partial x^*}\right|}}{\overline{\rho} D \left|\dfrac{\partial \widetilde{c^*}}{\partial x^*}\right|}. \tag{8.24}$$

The quantity $\alpha_c[\widetilde{c},\Delta]$ is estimated from the 1-D filtered flame solution and is tabulated as a function of $\widetilde{c}$ for a given value of filter size Δ.
Similarly, the energy-filtered laminar diffusion term is written as:

$$\nabla\cdot(\overline{\rho D\,\nabla h_s}) \;=\; \nabla\cdot\left(\alpha_E([\widetilde{c},\Delta])\,\overline{\rho} D\,\nabla\widetilde{h}_s\right), \tag{8.25}$$

where the correction factor $\alpha_E[\widetilde{c},\Delta]$ is defined as:

$$\alpha_E[\widetilde{c},\Delta] = \frac{\overline{\rho D \left|\dfrac{\partial h_s^*}{\partial x^*}\right|}}{\overline{\rho} D \left|\dfrac{\partial \widetilde{h}_s^*}{\partial x^*}\right|}. \tag{8.26}$$

The correction factors $\alpha_c[\widetilde{c},\Delta]$ and $\alpha_E[\widetilde{c},\Delta]$ are plotted in Fig. 8.3 for different values of filter size Δ. For small values of Δ, as $\alpha_c[\widetilde{c},\Delta]$ remains constant and close to 1, effects on the laminar diffusion fluxes modeling will be negligible. However, the profiles present strong variations in terms of $\widetilde{c}$ when the filter size Δ is larger than δ_l.

Unresolved convection terms $-\nabla\cdot(\overline{\rho\boldsymbol{u}\varphi} - \overline{\rho}\widetilde{\boldsymbol{u}}\widetilde{\varphi})$
The displacement speed $\boldsymbol{s_d}$, measuring the flame front local speed relative to the flow, *i.e.* the difference between the absolute flow velocity $\boldsymbol{u}$ and the absolute flame front speed $\boldsymbol{w}$, is first introduced:

$$\boldsymbol{u} = \boldsymbol{w} + \boldsymbol{s_d} \tag{8.27}$$

The filtered flame front speed $\boldsymbol{w}$ remains constant across the flame brush ($\widetilde{\boldsymbol{w}} = \overline{\boldsymbol{w}} = \boldsymbol{w}$), therefore after replacing the flow velocity by relation 8.27, the subgrid scale convection term then reads:

$$-\nabla\cdot(\overline{\rho\boldsymbol{u}\varphi} - \overline{\rho}\widetilde{\boldsymbol{u}}\widetilde{\varphi}) \;=\; -\nabla\cdot(\overline{\rho\boldsymbol{s_d}\varphi} - \overline{\rho}\widetilde{\boldsymbol{s_d}}\widetilde{\varphi}) \tag{8.28}$$

In a 1-D laminar premixed flame the laminar flame speed S_l^0 and the fresh gas mixture density ρ_0 are related to the displacement speed through the following relation:

$$\rho_0 S_l^0 = \overline{\rho} s_d^* \tag{8.29}$$

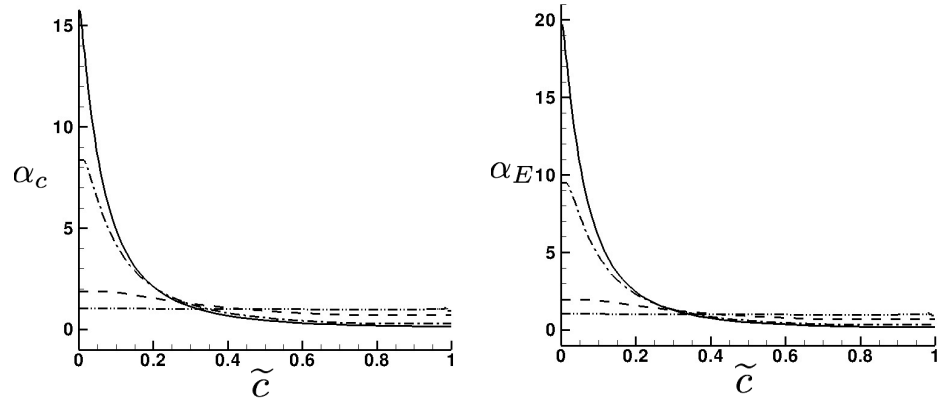

(a) α_c (b) α_E

Figure 8.3: *Diffusion correction factor α_c and α_E as a function of $\widetilde{c}$ for different values of Δ. Dashed dotted dotted lines: $\Delta = 0.2\delta_l$. Dashed lines: $\Delta = 1\delta_l$. Dashed dotted lines: $\Delta = 5\delta_l$. Solid lines: $\Delta = 25\delta_l$.*

Therefore, under the assumption that the flame remains planar at the subgrid scale level, the unresolved convection terms are directly estimated from the reference laminar 1-D detailed chemistry premixed flame:

$$-\nabla \cdot (\bar{\rho}\widetilde{\boldsymbol{u}\varphi} - \bar{\rho}\widetilde{\boldsymbol{u}}\widetilde{\varphi}) = -\frac{\partial}{\partial x^*}\left(\bar{\rho}\widetilde{s_d^*\varphi^*} - \bar{\rho}\widetilde{s}_d^*\widetilde{\varphi}^*\right) \quad (8.30)$$

$$= -\rho_0 S_l^0 \left(\frac{\partial \overline{\varphi^*}}{\partial x^*} - \frac{\partial \widetilde{\varphi^*}}{\partial x^*}\right). \quad (8.31)$$

$$= \Omega_\varphi[\widetilde{c}, \Delta] \quad (8.32)$$

The term $\Omega_c[\widetilde{c}, \Delta] = -\rho_0 S_L^0 \frac{\partial}{\partial x^*}(\overline{c} - \widetilde{c})$ is plotted in Fig. 8.2 for different values of filter size Δ (squares). For $\Delta < \delta_l$, unresolved convective fluxes are very small compared to other fluxes. However, when $\Delta \geq \delta_l$, these fluxes become important and are counter-gradient type. Note that this result is in agreement with recent experiments (Pfadler et al., 2009). The quantity $\Omega_\varphi[\widetilde{c}, \Delta]$, estimated from the 1-D filtered flame solution, is then tabulated as a function of $\widetilde{c}$ and Δ. In practice, as the unresolved convective terms are modeled as a source term, only the sum $\Sigma_\varphi[\widetilde{c}, \Delta] = \Omega_\varphi[\widetilde{c}, \Delta] + \widetilde{\dot{\omega}}_\varphi[\widetilde{c}, \Delta]$ is stored in the filtered database where ϕ denotes c or E quantities.

Pressure term

In a similar way, the pressure term in the energy equation (Eq. 8.4) is written as:

$$
\begin{aligned}
-\nabla\cdot(\overline{P\boldsymbol{u}}\underline{\delta}) &= -\nabla\cdot(\overline{P}\widetilde{\boldsymbol{u}}\underline{\delta}) - \left(\nabla\cdot(\overline{P\boldsymbol{u}}\underline{\delta}) - \nabla\cdot(\overline{P}\widetilde{\boldsymbol{u}}\underline{\delta})\right) && (8.33)\\
&= -\nabla\cdot(\overline{P}\widetilde{\boldsymbol{u}}\underline{\delta}) - \left(\nabla\cdot(\overline{\rho}\widetilde{rT\boldsymbol{u}}\underline{\delta}) - \nabla\cdot(\overline{\rho}\widetilde{rT}\widetilde{\boldsymbol{u}}\underline{\delta})\right) && (8.34)\\
&= -\nabla\cdot(\overline{P}\,\widetilde{\boldsymbol{u}}\,\underline{\delta}) + \Omega_p[\widetilde{c},\Delta] && (8.35)
\end{aligned}
$$

with

$$
\Omega_p[\widetilde{c},\Delta] = -\rho_0\, S_l^0 \left(\frac{\partial(\widetilde{\overline{rT^*}})}{\partial x^*} - \frac{\partial(\widetilde{rT^*})}{\partial x^*}\right). \qquad (8.36)
$$

Momentum equations

Unclosed terms in the filtered momentum equations may be modeled following the same approach. The subgrid scale convection term is written as:

$$
\begin{aligned}
-\nabla\cdot(\bar{\rho}\widetilde{\boldsymbol{u}\boldsymbol{u}} - \bar{\rho}\widetilde{\boldsymbol{u}}\widetilde{\boldsymbol{u}}) &= \frac{\partial}{\partial x^*}\left(\bar{\rho}\widetilde{s_d^* s_d^*} - \bar{\rho}\widetilde{s_d}^*\widetilde{s_d}^*\right)\boldsymbol{n} && (8.37)\\
&= \rho_0 S_l^0\left(\frac{\partial\widetilde{\overline{s_d}}^*}{\partial x^*} - \frac{\partial\widetilde{s_d}^*}{\partial x^*}\right)\boldsymbol{n} && (8.38)\\
&= \Omega_u[\widetilde{c},\Delta]\boldsymbol{n} && (8.39)
\end{aligned}
$$

The strain tensor is expressed by:

$$
\nabla\cdot\overline{\tau} = \nabla\cdot(\alpha_u[\widetilde{c},\Delta]\widetilde{\tau}) \quad \text{with} \quad \alpha_u[\widetilde{c},\Delta] = \frac{\overline{\tau}^*}{\widetilde{\tau}^*}. \qquad (8.40)
$$

where $\widetilde{\tau}$ is defined as:

$$
\widetilde{\tau} = \overline{\mu}\left(\nabla\widetilde{\boldsymbol{u}} + (\nabla\widetilde{\boldsymbol{u}})^T - \frac{2}{3}(\nabla\cdot\widetilde{\boldsymbol{u}})\underline{\delta}\right) \qquad (8.41)
$$

However, as shown further, the influence of these terms is moderate and can be neglected.

8.5.2 Summary of the model equations

The momentum, the progress variable and the energy equations are modeled as:

$$
\begin{aligned}
\frac{\partial\bar{\rho}\widetilde{\boldsymbol{u}}}{\partial t} + \nabla\cdot(\bar{\rho}\widetilde{\boldsymbol{u}}\widetilde{\boldsymbol{u}}) &= -\nabla\overline{P} + \nabla\cdot(\alpha_u[\widetilde{c},\Delta]\widetilde{\tau}) + \Omega_u(\widetilde{c})\boldsymbol{n} && (8.42)\\
\frac{\partial\bar{\rho}\widetilde{c}}{\partial t} + \nabla\cdot(\bar{\rho}\widetilde{\boldsymbol{u}}\widetilde{c}) &= \nabla\cdot(\alpha_c[\widetilde{c},\Delta]\,\overline{\rho}D\,\nabla\widetilde{c}) + \Sigma_c[\widetilde{c},\Delta] && (8.43)\\
\frac{\partial\bar{\rho}\widetilde{E}}{\partial t} + \nabla\cdot(\bar{\rho}\widetilde{\boldsymbol{u}}\widetilde{E}) &= -\nabla\cdot\left(\overline{P}\,\widetilde{u}\,\underline{\delta}\right) + \Omega_p[\widetilde{c},\Delta] + \nabla\cdot(\widetilde{\tau}\widetilde{\boldsymbol{u}})\\
&\quad +\nabla\cdot\left(\alpha_E[\widetilde{c},\Delta]\,\overline{\rho}D\,\nabla\widetilde{h}_s\right) + \Sigma_E[\widetilde{c},\Delta] && (8.44)
\end{aligned}
$$

These equations are implemented in the compressible LES code AVBP (CFD Team, 2010). The third-order finite element scheme TTGC (Colin and Rudgyard, 2000) is used. Boundary conditions are prescribed using Navier-Stokes Characteristic Boundary Conditions (Poinsot and Lele, 1992).
The sum of filtered chemical reactions rates and the subgrid scales fluxes $\Sigma_\varphi = \Omega_\varphi + \overline{\dot{\omega}}_\varphi$ and the diffusion fluxes correction factors α_φ are estimated after filtering a 1-D laminar stoichiometric premixed propane/air flame. These quantities are stored in a look-up table as a function of $\widetilde{c}$ and Δ.

8.5.3 1-D laminar premixed flame simulations

Filtered steady 1-D laminar flames are computed to verify the ability of the present model to reproduce both the correct flame front propagation speed and the filtered flame structure. Computations are performed on uniform meshes with a grid spacing of Δ_x. A parametric study is conducted for different filter sizes relative to the laminar flame thickness. For each case, a reference solution is obtained by filtering the 1-D laminar premixed flame detailed chemistry solution. The simulations are initialized with the reference solution and the overall physical time for each run is $t_{run} = 50\,\delta_{\widetilde{c}}\,/S_l^0$, where $\delta_{\widetilde{c}} = 1/\max(|\frac{\partial \widetilde{c}}{\partial x}|)$ is an estimation of the filtered flame thickness.
A comparison between the numerical solutions on uniform mesh (solid lines) and the reference solution (dashed line) with $\delta_{\widetilde{c}}/\Delta_x = 50$ and for different values of Δ/δ_l is first shown in Fig. 8.4. The predicted filtered progress variable profiles match the reference solution for all the filter size values. Figure 8.5(a) shows that the predicted filtered front propagation speed S_Δ(square symbols) remains very close to the reference laminar flame speed for various values of Δ/δ_l. The triangular symbol in Fig. 8.5(a) represents simulation results with the approximation given by Eq. (8.19), i.e., $\alpha_\varphi = 1$. This rough assumption leads to an under-prediction by a factor of 3 of the flame front propagation speed.
An important information for premixed combustion LES is the minimal number of grid points required to capture the filtered flame front without introducing numerical artifacts. The filtered flame front propagation speed is plotted as a function of the mesh resolution Δ_x in Fig.8.5(b). The flame speed is recovered with a good approximation for $\delta_{\widetilde{c}}/\Delta_x \geq 5$. Below this limit, numerical errors become important and the filtered flame front does not propagate at the correct speed. Then, for numerical reasons, the filter should be at least 5 times larger than the mesh size. Note that even approaches based on level-set transport that use sophisticated numerical methods to track the flame front position also require to filter the flame front at a scale larger than the mesh size in order to resolve density gradients (Moureau et al., 2009).
Finally, a simulation has been performed without considering the filtering effect on the momentum equations (Eq. 8.42), i.e., with $\alpha_u = 1$ and $\Omega_u = 0$

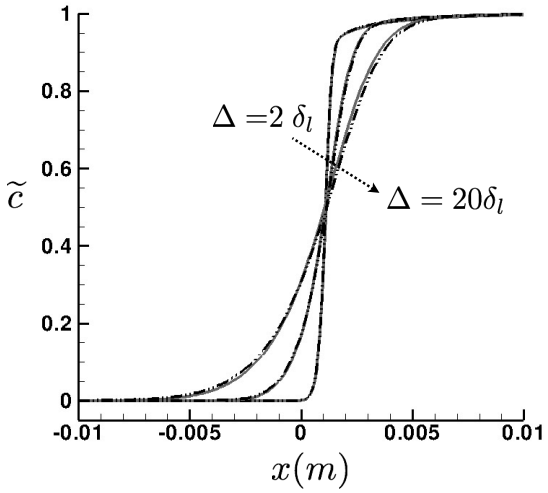

Figure 8.4: *Filtered 1-D premixed flame solutions. Filtered progress variable (solid) compared to the reference solution (dashed) for* $\Delta/\delta_l = 2$, 10 *and* 20.

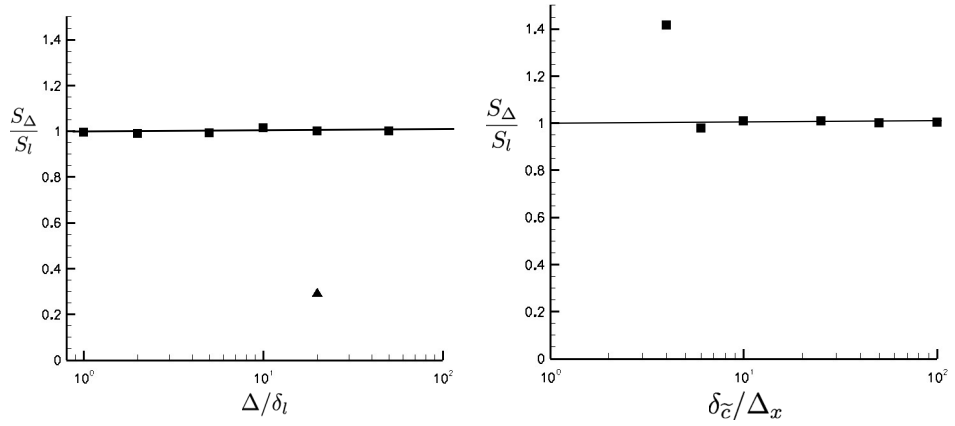

(a) $\delta_{\widetilde{c}}/\Delta_x = 50$ (b) $\Delta/\delta_l = 20$

Figure 8.5: *Predicted flame speed as a function of* Δ/δ_l *(left) and* $\delta_{\widetilde{c}}/\Delta_x$ *(right). Square symbols are the complete model solution and the triangle symbol is the solution with* $\alpha_\varphi = 1$.

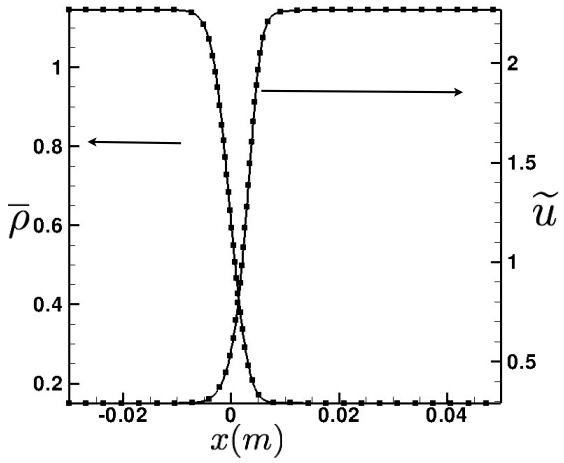

Figure 8.6: *Filtered 1-D premixed flame solutions. Effects of the flame filter in the momentum equation. Solid:* $\alpha_u = 1$ *and* $\Omega_u = 0$. *Symbols:* $\alpha_u(\widetilde{c})$ *and* $\Omega_u(\widetilde{c})$ *from the filtered database.*

and is compared with the complete model solution in Fig. 8.6. For both simulations, density as well as velocity profiles match perfectly. In fact, the induced differences are transfered to the pressure that becomes a macro-pressure. As this macro-pressure remains very close to the static pressure, effects on the thermodynamic state are very limited. Then, in order to simplify the model implementation in 3-D configurations, the contribution corresponding to the filtering of a laminar flame in the momentum equation will be neglected.

8.6 Filtered turbulent premixed flames modeling

In practical LES of turbulent combustion, turbulence may cause flame front wrinkling at the subgrid scale level. Here, a strategy is proposed to extend the previously described model to such situations.

8.6.1 Modeling

Turbulent structures induce flame wrinkling that increases the flame surface area at the subgrid scale. As a consequence the filtered flame front propagates at a subgrid scale turbulent flame speed S_t (Poinsot and Veynante, 2005) related to the laminar flame speed through the flame wrinkling factor $\Xi = S_t/S_l^0$. The model developed here ensures that the filtered flame front propagates at the turbulent flame speed S_t. The filtered flame thickness is assumed to be only related to the filter size Δ and is not altered by

small-scale eddies.
Then, the filtered progress variable turbulent reaction rate is modeled by:

$$\overline{\dot{\omega}}_{c_t} = \Xi \, . \, \overline{\dot{\omega}}_c^*[\widetilde{c}, \Delta] \tag{8.45}$$

and the turbulent diffusion term is expressed as follows:

$$\Omega_{c_t} = -\left(\nabla \cdot (\bar{\rho}\widetilde{\boldsymbol{u}c} - \bar{\rho}\widetilde{\boldsymbol{u}}\widetilde{c})\right)_t \quad = \quad \Xi \; \Omega_c[\widetilde{c}, \Delta] + (\Xi \, - \, 1) \, \nabla \cdot (\alpha_c[\widetilde{c}, \Delta] \, \overline{\rho D} \, \nabla \widetilde{c}) \tag{8.46}$$

The first term on the r.h.s corresponds to the thermal expansion and the second one models the unresolved turbulent fluxes. This formulation corresponds to multiply diffusion and source terms by the flame wrinkling factor in the laminar flame balance equation and then ensures that the unstretched filtered flame front propagates at the turbulent flame speed $S_t = \Xi S_l^0$ in the normal direction.

8.6.2 Summary of the model equations

To summarize, momentum, progress variable and energy equations for this new model called Filtered Tabulated Chemistry for LES (F-TACLES) can be written as follows:

$$\frac{\partial \bar{\rho}\widetilde{\boldsymbol{u}}}{\partial t} + \nabla \cdot (\bar{\rho}\widetilde{\boldsymbol{u}}\widetilde{\boldsymbol{u}}) \;=\; -\nabla \overline{P} + \nabla \cdot \widetilde{\tau} + \nabla \cdot \overline{\tau}^t \tag{8.47}$$

$$\frac{\partial \bar{\rho}\widetilde{c}}{\partial t} + \nabla \cdot (\bar{\rho}\widetilde{\boldsymbol{u}}\widetilde{c}) \;=\; \Xi \nabla \cdot (\alpha_c[\widetilde{c}, \Delta] \, \bar{\rho} D \, \nabla \widetilde{c}) + \Xi \Sigma_c[\widetilde{c}, \Delta] \tag{8.48}$$

$$\begin{aligned} \frac{\partial \bar{\rho}\widetilde{E}}{\partial t} + \nabla \cdot (\bar{\rho}\widetilde{\boldsymbol{u}}\widetilde{E}) \;=\; & -\nabla \cdot (\overline{P} \, \widetilde{\boldsymbol{u}} \, \underline{\delta}) \; + \Xi \Omega_p[\widetilde{c}, \Delta] + \nabla \cdot (\widetilde{\tau}\widetilde{\boldsymbol{u}}) \\ & + \Xi \nabla \cdot \left(\alpha_E[\widetilde{c}, \Delta] \, \bar{\rho} D \, \nabla \widetilde{h}_s \right) + \Xi \Sigma_E[\widetilde{c}, \Delta]. \end{aligned} \tag{8.49}$$

Note that here the effect of the flame filter Δ on the momentum equations is neglected and the subgrid scale turbulent fluxes $\nabla \cdot \overline{\tau}^t$ are modeled using the Smagorinsky model. Different alternatives exist to estimate the subgrid flame wrinkling factor that appears in Eqs 8.48 and 8.49. It can be either estimated from analytical models (Colin et al., 2000; Pitsch, 2005; Charlette et al., 2002a,b) or from the solution of a surface density balance equation (Hawkes and Cant, 2000; Richard et al., 2007).

8.6.3 Large Eddy Simulation of a swirled premixed burner

The proposed method is applied to the simulation of the complex PRECCINSTA swirled burner experimentally investigated by Meier *et al.* (Meier et al., 2007). The geometry, shown in Fig. 8.7, derives from an aeronautical

combustion device. It features a plenum, a swirl-injector and a combustion chamber. Details of the burner geometry and of the measurement can be found in Ref. (Meier et al., 2007). Different modeling strategies for LES have been used to numerically investigate this configuration : an LES of the combustor using the thickened flame model and a two-step mechanism has been first performed by Roux *et al.*. (Roux et al., 2005). Moureau *et al.* (Moureau et al., 2007) used this configuration to validate a new level-set algorithm to track the flame front position. Recently, Galpin *et al.* (Galpin et al., 2008b) performed the LES of this lean premixed burner by using a presumed β-PDF to couple a thermo-chemical look-up table with the filtered flow equations.

The operating conditions chosen in the present study correspond to an air mass flow rate of 12.2 g/s and to a methane mass flow rate of 0.6 g/s. In the experiment, air and methane are injected separately in the plenum inlet, however in the present simulation the mixing is assumed to be fast enough to burn a perfect mixing of oxidizer and fuel in the combustion chamber. Thus methane injection is not taken into account and a methane/air mixture characterized by an equivalence ratio of 0.83 is injected at the plenum inlet. These conditions correspond to a stable regime where laser Raman scattering has been performed, allowing comparison between predicted and measured thermo-chemical quantities such as temperature and species mass fractions. The boundary conditions and the computational geometry have been already described in (Roux et al., 2005). The mesh used to perform the computation is unstructured and made of 12.7 millions elements. The third-order finite element scheme TTGC (Colin and Rudgyard, 2000) is retained. For building-up the chemical look-up table, a 1-D laminar methane/air flame is first computed for an equivalence ratio equal to 0.83 using the GRI 3.0 mechanism (Smith et al., 2000). Then, according to the modeling procedure discussed previously, this laminar flame solution is filtered by the Gaussian function defined by Eq. 8.11.

Note that, as the mesh considered here is almost uniform in the filtered flame front region, a unique filter width Δ is considered. In order to ensure a sufficient meshing of the filtered flame front, the filter width has been set to $\Delta = 20\delta_l$. The progress variable is defined by $c = Y_{CO_2}/Y^{eq}_{CO_2}$, where $Y^{eq}_{CO_2}$ is the equilibrium CO_2 mass fraction in the fully burnt gases. The filtered quantities required by the model: $\Sigma_c[\widetilde{c},\Delta]$, $\alpha_c[\widetilde{c},\Delta]$, $\Omega_p[\widetilde{c},\Delta]$, $\Sigma_E[\widetilde{c},\Delta]$ and $\alpha_E[\widetilde{c},\Delta]$ are then tabulated as a function of $\widetilde{c}$ for $\Delta = 20\delta_l$. For strongly non-uniform meshes this procedure is not optimized and could lead to over-refined or under-refined flame front regions. Then, an additional coordinate, the filter width, can be easily considered when computing the look-up table. Following the system of equations 8.47-8.49, this new model F-TACLES has been implemented into the compressible LES code AVBP (CFD Team, 2010). The subgrid flame wrinkling factor Ξ is estimated from the analytical model developed by Colin *et al.* (Colin et al., 2000). Mean and resolved Root Mean

Square (RMS) quantities are computed by time averaging LES solutions over a physical time that correspond to 6 flow-through times based on the fresh gas inlet velocity. Mean temperature and CO_2 mass fractions are plotted on Figs. 8.8 (top) and 8.9 (top), respectively. A very good agreement is observed between experimental and numerical profiles, which demonstrated that the correct flame angle and mean flame thickness are reproduced by the model. Because heat losses have not been considered when generating the chemical database and in the numerical simulation, the LES slightly overestimates the temperature profiles close to the combustion chamber wall, in the outer recirculation zone for $x < 20\,mm$ and at a distance larger than $20\,mm$ from the jet axis. Note that heat losses effects on the flame structure can be taken into account with the addition of the enthalpy as a control parameter of the chemistry tabulation (Fiorina et al., 2003, 2005a).
Figs. 8.8 (bottom) and 8.9 (bottom) show a comparison between resolved LES RMS and measured RMS of the temperature and the CO_2 mass fraction, respectively. As the plotted LES RMS does not include the subgrid scale RMS, conclusions regarding the model performance in terms of flame turbulence interactions are more difficult. However, it is observed that LES RMS remains lower than measured RMS, as expected from theory.
As all thermo-chemical variables are related to $\widetilde{c}$, the post-processing of the filtered progress variable solution with the filtered chemical database allows to access all chemical species. As an example, Fig. 8.10(a) shows 2-D contours of $\widetilde{c}$ used to estimate HCO mass fraction plotted in Fig. 8.10(b).
Finally, Fig. 8.11 indicates the flame position in the Pitsch LES regime diagram for turbulent premixed combustion (Pitsch, 2006), where the ratio Δ/δ_l is expressed as a function of the Karlovitz number Ka in logarithmic scale. The Karlovitz number is related in LES to the subgrid velocity fluctuations v'_Δ and laminar flame scales (Pitsch, 2006):

$$Ka^2 = \frac{\delta_l}{{S_l^0}^3}\varepsilon = \frac{v'_\Delta}{S_l^0}\frac{\delta_l}{\Delta} \tag{8.50}$$

where ε is the kinetic energy transfer rate. The subgrid velocity fluctuations are computed as follow:

$$v'_\Delta = \frac{\mu_t}{\bar{\rho} C_k \Delta \sqrt{3/2}} \tag{8.51}$$

where the turbulent viscosity μ_t is estimated from Smagorinsky model. For $Ka < 1$, combustion takes place in the corrugated flame regime while the thin reaction zone regime is observed when $Ka > 1$. Computational nodes located in the filtered flame front are considered, *i.e.* for $0.01 < \widetilde{c} < 0.99$, and are plotted in the LES diagram (horizontal thick solid black line in Fig. 8.11). As a a unique filter width Δ is considered in the present simulation, the scatter plot reduced to the line $\Delta/\delta_l = 20$. The smallest size of the flame

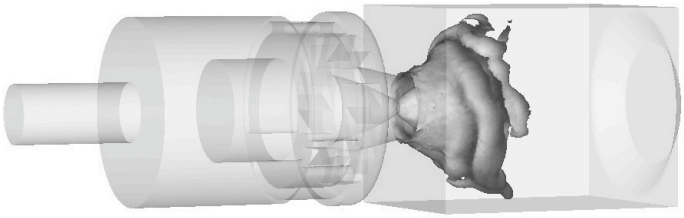

Figure 8.7: *LES of Preccinsta with F-TACLES turbulent combustion model. The computational domain features the plenum, the swirl-injector and the combustion chamber. An instantaneous view of the filtered flame front iso-surface ($\widetilde{c}$=0.8) is shown.*

wrinkling is given by the Gibson length (Peters, 2000):

$$\frac{\Delta}{l_G} = \frac{v'_\Delta}{S_l^0} \tag{8.52}$$

The substitution of Eq. 8.52 into Eq. 8.50 shows that $\Delta = l_G$ condition corresponds to $\Delta/\delta_l = Ka^{-2}$ represented by a line of slope -2 in the LES diagram (Fig. 8.11). In the corrugated flame regime, when the filter width becomes smaller than the Gibson length, the subgrid velocity fluctuation v'_Δ is smaller than the laminar flame speed S_l^0. In such cases, the flame wrinkling is fully resolved at the LES filter scale. At the opposite, on the right side of the $l_G = \Delta$ line, subgrid scale wrinkling exists and will impact the filtered flame front propagation speed S_Δ. The node distribution versus the Karlovitz number is plotted in Fig. 8.12. First, it can be observed that most of the points are located in the corrugated flame regime ($Ka < 1$). The chemical flame structure remains therefore laminar as assumed in the present model. Secondly, for a substantial area of the flame surface (about 30 %), the Gibson length l_G is larger than the filter width and consequently the flame wrinkling is fully resolved. With future increase of computational power, as meshes will be finer, this trend should be emphasized. It demonstrates the crucial need of ensuring a proper propagation of the laminar flame front when deriving a turbulent combustion model.

8.7 Conclusion

A new modeling strategy called Filtered Tabulated Chemistry for LES (F-TACLES) has been developed to introduce tabulated chemistry methods in premixed combustion LES. A filtered 1-D laminar premixed flame is used to build a filtered chemical look-up table. The model performances are demonstrated on 1-D filtered laminar flame computations. Finally the proposed

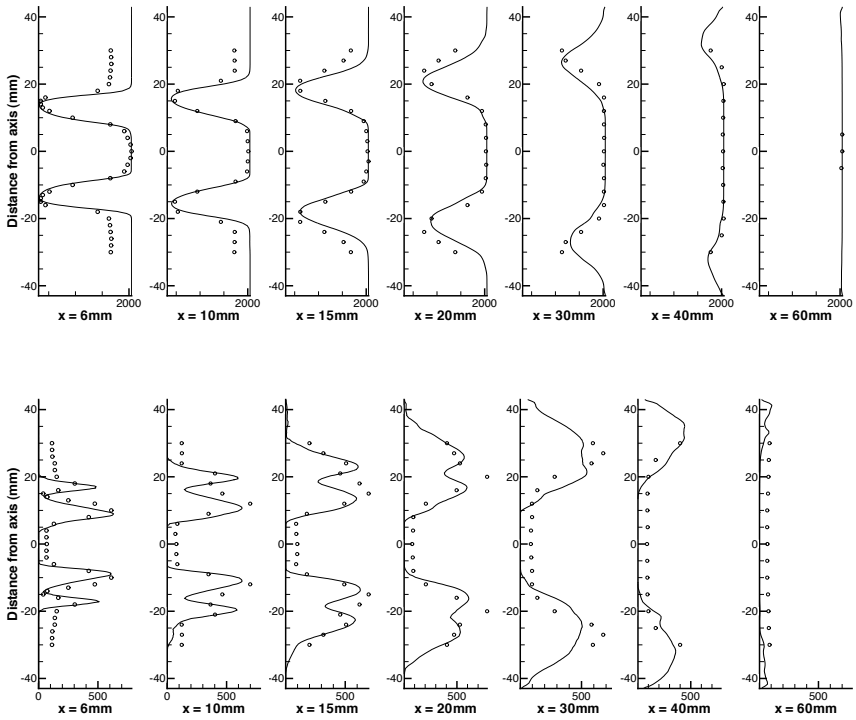

Figure 8.8: *Mean (top) and RMS (bottom) of temperature, case* $\phi = 0.83$. *Symbols: measurements. Lines: simulation with F-TACLES.*

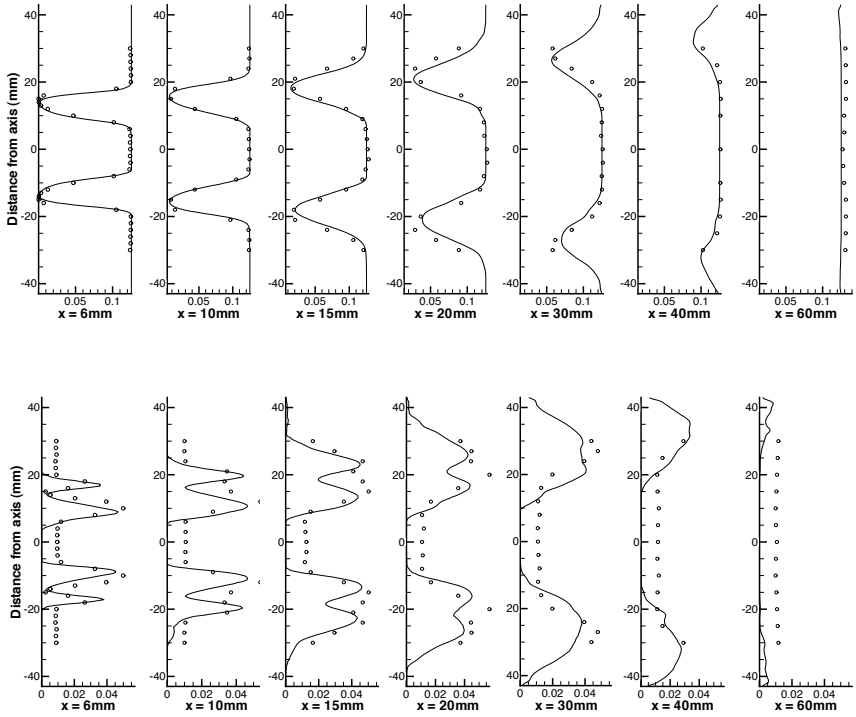

Figure 8.9: *Mean (top) and RMS (bottom) of CO_2 mass fraction, case $\phi = 0.83$. Symbols: measurements. Lines: simulation with F-TACLES.*

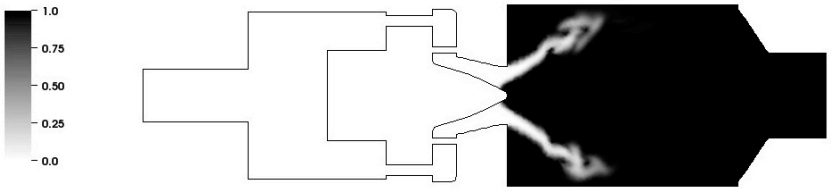

(a) $\widetilde{c}$

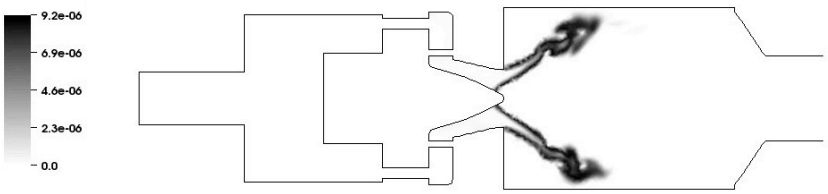

(b) $\widetilde{Y}_{HCO}$

Figure 8.10: *2-D instantaneous view of $\widetilde{c}$ and $\widetilde{Y}_{HCO}$.*

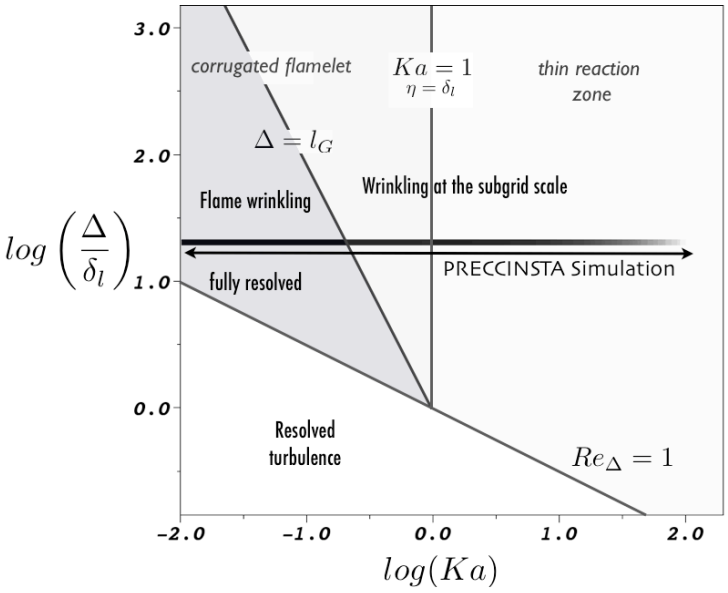

Figure 8.11: *LES regime diagram for turbulent premixed combustion. The thick solid black line represent the range covered by the Preccinsta flame simulation.*

strategy has been applied to perform a 3-D simulation of a swirled turbulent premixed flame. Good agreement between the numerical simulation and the experiments is observed.

This work was supported by the ANR-07-CIS7-008-04 Grant of the French Ministry of Research. We are grateful to the CERFACS (Toulouse, France) combustion team for providing the PRECCINSTA burner geometry. The authors warmly acknowledge the support of the 2008 Summer Program of the Center for Turbulence Research (Stanford University - NASA Ames) during which this work was initiated.

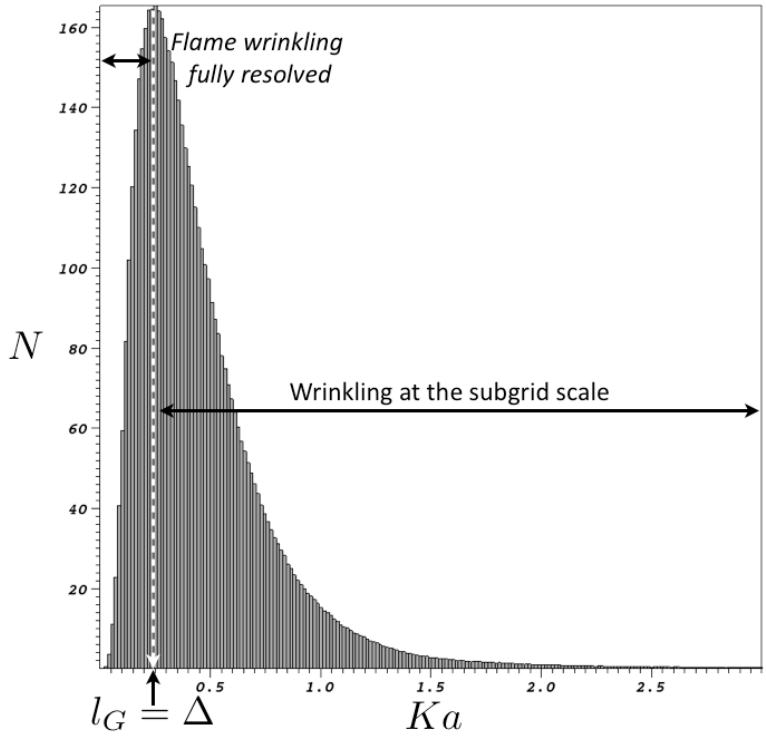

Figure 8.12: *Node distribution versus the Karlovitz number. Only nodes located into the filtered flame front have been considered,* i.e. *for* $0.01 < \widetilde{c} < 0.99$.

Conclusions

The general objective of this thesis is to extend the application range of tabulated chemistry models in order to predict temperature and chemical species in combustion processes. Flamelet models were first dedicated specifically for perfectly premixed or non-premixed flames. However, the flame structure is more complex in real applications. Hence, one trend in turbulence combustion modeling is to develop tabulated chemistry models that take into account realistic flame structure. In this thesis, this was done for flameless combustion, a promising combustion technology which reduces fuel consumption and NO_x emission. Another trend is the application of tabulated chemistry model in large eddy simulations. This combination allows a great description of both turbulence and chemistry but outlines additional issues. Motivated by this context the different points developed in this thesis led us to the following main achievements.

Main achievements

Tabulated Thermo-chemistry for Compressible flows (TTC) formalism

Several numerical codes dedicated to large eddy simulation are based on a fully compressible formulation of Navier-Stokes equations. However, tabulated chemistry models have first been dedicated to low Mach-number flow and do not take into account compressible effects. Consequently, in order to perform LES with compressible codes, a new tabulated chemistry formalism called TTC (Tabulated Thermo-chemistry for Compressible flows) has been derived for any kind of tabulation techniques. In this formulation, the temperature computation and the characteristic boundary treatment are reformulated to account for compressible effects.
The TTC formalism has been validated with 1D test cases and applied to a three-dimensional non-reactive LES. Tabulated chemistry simulations obtained same results as using multi-component formulation and assumptions made to derive the model were shown to be valid. The TTC formalism has then allowed to implement tabulated chemistry models efficiently in order to perform reactive simulation in the compressible code AVBP. A mono-

dimensional premixed flame was computed with the FPI (Flame Prolongation of ILDM) model and a 3D LES of a lifted flame in a vitiated coflow was realized with a new tabulated chemistry model for hot temperature diluted combustion.

Tabulated chemistry for hot temperature diluted combustion

In order to describe diluted combustion with hot temperature gases, a new tabulated chemistry model called UTaC (Unsteady flamelets Tabulated Chemistry) has been developed. The model is based on the tabulation of auto-igniting non-premixed flamelet solutions. The behavior of such solutions has been studied and a corrective source term has been introduced to retrieve auto-ignition time delays.
The UTaC model was applied in RANS computations of a round jet in a vitiated coflow for two fuel compositions: methane/air and hydrogen/nitrogen. In the first case, species and temperature profiles agreed with experimental data only upstream and downstream the flame stabilization zone. The flame lift-off height was however underestimated leading to poor comparison of profiles during the transition from unburnt to burnt state. The hydrogen/nitrogen case results were found better than those obtained in the methane/air case when compared to experimental profiles. Averaged and RMS quantities agree very well and the flame lift-off height sensitivity to the co-flow temperature was retrieved. Several hypotheses were suggested to explain the difference of results between both configurations: a change of flame structure between both cases, the validity of approximations made during the derivation of UTaC and the introduction of numerical errors in the methane/air case where ignition takes place in very lean mixtures.
Using the TTC formalism, the UTaC model was derived and applied in LES of the round jet in vitiated co-flow configuration using the methane/air mixture as fuel. Non-reactive case showed that mixing between the fuel jet and the hot coflow was well reproduced. Results in reactive case were found better than those obtained in RANS and it was shown that the independence assumption made in RANS between mixture fraction and progress variable is false.

Tabulated chemistry for perfectly premixed combustion in LES

Derivation of tabulated chemistry models for LES is usually done by a direct transplantation of the RANS model. With such an approach, tabulated chemistry models are not able to tackle specific characteristics of large-eddy simulations. For instance, PCM-FPI methods can not predict the correct flame speed of perfectly premixed turbulent flames when flame wrinkling is negligible at the subgrid scales and the filter size is still large in comparison

to the flame thickness. This is corrected by a new modeling strategy called F-TACLES (Filtered Tabulated Chemistry for Large Eddy Simulation). The filtered flame structure is mapped using 1-D filtered laminar premixed flames and the model was applied successfully in a LES of a 3-D turbulent premixed flame.

Future perspectives

The different points developed in this thesis open the way to further developments:

- The TTC formalism was derived for general tabulation techniques. It was here applied with FPI in a mono-dimensional premixed flame and with UTaC in a jet in a vitiated coflow. The model TTC can however be applied to much more models, which enlarges the range of possible applications: steady non-premixed flamelets, FPI-PCM, FPI-TFLES, F-TACLES, ... Finally, the TTC formalism was restricted to ideal gas but could be extended for real gas thermodynamics.

- The UTaC model was applied to RANS and LES in the Cabra burner configuration. On the one hand, application of the model to other configurations such as the Jet in Hot Coflow (Dally et al., 2002) for instance would be interesting to improve the model validation. On the other hand, LES has shown that mixture fraction and progress variable can not be assumed independent and a modification of the RANS model is therefore necessary. Finally, extensions of the model are required to apply UTaC to a flameless combustion furnace. Indeed, heat losses and burnt gases dilution must be addressed. Moreover, prediction of pollutants such as NO_x, which have a long chemical time scale, requires specific modeling and an extension of the UTaC model for NO_x chemistry would be necessary.

- Initiated from the error introduced by β PDF in LES, development of the F-TACLES was focused on perfectly premixed combustion. In such configurations, several works remain to be done: adding the filter size Δ as a dimension of the database, studying the impact of strain and curvature and improvement of the model when subgrid wrinkling of the flame exist. Finally, the application of the F-TACLES procedure to other combustion regime (partially premixed, non-premixed, flameless combustion) should be considered.

Bibliography

ANSYS (2010). Ansys cfx website. http://www.ansys.com/products/fluid-dynamics/cfx/.

Auzillon, P., Fiorina, B., Vicquelin, R., Darabiha, N., Gicquel, O., and Veynante, D. (2010a). Modeling chemical flame structure and combustion dynamics in les. *Submitted to Proceedings of the Combustion Institute*.

Auzillon, P., Vicquelin, R., Gicquel, O., Darabiha, N., Veynante, D., and Fiorina, B. (2010b). A filtered tabulated chemistry model for large eddy simulation of reactive flows. *AIAA Paper*.

Baum, M., Poinsot, T., and Thevenin, D. (1995). Accurate boundary conditions for multi-component reactive flows. *Journal of Computational Physics*, 116(2):247–261.

Bilger, R. W. (1993). Conditional moment closure for turbulent reacting flow. *Physics of Fluids A-Fluid Dynamics*, 5(2):436–444.

Bilger, R. W., Starner, S. H., and Kee, R. J. (1990). On reduced mechanisms for methane-air combustion in nonpremixed flames. *Combustion and Flame*, 80(2):135–149.

Boger, M., Veynante, D., Boughanem, H., and Trouvé, A. (1998). Direct numerical simulation analysis of flame surface density concept for large eddy simulation of turbulent premixed combustion. *Proceedings of the Combustion Institute*, 27:917–925.

Boileau, M., Staffelbach, G., Cuenot, B., Poinsot, T., and BÈrat, C. (2008). Les of an ignition sequence in a gas turbine engine. *Combustion and Flame*, 154(1-2):2–22.

Bray, K., Domingo, P., and Vervisch, L. (2005). Role of the progress variable in models for partially premixed turbulent combustion. *Combustion and Flame*, 141(4):431–437.

Butler, T. D. and O'Rourke, P. J. (1977). A numerical method for two-dimensional unsteady reacting flows. *Proceedings of the Combustion Institute*, 16:1503–1515.

Bykov, V. and Maas, U. (2007). The extension of the ILDM concept to reaction-diffusion manifolds. *Combustion Theory and Modelling*, 11(6):839–862.

Cabra, R. (2002). Cabra and co-workers webpage. http://www.me.berkeley.edu/cal/vcb/index.htm.

Cabra, R. (2004). turbulent jet flames into a vitiated coflow. Technical report, University of California, Berkeley.

Cabra, R., Chen, J. Y., Dibble, R. W., Karpetis, A. N., and Barlow, R. S. (2005). Lifted methane-air jet flames in a vitiated coflow. *Combustion and Flame*, 143(4):491–506.

Cabra, R., Myhrvold, T., Chen, J. Y., Dibble, R. W., Karpetis, A. N., and Barlow, R. S. (2002). Simultaneous laser raman-rayleigh-lif measurements and numerical modeling results of a lifted turbulent h2/n2 jet flame in a vitiated coflow. *Proceedings of the Combustion Institute*, 29(2):1881–1888.

Cao, R. R., Pope, S. B., and Masri, A. R. (2005). Turbulent lifted flames in a vitiated coflow investigated using joint pdf calculations. *Combustion and Flame*, 142(4):438–453.

Cavaliere, A. and de Joannon, M. (2004). Mild combustion. *Progress in Energy and Combustion Science*, 30(4):329–366.

CFD Team (2010). Avbp code. www.cerfacs.fr/4-26334-The-AVBP-code.php and http://www.cerfacs.fr/4-25719-Publications.php.

Chakravarthy, V.-K. and Menon, S. (2000). Subgrid modeling of turbulent premixed flames in the flamelet regime. *Flow, Turbulence and Combustion*, 65:133–161.

Chang, C. S., Zhang, Y., Bray, K. N. C., and Rogg, B. (1996). Modelling and simulation of autoignition under simulated diesel-engine conditions. *Combustion Science and Technology*, 114:205–219.

Charlette, F., Meneveau, C., and Veynante, D. (2002a). A power-law flame wrinkling model for les of premixed turbulent combustion, part i: non-dynamic formulation. *Combustion and Flame*, 131(1/2):159–180.

Charlette, F., Meneveau, C., and Veynante, D. (2002b). A power-law flame wrinkling model for les of premixed turbulent combustion, part ii: dynamic formulation. *Combustion and Flame*, 131(1/2):181–197.

Choi, B. C., Kim, K. N., and Chung, S. H. (2009). Autoignited laminar lifted flames of propane in coflow jets with tribrachial edge and mild combustion. *Combustion and Flame*, 156(2):396–404.

Coelho, P. J. and Peters, N. (2001). Numerical simulation of a mild combustion burner. *Combustion and Flame*, 124(3):503–518.

Colin, O., Ducros, F., Veynante, D., and Poinsot, T. (2000). A thickened flame model for large eddy simulations of turbulent premixed combustion. *Physics of Fluids*, 12(7):1843–1863.

Colin, O. and Rudgyard, M. (2000). Development of high-order taylor-galerkin schemes for les. *Journal of Computational Physics*, 162(2):338–371.

Curtiss, C. F. and Hirschfelder, J. O. (1949). Transport properties of multicomponent gas mixtures. *The Journal of Chemical Physics*, 17(6):550–555.

Dally, B. B., Karpetis, A. N., and Barlow, R. S. (2002). Structure of turbulent non-premixed jet flames in a diluted hot coflow. *Proceedings of the Combustion Institute*, 29(1):1147–1154.

Dally, B. B., Riesmeier, E., and Peters, N. (2004). Effect of fuel mixture on moderate and intense low oxygen dilution combustion. *Combustion and Flame*, 137(4):418–431.

de Ferrières, S., El Bakali, A., Lefort, B., Montero, M., and Pauwels, J. F. (2008). Experimental and numerical investigation of low-pressure laminar premixed synthetic natural gas/o2/n2 and natural gas/h2/o2/n2 flames. *Combustion and Flame*, 154(3):601–623.

DesJardin, P. and Frankel, S. (1998). Large eddy simulation of a non-premixed reacting jet: Application and assessment of subgrid-scale combustion models. *PHYSICS OF FLUIDS*, 10(9):2298–2314.

Domingo, P., Vervisch, L., Payet, S., and Hauguel, R. (2005). Dns of a premixed turbulent v flame and les of a ducted flame using a fsd-pdf subgrid scale closure with fpi-tabulated chemistry. *Combustion and Flame*, 143(4):566–586.

Domingo, P., Vervisch, L., and Veynante, D. (2008). Large-eddy simulation of a lifted methane jet flame in a vitiated coflow. *Combustion and Flame*, 152(3):415–432.

Donbar, J., Driscoll, J., and Carter, C. (2001). Strain rates measured along the wrinkled flame contour within turbulent non-premixed jet flames. *Combustion and Flame*, 125(4):1239–1257.

Duwig, C. (2007). Study of a filtered flamelet formulation for large eddy simulation of premixed turbulent flames. *Flow, Turbulence and Combustion*, 79(4):433–454.

Effelsberg, E. and Peters, N. (1989). Scalar dissipation rates in turbulent jets and jet diffusion flames. *Proceedings of the Combustion Institute*, 22(1):693–700.

Eggels, R. (1996). *Modelling of combustion processes and NO formation with reduced reaction mechanism.* PhD thesis, Eindhoven University of Technology.

El-Asrag, H. and Menon, S. (2009). Large eddy simulation of soot formation in a turbulent non-premixed jet flame. *Combustion and Flame*, 156(2):385–395.

Embouazza, M. (2005). *Etude de l'Auto-Allumage par Réduction des Schémas Cinétiques Chimiques. Application à la Combustion Homogène diesel.* PhD thesis, Ecole Centrale Paris.

Esnault, O., Boileau, M., Vicquelin, R., Fiorina, B., and Gicquel, O. (2010). A method to accelerate les explicit solvers using local time stepping. *AIAA Paper*.

Esnault, O., Vicquelin, R., Boileau, M., Fiorina, B., and Gicquel, O. (2009). Optimization of dns/les explicit solvers for combustor simulations using local time-stepping. 4th European Combustion Meeting, Vienna, Austria.

Fichet, V. (2008). *Modélisation de la combustion du gaz naturel par réseaux de réacteurs avec cinétique chimique détaillée.* PhD thesis, Ecole Centrale Paris.

Fiorina, B., Baron, R., Gicquel, O., Thevenin, D., Carpentier, S., and Darabiha, N. (2003). Modelling non-adiabatic partially premixed flames using flame-prolongation of ildm. *Combustion Theory and Modelling*, 7:449–470.

Fiorina, B., Gicquel, O., Vervisch, L., Carpentier, S., and Darabiha, N. (2005a). Approximating the chemical structure of partially premixed and diffusion counterflow flames using fpi flamelet tabulation. *Combustion and Flame*, 140(3):147–160.

Fiorina, B., Gicquel, O., Vervisch, L., Carpentier, S., and Darabiha, N. (2005b). Premixed turbulent combustion modeling using tabulated detailed chemistry and pdf. *Proceedings of the Combustion Institute*, 30:867–874.

Fiorina, B., Gicquel, O., and Veynante, D. (2009). Turbulent flame simulation taking advantage of tabulated chemistry self-similar properties. *Proceedings of the Combustion Institute*, 32(2):1687–1694.

Fiveland, W. A. (1984). Discrete-ordiantes solutions of the radiative transport-equation for rectangular enclosures. *Journal of Heat Transfer-Transactions of the ASME*, 106(4):699–706.

Galletti, C., Parente, A., and Tognotti, L. (2007). Numerical and experimental investigation of a mild combustion burner. *Combustion and Flame*, 151(4):649–664.

Galpin, J. (2007). *Modélisation LES de la combustion avec une prise en compte des effets de cinétique détaillée et en perspective d'apllication moteur*. PhD thesis, IFP.

Galpin, J., Angelberger, C., Naudin, A., and Vervisch, L. (2008a). Large-eddy simulation of h-2-air auto-ignition using tabulated detailed chemistry. *Journal of Turbulence*, 9(13):1–21.

Galpin, J., Naudin, A., Vervisch, L., Angelberger, C., Colin, O., and Domingo, P. (2008b). Large-eddy simulation of a fuel-lean premixed turbulent swirl-burner. *Combustion and Flame*, 155(1-2):247–266.

Gao, F. and Obrien, E. (1993). A large-eddy simulation scheme for turbulent reacting flows. *Physics of Fluids A-Fluid Dynamics*, 5(6):1282–1284.

Germano, M., Piomelli, U., Moin, P., and Cabot, W. H. (1991). A dynamic subgrid-scale eddy viscosity model. *Physics of Fluids A-Fluid Dynamics*, 3(7):1760–1765.

Gicquel, O. (1999). *Développement d'une nouvelle méthode de réduction des schémas cinétiques : Application au méthane*. PhD thesis, Ecole Centrale Paris.

Gicquel, O., Darabiha, N., and Thevenin, D. (2000). Laminar premixed hydrogen/air counterflow flame simulations using flame prolongation of ILDM with differential diffusion. *Proceedings of the Combustion Institute*, 28(Part 2):1901–1908. 28th International Symposium on Combustion, EDINBURGH, SCOTLAND, JUL 30-AUG 04, 2000.

Gicquel, O., Thevenin, D., Hilka, M., and Darabiha, N. (1999). Direct numerical simulation of turbulent premixed flames using intrinsic low-dimensional manifolds. *Combustion Theory and Modelling*, 3(3):479–502.

Girimaji, S. S. (1992). on the modeling of scalar diffusion in isotropic turbulence. *Physics of Fluids A-Fluid Dynamics*, 4(11):2529–2537.

Girimaji, S. S. and Zhou, Y. (1996). Analysis and modeling of subgrid scalar mixing using numerical data. *Physics of Fluids*, 8(5):1224–1236.

Gkagkas, K. and Lindstedt, R. P. (2007). Transported pdf modelling with detailed chemistry of pre- and auto-ignition in ch4/air mixtures. *Proceedings of the Combustion Institute*, 31(1):1559–1566.

Godel, G. (2010). *Modélisation de sous-maille de la combustion turbulente. Développement d'outils pour la prédiction de la pollution dans une chambre aéronautique.* PhD thesis, Institut National des Sciences Appliquées de Rouen.

Gordon, R. L., Masri, A. R., and Mastorakos, E. (2008). Simultaneous rayleigh temperature, oh- and ch2o-lif imaging of methane jets in a vitiated coflow. *Combustion and Flame*, 155(1-2):181–195.

Gordon, R. L., Masri, A. R., Pope, S. B., and Goldin, G. M. (2007a). A numerical study of auto-ignition in turbulent lifted flames issuing into a vitiated co-flow. *Combustion Theory and Modelling*, 11(3):351–376.

Gordon, R. L., Masri, A. R., Pope, S. B., and Goldin, G. M. (2007b). Transport budgets in turbulent lifted flames of methane autoigniting in a vitiated co-flow. *Combustion and Flame*, 151(3):495–511.

Gordon, R. L., Starner, S. H., Masri, A. R., and Bilger, R. W. (2005). Further characterisation of lifted hydrogen and methane flames issuing into a vitiated coflow. In *Proceedings of the 5th Asia-Pacific Conference on Combustion*, pages 333–336, University of Adelaide.

Grandmaison, E. W., Yimer, I., Becker, H. A., and Sobiesiak, A. (1998). The strong-jet/weak-jet problem and aerodynamic modeling of the cgri burner. *Combustion and Flame*, 114(3-4):381–396.

Gupta, A. K., Bolz, S., and Hasegawa, T. (1999). Effect of air preheat temperature and oxygen concentration on flame structure and emission. *Journal of Energy Resources Technology*, 121:209–216.

Gutmark, E. and Ho, C. (1983). Preferred modes and the spreading rates of jets. *Physics of Fluids*, 26(10):2932–2938.

Hasse, C. (2004). *A Two-Dimensional Flamelet Model for Multiple Injections in Diesel Engines.* PhD thesis, Fakultät für Maschinenwesen der Rheinisch-Westfälischen Technischen Hochschule Aachen.

Hasse, C. and Peters, N. (2005). A two mixture fraction flamelet model applied to split injections in a di diesel engine. *Proceedings of the Combustion Institute*, 30(2):2755–2762.

Hawkes, E. and Chen, J. (2004). Direct numerical simulation of hydrogen-enriched lean premixed methane-air flames. *Combustion and Flame*, 138(3):242–258.

Hawkes, E. R. and Cant, R. S. (2000). A flame surface density approach to large-eddy simulation of premixed turbulent combustion. *Proceedings of the Combustion Institute*, 28:51–58.

Hawkes, E. R. and Cant, R. S. (2001). Physical and numerical realizability requirements for flame surface denisty approaches and reynolds averaged simulation of premixed turbulent combustion. *Combustion Theory and Modelling*, 5:699–720.

Haworth, D. C. (2010). Progress in probability density function methods for turbulent reacting flows. *Progress in Energy and Combustion Science*, In Press, Corrected Proof:–.

Hilbert, R., Tap, F., El-Rabii, H., and Thevenin, D. (2004). Impact of detailed chemistry and transport models on turbulent combustion simulations. *Progress in Energy and Combustion Science*, 30(1):61–117.

Hilbert, R. and Thevenin, D. (2002). Autoignition of turbulent non-premixed flames investigated using direct numerical simulations. *Combustion and Flame*, 128(1-2):22–37.

Huang, Y., Sung, H., Hsieh, S., and Yang, V. (2003). Large-eddy simulation of combustion dynamics of lean-premixed swirl-stabilized combustor. *Journal of Propulsion and Power*, 19(5):782–794.

Ihme, M., Cha, C. M., and Pitsch, H. (2005). Prediction of local extinction and re-ignition effects in non-premixed turbulent combustion using a flamelet/progress variable approach. *Proceedings of the Combustion Institute*, 30:793–800.

Ihme, M. and Pitsch, H. (2008a). Modeling of radiation and nitric oxide formation in turbulent nonpremixed flames using flamelet/progress variable formulation. *Physics of Fluids*, 20(5):055110.

Ihme, M. and Pitsch, H. (2008b). Prediction of extinction and reignition in nonpremixed turbulent flames using a flamelet/progress variable model: 1. a priori study and presumed pdf closure. *Combustion and Flame*, 155(1-2):70–89.

Ihme, M., Schmitt, C., and Pitsch, H. (2009). Optimal artificial neural networks and tabulation methods for chemistry representation in LES of a bluff-body swirl-stabilized flame. *Proceedings of the Combustion Institute*, 32(Part 1):1527–1535.

International Energy Agency (2010). International energy agency (iea) website. http://www.iea.org/stats/.

Jones, W. P. and Launder, B. E. (1972). Prediction of laminarization with a 2-equation model of turbulence. *International Journal of Heat and Mass Transfer*, 15(2):301–&.

Jones, W. P. and Navarro-Martinez, S. (2007). Large eddy simulation of autoignition with a subgrid probability density function method. *Combustion and Flame*, 150(3):170–187.

Katsuki, M. and Hasegawa, T. (1998). The science and technology of combustion in highly preheated air. In *27th Symposium on Combustion*, pages 3135–3146.

Kee, R. J., Grcar, J. F., Smooke, M. D., and Miller, J. A. (1985a). A fortran program for modelling steady laminar one-dimensional premixed flames. Technical Report SAND85-8240-UC-401, Sandia National Laboratories.

Kee, R. J., Grcar, J. F., Smooke, M. D., and Miller, J. A. (1992). A fortran program for modelling steady laminar one-dimensional premixed flames. Technical report, Sandia National Laboratories.

Kee, R. J., Grear, J. F., Smooke, M. D., and Miller, J. A. (1985b). A fortran program for modeling steady laminarone-dimensional premixed flames. Technical Report SAND85-8240, Sandia National Laboratories.

Kempf, A., Forkel, H., Chen, J. Y., Sadiki, A., and Janicka, J. (2000). Large-eddy simulation of a counterflow configuration with and without combustion. *Proceedings of the Combustion Institute*, 28(1):35–40.

Kim, J. P., Schnell, U., Scheffknecht, G., and Benim, A. C. (2007). Numerical modelling of mild combustion for coal. *Progress in computational fluid dynamics*, 7(6):337–346.

Kumar, S., Paul, P. J., and Mukunda, H. S. (2007). Prediction of flame liftoff height of diffusion/partially premixed jet flames and modeling of mild combustion burners. *Combustion Science and Technology*, 179(10):2219–2253.

Lesieur, M., Métais, O., and Comte, P. (2005). *Large-Eddy Simulations of Turbulence*. Cambridge University Press.

Lodato, G., Domingo, P., and Vervisch, L. (2008). Three-dimensional boundary conditions for direct and large-eddy simulation of compressible viscous flows. *Journal of Computational Physics*, 227(10):5105–5143.

Lodato, G., Vervisch, L., and Domingo, P. (2009). A compressible wall-adapting similarity mixed model for large-eddy simulation of the impinging round jet. *Physics of Fluids*, 21(3).

Lu, T. and Law, C. K. (2005). A directed relation graph method for mechanism reduction. *Proceedings of the Combustion Institute*, 30(1):1333–1341.

Maas, U. and Pope, S. B. (1992). Simplifying chemical kinetics: Intrinsic low-dimensional manifolds in composition space. *Combustion and Flame*, 88(3-4):239–264.

Magnussen, B. F. and Hjertager, B. H. (1976). On the mathematical modelling of turbulent combustion with special emphasis on soot formation and combustion. In combustion institute, T., editor, *Proceedings of the 16th Symposium (Int.) on combustion*, pages 719–729.

Mancini, M., Schwoppe, P., Weber, R., and Orsino, S. (2007). On mathematical modelling of flameless combustion. *Combustion and Flame*, 150(1-2):54–59.

Masri, A. R. (2003). Masri and co-workers webpage. http://www.aeromech.usyd.edu.au/thermofluids/.

Masri, A. R., Cao, R., Pope, S. B., and Goldin, G. M. (2004). Pdf calculations of turbulent lifted flames of h_2/n_2 fuel issuing into a vitiated co-flow. *Combustion Theory and Modelling*, 8:1–22.

Masson, E. (2005). *Etude expérimentale des champs dynamiques et scalaires de la combustion sans flamme*. PhD thesis, Institut National des Sciences Appliquées de Rouen.

Mastorakos, E. (2009). Ignition of turbulent non-premixed flames. *Progress in Energy and Combustion Science*, 35(1):57–97.

Medwell, P. R., Kalt, P. A. M., and Dally, B. B. (2007). Simultaneous imaging of oh, formaldehyde, and temperature of turbulent nonpremixed jet flames in a heated and diluted coflow. *Combustion and Flame*, 148(1-2):48–61.

Medwell, P. R., Kalt, P. A. M., and Dally, B. B. (2008). Imaging of diluted turbulent ethylene flames stabilized on a jet in hot coflow (jhc) burner. *Combustion and Flame*, 152(1-2):100–113.

Meier, W., Weigand, P., Duan, X., and Giezendanner-Thoben, R. (2007). Detailed characterization of the dynamics of thermoacoustic pulsations in a lean premixed swirl flame. *Combustion and Flame*, 150(1-2):2 – 26.

Menon, S. and Jou, W. (1991). Large eddy simulations of combustion instability in an axisymetric ramjet combustor. *Combustion Science and Technology*, 75:53–72.

Michel, J.-B., Colin, O., Angelberger, C., and Veynante, D. (2009). Using the tabulated diffusion flamelet model adf-pcm to simulate a lifted methane-air jet flame. *Combustion and Flame*, 156(7):1318 – 1331.

Michel, J.-B., Colin, O., and Veynante, D. (2008). Modeling ignition and chemical structure of partially premixed turbulent flames using tabulated chemistry. *Combustion and Flame*, 152(1-2):80–99.

Mizobuchi, Y., Tachibana, S., Shinjo, J., Ogawa, S., and Takeno, T. (2002). A numerical analysis on structure of turbulent hydrogen jet lifted flame. In *The proceedings of the Twenty-Ninth Symposium (Int.) on Combustion.*, pages 2009–2015. The Combustion Institute, Pittsburgh.

Mizobushi, Y., Tachibana, S., Shino, J., Ogawa, S., and Takeno, T. (2002). A numerical analysis of the structure of a turbulent hydrogen jet lifted flame. *Proceedings of the Combustion Institute*, 29:2009–2015.

Moureau, V., Fiorina, B., and Pitsch, H. (2009). A level set formulation for premixed combustion LES considering the turbulent flame structure. *Combustion and Flame*, 156(4):801–812.

Moureau, V., Lartigue, G., Sommerer, Y., Angelberger, C., Colin, O., and Poinsot, T. (2005). Numerical methods for unsteady compressible multi-component reacting flows on fixed and moving grids. *Journal of Computational Physics*, 202(2):710–736.

Moureau, V., Minot, P., Pitsch, H., and Berat, C. (2007). A ghost-fluid method for large-eddy simulations of premixed combustion in complex geometries. *Journal of Computational Physics*, 221(2):600 – 614.

Mura, A., Robin, V., and Champion, M. (2007). Modeling of scalar dissipation in partially premixed turbulent flames. *Combustion and Flame*, 149(1-2):217–224.

Naudin, A. (2008). *Simulation des grandes échelles de la combustion turbulente avec chimie détaillée tabulée.* PhD thesis, Institut National des Sciences Appliquées de Rouen.

Nguyen, P.-D., Vervisch, L., Subramanian, V., and Domingo, P. (2010). Multidimensional flamelet-generated manifolds for partially premixed combustion. *Combustion and Flame*, 157(1):43–61.

Nicoud, F. and Ducros, F. (1999). Subgrid-scale stress modelling based on the square of the velocity gradient tensor. *Flow, Turbulence and Combustion*, 62(3):183–200.

Ó Conaire, M., Curran, H. J., Simmie, J. M., Pitz, W. J., and Westbrook, C. K. (2004). A comprehensive modeling study of hydrogen oxidation. *International Journal of Chemical Kinetics*, 36(11):603–622.

Oberlack, M. and Peters, N. (2000). On stochastic damköhler number variations in a homogeneous flow reactor. *Combustion Theory and Modelling*, 4:495–509.

Okong'o, N. and Bellan, J. (2002). Consistent boundary conditions for multicomponent real gas mixtures based on characteristic waves. *Journal of Computational Physics*, 176(2):330–344.

Parente, A., Galletti, C., and Tognotti, L. (2008). Effect of the combustion model and kinetic mechanism on the MILD combustion in an industrial burner fed with hydrogen enriched fuels. *International journal of Hydrogen Energy*, 33(24):7553–7564.

Patankar, S. (1980). *Numerical heat transfer and fluid flow*. Washington: Hemisphere Publishing Corp.

Peters, N. (1985). Numerical and asymptotic analysis of systematically reduced reaction schemes for hydrocarbon flames. *Lecture Notes in Physics*, 241:90–109.

Peters, N. (2000). *Turbulent combustion*. Cambridge University Press.

Pfadler, S., Kerl, J., Beyrau, F., Leipertz, A., Sadiki, A., Scheuerlein, J., and Dinkelacker, F. (2009). Direct evaluation of the subgrid scale scalar flux in turbulent premixed flames with conditioned dual-plane stereo piv. *Proceedings of the Combustion Institute*, 32(2):1723 – 1730.

Pierce, C. D. and Moin, P. (2004). Progress-variable approach for large-eddy simulation of non-premixed turbulent combustion. *Journal of Fluid Mechanics*, 504:73–97.

Pitsch, H. (1998). A c++ computer program for 0-d combustion and 1-d laminar flame calculations. Technical report, RWTH Aachen.

Pitsch, H. (2000). Unsteady flamelet modeling of differential diffusion in turbulent jet diffusion flames. *Combustion and Flame*, 123(3):358–374.

Pitsch, H. (2005). A consistent level set formulation for large-eddy simulation of premixed turbulent combustion. *Combustion and Flame*, 143:587–598.

Pitsch, H. (2006). Large-eddy simulation of turbulent combustion. *Annual Review of Fluid Mechanics*, 38:453–482.

Pitsch, H., Chen, M., and Peters, N. (1998). Unsteady flamelet modeling of turbulent hydrogen-air diffusion flames. *Proceedings of the Combustion Institute*, 27:1057–1064.

Pitsch, H. and Peters, N. (1998). A consistent flamelet formulation for non-premixed combustion considering differential diffusion effects. *Combustion and Flame*, 114(1-2):26–40.

Pitsch, H. and Steiner, H. (2000). Large-eddy simulation of a turbulent piloted methane/air diffusion flame (sandia flame d). *Physics of Fluids*, 12(10):2541–2554.

Poinsot, T. and Veynante, D. (2005). *Theorical and Numerical Combustion*. R. T. Edwards, Inc., 2nd edition.

Poinsot, T. J. and Lele, S. K. (1992). Boundary-conditions for direct simulations of compressible viscous flows. *Journal of Computational Physics*, 101(1):104–129.

Pope, S. (1997). Computationally efficient implementation of combustion chemistry using in situ adaptive tabulation. *Combustion Theory and Modelling*, 1(1):41–63.

Pope, S. (2004). Ten questions concerning the large-eddy simulation of turbulent flows. *New Journal of Physics*, 6.

Pope, S. B. (1978). An explanation of the turbulent round-jet/plane-jet anomaly. *AIAA Journal*, 16(3):279–281.

Pope, S. B. (2000). *Turbulent Flows*. Cambridge University Press.

Raman, V. and Pitsch, H. (2005). Large-eddy simulation of a bluff-body-stabilized non-premixed flame using a recursive filter-refinement procedure. *Combustion and Flame*, 142(4):329–347.

Ren, Z., Pope, S., Vladimirsky, A., and Guckenheimer, J. (2006). The invariant constrained equilibrium edge preimage curve method for the dimension reduction of chemical kinetics. *Journal of Chemical Physics*, 124(11):114111.

Ren, Z. and Pope, S. B. (2006). The use of slow manifolds in reactive flows. *Combustion and Flame*, 147:243–261.

Ren, Z., Pope, S. B., Vladimirsky, A., and Guckenheimer, J. M. (2007). Application of the ice-pic method for the dimension reduction of chemical kinetics coupled with transport. *Proceedings of the Combustion Institute*, 31(1):473–481.

Ribert, G. (2005). *Développement d'un schéma cinétique réduit du kérosène : Application au calcul d'une chambre de turboréacteur*. PhD thesis, Ecole Centrale Paris.

Ribert, G., Gicquel, O., Darabiha, N., and Veynante, D. (2006). Tabulation of complex chemistry based on self-similar behavior of laminar premixed flames. *Combustion and Flame*, 146(4):649–664.

Richard, S., Colin, O., Vermorel, O., Benkenida, A., Angelberger, C., and Veynante, D. (2007). Towards large eddy simulation of combustion ib spark ignition engines. *Proceedings of the Combustion Institute*, 31:3059–3066.

Rottier, C. (2010). *Etude expérimentale de l'influence des mélanges gazeux sur la combustion sans flamme*. PhD thesis, INSA de Rouen.

Roux, S., Lartigue, G., Poinsot, T., Meier, U., and Berat, C. (2005). Studies of mean and unsteady flow in a swirled combustor using experiments, acoustic analysis, and large eddy simulations. *Combustion and Flame*, 141(1-2):40 – 54.

Rudy, D. and Strikwerda, JC, J. (1980). A nonreflecting outflow boundary condition for subsonic navier-stokes calculations. *Journal of Computational Physics*, 36(1):55–70.

Schaffel, N., Mancini, M., Szlęk, A., and Weber, R. (2009). Mathematical modeling of mild combustion of pulverized coal. *Combustion and Flame*, 156(9):1771–1784.

Selle, L., Lartigue, G., Poinsot, T., Koch, R., Schildmacher, K., Krebs, W., Prade, B., Kaufmann, P., and Veynante, D. (2004). Compressible large eddy simulation of turbulent combustion in complex geometry on unstructured meshes. *Combustion and Flame*, 137(4):489–505.

Shah, N. (1979). *New method of computation of radiation heat transfer in combustion chambers*. PhD thesis, Imperial College, University of London, UK.

Smagorinsky, J. (1963). General circulation experiments with the primitive equations. *Monthly Weather Review*, 61:99–164.

Smirnov, A., Shi, S., and Celik, I. (2001). Random flow generation technique for Large Eddy Simulations and particle-dynamics modeling. *Journal of Fluids Engineering-Transactions of the ASME*, 123(2):359–371.

Smith, G., Golden, D. M., Frenklach, M., Moriarty, N. W., Eiteneer, B., Goldenberg, M., Bowman, C. T., Hanson, R. K., Song, S., William C. Gardiner, J., Lissianski, V. V., and Q, Z. (2000). Gri-mech web site. `http://www.me.berkeley.edu/gri-mech/`.

Stull, D. and Prophet, H. (1971). *Janaf thermochemical tables*, volume Tech. Rep. NSRDS-NBS 37. US National Bureau of Standards, 2nd edition.

Szegö, G. G., Dally, B. B., and Nathan, G. J. (2009). Operational characteristics of a parallel jet mild combustion burner system. *Combustion and Flame*, 156(2):429–438.

Thompson, K. (1987). Time-dependent boudary-conditions for hyperbolic systems. *Journal of Computational Physics*, 68(1):1–24.

Tomlin, A. S., Turànyi, T., Pilling, M. J., and Pilling, M. J. (1997). *Chapter 4 Mathematical tools for the construction, investigation and reduction of combustion mechanisms*, volume Volume 35, pages 293–437. Elsevier.

Turanyi, T. (1990). Reduction of large reaction-mechanisms. *New Journal of Chemistry*, 14(11):795–803.

Undapalli, S., Srinivasan, S., and Menon, S. (2009). Les of premixed and non-premixed combustion in a stagnation point reverse flow combustor. *Proceedings of the Combustion Institute*, 32(1):1537–1544.

Vajda, S., Valko, P., and Turanyi, T. (1985). Principal component analysis of kinetic-models. *International Journal of Chemical Kinetics*, 17(1):55–81.

van Oijen, J. and de Goey, L. (2000). Modelling of premixed laminar flames using flamelet-generated manifolds. *Combustion Science and Technology*, 161:113–137.

van Oijen, J. A. (2002). *Flamelet-Generated Manifolds: Development and Application to Premixed Laminar Flames*. PhD thesis, Eindhoven University of Technology.

van Oijen, J. A., Lammers, F. A., and de Goey, L. P. H. (2001). Modelling of complex premixed burner systems by using flamelet-generated manifolds. *Combustion and Flame*, 127(3):2124–2134.

Vervisch, L., Haugel, R., Domingo, P., and Rullaud, M. (2004). Three facets of turbulent combustion modelling: Dns of premixed flame, les of lifted nonpremixed v-flame and rans of jet-flame. *Journal of Turbulence*, 5(4):1–36.

Veynante, D., Fiorina, B., Domingo, P., and Vervisch, L. (2008). Using self-similar properties of turbulent premixed flames to downsize chemical tables in high-performance numerical simulations. *Combustion Theory and Modelling*, 12(6):1055–1088. 21st International Colloquium on the Dynamics of Explosion and Reactive Systems, Poitiers, FRANCE, JUL 22-26, 2007.

Veynante, D. and Vervisch, L. (2002). Turbulent combustion modeling. *Progress in Energy and Combustion Science*, 28(3):193–266.

Vicquelin, R., Fiorina, B., Darabiha, N., Gicquel, O., and Veynante, D. (2009). Coupling tabulated chemistry with large eddy simulation of turbulent reactive flows. *Comptes Rendus Mecanique*, 337(6-7):329–339.

Vicquelin, R., Fiorina, B., Darabiha, N., Veynante, D., Moureau, V., and Vervisch, L. (2008a). Coupling tabulated chemistry with large eddy simulation of turbulent reactive flows. Technical report, Center for Turbulence Research.

Vicquelin, R., Fiorina, B., Gicquel, O., Lartigue, G., and Poinsot, T. (2007). Large eddy simulations of mild combustion. 21th ICDERS, Poitiers, France.

Vicquelin, R., Fiorina, B., Lartigue, G., and Gicquel, O. (2008b). Large eddy simulation of a methane-air turbulent jet flame in a vitiated co-flow. SIAM, 11th International Conference on Numerical Combustion, Monterey, USA.

Vreman, A. W., van Oijen, J. A., de Goey, L. P. H., and Bastiaans, R. J. M. (2009). Subgrid scale modeling in large eddy simulation of turbulent combustion using premixed flamelet chemistry. *Flow, Turbulence and Combustion*, 82:511–535.

Warnatz, J., Mass, U., and Dibble, R. W. (2006). *Combustion: Physical and Chemical Fundamentals, Modeling and Simulation, Experiments, Pollutant formation*. Spinger, 4th edition.

Williams, F. (1985). *Combustion Theory*. Persus Books, 2nd edition.

Wu, Z., Starner, S. H., and Bilger, R. W. (2003). Lift-off heights of turbulent h_2/n_2 jet flames in a vitiated coflow. In *Proceedings of the 2003 Australian Symposium on Combustion and the 8th Australian Flame Days*, Monash University, Australia.

Wu, Z. J., Masri, A. R., and Bilger, R. W. (2006). An experimental investigation of the turbulence structure of a lifted h-2/n-2 jet flame in a vitiated co-flow. *Flow, Turbulence and Combustion*, 76(1):61–81.

Wunning, J. A. and Wunning, J. G. (1997). Flameless oxidation to reduce thermal no-formation. *Progress in Energy and Combustion Science*, 23(1):81–94.

Yang, W. and Blasiak, W. (2005). Numerical simulation of properties of a lpg flame with high-temperature air. *International Journal of Thermal Sciences*, 44(10):973–985.

Yimer, I., Becker, H. A., and Grandmaison, E. W. (2001). The strong-jet/weak-jet problem: new experiments and cfd. *Combustion and Flame*, 124(3):481–502.

Yoo, C. S., Sankaran, R., and Chen, J. H. (2009). Three-dimensional direct numerical simulation of a turbulent lifted hydrogen jet flame in heated coflow: flame stabilization and structure. *Journal of Fluid Mechanics*, 640(-1):453–481.

Yoshizawa, A. (1986). Statistical-theory for compressible turbulent shear flows, with the application to subgrid modeling. *Physics of Fluids*, 29(7):2152–2164.

Zhang, Y., Rogg, B., and Bray, K. N. C. (1995). 2-d simulation of turbulent autoignition with transient laminar flamelet source term closure. *Combustion Science and Technology*, 105(4-6):211–227.